

MICROSTRUCTURE FORMATION IN THE
FE-BASED HARDFACING ALLOY 5183 AND ITS
SLIDING WEAR BEHAVIOUR IN HIGH
TEMPERATURE WATER



The University of
Nottingham

UNITED KINGDOM • CHINA • MALAYSIA

MATTHEW JOHN CARRINGTON

*A thesis submitted to the University of Nottingham
for the degree of Doctor of Philosophy*

AUGUST 2020

DECLARATION

I declare that the thesis is the result of my own work which has been mainly undertaken during my period of registration for this degree at The University of Nottingham. I have complied with the word limit of 100,000 words. Work other than my own has been suitably referenced when included in the thesis.

Matthew J. Carrington

AUGUST 2020

ABSTRACT

Hardfacing alloys are used to minimise the tribological degradation of components subjected to sliding contact in the primary cooling systems of pressurised water reactors (PWRs). The combined effects of loaded sliding contact and corrosion within this environment ($\sim 200 - 300$ °C) currently require the extensive use of Stellite 6TM (Co-27-32%Cr-4-6%W-0.9-1.4%C in wt%). However, within the primary system, ⁵⁹Co-based wear debris is transmuted to the γ -emitting ⁶⁰Co which is hazardous for maintenance personnel. Therefore, significant efforts are being made to develop alternative Fe-based hardfacings manufactured by gas atomisation and powder (hot isostatic pressing) HIPing. Tristelle 5183 (Fe-21%Cr-10%Ni-7.5%Nb-5%Si-2%C in wt%) is one of several Fe-based hardfacings that have been developed to reduce the dependence on Stellite 6. However, none of these alloys possess a tribological performance that matches that of Stellite 6. The development of new and improved Fe-based hardfacings is restricted by two factors. Firstly, an incomplete understanding of phase and microstructural evolution during their processing. Secondly, the mechanical deformation and tribological/chemical degradation mechanisms during sliding contact in a PWR environment are not sufficiently well understood.

This thesis reports investigations into the microstructural evolution of HIPed Tristelle 5183 during processing and the tribological performance of both HIPed Tristelle 5183 and Stellite 6 over a range of temperatures in a simulated primary system PWR environment. These investigations give an improved understanding of tribological degradation within a primary system environment and provide insights needed for the development of future Fe-based hardfacings. This was made possible by using a bespoke tribometer which simulates a primary system PWR environment and microstructural characterisation techniques including, transmission electron microscopy (TEM), scanning electron microscopy (SEM), and X-ray diffraction (XRD). Particular attention has been given to understanding the nanoscale aspects of subsurface microstructural evolution leading to degradation

during sliding wear via the use of focused ion beam (FIB) produced site-specific lamellae and TEM.

Phase and microstructure formation in gas atomised Tristelle 5183 is highly dependent on particle size and thus cooling rate during atomisation. Powder particles $\gtrsim 53 \mu\text{m}$ are principally composed of γ -Fe dendrites with smaller quantities of α -Fe, an interdendritic silicide phase and NbC. Powder particles $\lesssim 53 \mu\text{m}$ also contain NbC and have increasing quantities of either dendritic α -Fe or cellular silicide phase; with decreasing amounts of γ -Fe as the particle size decreases. In contrast, HIPed Tristelle 5183 powder is principally composed of a γ -Fe solid solution matrix which surrounds both equiaxed Cr-based M_7C_3 ($\sim 14.0 \text{ vol}\%$) and Nb-based MX ($\sim 9.6 \text{ vol}\%$) precipitates, a small fraction of ferrite ($\sim 1.0 \text{ vol}\%$), and a π -ferrosilicide ($\sim 0.3 \text{ vol}\%$) phase. HIPing largely homogenises the microstructure, enables M_7C_3 precipitation and permits the decomposition of the metastable phases formed during atomisation.

The tribological degradation mechanisms of self-mated HIPed Tristelle 5183 during sliding in lithiated water are sensitive to test temperature between 20 - 250 °C. The modes of plastic deformation at low strains were revealed by TEM to be highly dependent on matrix stacking fault energy and thus test temperature. However, at high strains extensive TEM showed that the subsurface is completely engulfed by strain localisation phenomena irrespective of test temperature and very large strains are accommodated via grain boundary mediated deformation mechanisms and crystallographic slip. At 20 °C, degradation principally occurs via plastic ratcheting wear; the extrusion of metallic slivers permits the formation of ductile shear cracks and the failure of these slivers generates plate/flake like wear debris. At 250 °C, degradation occurs via several mechanisms: (i) the breakdown of oxide-based tribofilms, (ii) wear enhanced corrosion, and (iii) corrosion enhanced plasticity-type wear.

During the self-mated sliding contact of HIPed Stellite 6, the amount of material removal increases (16 - 39 times) between testing at 20 and 250 °C but the general degradation and deformation mechanisms largely remain the same. The deformation response of Stellite 6 is resistant to plastic strain localisation and

the removal of material is confined to the nanoscale where the synergistic effects of the chemical degradation and mechanical deformation permit the removal of nanoscale particulates via tribocorrosion. A temperature dependent increase in corrosion rate and SFE are believed to be the principal factors influencing the temperature dependent increase in wear by tribocorrosion, although corrosion is believed to be the dominant factor.

ACKNOWLEDGEMENTS

The work presented in this thesis would not have been possible without the guidance and encouragement from numerous individuals. Firstly, I would like to express my gratitude to Prof. David Graham McCartney (University of Nottingham) for his support, advice, and technical input through all stages of this research. His unwavering attention to detail, passion for materials science, and perpetual optimism have always been enlightening and I would most definitely not have progressed to this stage without him. I would also like to thank, Prof. Philip Shipway (University of Nottingham) and Dr. David Stewart (Rolls-Royce) for their excellent discussion, feedback, and direction throughout the project. The backing and financial support provided by Rolls-Royce has been greatly appreciated and it is acknowledged that without this funding the present research would not have been possible.

Within my research group, I gratefully acknowledge Dr. Jamie Daure for technical support and both Dr. Deen Zhang and Dr. Vilma Ratia for operating the in autoclave tribometer. I would like to extend my thanks to the academics and technical staff in the Wolfson building and Nanoscale and Microscale Research Centre (NMRC) at the University of Nottingham for their support and assistance in experimental work. These include Mr. Max Mason, Dr. Nigel Neate, Dr. Elisabeth Steer, Mr. Martin Roe, Dr. Hannah Constantin, Prof. Paul Brown, Mr. Graham Malkinson, Mr. Thomas Buss and Mr. Jason Greaves. Mr. Max Mason and Dr. Nigel Neate deserve special reference and their exceptional expertise and impact on this work merits additional recognition. Additionally, I would like to extend my gratitude to Dr. Geoff West and Dr. Fengzai Tang from the University of Warwick for their assistance with FIB sample preparation and TEM analysis. I also gratefully appreciate Dr. Caroline Langensiepen for her excellent support and feedback throughout the latter stages of the project.

Finally, and most importantly, I would like to thank my family and close friends for their enduring support and encouragement.

PUBLICATIONS

1. M. J. Carrington J. Daure, V. L. Ratia, P. H. Shipway, D. G. McCartney, D. A. Stewart, Microstructural characterisation of Tristelle 5183 (Fe-21%Cr-10%Ni-7.5% Nb-5%Si-2%C in wt%) alloy powder produced by gas atomisation. *Materials & Design*, volume 164, 2019.
2. V. L. Ratia, D. Zhang, M. J. Carrington J. L. Daure, D. G. McCartney, P. H. Shipway, D. A. Stewart, The effect of temperature on sliding wear of self mated HIPed Stellite 6 in a simulated PWR water environment. *Wear*, volume 420-421, pages 215-225, 2019.
3. V. L. Ratia, D. Zhang, M. J. Carrington J. L. Daure, D. G. McCartney, P. H. Shipway, D. A. Stewart, Comparison of the sliding wear behaviour of self mated HIPed Stellite 3 and Stellite 6 in a simulated PWR water environment. *Wear*, volume 426-427, pages 1222-1232, 2019.
4. G. N. Karimi, M. J. Carrington J. Thomas, P. H. Shipway, D. A. Stewart, T. Hussain, The role of microstructural development in the hydrothermal corrosion of cast and HIPed Stellite 6 analogues in simulated PWR conditions. *Corrosion Science*, volume 159, 2019.
5. J. L. Daure, M. J. Carrington, P. H. Shipway, D. G. McCartney, D. A. Stewart, A comparison of the galling wear behaviour of PVD Cr and electroplated hard Cr thin films. *Surface and Coatings Technology*, volume 350, pages 40-47, 2018.
6. J. Bame, C. Hoeck, M. J. Carrington, C. P. Butts, C. M. Jäger, A. K. Croft, Improved NOE fitting for flexible molecules based on molecular mechanics data a case study with S-adenosylmethionine. *Physical Chemistry Chemical Physics*, volume 20, pages 7523-7531, 2018.

CONTENTS

1	Introduction	1
2	Literature Review	5
2.1	Operation of a pressurised water reactor (PWR)	5
2.1.1	Introduction	5
2.1.2	Materials in the primary cooling circuit	5
2.1.3	Hardfacing alloys in the primary system of a PWR	9
2.2	Degradation of alloys within a PWR environment	10
2.2.1	Water chemistry within a PWR	10
2.2.2	Chemical degradation (corrosion and oxidation)	12
2.2.3	Mechanical degradation and wear	14
2.2.4	Tribocorrosion	19
2.3	Hardfacing processes	28
2.3.1	Hardfacing deposition from the liquid state	28
2.3.2	Hardfacing by Hot isostatic pressing (HIP) and HIP bonding	30
2.4	Stellite hardfacing alloys	36
2.4.1	Introduction to Stellite	36
2.4.2	The allotropic fcc \leftrightarrow hcp transformation in cobalt and its alloys	37
2.4.3	Metallurgy and microstructure of Stellite 6	40
2.4.4	Deformation behaviour of Stellite alloys	44
2.4.5	Degradation of Stellite in a PWR environment	46
2.4.6	Related wear and degradation studies on Stellite and other Co-based alloys	48
2.5	Fe-based Hardfacing alloys	53
2.5.1	Introduction to Fe-based hardfacing alloys	53
2.5.2	Deformation structures in austenitic Fe-based alloys	55
2.5.3	Evolution and development of Fe-based hardfacings	66

2.5.4	Related studies on the tribological degradation of stainless steels	81
2.6	Summary	83
3	Experimental Methodology	86
3.1	Materials and heat treatments	86
3.1.1	Nitrogen gas atomised Tristelle 5183	86
3.1.2	HIPed and HIP bonded Tristelle 5183	86
3.1.3	Cast Tristelle 5183	87
3.1.4	HIPed Stellite 6	88
3.2	X-Ray diffraction and Rietveld analysis	88
3.2.1	Principles of XRD	89
3.2.2	Laboratory X-ray diffractometers	94
3.2.3	Sample Preparation	94
3.2.4	Principles of Rietveld	95
3.3	Optical and Scanning Electron Microscopy (SEM)	99
3.3.1	Principles of scanning electron microscopy (SEM)	99
3.3.2	Laboratory scanning electron microscopy	108
3.3.3	Metallurgical sample preparation for microscopy	108
3.3.4	Optical microscopy and metallurgical sample preparation	109
3.4	Transmission electron microscopy (TEM)	109
3.4.1	Principles of TEM	109
3.4.2	Sample preparation using a focused ion beam (FIB)	114
3.4.3	Laboratory TEM and Dual beam instrumentation	116
3.5	Mechanical testing	116
3.5.1	Hardness testing	117
3.5.2	Wear Testing	117
4	Microstructural evolution and formation in gas atomised Tristelle 5183 powder	121
4.1	Introduction	121
4.2	Results	122

4.2.1	Phase identification of gas atomised Tristelle 5183 powder using XRD	122
4.2.2	Microstructure of 63-75 μm sized powder	125
4.2.3	Microstructure of < 20 μm sized powder	127
4.2.4	Microstructural characterisation of cast Tristelle 5183	133
4.3	Discussion	134
4.3.1	Mould cast Tristelle 5183	134
4.3.2	Phase selection and microstructure formation in gas atomised Tristelle 5183 powder particles	137
4.3.3	Analytical droplet cooling rate model	143
4.4	Conclusions	147
5	Microstructural characterisation of hot isostatically pressed Tristelle 5183	149
5.1	Introduction	149
5.2	Results	149
5.2.1	Phase identification using XRD	150
5.2.2	Microstructural characterisation - Optical microscopy	150
5.2.3	Microstructural characterisation - SEM	151
5.2.4	Microstructural characterisation - TEM	155
5.3	Discussion	158
5.3.1	Matrix evolution during HIPing	160
5.3.2	Phase evolution during HIPing	164
5.3.3	Oxide inclusions and prior particle boundaries (PPBs)	167
5.4	Conclusions	168
6	Tribological assessment of self-mated HIPed Stellite 6 subjected to sliding in lithiated water	170
6.1	Introduction	170
6.2	Results	171
6.2.1	As-received HIPed Stellite 6: Phases and microstructures . .	171
6.2.2	Autoclave sliding contact test results - mass and volume loss	173

6.2.3	Microstructural characterisation of the contacting surfaces - surface topography	175
6.2.4	X-ray diffraction from the worn surface	177
6.2.5	Sub-surface microstructural characterisation of Stellite 6 . . .	178
6.3	Discussion	186
6.3.1	Matrix deformation and role of the carbide phase during sliding contact	188
6.3.2	Mechanical removal of material	194
6.3.3	Oxidation and tribocorrosion in lithiated water	196
6.3.4	Synergistic degradation effects in lithiated water	197
6.4	Conclusions	201
7	Tribological assessment of self-mated HIPed Tristelle 5183 subjected to sliding in lithiated water	203
7.1	Introduction	203
7.2	Results	204
7.2.1	Autoclave sliding contact test results - mass and volume loss measurements	204
7.2.2	Sub-surface microhardness profiles	206
7.2.3	Microstructural characterisation of the contacting surfaces - surface topography	206
7.2.4	X-ray diffraction analysis of sliding contact test samples . . .	212
7.2.5	Sub-surface microstructural characterisation - SEM	213
7.2.6	Sub-surface microstructural characterisation following 20 °C testing - TEM	217
7.2.7	Sub-surface microstructural characterisation following 250 °C testing - TEM	222
7.3	Discussion	226
7.3.1	Layer 1 - homogeneous modes of deformation	229
7.3.2	Layer 2 - strain localisation and inhomogeneous modes of deformation	236
7.3.3	Layer 3 - The tribological interaction layer	241

7.3.4	Evaluating the TAM via X-ray diffraction	253
7.4	Conclusions	261
8	A comparative assessment of the tribological performance of Tristelle 5183 and Stellite 6	263
8.1	Introduction	263
8.2	An overview of degradation mechanisms in response to autoclave sliding contact	263
8.2.1	Stellite 6	263
8.2.2	Tristelle 5183	265
8.3	Results - Autoclave sliding contact tests at temperatures between 20 and 250 °C	266
8.4	Discussion - The mechanistic differences in tribological performance	271
8.4.1	Deformation characteristics in response to sliding contact .	271
8.4.2	Chemical degradation during sliding contact	276
8.4.3	The influence of frictional heating	278
8.5	Discussion - The suitability of Tristelle 5183 in PWR primary circuit operating conditions (250 °C)	279
8.6	Conclusions	281
9	Conclusions and future research	283
9.1	Conclusions	283
9.1.1	Microstructural characterisation of Tristelle 5183	283
9.1.2	Sliding contact tribological behaviour of Tristelle 5183	284
9.1.3	Sliding contact tribological behaviour of Stellite 6	286
9.1.4	Comparison of Stellite 6 and Tristelle 5183	287
9.2	Future research	287

LIST OF FIGURES

2.1	Simplified schematic of a typical pressurised water reactor. (1) illustrates the reactor core where heat is generated as a result of nuclear fission. (2) pressurised water in the primary cooling circuit is transported to the steam generator. (3) inside the steam generator heat is exchanged from the primary coolant loop to the secondary loop where water is vaporised producing steam. (4) The steam-line directs steam to the turbine which in turn drives an electrical generator.	6
2.2	Simplified schematic of a primary system of a PWR (two-loop Westinghouse plant) which in this case is comprised of two cooling loops therefore it contains two steam generators, two reactor coolant pumps, and a pressuriser.	7
2.3	Simplified schematic of a typical gate valve cross section in its closed position. The valve seats and components subjected to wear are shown in orange and these components require hardfacing.	8
2.4	Schematic of the modified chemistry regime at 300 °C.	11
2.5	Schematic of the coordinated chemistry at elevated pH (7.1) regime at 300 °C with lithium below 3.5 ppm.	12
2.6	Schematic illustrating the material flows which result in the formation of third bodies during the tribocorrosion of a passive metal.	25
2.7	Simplified schematic illustrating the different regions beneath a worn surface of a metal to metal sliding contact.	27
2.8	Longitudinal wear track FIB cross section taken from 304L post reciprocating sliding against a alumina ball at a passive potential (-0.5 V) under a load of 7 N.	28
2.9	Simplified schematic of a cross sectioned HIP unit.	30
2.10	Simplified schematic of the main stages of the HIP consolidation cycle.	32

2.11 Schematic illustrating the paths through which matter is transported during neck growth.	34
2.12 Idealised schematic of the main stages of atomisation.	35
2.13 (a) shows the stacking sequence of untransformed fcc Co. (b) illustrates an intrinsic stacking fault which is the embryo for hcp transformation. (c) shows a completely transformed hcp region resulting from the ordered glide of a uniform array of Shockley partials.	39
2.14 Graph illustrating the relationship between carbon (plus boron) content on the hardness of Stellite alloys. Both the compositions and hardness values are from the work of Antony.	42
2.15 (a) Secondary electron image of etched Stellite 6 powder. (b) BSE micrograph of the typical cast microstructure of Stellite 6. (c) BSE micrograph of the typical HIPed microstructure of Stellite 6.	45
2.16 Deformation structures observed in Co-Ni-Cr-Mo alloys near room temperature as a function of stacking fault energy.	47
2.17 HR-TEM illustrating the alignment of the basal planes parallel to the direction of shear in a Stellite alloy.	52
2.18 Data from the work of Buckley and Johnson illustrating the coefficient of friction for various hcp metals sliding against 440C steel in a vacuum with a 100 g load and a sliding velocity of 2 m/s.	53
2.19 (a) Idealised schematic depicting the dissociation of a perfect dislocation b_1 into Shockley partials b_2 and b_3 . (b) (lower) Hard sphere model of a close packed plane of atoms which resides just below a (111) glide plane with atoms situated just above the plane positioned at a sites. (b) (upper left) glide of a perfect dislocation from the lower to the upper right of the figure with burgers vector b_1 and line sense ζ . (b) (upper right) vector diagram illustrating a perfect dislocation b_1 and Shockley partial dislocations b_2 and b_3	56

2.20	Schematic of an intrinsic stacking fault generated by shearing operations on the $\{111\}$ planes. In this instance, the B plane and all planes above it undergo a shear displacement $\frac{1}{6}[\bar{2}11]$ parallel to the B plane. Therefore, the B plane moves into the C position and each plane above it undergoes the transition $A \rightarrow B, B \rightarrow C$ or $C \rightarrow A$.	57
2.21	(a) Schematic depicting the temperature dependence of the fault energy (γ) for three faults of different thickness. (b) Illustration depicting the total free energy (G) as a function of partial dislocation separation (r) for partial dislocations bounding a faulted region. . .	58
2.22	Bright field image and accompanying diffraction pattern illustrating the formation of ϵ -martensite shear bands which results from the so called bundling of stacking faults.	59
2.23	The formation of an α' needle at the intersection between two ϵ laths.	60
2.24	A schematic depicting the Olson and Cohen model for the strain induced nucleation of α' -martensite. The left and right images show a before and after schematic representation of the intersection of localised slip bands respectively.	61
2.25	TEM micrograph depicting the intersection of two ϵ -martensite laths resulting in the formation of α' -martensite. It is clear that one of the ϵ -martensite laths contains regions of austenite.	62
2.26	Schematics taken from the work of Fujita and Katayama. (a) illustrates the nucleation and growth of α -martensite via the aid of the stair-rod type cross slip of partial dislocations from the coplanar primary slip plane (P_c) to the coplanar conjugate slip plane (S_c). (b) depicts the growth of α' -martensite via the coalescence of several α' -crystallites which formed by localised $\epsilon \rightarrow \alpha'$ transformations. .	63
2.27	The direct nucleation of α' at a grain boundary in 304 stainless steel ($\gamma \rightarrow \alpha'$).	64

2.28	TEM micrographs taken from the work of Huang et al. illustrating the nucleation of α' -martensite at the intersection of deformation twins. (a) Bright-field TEM micrograph. (b) Dark-field image of α' -martensite taken from the diffraction spot 1 in (e,f). (c) and (d) correspond to dark field images of deformation twins taken from the diffraction spots 2 and 3 in (e,f) respectively. (e) depicts a SAD pattern of (a) with zone axis $[011]_{\gamma} \parallel [111]_{\alpha'}$. (f) is an indexed pattern corresponding to (e). The regions of α' -martensite are marked by arrows in (a) and (b).	65
2.29	Illustration taken from the work of Fujita and Katayama depicting the direct $\gamma \rightarrow \alpha'$ at a γ -grain boundary.	66
2.30	Optical micrograph depicting the microstructure of Norem 02 deposited via PTA welding. The regions denote the following: (A) austenite dendrites, (B) ferrite islands, (C) interdendritic eutectic region principally comprised of a M_7C_3 type carbide and austenite eutectic and (D) precipitate regions, namely $M_{23}C_6$ and or M_3C carbides and ferrite.	72
2.31	Summary data taken form the work of Smith et al. illustrating the dependence of the relative α'/γ ratio, the γ and α peak width, and the true stress on both true strain and test temperature.	74
2.32	Graphs taken from the work of Kim and Kim.(a) Mass loss measurements of Norem 02 and Stellite 6 as a function of test temperature after reciprocating self-mated sliding wear testing in air for 100 cycles (9 mm stroke) with a contact stress of 103 MPa. (b) Microhardness profiles beneath the worn surface of Norem 02 tested at different temperatures.	75
2.33	TEM brightfield micrographs of the worn surfaces of Norem 02 taken from the work of Kim and Kim.	76
2.34	Microstructure of HIPed and solution annealed Nitromaxx where region (A) γ -Fe matrix phase, (B) $M_{23}C_6$ type carbide, and (C) Cr_2N type nitride.	77

2.35	Computationally predicted equilibrium phase fraction diagram for Nitromaxx.	78
3.1	Diffraction of X-rays by a crystal.	91
3.2	X-ray scattering from two planes in a primitive crystal.	92
3.3	Vector phase diagram illustrating the superposition of two waves diffracted from two different atoms which make up a simple unit cell.	93
3.4	Vector phase diagram illustrating the superposition of 5 waves diffracted waves scattered from a primitive unit cell.	93
3.5	Schematic illustration of interaction volume between an incident electron beam and matter.	101
3.6	Schematic of the energy spectrum of electrons emitted from the sample surface. SE, BSE, AE and E_0 respectively represent secondary electrons, backscattered electrons, Auger electrons and the electron energy of the primary incident electron beam.	102
3.7	Schematic illustrating the geometric set-up of an EBSD measurement system.	106
3.8	Schematic illustrating the formation of an electron backscatter pattern (EBSP).	107
3.9	Schematic of the optical components in a basic TEM.	110
3.10	(a) Secondary electron image depicting a Tristelle 5183 powder particle with a platinum strip which has trenches ion milled on either side. (b) secondary electron image of the nanomanipulator performing the lift-out on a Tristelle 5183 powder particle. (c) HAADF-STEM image of a bulk HIP and HIP bond Tristelle 5183 lamella after final thinning and cleaning. (d) BF-TEM image of a Tristelle 5183 wear track lamella after final thinning and cleaning.	115
3.11	Simplified schematic of a pin on disk wear test apertures.	118

3.12	Subsurface Hertzian contact stresses for a point contact along the contacts axis of symmetry for Stellite 6 (a) and Tristelle 5183 (b). σ_r (red), σ_θ (red) and σ_z (blue) are the principal stresses, τ_1 (green) and τ_2 (green) are the principal shear stresses, and σ_{VM} is the Von Mises stress. These stresses wear calculated for a 50 mm radius sphere in contact with a flat plate under a 39.24 N load.	120
4.1	XRD patterns obtained from the different powder size fractions of gas atomised Tristelle 5183. The vertical markers indicate the Bragg peak positions for the different phases.	123
4.2	Experimental XRD patterns (black) for the $< 20 \mu\text{m}$ and $63\text{-}75 \mu\text{m}$ powder size fractions. Calculated patterns determined via Rietveld refinement are indicated in red and the difference between experimental and calculated diffraction patterns is presented in grey. The vertical markers indicate the refined Bragg peak positions (based on the $< 20 \mu\text{m}$ powder fraction).	126
4.3	(a) Depicts a bar chart showing the proportions of phases in the $< 20 \mu\text{m}$ and $63\text{-}75 \mu\text{m}$ powder size fractions from Rietveld refinements of XRD data. (b) shows a plot of refined lattice parameters for MX-1, MX-2 and MX-3 against powder size fraction obtained by Rietveld refinement.	127

-
- 4.4 (a) and (b) show SEM images of a cross section through powder particles consistent with the 63-75 μm powder size fraction. (a) is a low magnification BSE image showing a bright contrast rounded pre-existing Nb(C,N) particle and uniformly distributed primary Nb(C,N) particles. (b) is a high magnification BSE image showing the micron-sized primary Nb(C,N) particles within a dendritic matrix and secondary, nanoscale Nb(C,N) particles in the interdendritic regions. (c) and (d) respectively depict EBSD derived IPFZ orientation phase distribution maps. The colours of the grains in (c) correspond to the crystallographic axes in the relevant stereographic triangles, the corresponding phases can be identified in (d). 128
- 4.5 Representative microstructure of a powder particle from the 63-75 μm size fraction. (a) is a bright field STEM image showing a dendritic matrix, an interdendritic phase as well as primary and secondary Nb(C,N) structures. (b), (c) and (f) show X-ray maps of the same region depicted in (a) and correspond to maps for Cr, Ni and Nb respectively. (d) and (e) show SAD patterns from the areas marked as e and d in (a). (d) shows an SADP indexed to fcc $\gamma\text{-Fe}$ [1 – 10] zone axis and the pattern in (e) is indexed to a [0 – 10] zone axis of a phase isostructural to $\text{Fe}_5\text{Ni}_3\text{Si}_2$. (f) clearly shows the locations of the Nb-rich particles. 129
- 4.6 (a) and (b) show representative BSE-SEM micrographs of powder cross sections consistent with the < 20 μm powder size fraction. (c) and (d) respectively show EBSD derived IPFX orientation and phase distribution maps of a powder cross section consistent with the < 20 μm powder size fraction. The colours of the grains in (d) correspond to the crystallographic axes in the relevant stereographic triangles, the corresponding phases can be identified in (c). 131

4.7	Representative microstructure of a powder particle from the < 20 μm size fraction. (a) depicts an STEM bright field image where the regions marked (a), (b), (c) and (d) correspond to the respective SADP's. (a) shows a dendritic region (b), an angular particle (c), a matrix phase with a cellular structure (d) and a cellular boundary region (e). (b) is indexed to $\alpha\text{-Fe}$ [001], (c) is Nb(C,N) [010], (d) and (e) exhibit the zone axes [010] and [001] of a phase isostructural to $\text{Fe}_5\text{Ni}_3\text{Si}_2$	132
4.8	Microstructure of the intercellular region of a particle consistent with the < 20 μm size fraction. (a) illustrates a STEM bright field image which shows nanoscale particles in the silicide matrix. (b) illustrates a Nb EDS map of the region depicted in (a). (c) shows a HRTEM micrograph of a Nb-rich precipitate and (d) shows the corresponding FFT diffraction pattern from the box region depicted in (c), indexed to Nb(C,N) [101] zone axis.	133
4.9	Typical microstructure of cast Tristelle 5183 alloy. (a) Shows a phase distribution map overlaid onto a band contrast map derived from EBSD data showing large Nb(C,N) crystals in a $\gamma\text{-Fe}$ dendritic matrix (grey) with interdendritic Cr_7C_3 , Nb(C,N), bcc $\alpha\text{-Fe}$ and a phase isostructural to $\text{Fe}_5\text{Ni}_3\text{Si}_2$. (b) shows a IPFY orientation map, where the colours of the grains correspond to the crystallographic axes in the stereographic triangle for each phase. (c) and (d) are EDS maps of Nb and Si respectively confirming that the large crystals are Nb-rich and that Si is preferentially segregated to the interdendritic $\alpha\text{-Fe}$ and silicide phases.	135
4.10	Phase fraction diagram for Tristelle 5183 calculated using ThermoCalc and the TcFe7 database.	137
4.11	Plots of cooling rate versus particle diameter during nitrogen gas atomisation for different relative gas velocities. The cooling rate is calculated at the liquidus temperature of 316 stainless steel.	146

5.1	XRD pattern obtained from the polished surface of the as-received, HIPed Tristelle 5183. The ICDD database files used to index the diffractogram are shown in the legend. Tristelle 5183 exhibits reflections for γ -Fe (fcc), M_7C_3 , NbC (MX), α -Fe (bcc), and a trace of π -ferrosilicide.	151
5.2	Optical micrograph of etched HIPed Tristelle 5183 revealing prior particle boundaries, carbide precipitates and matrix phase grain boundaries.	152
5.3	BSE-SEM micrographs (a-c) and EDX maps (d-h) depicting the microstructural detail of as-received HIPed Tristelle 5183. The BSE-SEM micrographs show MX precipitates (bright contrast), M_7C_3 carbides (darkest contrast) and matrix grains (varying grey contrast) which are principally γ -Fe. The EDX maps (d), (e), (f), (g) and (h) are from the same region shown in (c) and are maps for Fe, Cr, Si, Ni and Nb respectively.	153
5.4	BSE-SEM micrographs depicting dark contrast (low mean atomic number) precipitates which reveal the prior particle boundaries within HIPed microstructure of Tristelle 5183. (b) shows the boxed region in (a) and the dark contrast precipitates are indicated by red arrows in (b).	154
5.5	EBSD-derived phase and IPFZ orientation maps of the typical microstructure of HIPed Tristelle 5183. The superimposed dashed white lines indicate the averaged positions of prior particle boundaries.	155
5.6	EBSD-derived kernel average misorientation (KAM) map of the γ -Fe grains with the HIPed microstructure of Tristelle 5183 revealing the intragrain localised orientation changes and thus subgrain structures. All the other phases within HIPed Tristelle 5183 are shown in grey.	156

5.7	(a) depicts a HAADF-STEM micrograph of HIPed Tristelle and (b), (c), (d), (e) and (f) are corresponding EDX maps for Fe, Cr, Ni Si and Nb respectively. (a) shows a grey contrast austenitic matrix with bright (Cr-rich (c)) and dark (Nb-rich (f)) contrast precipitates (M_7C_3 and MX carbonitride respectively) and (e) reveals the Si-rich π -ferrosilicide phase.	157
5.8	(a) depicts a representative BF-STEM micrograph showing the heavily flawed microstructure of the M_7C_3 precipitates within HIPed Tristelle 5183 and (b) shows an accompanying EDX Cr map of this same region. (c) shows a BF-TEM micrograph of the same precipitate shown in (a) and (d) is the SADP corresponding to (c).	159
5.9	(a), (b) and (c) show BF-TEM micrographs depicting the morphologies of several different π -ferrosilicide regions of dark contrast within the HIPed microstructure of Tristelle 5183. (a) and (b) show plate-like grains whereas (c) depicts a π -ferrosilicide grain which forms at the triple junction. (d) shows a SADP from the triple junction π -ferrosilicide phase (at a different tilt to (c)) indexed to a [213] zone axis of the π -ferrosilicide phase identified by Bowden et al. . .	160
6.1	XRD pattern obtained from the polished surface of the as-received, HIPed Stellite 6. The ICDD database files used to index the diffractogram is shown in the legend. Stellite 6 exhibits reflections for γ -Co (fcc), M_7C_3 and a very small fraction of ϵ -Co (hcp).	172
6.2	BSE-SEM channelling contrast micrographs of HIPed Stellite 6 showing M_7C_3 carbides (darkest contrast) and cobalt-based matrix grains with annealing twins.	173
6.3	EBSD-derived phase and IPFZ orientation maps of the typical microstructure of HIPed Stellite 6.	173

6.4	Graph showing the effect of autoclave test temperature on the mass and volume loss following 5 h sliding contact testing with a 4 kg dead load. The bars represent mean values and the error bars represent the minimum and maximum values of combined pin and disk wear ($n_{20}=3$, $n_{250}=6$).	174
6.5	Stereoscope optical micrographs of Stellite 6 disk ((a) and (b)) and pin ((c) and (d)) tribologically affected surfaces following sliding contact autoclave tests at 20 ((a) and (c)) and 250 °C ((b) and (d)). .	176
6.6	Plan view BSE-SEM micrographs showing the microstructure of the tribologically affected surface of Stellite 6 disk samples after sliding contact tests in an autoclave environment at 20 °C (a and c) and 250 °C (b and d) for 5 hours. Sliding direction was horizontal on the image.	177
6.7	XRD patterns of Stellite 6 from the ground surface prior to testing and from within the wear track (following testing at 25 and 250 °C). Patterns normalised to the reflection of maximum intensity. . . .	179
6.8	Cross-sectional BSE-SEM channelling contrast micrographs of Stellite 6 taken from within the wear track (parallel to the sliding direction) after testing at 20 °C (a, c) and 250 °C (b, d). M_7C_3 (dark contrast) carbides are distributed in Co-rich matrix with planar deformation structures.	180
6.9	EBSD derived phase maps ((a) and (b)), band contrast maps ((c) and (d)) and inverse pole figures ((e) and (f)) taken perpendicular to the sliding direction of HIPed Stellite 6 following autoclave sliding wear testing at 20 ((a), (c) and (e)) and 250 °C ((b), (d) and (f)). . . .	182
6.10	Representative BF-STEM micrographs of Stellite 6 taken from within the wear track (parallel to the sliding direction) after testing at 20 °C (a, c) and 250 °C (b, d).	183

6.11	Representative BF-TEM micrographs ((a) and (c)) and SADPs ((c) and (d)) from samples taken parallel to the direction of shear, showing the deformation structures directly beneath the contacting surface of Stellite 6 after exposure to sliding contact at 20 °C ((a) and (b)) and 250 °C ((c) and (d)). The SADPs, (b) and (d), index to hcp ϵ -Co and have been recorded from the regions marked with circles in (a) and (c) respectively.	184
6.12	(a) BF-STEM micrograph of Stellite 6 taken parallel to the direction of shear following exposure to sliding contact at 250 °C. (b), (c) and (d) show EDX maps of the same region depicted in (a) and correspond to maps for O, Cr and Co respectively.	185
6.13	Micrographs taken parallel to the direction of sliding which show the formation of a mechanically mixed nanolayer over an M_7C_3 carbide positioned at the contacting surface of Stellite 6 following testing at 250 °C. (a) depicts a HAADF-STEM micrograph and (b) shows an accompanying Co map. (c) and (d) show higher magnification BF-TEM micrographs of this same carbide.	186
6.14	BF-STEM (a) and HAADF-STEM (b) micrographs taken parallel to the sliding direction showing a thin ~ 100 nm thick fractured M_7C_3 carbide situated at the contacting surface of Stellite 6 following testing at 20 °C.	187
6.15	Schematic illustrating the different layers within the TAM used to describe the continuum of plastic deformation within the subsurface. The dashed line is an idealised representation of the extent of plastic flow within the subsurface (not to scale).	189
7.1	Graph showing the effect of autoclave test temperature on the mass and volume loss of self-mated Tristelle 5183 following 5 h sliding contact testing with a 4 kg dead load. The bars represent mean values and the error bars represent the minimum and maximum values of combined pin and disk wear ($n_{20}=3$, $n_{250}=6$).	205

7.2	Hardness microhardness (10 g load) profiles taken from perpendicular cross sections of wear tracks following autoclave sliding contact at both 20 and 250 °C. The errors have been reported as the standard error of the mean (n = 3).	207
7.3	Stereoscope optical micrographs of Tristelle 5183 disk ((a) and (b)) and pin ((c) and (d)) tribologically affected surfaces following sliding contact autoclave tests at 20 ((a) and (c)) and 250 °C ((b) and (d)).	208
7.4	SE (a) and BSE (b and c) SEM micrographs showing the microstructure of the tribologically affected surface of Tristelle 5183 disk samples after sliding contact tests in an autoclave environment at 20 °C for 5 hours. (c) is a higher magnification image of the region marked with the white square in (b). The sliding direction is horizontal to the figure in all cases.	209
7.5	BSE (a and b) and SE (c) SEM micrographs showing the microstructure of the tribologically affected surface of Tristelle 5183 disk samples after sliding contact tests in an autoclave environment at 250 °C for 5 hours. (a) covers the entire width of the wear track and the sliding direction is horizontal. The sliding direction is vertical in (b) and (c). (d), (e), (f) and (g) show EDX maps of the same region depicted in (b and c) and correspond to the maps for O, Fe, Nb and Cr respectively. The sliding direction is horizontal in (a) and vertical in (b - g).	211
7.6	High magnification BSE (a) and SE (b) SEM micrographs showing the microstructure of the tribologically affected surface of Tristelle 5183 disk samples after sliding contact tests in an autoclave environment at 250 °C for 5 hours. The sliding direction is horizontal to the figure in all cases.	212
7.7	XRD patterns of Tristelle 5183 in the as-received HIPed form and from within the wear track (following testing at 20 and 250 °C). Patterns normalised to the reflection of maximum intensity.	214

7.8	<p>Cross-sectional BSE-SEM channelling contrast micrographs of Tristelle 5183 taken from within the wear track (parallel to the sliding direction) after testing at 20 °C (a, c and f) and 250 °C (b, e and g). The insert in (b) shows the contacting surface at a different brightness and contrast revealing the presence of a tribofilm. (d) shows an oxygen EDX map of the surface region depicted in (b). (c) and (e) show higher magnification images of the regions marked with the white square in (a) and (b) respectively. The sliding direction is horizontal to the figure in all cases.</p>	216
7.9	<p>Cross-sectional BSE-SEM channelling contrast micrographs of Tristelle 5183 plate-like wear debris retrieved after testing at 20 °C. (b) is a higher magnification image of the region marked with the white square in (a).</p>	217
7.10	<p>Representative BF-STEM micrographs depicting the tribologically induced deformation structures in a FIB lamellae of Tristelle 5183 taken from 60 μm beneath the contacting surface (parallel to the sliding direction) following autoclave sliding testing at 20 °C. (c) shows the microstructural detail of the region marked with the white box in (b). The sliding direction is indicated by the red arrows.</p>	218
7.11	<p>TEM analysis illustrating the $\gamma \rightarrow \epsilon$ deformation induced martensitic transformation in Tristelle 5183. (a) shows a representative BF-TEM micrograph of Tristelle 5183 taken from 60 μm beneath the contacting surface (parallel to the sliding direction) following autoclave sliding testing at 20 °C. (b and c) show the same select area diffraction pattern taken from the region marked with the white circle in (a). (c) shows that this SADP indexes to both fcc γ-Fe (red) and hcp ϵ-Fe (blue). (d) shows a DF-TEM micrograph of the same region depicted in (a), taken with the ϵ-Fe diffraction spot marked with the blue circle in (b).</p>	220

7.12	TEM analysis illustrating the $\gamma \rightarrow \epsilon \rightarrow \alpha'$ deformation induced martensitic transformation in Tristelle 5183. (a) shows a representative BF-TEM micrograph of Tristelle 5183 taken from 60 μm beneath the contacting surface (parallel to the sliding direction) following autoclave sliding testing at 20 °C. (b and c) show the same select area diffraction pattern taken from the region marked with the white circle in (a). (c) shows that this SADP indexes to fcc γ -Fe (red), bcc α' -Fe (green) and hcp ϵ -Fe (blue and orange). (d), (e) and (f) show DF-TEM micrographs of the same region depicted in (a). (d) was taken with the ϵ -Fe diffraction spot marked with the orange circle in (b). (e) was taken with ϵ -Fe diffraction spot marked with the blue circle in (b). (f) was taken with α' -Fe diffraction spot marked with the green circle in (b). The sliding direction is indicated the by red arrow.	221
7.13	(a) and (b) show representative HAADF-STEM micrographs taken parallel to the sliding direction showing the deformation structures directly beneath the contacting surface following sliding contact at 20 °C. (c), (d), (e), (f), (g) and (h) show EDX maps of the same region depicted in (a) and correspond to the maps for Fe, Cr, Nb, Si, Ni and Pt respectively. The sliding direction is horizontal to the figure in all cases.	223
7.14	(a) and (b) show representative BF-STEM micrographs taken parallel to the sliding direction showing the deformation structures directly beneath the contacting surface following sliding contact at 20 °C. (b) shows the microstructural detail of the region marked with the white box in (a). The sliding direction is horizontal to the figure in all cases.	224

7.15	Representative HAADF-STEM (a and b) and BF-TEM (c) micrographs taken parallel to the sliding direction showing the deformation structures directly beneath the contacting surface following autoclave sliding contact at 250 °C. (b) shows the microstructural detail of the region marked with the white box in (a). (d) shows a SADP from the circled region in (c) and indexes to γ -Fe (fcc). The sliding direction is horizontal to the figure in all cases.	225
7.16	(a) HAADF-STEM micrograph of Tristelle 5183 taken parallel to the direction of shear following exposure to sliding contact at 250 °C showing the microstructural detail of a duplex-type corrosion product on the contacting surface. (b), (c), (d), (e), (f), (g) and (h) show EDX maps of the same region depicted in (a) and correspond to maps for O, Fe, Cr, Ni, Si, Nb and Pt respectively. The sliding direction is horizontal to the figure in all cases.	226
7.17	Schematic illustrating the different layers within the TAM used to describe the continuum of plastic deformation within the subsurface. The dashed line is an idealised representation of the extent of plastic flow within the subsurface (not to scale).	228
7.18	Simplified flow diagram showing the key phenomena and modes of degradation which occur during autoclave sliding contact at 250 °C.	247
7.19	XRD patterns of Tristelle 5183 from within the wear track following testing at 20 °C and from within the wear track of a controlled grinding experiment conducted at room temperature. Patterns normalised to the reflection of maximum intensity.	255

7.20	Schematic showing the accumulated strain (black) and thermal (red) profiles against the depth beneath the contacting surface for two hypothetical sliding situations following steady state wear. The thermal profile represents the temperature gradient at the point of sliding contact and encompasses a flash heating component in addition to a steady state temperature. The M_d temperature represents the limit for deformation induced martensitic transformation, and no deformation induced martensite can form above this temperature. D_c and ϵ_{max} correspond to the critical transformation depth and the max strain for transformation respectively.	257
8.1	Graph showing the effect of autoclave test temperature on the volume loss of self-mated Tristelle 5183 and Stellite 6 following 5 h sliding contact testing with a 4 kg dead load. The bars represent mean values and the error bars represent the minimum and maximum values of combined pin and disk wear.	267
8.2	Graph showing the effect of autoclave test temperature on the volume loss of self-mated Stellite 6 following 5 h sliding contact testing with a 4 kg dead load. The bars are composed of two separate components relating to the mean values of pin (dark grey) and disk (light grey) volume loss. The error bars represent the minimum and maximum values of combined pin and disk wear.	268
8.3	Graph showing the effect of autoclave test temperature on the volume loss of self-mated Tristelle 5183 following 5 h sliding contact testing with a 4 kg dead load. The bars are composed of two separate components relating to the mean values of pin (dark grey) and disk (light grey) volume loss. The error bars represent the minimum and maximum values of combined pin and disk wear.	269

8.4	BSE (a and c) and SE (b and d) SEM micrographs showing the microstructure of the tribologically affected surface of Tristelle 5183 disk samples after sliding contact tests in an autoclave environment at 150 °C (a and b) and 200 °C (c and d) for 5 h. The sliding direction is horizontal to the figure in all cases.	270
8.5	High magnification SE-SEM micrographs showing the microstructure of the tribologically affected surface of Tristelle 5183 disk samples after sliding contact tests in an autoclave environment at 150 °C (a) and 200 °C (b) for 5 hours. The sliding direction is horizontal to the figure in all cases.	271
8.6	The effect of temperature on the thermal conductivity (k) and thermal diffusivity (α) of Stellite 6, Nitronic 60 and 316L stainless steel .	280

LIST OF TABLES

2.1	Material usage in the primary system of a PWR.	8
2.2	Table of a selection of hardfacing alloys and wear resistant stainless steels.	10
2.3	Guidelines for primary water coolant chemistry.	12
2.4	Nominal composition of Stellite 6 in wt%.	37
2.5	A selection of physical properties of Stellite 6.	37
2.6	Table of a selection of hardfacing alloys and wear resistant stainless steels.	67
2.7	Nominal composition of Nitronic 60 in wt%.	68
2.8	Nominal composition of GallTough in wt%.	70
2.9	Compositional ranges for the major alloying elements of the Norem family of alloys in wt%.	71
2.10	Nominal composition of Nitromaxx in wt%.	77
2.11	Nominal composition of Tristelle 5183 in wt%.	79
2.12	Approximate phase fractions in HIPed Tristelle 5183 as evaluated by Bowden and Zhao et al. by Rietveld and EBSD respectively.	80
2.13	Nominal composition of RR2450 in wt%.	81
3.1	Chemical compositions of powder Tristelle 5183 as determined by chemical analysis.	87
3.2	Chemical composition of cast Tristelle 5183 as determined by chemical analysis.	88
3.3	Chemical composition of HIPed Stellite 6 as determined by chemical analysis.	89
4.1	Comparison of measured and literature values for the lattice parameters of the silicide phases.	124

4.2	Compositions in at.% (excluding carbon) of phases present in gas atomised powder from different size ranges obtained by EDS in the TEM.	130
4.3	Proportions of phases in cast Tristelle 5183 from EBSD-derived data (unindexed indicates fraction of analysed area which could not be assigned to a phase).	134
4.4	Data for heat transfer coefficient and cooling rate calculations for nitrogen gas atomisation Tristelle 5183 (1 atm pressure)	147
4.5	Nomenclature defining the symbols used in the analytical droplet cooling rate model.	147
5.1	Phase fractions and lattice parameters of phases identified within Tristelle 5183 determined via Rietveld analysis.	150
5.2	Composition of γ -Fe in HIPed Tristelle 5183 as determined by EDX-SEM. The results are presented as the mean \pm standard error of the mean (n=6).	155
5.3	Composition in wt% of the γ -Fe and π -ferrosilicide phases in HIPed Tristelle 5183 as determined by EDX-STEM. The results are presented as the mean \pm standard error of the mean ($n_\gamma = 6, n_\pi = 1$).	156
5.4	Phase fractions (wt%) of HIPed Tristelle 5183 and two different size fractions of gas atomised powder determined by Rietveld analysis.	161
6.1	Phase fractions of as-received Stellite 6 determined via Rietveld analysis.	171
6.2	The effect of test temperature on the individual components of pin and disk mass loss of Stellite 6 following 5 h autoclave sliding contact testing with a dead load of 4 kg. The errors have been reported as the standard error of the mean ($n_{20}=3, n_{250}=6$).	175
6.3	Summary of the dominant mechanisms governing the subsurface microstructural evolution beneath the contacting surface of Stellite 6 in response to sliding in lithiated water.	188

7.1 The effect of test temperature on the individual components of pin and disk mass loss of Tristelle 5183 following 5 h autoclave sliding contact testing with a dead load of 4 kg. The errors have been reported as the standard error of the mean ($n_{20}=3$, $n_{250}=6$). 206

INTRODUCTION

Hardfacing alloys are used to minimise tribological degradation of the surfaces of components subjected to sliding contact in the primary cooling systems of pressurised water reactors (PWRs). Primary cooling systems use lithiated water at 200 to 300 °C and within this aggressive environment, a number of critical components including valves, bearings, pumps (reactor coolant pumps) and control element drive mechanisms are exposed to degradation by the combined effects of loaded sliding contact and corrosion. The Co-based StelliteTM family of hardfacing alloys (Co-Cr-Si-W-C type alloys) are used extensively because of their excellent performance in minimising both wear and corrosion. However, when ⁵⁹Co-based wear debris is circulated through the reactor core, neutron bombardment permits nuclear activation and ⁵⁹Co is transmuted to the γ -emitting isotope ⁶⁰Co which has both a high and long-lived nuclear activity (half-life: \sim 5.3 years). This is a major source of radiation exposure for plant maintenance workers which needs to be reduced [1, 2].

Over the past 50 years, significant research efforts have been made to develop wear and corrosion resistant Fe-based hardfacing alloys which can replace or at least significantly minimise the extensive use of Co-based StelliteTM alloys within the primary coolant systems of PWRs. These alloys are typically Fe-Cr-Ni-Si-C alloys that may also contain elements such as Mn, Mo, N and Nb and normally have a principally austenitic fcc or duplex fcc/bcc matrix which surrounds hard second-phase particles such as transition metal carbides or nitrides [3–5]. Tristelle 5183 (Fe-21%Cr-10%Ni-7.5%Nb-5%Si-2%C in wt%) [6–9] is an alloy that has received particular attention and is one of a small number of hardfacings developed to reduce the extensive use of Stellite 6. It is currently used in service for low load sliding applications [10] and can be regarded as one of the first generation alloys from which improved Fe-based hardfacings can be developed.

Traditionally, hardfacing alloys have been applied to component substrate surfaces (typically 316 stainless steel) by techniques which are reliant upon solidification such as weld overlay or laser cladding where pores or cracks can readily form [3, 11]. However, due to the safety critical nature and the long design lives required of the hardfaced components used in PWR applications, it is essential that the hardfacings are of high quality. Therefore, interest has grown in manufacturing hardfacing alloys by the consolidation of gas atomised powder using hot isostatic pressing (HIPing) and subsequently joining hardfacing inserts to substrate surfaces via a HIP-diffusion bonding process. Compared to traditional hardfacing processes, the powder HIP manufacturing route offers advantages which include better chemical and microstructural homogeneity and fewer defects [12]. However, the deployment and development of powder HIPed Tristelle 5183 is restricted due to a paucity of information concerning the phase and microstructure evolution during gas atomisation and subsequent HIPing of the powder.

It has been found from several studies that the exceptional wear, corrosion and tribocorrosion resistance of StelliteTM alloys are not easily reproduced in Fe-based hardfacings including Tristelle 5183 [13, 14], and the reasons for this are not comprehensively understood at present. In both Co and Fe-based hardfacing alloy systems, a fundamental mechanistic understanding of the deformation and tribological degradation mechanisms within a primary cooling system environment remains somewhat fragmented and incomplete. This large gap in understanding significantly hinders the development of improved Fe-based hardfacings.

In light of the gaps in understanding highlighted above, this present study had two main aims: (i) to provide a detailed understanding of the microstructural evolution of gas atomised and HIPed Tristelle 5183; and (ii) to identify the metallurgical and tribological characteristics which promote excellent tribological performance during sliding contact within a primary cooling system environment and to understand the reasons for the disparity in tribological performance between Fe and Co-based hardfacings. Therefore, the specific objectives of the present work were:

- To characterise the microstructure of nitrogen gas atomised and HIPed

Tristelle 5183 and understand the significance of phase and microstructure evolution during processing.

- To comprehensively evaluate the deformation and degradation evolution leading to material removal in the HIPed hardfacing alloys Tristelle 5183 and Stellite 6 during self-mated sliding contact in lithiated water at 25 and 250 °C.
- To conduct a comparative assessment on the tribological behaviour of Stellite 6 and Tristelle 5183 during self-mated sliding contact in lithiated water at temperatures between 25 and 250 °C.

These objectives have been met by employing a range of materials characterisation and mechanical testing techniques (Chapter 3) including: optical microscopy, scanning and transmission electron microscopy (SEM and TEM), X-ray diffraction (XRD), and wear testing using a bespoke tribometer designed to operate in an autoclave to simulate a PWR environment.

The work undertaken is reported in this thesis as follows:

- In Chapter 4, the phase and microstructure formation in nitrogen gas atomised Tristelle 5183 powder as a function of cooling rate has been investigated and specific attention has been given to understanding phase selection during solidification by comparing rapidly solidified gas atomised microstructures with that of a slowly cooled cast alloy sample.
- In Chapter 5, commercially available HIPed Tristelle 5183 has been comprehensively characterised and the microstructure development during HIPing has been evaluated.
- In Chapter 6, the self-mated sliding wear performance of HIPed Stellite 6 within lithited water at 20 and 250 °C has been evaluated. This section specifically focuses on developing an improved knowledge of the sub-surface micro-scale and nano-scale structural evolution in response sliding contact and the contacting surface mechanical and chemical phenomena which cause degradation.

- In Chapter 7, the self-mated sliding wear performance of HIPed Tristelle 5183 within a lithiated water environment at 20 and 250 °C has been investigated. The mechanistic details and evolution in the modes of plastic deformation, including deformation induced martensitic (DIM) transformation, in response to sliding contact are evaluated. The combined mechanical and chemical phenomena which occur at the contacting surface have also been examined and the wear mechanisms are discussed.
- In Chapter 8, the mechanistic differences and alloy characteristics leading to the disparity in tribological performance between Stellite 6 and Tristelle 5183 following self-mated sliding in lithiated water are evaluated and discussed.

The studies presented in this body of work more generally encapsulate the fundamental background investigations that are essential to accelerate the development of new and improved Fe-based hardfacings intended for application within the primary cooling systems of PWRs.

LITERATURE REVIEW

2.1. OPERATION OF A PRESSURISED WATER REACTOR (PWR)

2.1.1. Introduction

The main objective of a pressurised water reactor PWR is to control and regulate the nuclear fission process (the splitting of large radioactive atoms) in order to produce steam; in turn this steam is expanded through turbines which subsequently drives electrical generators. A PWR is comprised of two types of closed circuit separated by a steam generator, more specifically (i) a pressurised water containing primary circuit which transfers heat from the fuel to a steam generator, and (ii) a secondary circuit which feeds steam to turbine generators where electricity is generated (Fig. 2.1). The operation of a PWR can be subdivided into the following steps: (i) fission reactions inside the reactor core generate heat which is transferred to the water of the primary cooling system, (ii) the high pressure water of the primary circuit transports this thermal energy to the steam generator, (iii) heat is exchanged from the primary to the secondary loop inside the steam generator where water is turned into steam, and (iv) this steam is expanded through turbines which drive electrical generators (Fig. 2.1).

2.1.2. Materials in the primary cooling circuit

The primary system, otherwise known as the reactor coolant system of a PWR, is comprised of a series of fundamental constituent components, namely the reactor vessel, steam generators, reactor coolant pumps, a pressuriser, and connecting piping. The primary system may be comprised of one or more reactor coolant loops which contain a reactor coolant pump, a steam generator, and piping which

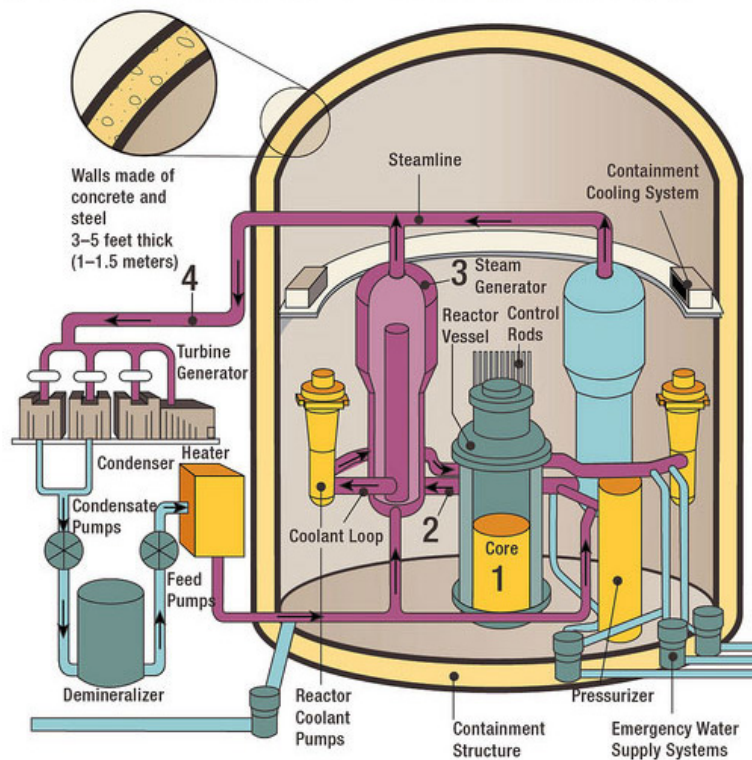


Figure 2.1: Simplified schematic of a typical pressurised water reactor [15]. (1) illustrates the reactor core where heat is generated as a result of nuclear fission. (2) pressurised water in the primary cooling circuit is transported to the steam generator. (3) inside the steam generator heat is exchanged from the primary coolant loop to the secondary loop where water is vaporised producing steam. (4) The steamline directs steam to the turbine which in turn drives an electrical generator.

connects these components to the reactor core (Fig. 2.2) [16].

The temperatures, pressures and water chemistry within the primary system of a PWR lend themselves to the use of highly corrosion resistant materials for the construction of a PWR (Table 2.1). Austenitic stainless steels such as 304 or 316 grades are ideally suited to this environment and are used extensively within PWR's (Table 2.1). However, austenitic stainless steels are known to exhibit poor tribological properties and are therefore not suitable for applications involving wear, for example in valves (Fig. 2.3), bearings, pumps (reactor coolant pumps) and control element drive mechanisms etc. In order to protect the faces of component surfaces that are subject to wear it is necessary to use wear resistant coatings, more specifically hardfacing materials [3]. Hardfacing materials can be described as coatings which are applied to the surface of structural substrate materials

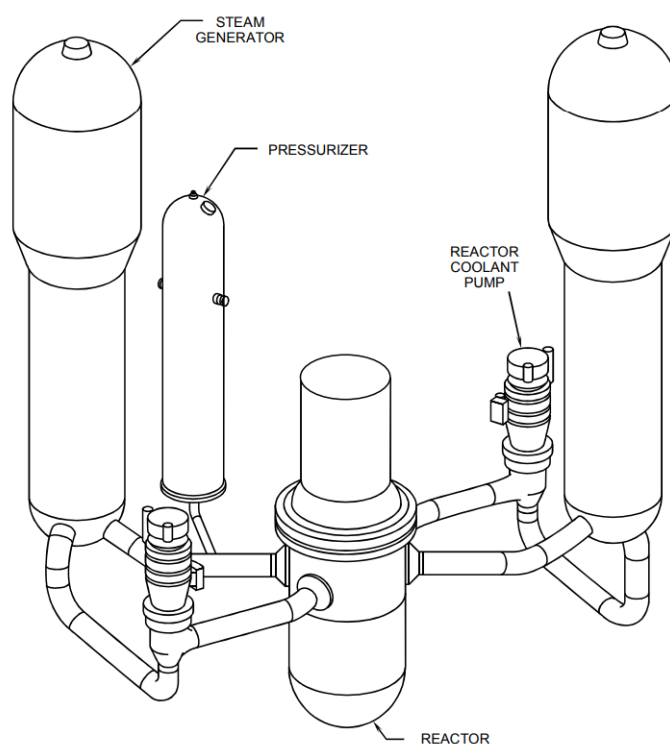


Figure 2.2: Simplified schematic of a primary system of a PWR (two-loop Westinghouse plant), which in this case is comprised of two cooling loops therefore it contains two steam generators, two reactor coolant pumps, and a pressuriser [16].

in order to provide a suitable wear resistant tribological surface. The highly corrosive environment generated within the primary coolant system of a PWR means corrosion resistance hardfacings must be used. A family of Co-based alloys known as StelliteTM is widely used for the hardfacing of PWR components because StelliteTM, more specifically Stellite 3 and 6 offer excellent wear, toughness and corrosion resistance. These desirable properties are attributed to a metal matrix composite microstructure of hard carbides dispersed in a corrosion resistant Co-based solid solution matrix.

Unfortunately, the use of Co and its alloys needs to be minimised within the primary system of a PWR [1,2]. When circulated through the reactor core Co-based wear debris undergoes nuclear activation via neutron bombardment whereby ^{59}Co is transmuted to the γ -emitting isotope ^{60}Co . This ^{60}Co based radioactive debris has both a high and long-lived nuclear activity which is the leading cause of occupational radiation exposure for plant maintenance personnel. The extensive

Table 2.1: Material usage in the primary system of a PWR [17].

Primary components	Material
Reactor pressure vessel	Low-alloy steel with stainless steel cladding
Pressuriser	Low-alloy steel with stainless steel cladding
Surge line	Stainless steels
Nozzles	Stainless steels, Ni-alloys (Alloys 600 or 690)
Main reactor coolant piping system	Cast or forged stainless steels or carbon/low-alloy steels with stainless steel cladding
Steam generator heat exchanger tubing	Ni-alloys (Alloy 600 or 690), Fe-Cr-alloys (alloy 800)
Pump and valve bodies	Cast or forged stainless steel
Hardfacing coatings	Cobalt, nickel or iron based alloys

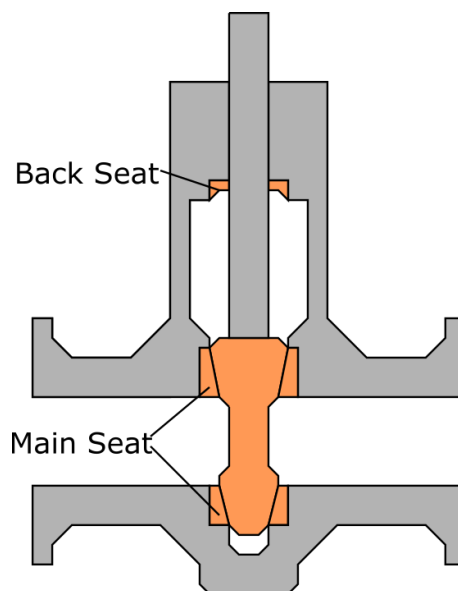


Figure 2.3: Simplified schematic of a typical gate valve cross section in its closed position. The valve seats and components subjected to wear are shown in orange and these components require hardfacing.

use of cobalt should also be minimised for the following additional reasons: (i) cobalt reserves are far from abundant and are notably concentrated in a geographical sense thus making it an expensive commodity [18]; and (ii) the political and environmental pressures associated with the electrification of technology means cobalt is in ever increasing global demand as it is a key constituent in the manufacture of certain batteries [18, 19]. In light of the above, it is clear that alternative

corrosion resistance cobalt-free hardfacings need to be developed which exhibit a corrosion resistance and tribological performance at least equivalent to Stellite alloys. Research has been under way since the 1970's to identify suitable Iron-based hardfacing alloys, but to date a fully satisfactory replacement has yet to be identified.

2.1.3. Hardfacing alloys in the primary system of a PWR

Cobalt-based alloys, nickel-based alloys, and iron-based alloys are the subsets within which hardfacing alloys can generally be characterised. However, with specific reference to the use of hardfacings within PWR's, Fe-based alloys are generally regarded as the most likely candidate to replace Co-based hardfacings due to the inherently good corrosion resistance possessed by high chromium steels. Iron-based hardfacing alloys typically include, high-chromium white cast irons, low-alloy steels, austenitic manganese steels, and stainless steels. stainless steels are of particular interest to the present work and are generally characterised as martensitic and austenitic grades. Table 2.2 lists a selection of Co and Fe-based hardfacings illustrating metallurgical trends in the design of hardfacings.

From a compositional point of view, the design of austenitic hardfacing stainless steel alloys is generally and somewhat loosely centred around either the 300 series stainless steel composition or the manganese and nitrogen containing 200 series stainless steel composition [3] (Table 2.2). High silicon additions are particularly prevalent within austenitic stainless steel hardfacing alloys as silicon imparts a solid solution strengthening effect to the matrix and also promotes good alloy fluidity in the liquid state. Austenitic hardfacing stainless steels inherently exhibit relatively good corrosion resistance as a result of being heavily alloyed with chromium and nickel; these solute atoms also provide solid solution strengthening. A carbide strengthened austenitic matrix is a fundamental design criterion in the conventional alloy design of commercially available austenitic stainless steel hardfacing alloys. Additionally, the strain hardenability of the austenitic matrix phase is also reported to be significantly important in Fe-based hardfacing alloy design [5]. It is generally accepted that the following traits are the key performance

metrics in the design of austenitic stainless steel hardfacing alloys [5]: high work hardening rate, solid solution strengthening, elevated temperature hardness and strength (up to 300 °C), an appreciable volume fraction of secondary hard phases, both room and elevated temperature corrosion and oxidation resistance in a PWR primary system aqueous environment, and high toughness.

In light of the above, the principal focus of this work was to develop a comprehensive understanding of the microstructural formation in a commercial available Fe-based hardfacing alloy designated Tristelle 5183 and to understand the mechanisms governing the tribological performance of Tristelle 5183 in a high temperature water environment. This work is of importance as an extensive understanding of the mechanisms dictating the tribological performance of Fe-based hardfacings in a PWR environment is a mandatory prerequisite in order to be able to develop new and improved Fe-based hardfacings.

Table 2.2: Table of a selection of hardfacing alloys and wear resistant stainless steels.

Alloy	Element wt%													
	Co	Fe	C	Cr	Cu	Mn	Mo	Ni	Nb	N	Si	Ti	W	V
Stellite 6 [20]	bal.	-	0.90-1.40	27.00-32.00	-	-	-	-	-	-	-	-	4.00-6.00	-
Stellite 3 [21]	bal.	-	2.30	30.50	-	-	-	-	-	-	-	-	12.50	-
Nitronic 60 [22]	-	bal.	0.05-0.10	15.00-17.00	0.50 max	7.50-8.50	0.50 max	6.00-10.00	-	0.10-0.20	3.70-4.20	-	-	-
Tristelle 5183 [6,23]	-	bal.	1.90	21.00	-	-	-	10.00	7.50	-	5.00	-	-	-
RR2450 [24]	-	bal.	1.70-2.00	19.00-22.00	-	-	-	8.5-10.50	8.00-9.00	-	5.25-5.75	0.30-0.50	-	-
Gall Tough [25]	-	bal.	0.25 max	12.00-20.00	3.00 max	2.00-7.00	3.00 max	2.00-7.75	-	0.35 max	1.00-5.00	-	-	-
GallTough plus [26]	-	bal.	0.05-0.12	17.50-19.00	-	5.00-7.00	0.75-1.50	6.00-9.00	-	0.10-0.20	3.00-4.00	-	-	-
Norem [27]	-	bal.	0.85-1.40	18.00-27.00	-	5.00-13.00	6.00 max	4.00-12.00	-	0.10-0.30	1.50-5.50	-	-	-
Norem 02 [28]	-	bal.	1.10-1.35	22.50-26.00	-	4.00-5.00	1.80-2.20	3.70-4.20	-	0.02-0.18	3.00-3.50	-	-	-
Nitromaxx [29]	-	bal.	0.90-1.30	21.00-27.00	-	3.00-7.00	1.00-5.00	2.00-6.00	-	0.30-0.60	1.50-4.00	-	-	-
Everit 50 [14,23]	-	bal.	2.50	25.00	-	-	3.20	-	-	-	-	-	-	0.50
Elmax [23]	-	bal.	1.70	17.00	-	0.30	1.00	-	-	-	0.40	-	-	3.00

2.2. DEGRADATION OF ALLOYS WITHIN A PWR ENVIRONMENT

2.2.1. Water chemistry within a PWR

Prior to discussing material degradation mechanisms within a PWR, one must first consider the operational water chemistry within the primary system of a PWR. The water chemistry of a PWR's primary system is controlled in order to achieve the following [30,31]: (i) to assure primary system boundary integrity; (ii)

to assure fuel-cladding integrity and achievement of design fuel performance; and (iii) to minimise radioactive transport and therefore reduce out-of-core radiation fields. Unfortunately, the optimised primary water chemistry's for each of the above goals are mutually exclusive, therefore the water chemistry is prescribed such that a balance between the three goals is achieved. However, a lower priority is assigned to radiation field control compared to the materials and fuel integrity goals.

The formation of radiolytic hydrogen is suppressed via maintaining an over-pressure of hydrogen within the primary water whereby 25-30 cc/kg is generally used to maintain an oxygen content below 5 ppb. Boric acid is utilised within the primary water as a chemical shim to control nuclear reactivity [30,31]. Therefore, in order to control the pH of the primary water, lithium or potassium hydroxide is used to avoid a continuously changing pH throughout the fuel cycle. Four main chemistry regimes exist to date: (i) coordinated Li-B-chemistry, (ii) elevated Li-B-chemistry, (iii) modified Li-C-chemistry and (iv) coordinated chemistry at elevated pH. At present the most common chemistry regimes are the modified chemistry and coordinated chemistry at elevated pH which are depicted in Fig. 2.4 and Fig. 2.5 respectively. Additional water chemistry constraints are presented in Table 2.3.

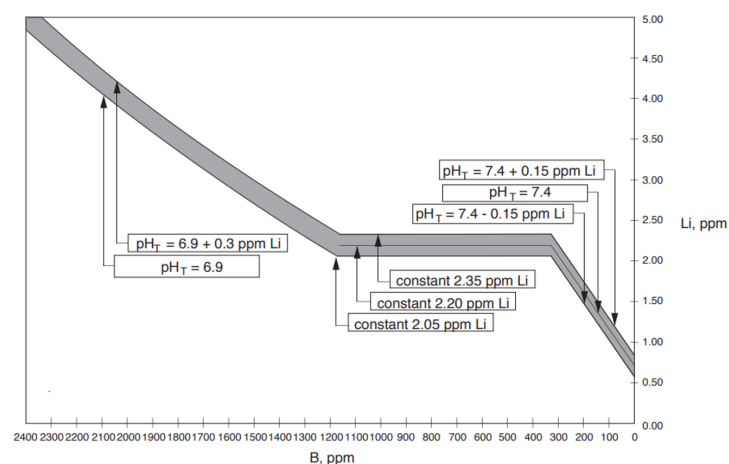


Figure 2.4: Schematic of the modified chemistry regime at 300 °C [31].

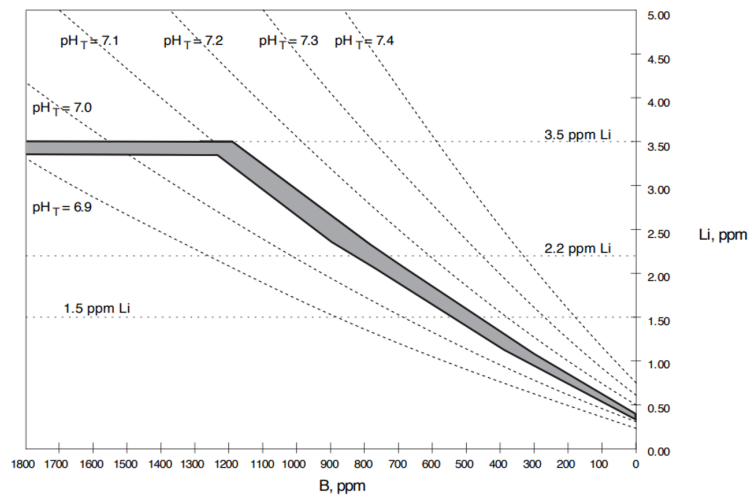


Figure 2.5: Schematic of the coordinated chemistry at elevated pH (7.1) regime at 300 °C with lithium below 3.5 ppm [31].

Table 2.3: Guidelines for primary water coolant chemistry [30,31].

Hydrogen (cm^3) (SPT)/ kg H_2O	20 - 50
Chlorides (mg/kg)	< 0.15
Fluorides (mg/kg)	< 0.15
Dissolved oxygen (mg/kg)	< 0.01
Lithium (mg/kg)	consistent with water chemistry regime

2.2.2. Chemical degradation (corrosion and oxidation)

Due to their excellent uniform corrosion resistance and bulk mechanical properties at operating temperatures, stainless steels (specifically 304 and 316 grades) are used extensively throughout the primary system of a PWR. Very little work exists on the corrosion of Fe-based hardfacings; however, the matrix of Fe-based hardfacing alloys is generally analogous to the compositions of stainless steel on which there exists a large volume of published work. The superior corrosion resistance within an oxidative environment associated with stainless steels results from the presence of a thin (typically 1-3 nm) self-healing passive Cr_2O_3 film which forms on the metal surface. However, the passive film which forms on any given stainless steel notably changes depending on the surrounding environment such that it may grow or dissolve and adsorb or incorporate anions [32].

The present work is focused on the use of austenitic hardfacing stainless steels

within primary system environment, therefore the formation of oxide films under elevated temperature water environments will be discussed here after. X-ray photoelectron spectroscopy (XPS) studies performed by Castle and Clayton [33] reported the presence of a duplex type corrosion product on the surfaces of 18Cr-8Ni stainless steel after immersion in deionised water at 40 and 80 °C. This work proposed that only the innermost layer is rich in Cr whilst the outer layer is rich in OH⁻ ions which could possibly be attributed to a layer of bound water [34]. Under a high temperature water environment (generally at temperatures above 250 °C [35]), the oxide film which forms on austenitic stainless steels is commonly reported to be comprised of two layers: (i) an Fe-rich outer layer of faceted magnetite (Fe₃O₄) crystals which also contain Ni; and (ii) an inner Cr-rich spinel layer [35–37]. Lister et al. [36] suggest that the composition of the outer oxide crystal layer most likely conforms to a non-stoichiometric structure of the form Ni_xFe_{3-x}O₄, and report that such a structure manifests in abundance within a high temperature water environment under reducing conditions. The composition of the inner most Cr-rich spinel layer appears less clearly defined and a plethora of non-stoichiometric compositions (Ni_xCr_yFe_{3-(x+y)}O₄) have been proposed. However, Lister et al. [36] and Stellwag [35] have proposed some limiting compositions of the form Fe₂CrO₄, FeCr₂O₄ and NiCr₂O₄.

Lister et al. [36] and Szklarska-Smialowska et al. [38] both propose that the inner oxide layer forms by a solid growth process and that the outer layer forms by a mechanism involving metal dissolution and oxide precipitation. In contrast, the work of Robertson [39] suggests that both the inner and outer oxide films form via a solid state growth mechanism. A growth mechanism where both layers form by metal dissolution and oxide precipitation has also been discussed [35]. Asakura et al. [37] conclude that the inner oxide layer has an insulating effect and acts to suppress corrosion in a high temperature water environment. Additionally, this work reports a significant increase in the growth of the Cr-rich inner layer at temperatures in excess of 260 °C which yields a reduction in the corrosion rate.

Sun et al. [40] investigated the effects of temperature on the oxide film properties of 304 stainless steel within a high temperature lithiated borate buffer solution.

This work suggests that the stability and the protective nature of the oxide film which forms on 304 stainless steel degrades with respect to increasing temperature whereby the oxide film remains passive in the temperature range of 25-200 °C and can be considered a corrosion product film between 250 and 300 °C. Electrochemical impedance measurements (EIM) also conducted in this work suggest that the oxide film was a single layer structure at 25 °C whilst a duplex type oxide film forms at temperatures between 100 and 300 °C. Additionally, this work concluded that a degradation in the protective nature of the oxide film can be attributed to a reduction in the films electrical resistance with respect to increasing temperature. The barrier layer which forms at the metal-film interface is reportedly able to suppress the dissolution of the alloy at 25 °C; this barrier layer degrades with respect to increasing temperature, thus enabling the formation of the duplex oxide structure at temperatures between 100 and 300 °C [40].

2.2.3. Mechanical degradation and wear

Wear will occur when two contacting surfaces move over one another and damage to one or both of these contacting surfaces will invariably arise, usually in the form of progressive material loss. The removal of material via the action of wear is, in the vast majority of cases, detrimental and may result in component issues, for example increased clearances between moving surfaces, undesirable component freedom, and loss of precision. Wear of components may lead to unwanted extensive vibration which subsequently acts to increase mechanical loading that may accelerate wear or lead to fatigue failure [11]. Even the small loss of material through the action of wear can be sufficient to cause the failure of large complex machines, and unfortunately wear is often the root cause of many engineering disasters. The word wear is generically used to describe the mechanical degradation of contacting surfaces, however the terms 'sliding wear', 'abrasion', 'corrosion enhanced wear', and 'erosion' form more specific classifications under the blanket term of wear [11].

With specific reference to this work, there is a large volume of literature which attempts to rationalise the in air sliding wear and galling behaviour of iron-based

hardfacings for example in references [2,28,41,42]. However, there is currently little in the way of comprehensive literature which focuses on the tribological performance of hardfacings in a simulated PWR environment due to the inherent experimental complexities associated with performing such studies. In light of the above, the tribological studies presented in this work will aim to improve the current understanding of the mechanisms which govern the wear of Fe-based hardfacings in a simulated primary cooling system PWR environment.

2.2.3.1. Asperity contacts and contact mechanics

When two surfaces are brought together contact will only occur at a few points otherwise known as asperities [11,43]. If the normal load between these contacting surfaces is increased, a larger number of asperities come into contact between the two surfaces. As asperities solely account for the contact between two surfaces they are responsible for supporting the normal load on the surface in addition to generating any frictional forces that act between them.

2.2.3.2. Sliding and galling wear

Sliding wear can be characterised as the surface damage that occurs between two solid surfaces subject to a relative motion in loaded contact, where the damage does not occur as a result of deep surface grooving from penetrating asperities and/or foreign particles [44]. Sliding wear is often termed adhesive wear, however this is somewhat misleading as adhesion in addition to other physical and chemical phenomenon may be involved in sliding wear. The topography of a surface subjected to sliding wear can be described by the somewhat poorly defined words, scuffing, scoring, and galling. Scuffing can be described as damage arising from the shearing of cold welded metallic junctions resulting in macroscopically observable changes in the topography of the worn surface which relate to the direction of shear. Scoring entails the formation of scratches and grooves on the worn surface in the direction of the relative motion and can allude to scratching by abrasive particles. Galling is often regarded as a more severe form of sliding wear and can be characterised by gross surface damage as a result of local solid-state welding [11].

When two surfaces are brought together under loaded sliding conditions, plastic deformation and solid phase welding of the surface asperities will occur. The strength of the bonded asperities is dependent upon the surfaces crystal structure and the mutual solubility of the two contacting materials. Therefore, sliding contact results in the tearing of either the base material (cohesive tearing) or the asperity interface (adhesive tearing) depending on which is weaker. In a broader sense, the contact of two materials results in the formation of an adhesive joint caused by interatomic attraction between contacting asperities. This adhesion can be regarded as either physical, like in the case of hydrogen bonds and Van der Waals forces; or chemical, like in the case of metallic, covalent or ionic bonding. The strength of the adhesion between two contacting surfaces is dependent upon: normal load, temperature, duration of contact, surface cleanliness, separation rate, crystal structure, crystallographic orientation, solubility of one material in the other, and chemical activity [11].

It should be noted that cohesion represents the atomic bonding forces present in the bulk material and adhesion represents the bonds formed at the mating interface [45]. If the interface bond is stronger than the cohesive bond in the weaker of the two materials in sliding contact, the separation of the two mated materials results in the transfer of material from the cohesively weaker to the cohesively stronger material [46]. For example, when metallurgically similar materials are subjected to sliding contact, the bonded interfaces and adjacent plastically deformed regions are generally stronger than the base material due to work hardening. Therefore, tearing occurs in the base material (cohesive tearing) and material is lost via material transfer. In these cases, tearing occurs in the bulk of softer material [45,47]. In contrast, detachment occurs at the bonded asperity interface (adhesive tearing) when the strength of the bonded asperity interface is low relative cohesive bonding associated with the bulk. Therefore, the adhesive tearing of a bonded interface is particularly prevalent in for example: (i) dissimilar contacting surfaces with a low mutual solubility, and (ii) metallic surfaces which are separated by a coherent oxide layer. Generally speaking, the material loss and transfer associated with adhesive tearing is likely to be lower than that seen in the

cohesive tearing of the bulk material [46,47].

The detachment of material from one surface to another has been described by several mechanisms. One well recognised mechanism proposed by Archard suggests that shearing occurs at either the interface or at the weakest region within the bulk of the two mating surfaces [11,48]. In the majority of cases the adhesive bond strength at the contacting asperity interface is comparably lower than that of the cohesive bond strength; therefore, shearing occurs at the adhesively bonded asperity interface. However, this is not always the case and in a small fraction of contacting asperities the cohesive bond within the bulk material is weaker than the adhesive bond; therefore, a small (irregular shaped) fragment is transferred between surfaces during shearing [48]. Alternatively, it has been proposed that a wear fragment results from the plastic shearing of successive layers of a contacting asperity [49]. This theory suggests that a shear crack propagates in conjunction with the plastic shearing of successive layers along a slip plane. This mechanism results in a thin wedge-shaped fragment that gets transferred to the opposing surface due to adhesion.

During continued sliding, transferred material can either be transferred back to the original surface or detach from parent surfaces to form wear debris. Some wear fragments are detached due to fatigue as a result of repeated loading and unloading. Loose wear particles can also result from chemical changes in the fragment. Wear fragments have a high tendency to oxidise due to their relatively large surface area. In light of this, the adhesive strength supporting wear fragments can be compromised due to oxidation and this means the fragments can break free more readily. Wear fragments can also become detached when their residual elastic energy due to cyclic loading exceeds that of the adhesive energy [46].

Galling can be described as a particularly severe form of sliding wear that results in significant surface damage at the interface between mated sliding material couples [11]. Galling can be characterised by localised macroscopic roughening and the creation of heavily deformed protrusions which can be attributed to adhesion and plastic deformation at the mating surface [50]. Susceptibility to galling wear is governed by: (i) the presence of surface films and their ability to prevent

adhesion, (ii) the coherency of surface films and their resistance to degradation and breakdown, (iii) the strength of adhesion at the interface once any surface films break down, and (iv) the increase in junction growth after adhesion and further sliding [11].

2.2.3.3. Abrasive wear

During abrasive wear, the asperities of the harder mating surface or the presence of hard particles at the interface results in the damage of the softer mating material via either fracture or plastic deformation. Abrasive wear can be characterised into two mechanisms, specifically two-body and three-body abrasion. Two-body abrasive wear entails the asperities of harder mating surface directly damaging the softer of the two mating faces. On the other hand, damage is caused in three-body wear by the presence of a hard abrasive particle (the third body) at the interface between two mating surfaces [11].

Material removal and displacement during abrasive wear can be characterised into three main modes, more specifically ploughing, wedge formation, and cutting. During ploughing, plastic flow enables the formation of ploughed grooves within the softer material of the two mating surfaces. A ploughed groove consists of a lower central region from which material has been displaced to ridges that are situated at the sides of the groove. When a surface is repeatedly ploughed the material is subjected to cyclic loading and unloading which can result in material loss via mechanisms including low cycle fatigue or delamination. Additionally, ploughed ridges become flattened due to cyclic loading and ultimately fracture off forming wear debris [11, 51]. It has also been reported that the subsurface plastic deformation associated with ploughing can contribute to the nucleation of surface and subsurface cracks. Further cyclic loading can cause these cracks as well as surface defects and pre-existing cracks to propagate. This cracked surface is ultimately sheared off and detached from the parent material thus creating wear debris [52]. In wedge formation, a wedge of material forms at the front of an abrasive tip and leaves a groove in the contacting surface. In cutting the abrasive tip removes discontinuous or ribbon shaped material from the contacting

surface thus leaving behind a groove. The cutting abrasive wear mechanism is a particularly aggressive with regards to material removal [11,51]. The extent of cutting, wedge formation and ploughing is controlled by the attack angle, the degree of penetration, and the interfacial shear strength of the interface [53].

2.2.4. Tribocorrosion

2.2.4.1. Introduction to Tribocorrosion

Unavoidable sliding contact and the passive/corrosive nature of hardfacings in a primary system PWR environment results in a situation which strongly favours degradation via tribocorrosion. Tribocorrosion is a degradation process which arises as a result of the simultaneous action of both chemical and mechanical effects in a tribological contact. In other words, tribocorrosion may occur in a corrosive medium under a variety of mated conditions, for example sliding, fretting, rolling and impingement [54]. When subjected to a tribocorrosive environment, different phenomena contribute to material degradation and the independent consideration of wear and corrosion is an insufficient means of explaining the overall tribocorrosion phenomenon [11,54]. The literature discusses four main approaches to tribocorrosion which have successfully been used to describe the behaviour of passive metals in a corrosive medium in sliding contact, more specifically (i) the synergistic approach, (ii) the mechanistic approach, (iii) the third body approach, and (iv) the nanochemical wear approach [54].

If a passive material immersed within an electrolyte is subjected to some form of mechanical stimulation which results in the removal or thinning of the passive film (depassivation), the material becomes locally exposed to the electrolyte and therefore to active dissolution. The active dissolution of the metal may be accompanied by the restoration of the passive film. Active dissolution during depassivation followed by repassivation is one of the principal corrosion mechanisms that needs to be considered when investigating tribocorrosion systems [54]. In addition to active dissolution, one must also consider passive dissolution, transpassive dissolution, absorption and localised corrosion in the context of this work [54]. Passive dissolution involves the formation of cations at the metal passive film interface;

these cations migrate across the passive film where they dissolve in solution at the electrolyte interface as hydrated or complex ions. Transpassive dissolution arises when the passive film oxidises to a species of higher solubility in the electrolyte. Adsorption involves the reaction of atoms at the metal surface which exhibit unsaturated bonds that are available for fixing reactive species, atoms or molecules which are present at the surface. Localised corrosion is the site-specific removal of material due to corrosion in localised regions.

2.2.4.2. *The synergistic approach to tribocorrosion*

Tribocorrosion is a degradation process in which both corrosion and mechanical mechanisms operate synergically and cannot be considered independently. Typically, this involves both material loss and growth of oxide layers by corrosion and the subsequent removal of oxide layers by mechanical stimulation. The rate of material loss as a result of tribocorrosion is not simply the sum of the mechanical wear rate in the absence of corrosion (W_o) and the corrosion rate in the absence of the applied mechanical stimulus (C_o). One must also consider an additional synergetic contribution (S) which may be either positive or negative (Eq. (2.1)) [11,54–56].

$$T = W_o + C_o + S \quad (2.1)$$

The synergistic contribution (S) can be broken down into the change in wear rate caused by corrosion ΔW_C (known as the 'additive effect'), and the change in corrosion caused by the applied mechanical stimulus ΔC_W (known as the 'antagonistic effect') [55]. Therefore, Eq. (2.1) can be expressed as:

$$T = W_o + C_o + \Delta W_C + \Delta C_W \quad (2.2)$$

The relative importance of both mechanical W and chemical C degradation can be described by the following ratio [11]:

$$\frac{C}{W} = W_o + C_o + \Delta W_C + \Delta C_W \frac{C_o + \Delta C_W}{W_o + \Delta W_C} \quad (2.3)$$

The $\frac{C}{W}$ ratio can subsequently be used to define different regimes [11] of tribo-

corrosion, more specifically:

$$\text{Wear dominated} : \frac{C}{W} < 0.1 \quad (2.4)$$

$$\text{Wear} - \text{corrosion} : 0.1 \leq \frac{C}{W} < 1 \quad (2.5)$$

$$\text{Corrosion} - \text{wear} : 1 \leq \frac{C}{W} < 10 \quad (2.6)$$

$$\text{Corrosion} - \text{dominated} : \frac{C}{W} \geq 10 \quad (2.7)$$

2.2.4.3. *The mechanistic approach to tribocorrosion*

The mechanistic approach subdivides the phenomenon of tribocorrosion into two main contributors: (i) anodic dissolution (wear accelerated corrosion), and (ii) the mechanical removal of metal particles (mechanical wear). A methodology for evaluating these two contributions was devised by Mischler et al. [57–59]. This work reported that the electrochemical material removal rate is strongly affected by mechanical parameters and the mechanical removal rate is dependent on the electrochemical conditions. The total wear volume (V_t) is defined as the sum of the metal loss due to chemical or electrochemical oxidation (V_{chem}) and the metal loss arising from mechanical wear (V_{mech}) (Eq. (2.8)).

$$V_t = V_{mech} + V_{chem} \quad (2.8)$$

In the case of passive metals, V_{chem} is the sum of the corrosion in both the passivating and depassivating areas, however the magnitude of the former is usually sufficiently small that it can be neglected. In light of this, the oxidation kinetics can be evaluated in situ by way of measuring the current flowing through the metal electrode (I_p) in potentiostatically controlled experiments [59]. The anodic dissolution (V_{chem}) can subsequently be evaluated in a potentiostatic tribocorrosion

experiment in accordance to the following (Faraday's law):

$$V_{chem} = \frac{QM}{nF\rho} \quad (2.9)$$

$$Q = \int_0^t I_p dt \quad (2.10)$$

Where Q is the electrical charge flowing in the wear track which is obtained from Eq. (2.10) and t is the exposure time. M denotes the atomic mass of the metal, n is the apparent valence, F is the Faraday constant and ρ is the density of the metal. It should be noted that Eq. (2.9) can only be applied under two crucial assumptions reported by Landolt et al. [60]. Another method for quantifying V_{chem} has been reported by Diomidis et al. [54,61].

The total wear volume (V_T) can simply be ascertained via profilometry post tripocorrosion experiment [62] or by the vertical displacement of the pin during the experiment [60]. Subsequently, the mechanical volume loss (V_{mech}) may be calculated by subtracting V_{chem} from V_t . As previously mentioned, the mechanical and chemical degradation mechanisms in a tribocorrosion system do not operate independently and therefore interact with one another. Therefore, simply evaluating both V_{chem} and V_{mech} may not be adequate when attempting to fundamentally understand tribocorrosion systems. In light of the above, the mechanistic approach to understanding tribocorrosion is inadequate in many cases and fails to explain phenomena, for example the build-up of third bodies.

2.2.4.4. The third body approach to tribocorrosion

The presence of third bodies is known to play a key role in tribocorrosive systems despite the fact the third body may dissolve in the corrosive medium. The third body approach to tribocorrosive systems was first proposed by Mischler et al. [62] in an effort to explain the differences in wear mechanism exhibited by carbon steel when exposed to different corrosive media. The third body approach to tribocorrosion originates from the observation that mechanical wear often results in wear debris which remains in tribological contact for a given time prior to being

removed [63]. In the third body approach to tribocorrosion the volume loss of metal (V_{met}) is defined by the sum of three contributors (Eq. (2.11)): (i) a volume of material which becomes detached in the form of solid metal particles as a result of abrasion, adhesion or delamination ($V_{met}^{particle}$); (ii) a volume of material lost via the dissolution of metal ions in the electrolyte (V_{met}^{ions}); and (iii) a volume of metal oxidised to form a passive film (V_{met}^{oxide}).

$$V_{met} = V_{met}^{particle} + V_{met}^{ions} + V_{met}^{oxide} \quad (2.11)$$

In accordance to the third body concept [64], the metal particles within the wear track $V_{met}^{particle}$ are subjected to both mechanical and chemical effects. Therefore, the volume of metal particles within the wear track ($V_{met}^{particle}$) can be subdivided into several contributions: the volume of metal particles ejected from the contact ($V_{met,particle}^{ejected}$), the volume of particles which get oxidised ($V_{met,particle}^{ion}$ or $V_{met,particle}^{oxide}$), and the volume of metal which is transferred back onto the metal surface by the action of smearing ($V_{met,particle}^{smearred}$). The volume of metal particles in the wear track can thus be expressed as:

$$V_{met}^{particle} = V_{met,particle}^{ejected} + V_{met,particle}^{ion} + V_{met,particle}^{oxide} + V_{met,particle}^{smearred} \quad (2.12)$$

In light of the above, the measurable wear track volume (V_t) at the end of a tribocorrosion experiment can be expressed as:

$$V_t = V_{met} - V_{met,particle}^{smearred} \quad (2.13)$$

The three body approach to tribocorrosion does not consider the recombination of oxidised metal particles with the metal surface to form a thicker compacted oxide layer, therefore Eq. (2.11) and Eq. (2.12) can be substituted into Eq. (2.13) to give the following expression for the wear track volume (V_t):

$$V_t = V_{met,particle}^{ejected} + V_{met,particle}^{ion} + V_{met,particle}^{oxide} + V_{met}^{ions} + V_{met}^{oxide} \quad (2.14)$$

If one now considers the situation where the metal and metal particles only oxidise electrochemically, the following volumes can be defined as an anodic volume (V_{chem}):

$$V_{chem} = V_{met,particle}^{ion} + V_{met,particle}^{oxide} + V_{met}^{ions} + V_{met}^{oxide} \quad (2.15)$$

Therefore, Eq. (2.14) may be rewritten as:

$$V_t = V_{met,particle}^{ejected} + V_{chem} \quad (2.16)$$

Fig. 2.6 [54, 65, 66] depicts the material flows which occur in the formation of third-bodies during the tribocorrosion of a passive metal. The calculated mechanical wear (V_{mech}) equates to the volume of metal particles ejected from the tribological contact and is therefore not definitively equal to the metal volume loss removed from the metal surface

When employing the three body approach to tribocorrosion three limiting situations can be found [65,66]. Firstly, the first and third bodies do not undergo an anodic reaction, therefore $V_t = V_{mech} = V_{met}^{particle}$. In this instance V_{mech} represents the mechanical material removal from the first body. Secondly, the first body is susceptible to anodic oxidation or dissolution, however the third body does not anodically oxidise or dissolve in the contact. In this limiting case $V_{met,particle}^{ion}$ is the mechanical metal removal rate from the first body and is equal to the difference between V_t and V_{chem} . Finally, all metallic wear particles either dissolve or are oxidised prior to being ejected from the contact ($V_{met,particle}^{ejected} = 0$ thus $V_{chem} = V_t$). In this situation the measured anodic current accounts for the entire material loss.

The physical properties of the third body particles in a tribocorrosion system are particularly important as they may act as an abrasive which accelerates wear [67,68] or as a solid state lubricant which minimises both friction and wear [69]. Therefore, the following parameters are believed to influence the properties and behaviour of third bodies [54]: (i) Mechanical parameters, namely contact pressure [70,71], sliding velocity and lubrication; (ii) Chemical surface effects, more specifically metal oxidation, metal dissolution and the adsorption of

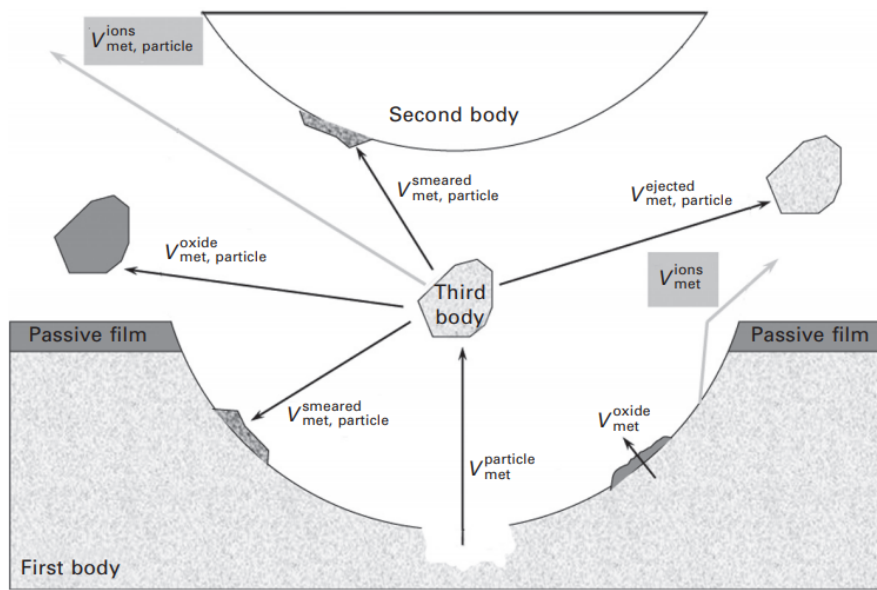


Figure 2.6: Schematic illustrating the material flows which result in the formation of third bodies during the tribocorrosion of a passive metal [54,65,66].

chemical compounds present in the surrounding environment; and (iii) Material properties, namely composition, microstructure and hardness [72].

2.2.4.5. *The nanochemical approach to tribocorrosion*

It is widely known that the contact area subjected to sliding wear (both in dry and corrosive media) incurs subsurface deformation and that this subsequently influences wear behaviour [73–75]. Therefore, subsurface deformation can be held accountable for the inconsistencies observed when interpreting the tribocorrosion phenomena using the synergistic, mechanistic, and third body approaches. Although the influence of subsurface deformation on wear has been extensively studied, the role of subsurface deformation with respect to tribocorrosion has only been considered in more recent years. In light of the above, the term ‘nanochemical wear’ Fig. 2.7 has been used to describe tribocorrosion mechanisms which involve nano-scale subsurface structural or chemical adaptation.

The phenomenon of nanochemical wear can be subdivided up into two steps, more specifically (i) strain accumulation which results in the generation of a nanocrystalline microstructure beneath the contacting surface, and (ii) the detach-

ment of nano-grains resulting in wear. This approach is based on the fundamental consideration that both friction and wear are directly related to both the physical properties of the interface and the mechanical properties of the subsurface [76]. Fig. 2.7 is a simplified schematic showing the different subsurface regions beneath a metal to metal sliding contact affected by nanochemical wear. Zone 3 is comprised of mixed material from both the bulk and counterpart and can be subdivided into two layers: (i) a tribochemical reaction layer, and (ii) a nanocrystalline mechanically mixed layer. Zone 2 is comprised of plastically deformed material which is subject to a deformation gradient whereby the material closest to Zone 3 incurs the highest strains. The interface between Zones 3 and 2 is microstructurally distinct and generally coincides with a shift in composition. Zone 1 is simply unaffected bulk material. The mechanically mixed layer exhibits different mechanical properties relative to the bulk material, for example: (i) the incorporation of hard particles via the action of mixing, chemical changes and work hardening are all possible reasons for an increase in hardness within the mechanically mixed layer; (ii) the heavily refined nanocrystalline structure associated with the mechanically mixed zone may result in a change to the stress-strain response of the material; and (iii) the act of mechanical mixing may also result in a change to the materials strain to failure, Young's modulus and coefficient of friction.

The generation of the nanocrystalline layer has been attributed to the formation and motion of dislocations and/or the generation of stacking faults and twins in response to sliding induced plastic deformation. Therefore, dynamic recrystallisation in conjunction with mechanical mixing results in the formation of the nanocrystalline layer. Subsurface phase transformations in sliding tribocorrosion systems have previously been observed and are reportedly dependent on material properties and the electrochemical conditions associated with the contact [74,77,78]. In the case of low SFE materials (austenitic stainless steels or Co-Cr (Stellite type) alloys), the cyclic shear stresses associated with the action of sliding results in localised plastic deformation along discrete sliding planes thus, one sees the generation of dislocation, micro twins, twins and stacking faults resulting in work hardening [54,77]. In this instance, dynamic recrystallization reportedly

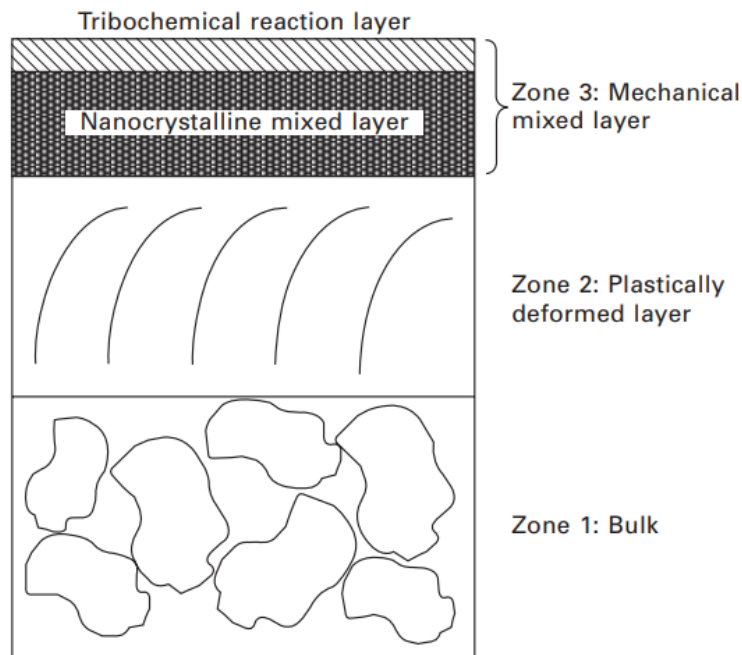


Figure 2.7: Simplified sheamatic illustrating the different regions beneath a worn surface of a metal to metal sliding contact [11,54].

results from two phenomena: (i) the shearing of cells generated by stacking faults, micro twins, twins and transformed regions; and (ii) the rotation of clusters of atoms in response to the applied mechanical stimulus [77,79,80]. In contract, in high stacking fault energy materials (for example aluminium) the dissociation of a full dislocation into two partials is less energetically favourable. Therefore, the material has a tendency to accommodate the plastic deformation induced by sliding via dislocation glide or cross-slip. This facilitates dislocation cell formation which enables dynamic recrystallisation and the formation of the mechanically mixed nanocrystalline layer [54,77,79,80]. Irrespective of the materials SFE, the formation of the nanocrystalline layer can be attributed to multi-directional loading as well as the large strains and strain rates imposed onto a surface during sliding [54].

The role of the nanocrystalline layer in tribocorrosion systems is still subject to much debate. Investigations conducted on sliding metal to metal contacts in distilled water [77] and biological media [81,82] suggest that a mechanism involving the detachment of the nanocrystals which form in the mechanically mixed layer is responsible for the removal of material. These studies suggest that

the detachment of nanocrystals occurs in preference to other material removal mechanisms involving delamination or fatigue. In some cases, the removal of nano crystals reportedly causes abrasion marks on the contacting surface. This mechanism of material removal has been reported in AISI 304L stainless steel (Fig. 2.8) [75] and Ni-Cr alloys [83].

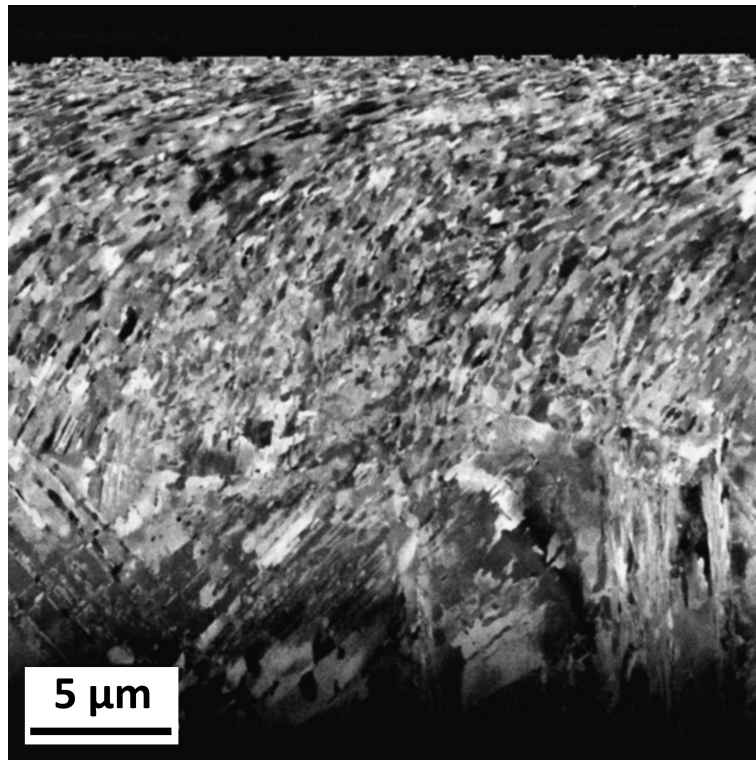


Figure 2.8: Longitudinal wear track FIB cross section taken from 304L post reciprocating sliding against a alumina ball at a passive potential (-0.5 V) under a load of 7 N [75].

2.3. HARDFACING PROCESSES

2.3.1. Hardfacing deposition from the liquid state

Traditionally, hardfacing materials have been applied to substrate surfaces via methods reliant upon solidification from the liquid state (or a mixed liquid-solid state) whereby the hardfacing coating is formed via solidification from a melt. Examples of such techniques include, thermal spraying, weld hardfacing and laser cladding. To date, these hardfacing deposition methods have been used extensively throughout PWR's, however the advent of powder metallurgy has

seen a demographic shift in favour of hot isostatic pressing (HIP) as the processing route of choice in the application of hardfacing materials [10].

Thermal spraying involves the heating of the hardfacing in the form of either powder or wire to produce molten or partially molten droplets via the combustion of fuel or by electrical discharge (arc or plasma). These droplets are subsequently accelerated towards the substrate surface where upon impact they splat and solidify to form the coating [3]. Thermal spraying is therefore regarded as a line of sight processing method which inherently places certain restrictions upon its applications. Unfortunately, thermally sprayed coatings often suffer from, (i) inclusions for example oxide stringers, (ii) porosity, (iii) a characteristically low bond strength, (iv) anisotropic materials properties, and (v) a low loading capacity. Thermally sprayed hardfacings coatings often also require additional costly post spray heat treatments in order to, (i) improve the substrate-coating bond strength, (ii) relax residual stresses, (iii) increase interparticle cohesion, iv microstructural improvement, and (V) reduce porosity [84].

Hardfacing materials can be applied to substrate surface via fusion welding, for example by manual metal arc or plasma-transferred arc (PTA) welding etcetera (GTAW, SMAW and SAW). Depending on the process, the hardfacing is fed into the fusion zone as a consumable electrode or filler rod where it solidifies to form a strong metallurgical bond with the substrate. Alternatively, a laser clad hardfacing coating is produced by laser melting a stream of hardfacing powder across the substrate surface in a controlled manner. Weld deposited and laser clad hardfacings inherently suffer from: (i) inhomogeneity, (ii) high inclusion and porosity levels, (iii) base metal dilution, (iv) cracking, (v) anisotropic mechanical properties resulting from a microstructure with elongated grains, (vi) component distortion, (vii) heat affected zones within the substrate, (viii) residual stresses which leave components vulnerable to fatigue and stress corrosion cracking mechanisms, and (ix) the need for costly subsequent machining operations in order to achieve a final net shape.

Due to the safety critical nature and the long design lives required of the components used in nuclear applications it is mandatory that the highest quality

hardfacings are used. In light of the disadvantages associated with the deposition methods highlighted above, interest has grown in producing hardfacing alloys by powder hot isostatic pressing (HIP). Additionally, HIPed powder compacts can subsequently be attached to substrate surfaces by HIP diffusion bonding.

2.3.2. Hardfacing by Hot isostatic pressing (HIP) and HIP bonding

This section aims to detail the use of both powder HIP and HIP bonding to produce and attach hardfacing materials to substrate surfaces. In short, the HIP and HIP bond processes entail the application of high isostatic pressures to a workpiece at elevated temperature in a specifically designed pressure vessel (Fig. 2.9).

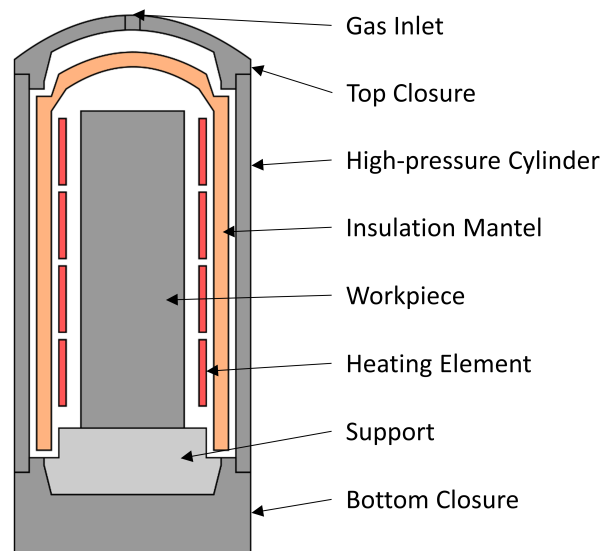


Figure 2.9: Simplified schematic of a cross sectioned HIP unit.

2.3.2.1. HIP bonding

HIP diffusion bonding is a solid state processing route through which both similar and dissimilar metals can be joined [85–88]. Diffusion bonding can be characterised by two fundamental stages where no more than a few percent microscopic deformation occurs. Firstly, the application of heat and pressure results in the collapse of the surface asperities between the two mating surfaces resulting in a

network of pores at the interface. Secondly, bond development ensues via mechanisms such as grain boundary diffusion and power law creep [89]. Diffusion bonding offers potential benefits relative to more traditional hardfacing deposition methods, more specifically high bond strength, microstructural integrity, and low distortion [89].

2.3.2.2. Hot isostatic pressing (HIP)

From both a metallurgical and microstructural point of view, hot isostatic pressing (HIP) is a particularly attractive solid state diffusion based process through which metal powder can be consolidated [85–88, 90]. The application of sufficient heat and pressure to metal powders contained within hermetically sealed mild steel canisters enables the eradication of the porosities between adjacent powder particles and permits the manufacture of components which exhibit 100 % theoretical densities [91]. Powder HIP permits the production of hardfacings with highly alloyed compositions which do not suffer from segregation effects. The microstructures of HIPed powder compacts can be regarded as isotropic and equiaxed moreover, fine grain sizes are generated that are otherwise not easily achievable through other processing methods. Powder HIP compacts exhibit isotropic mechanical and physical properties because of a chemically homogenised microstructure composed of fine equiaxed grains. The quality and assurance of structural integrity that results from HIPing permits extended component life cycles or allows lesser grade materials to be used for more stringent applications [90].

There are a number of drawbacks associate with the powder HIPing, more specifically (i) its relative cost is high relative to other powder metallurgical and hardfacing deposition methods, and (ii) HIPing is only generally suited to small scale production. Additionally, some alloy powders are inherently more difficult to consolidate via HIPing, for example alloys that readily form oxidises on the powder surface. Such oxides promote inclusions which result in a degradation of the mechanical properties in the final HIPed component [92].

The main stages of the powder HIP process are summarised in Fig. 2.10. Powder filled compacts are placed in a furnace which is situated in a HIP pressure

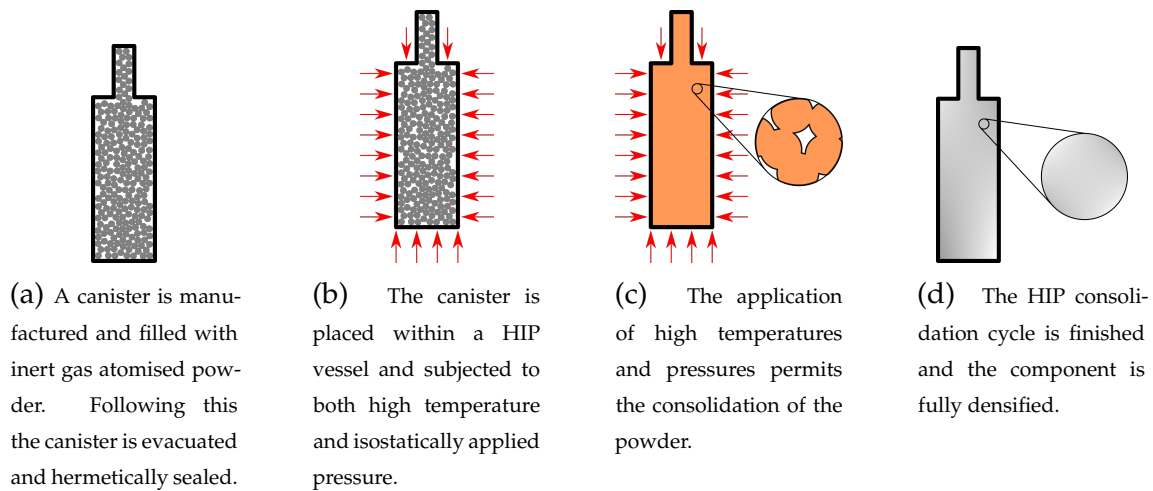


Figure 2.10: Simplified schematic of the main stages of the HIP consolidation cycle.

vessel (Fig. 2.9). The HIP pressure vessel is subsequently evacuated and purged with inert pressurising gas to remove any traceable remnants of both air and moisture. High purity inert gas is then used to equalise the pressure within the HIP pressure vessel prior to heating and pressurisation. The heating and (autogenously assisted) pressurisation stages are usually conducted simultaneously up to the required holding temperature and pressure. The heating and pressurisation rates as well as the holding temperature and pressure are prescribed on a case by case basis based upon the properties of the material being consolidated. The hold time is based on both material properties and the size of the compact. Following the completion of the holding period the HIP pressure vessel is equalized and the temperature is reduced at a prescribed rate. Following HIP consolidation, the canister used to encapsulate the powder is removed by either machining, grinding or chemical dissolution etcetera.

Although a variety of different powder production methods are suitable for HIPing, the preferred methods are those that produce a pre-alloyed, spherical shaped powder which is free from surface oxides and oxide inclusions. These preferred powder properties are characteristic of powder produced via gas atomisation. Consistently repeatable and high pre-HIP packing densities are achievable through the use of spherical shaped gas atomised powder. Higher initial packing densities can be achieved using powder with broad size distributions as opposed

to mono-sized powder, irregular shaped powder, or powder with narrow size distributions. This is because smaller powder particles are capable of filling the interstices between larger powder particles thus, increasing the overall packing density [90]. Information of the HIP canisters and the canning process can be found in references [85–87, 90].

The consolidation of metal powder via HIPing can be described by three main physical mechanisms: (i) powder consolidation, (ii) neck growth and (iii) final densification. Prior to HIPing, powder filled canisters have a relatively low density of approximately 60 to 80 % of the theoretical density. The powder consolidation phase involves both particle rearrangement and macroscopic deformation. In other words, the metallic powder can be described as a cohesionless granular material in which particles can slide freely over one another without any meaningful particle deformation [90]. This particle rearrangement ultimately ceases as particles are no longer able to freely pass one another without considerable particle deformation and this point marks the onset of neck growth between contacting particles. Neck formation involves the generation of bonds between contacting particles, however the porosity within the compact is still interconnected. Neck growth mechanisms include: plastic deformation of particles via dislocation motion, power law creep (dislocation creep) [93], Nabarro-Herring creep (volume diffusion creep), and Coble creep (grain boundary creep) (Fig. 2.11 (transport paths 1, 2 and 6)) [85, 86, 88, 90, 94–96]. Neck growth is also increased through transport paths 3, 4 and 5 which are illustrated in Fig. 2.11, however these mechanisms do not result in densification as matter is only moved from one place within a pore to another. These material transfer mechanisms result in a change in pore shape, however the volume of the pore remains the same [87]. The material during the final densification stage can be described as solid containing isolated pores that of which are separated by grain boundaries.

2.3.2.3. Gas atomisation

Atomisation can be described as the transformation of a bulk liquid into a spray of fine liquid droplets. In gas atomisation, liquid metal is disrupted by high velocity

Mechanism	Transport path	Source of matter
1	Grain boundary diffusion	Grain boundary
2	Lattice diffusion	Grain boundary
3	Lattice diffusion	Surface
4	Surface diffusion	Surface
5	Vapour transport	Surface
6	Lattice diffusion	Dislocation

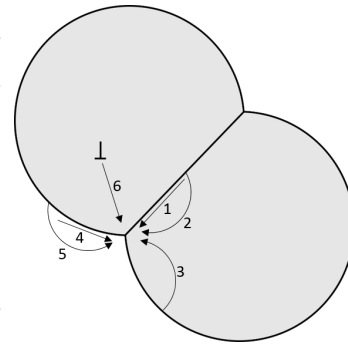


Figure 2.11: Schematic illustrating the paths through which matter is transported during neck growth.

gas jets of typically nitrogen, argon, or helium. Atomisation is achieved through the transfer of kinetic energy from the atomising gas to the melt. Information on the different configuration of gas atomiser can be found in references [90,97,98].

Generally speaking, atomisation can be characterised into three main stages Fig. 2.12 [97]: (i) Primary atomisation - the initial breakup of the liquid sheet or column; (ii) Secondary atomisation - the breakup of a liquid drop in gaseous surroundings; and (iii) Spheroidisation - the melt droplets are stabilised into spheres due to surface tension. However, it should be noted that breaking atomisation down into these distinct separate stages can be regarded as an oversimplification of the actual real-world process. In simple terms, atomisation is the result of the conflict between disruptive forces and the stabilising influences of surface tension, viscosity and density [99]. The disruptive forces can be attributed to turbulence within the liquid stream and aerodynamic interactions with high velocity inert gas etcetera. Atomisation ultimately occurs when the magnitude of the disruptive forces exceeds the consolidative force provided by surface tension. When a stream of liquid metal is subjected to high velocity gas, disturbances grow in the metal stream and cause its disintegration into ligaments and subsequently droplets. This process can be regarded as primary atomisation. If a droplet is formed early on in the atomisation process, it may still be subjected to a high velocity environment furthermore, this can promote secondary atomisation which results in the breakup of the droplet. The extent to which secondary atomisation occurs is largely dependent upon the surface tension of the droplet and to a lesser extent the viscosity and density of the liquid. Spheroidisation can be described as the region during

atomisation in which any oscillations in the shape of droplets is damped out by internal viscous stresses.

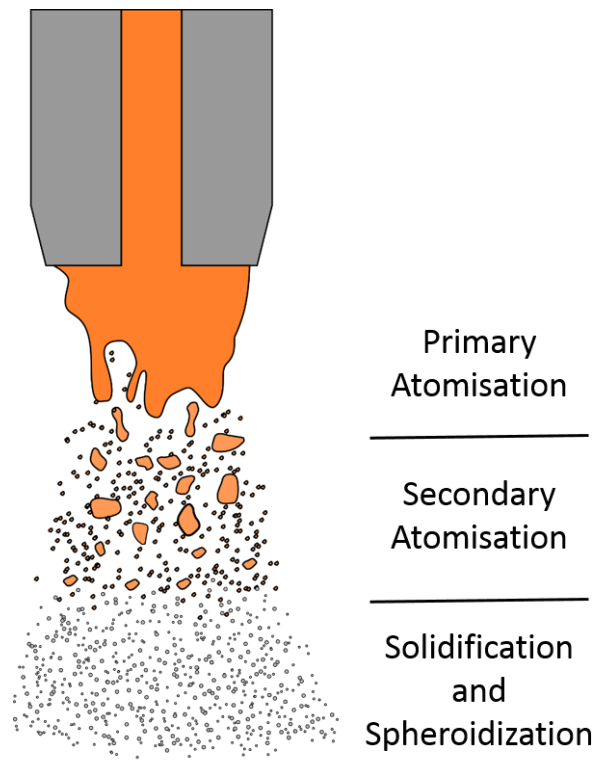


Figure 2.12: Idealised schematic of the main stages of atomisation.

Various factors influence the shape of powder particles [97], more specifically (i) the atomisation technique, (ii) the chemistry of the alloy, (iii) the environment within which atomisation is carried out, (iv) the cooling rate of freezing particles, (v) the particle-gas interaction during solidification, and (vi) the breakup time of melt drops. In light of the above, it can be assumed that the architectures of atomised powder particles are generally spherical except for when [97]: (i) oxide layers form as a result of oxidation reactions that take place between the alloy and the atomising atmosphere; (ii) the particle is subjected to extremely rapid cooling in turbulent conditions; (iii) in flight impacts occur between particles in the freezing zone thus leading to satelliting or splat caps [100, 101]; and (iv) the viscosity of the melt is sufficiently high that breakup times are longer than freezing times.

It can be concluded that powder particles produced by gas atomisation are generally smooth and spherical in shape and can deviate from this morphology due to

satelliting and the presence of splat caps. It has been proposed that satelliting is a result of finer powder particles being drawn back into the spray plume due to the circulation of gas within the atomisation chamber. These finer powders potentially collide with partially molten powders resulting in the formation of satellites [100]. The size distributions of powder produced via inert gas atomisation are generally broad (standard deviation, $\sigma \approx 1.9-2.2$ [90,102]) and usually conform to log normal or Weibull distributions.

2.4. STELLITE HARDFACING ALLOYS

2.4.1. Introduction to Stellite

Amidst several notable metallurgical discoveries made by Elwood Haynes, arguably his greatest and longest lasting contribution to the field of materials science was his unique development of a series of cobalt, chromium, and tungsten and or molybdenum alloys between 1899 and 1915, which he named Stellite [103,104]. The name Stellite was derived from the Latin word *stella* meaning star due to the bright lustre in appearance exhibited by the Stellite family of alloys. Haynes's patent for an early binary, Co-Cr based predecessor to Stellite [104] was designed for, "the manufacture of articles requiring a high and durable lustre, and possessing a degree of hardness adapting it to be substituted for mild tempered steel in the manufacture of edge tools, as table and pocket cutlery, physicians' and dentists' instruments, or standards of weight, measures, etc.". Stellite alloys are now extensively used for hardfacing applications in engineering components because of their inherently good wear and corrosion resistance within even the most aggressive environments [105]. Generally speaking, Stellite alloys comprise around 30 wt% chromium which is principally added for corrosion resistance and solid solution strengthening, tungsten additions between 4 and 17 wt%, primarily added for solid solution strengthening, and carbon additions of up to ~ 2 wt% for the precipitation of hard carbide phases the nature of which depends on the precise alloy chemistry [106]. However, the importance of controlling minor element contents has been recognised, therefore the control of Fe, Si, Mo, Ni, Mn and B is

becoming more stringent to ensure optimum properties.

Table 2.4: Nominal composition of Stellite 6 in wt% [20].

Element wt%				
Co	Cr	W	C	Other
Bal.	27-32	4-6	0.9-1.4	Ni, Fe, Si, Mn, Mo

Table 2.5: A selection of physical properties of Stellite 6 [20].

Physical property		
Hardness (Hv)	Density (kg/m^3)	Melting Range ($^{\circ}\text{C}$)
380-490	8440	1285-1410

Whilst a range of Stellite alloys are available, Stellite 6 (Table 2.4 Table 2.5) exhibits a particularly attractive combination of both wear and corrosion resistance for hardfacing applications in the primary cooling system of a PWR. The alloying addition of Cr is of paramount importance to the matrix of Stellite 6 as it provides solid solution strengthening in addition to conferring oxidation and corrosion resistance. The most prevalent carbide phases in Stellite 6 is an M_7C_3 type carbide where M typically represents Cr, Co, Fe. The alloying addition of W gives additional solid solution strengthening to the matrix and can also lead to the formation of an η -type carbide that exhibits a cubic crystal structure and is typically M_6C or $M_{12}C$ where M is principally tungsten.

2.4.2. The allotropic fcc \leftrightarrow hcp transformation in cobalt and its alloys

Before elaborating on the metallurgy of Stellite 6, one must first consider the allotropic fcc \leftrightarrow hcp transformation that cobalt can impart to its alloys including Stellite 6. Under equilibrium conditions and at temperatures below ≈ 700 K pure Co exhibits a hexagonal close-packed (hcp) crystal structure; above this temperature Co undergoes a transformation to a face-centred cubic (fcc) crystal structure [107]. The fcc-hcp allotropic transformation is unique among the known

elements and is extensively exploited in industry [108]. Uhl and Kübler [109] suggest that spin fluctuations and the reduction of the magnetic moments with increasing temperature govern the phase transformation in Co. Unfortunately, this work fails to explain the fundamental fact that Co-remains magnetic up to its Curie temperature of ≈ 1400 K [110] which suggests that there are additional temperature dependent energy contributions governing the fcc-hcp transformation in Co. A recent study by Lizárraga et al. [111] on the free energies of both the hcp and fcc phases of Co suggests that the energy of the lattice vibrations, the magnetic and electronic entropies in addition to the volume expansion effect are all crucial in stabilizing the fcc phase above 700 K. Contrary to the work of Uhl and Kübler [109], the work of Lizárraga et al. [111] shows that the vibrations of the ionic lattice are the largest energy contributor in the destabilisation of the hcp Co phase with increasing temperature.

The mechanism through which the temperature induced fcc \rightarrow hcp and hcp \rightarrow fcc allotropic transformations occur in Co are known to be governed by the dissociation of an ordered array of perfect dislocations and association of an ordered array of Shockley partials respectively. The spacing between two partial dislocations is governed by an energy balance between the energy associated with the stacking fault and the energy of interaction between the two partials. The formation of an intrinsic stacking fault (Fig. 2.13b) can result from the motion of a Shockley partial dislocation along a single close packed plane i.e. the embryo for hcp transformation with a thickness of two planes. If one now considers a the motion of such a dislocation on every second plane of the fcc structure the result is a bulk transformed region which exhibits a hcp crystal structure with an ... ABABAB... stacking sequence [112–114] (Fig. 2.13c). Similarly, the hcp \rightarrow fcc occurs via the association of an ordered array of Shockley partials [113,114] (Fig. 2.13). Whilst at temperatures within the fcc phase field the fcc \rightarrow hcp transformation is prevented due to the high energy relative to the fcc parent phase associated with the defect structure which resides between the ordered array of Shockley partial dislocations. Upon cooling into the hcp regime, the above is no longer the case as the hcp structure is now the stable phase [113].

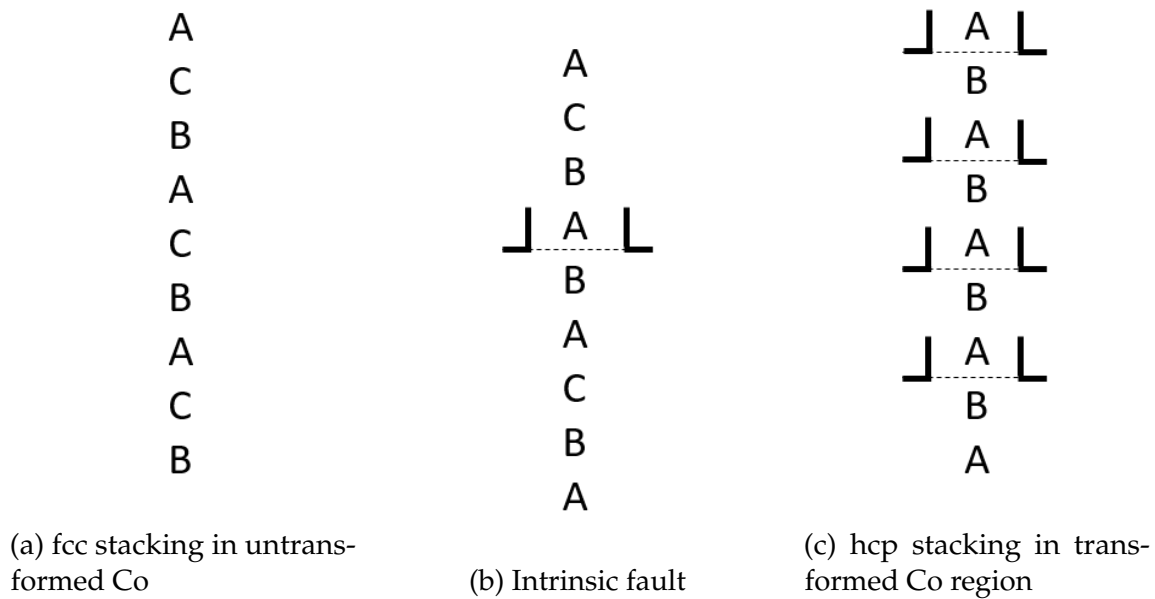


Figure 2.13: (a) shows the stacking sequence of untransformed fcc Co. (b) illustrates an intrinsic stacking fault which is the embryo for hcp transformation. (c) shows a completely transformed hcp region resulting from the ordered glide of a uniform array of Shockley partials.

One also needs to consider the multivariant nature of the transformation whereby, a multivariant transformation is one which takes place on more than one plane available for transformation. In the case of the above, this is the $\{111\}$ type planes (defined by Thompson's tetrahedron). Transformation in more than one direction on a particular type of plane is termed coplanar multivariance. This is the case for the mechanism outlined above whereby different $\frac{1}{6}\langle 11\bar{2} \rangle$ partial dislocations are operative in a given $\{111\}$ plane [114].

At room temperature, polycrystalline Co comprises a mixture of both the fcc and hcp phases [113,114]. The retention of the metastable fcc structure arises from both the multivariant nature of the transformation in addition to the minimal thermodynamic driving force promoting the complete transformation [105,114]. In addition to the above, other factors influencing the retention of the fcc phase are the grain size, purity and defects within the Co sample [114]. The fcc \rightarrow hcp transformation occurs at notably low temperatures where significant large-scale dislocation redistribution is prohibited although, some localised annihilation and redistribution may take place. Therefore, some of the fcc crystal structure remains as the material cannot accommodate the volume change associated with

the transformation or as a result of an absence of suitable dislocations sources [114].

The unique fcc-hcp transformation exhibited by Co has, unsurprisingly, been exploited in its alloys including the Stellite family. The matrix phase makeup of the vast majority Stellite alloys, in particular Stellite 6, depart from equilibrium in that they exhibit the metastable fcc crystal structure at room temperature. As previously discussed, due to the low temperature nature of the hcp \rightarrow fcc transformation and the mechanisms involved, it is possible that Co and its alloys can retain some the metastable fcc crystal structure at room temperature. Additionally, it has been reported that the fcc \rightarrow hcp transformation in alloyed Co is sluggish in nature [115,116]. The above therefore explains why Stellite alloys invariably exhibit the metastable fcc matrix structure in their undeformed state. With special reference to the Stellite family of alloys, the addition of small quantities of alloying elements can greatly affect the stability of either fcc or hcp phases and thus alter the equilibrium allotropic transformation temperature. The alloying additions of Cr, Mo and W are known to increase the transformation temperature and thus stabilise the hcp phase whilst the additions of Ni, C and Fe reportedly stabilise the fcc allotrope and thus reduce the transformation temperature [115,117].

2.4.3. Metallurgy and microstructure of Stellite 6

2.4.3.1. Cobalt

Stellite alloys possess a cobalt based solid solution matrix which at room temperature will typically exhibit a metastable fcc crystal structure with an inherently low stacking fault energy. The retention of the metastable fcc phase in Stellite alloys at room temperature is essential to their attractive wear characteristics as the fcc \rightarrow hcp phase transformation can be induced by mechanical deformation at low temperature (< 700 °C). The metastable fcc structure and strain induced transformation exhibited by Stellite alloys contributes significantly to their high yield strengths, high work-hardening rates, and characteristically low susceptibility to fatigue damage under cyclic loading [116].

2.4.3.2. Chromium

The alloying addition of chromium within Stellite alloys serves as the principal carbide former in addition to being the most important alloying element in the matrix. Cr resides as a substitutional solute atom within the Co-based matrix and strengthens the matrix via substitutional solid solution strengthening [116,118]. Additionally, Cr imparts a high degree of corrosion and oxidation resistance to the Co-based matrix because it in part facilitates the formation of a passive Cr_2O_3 oxide on the surface. Cr also has a high affinity for C thus permitting the precipitation of M_7C_3 carbide where M represents Cr, Fe and Co.

2.4.3.3. Tungsten and molybdenum

Alloying with refractory metals namely W or Mo imparts a solid solution strengthening effect to the Co-based matrix of Stellite alloys [116,118]. The substitution of W and Mo within the Co-based matrix has a strengthening effect as their large atomic sizes distorts the Co lattice; the resulting strain field subsequently impedes dislocation motion and slip [119]. Although W is known to partition to the carbide phases within some Stellite alloys, its slow kinetics of diffusion within the Stellite alloy systems dictates that W predominantly remains in the Co-based matrix solid solution [120]. When present in large quantities such alloying additions can also lead to the precipitation of additional carbide phases principally of the (η)-type. It is also commonly accepted that these alloying additions improve the general corrosion resistance of Stellite alloys [116].

2.4.3.4. Carbides

The hardness associated with Stellite alloys is predominantly governed by the dispersion of hard carbide phases within a softer matrix solid solution [115]. Fig. 2.14 illustrates the relationship between the carbon (plus boron) content and hardness for a number of Stellite alloys [115]. This is based on data from cast, arc-welded and wrought microstructures. Evidently, the hardness of Stellite alloys is principally governed by the carbon (or carbon + boron) content within the

alloy [106,115] and therefore hard phase precipitation. Obviously, solid solution and grain size strengthening contribute to the actual hardness of Stellite alloys, however Fig. 2.14 highlights the importance of carbon and subsequently carbide (and boride) precipitation on the hardness of Stellite alloys.

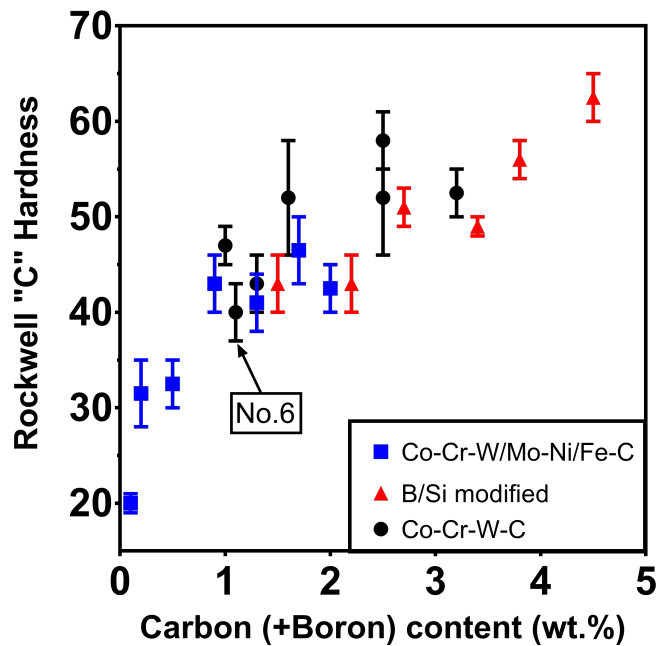


Figure 2.14: Graph illustrating the relationship between carbon (plus boron) content on the hardness of Stellite alloys. Both the compositions and hardness values are from the work of Antony [115].

The most notable elemental difference between the different Stellite grades is the carbon content and therefore the carbide fraction in the different grades of Stellite. For example, Stellite 6 contains ~ 1 wt% carbon which results in the alloy being composed ~ 13 wt% Cr-rich M_7C_3 type carbide [115]. In the case of Stellite 3, a carbon level of 2.4 wt% results in an alloy where carbides constitute ~ 30 wt% of the material; these carbides are M_7C_3 type Cr-based carbide and an eta (η) type tungsten-rich carbide [115]. As expected, the morphology of the carbide phases within Stellite alloys depend on the manufacturing method.

2.4.3.5. Microstructure and phase formation in Stellite 6

Both the phase makeup and microstructure of Stellite 6 are dependent upon the processing routes employed during manufacture. In the case of gas atomised,

weld deposited and conventionally cast variants of Stellite 6, the phase makeup and microstructure depend upon the cooling rate and therefore the degree of undercooling during processing. In contrast, Stellite 6 obtained by solid state processing e.g. HIPing (hot isostatically pressed) or forging exhibits a microstructure which is closer to equilibrium.

X-ray diffraction studies conducted by Kong et al. [121] and Sassatelli et al. [122] suggest that the phase makeup of gas atomised Stellite 6 powder was principally comprised of an fcc Co-based matrix with only a small fraction ($\sim 5\%$) of sub-micron Cr-based M_7C_3 type carbide. The fraction of M_7C_3 type carbide reported in Stellite 6 powder is significantly less than the ~ 13 wt% expected for the Stellite 6 composition [116, 122] at equilibrium, therefore suggesting that the precipitation of the M_7C_3 phase is largely suppressed as a result of rapid cooling rates and deep undercoolings associated with gas atomisation [122].

The hypoeutectic conventionally cast microstructure of Stellite 6 can be described as predominantly fcc Co-rich dendrites which are surrounded by a dispersion of M_7C_3 Cr-rich eutectic carbides with a small fraction of W-rich eta carbide [106, 123] (Fig. 2.15). From studies of sand cast, gas tungsten arc weld and wrought Stellite 6 (Co-28Cr-4W-1.1C in wt%), Antony [115] reports a matrix composition of Co-23%Cr-4.5%W. This work also suggests that cast Stellite 6 contains ~ 12.6 wt.% Cr-based M_7C_3 type carbides with a proposed composition of $(Cr_{0.8}Co_{0.15}M_{0.05})_7C_3$ where the M denotes W in addition to other residual elements.

Atermert and Badeshia [124, 125] conducted in-depth microstructural analysis of Stellite 6 deposited by manual metal arc (MMA) welding, tungsten inert gas (TIG) welding and laser cladding onto low carbon steel. This work showed that for all of the above cases the major microstructural constituents were the same, more specifically cobalt-rich fcc dendrites and an interdendritic mixture of the cobalt-rich fcc phase and eutectic M_7C_3 carbides. However, MMA resulted in the coarsest microstructure whilst laser cladding resulted in the finest microstructure. TEM studies of the as deposited Stellite 6 hardfacings revealed intrinsic stacking faults on all the close packed $\{111\}$ planes which are believed to arise as a result of

residual stresses post deposition. These intrinsic flaws represent a three layer thick region of transformation to the HCP crystal structure. Atermert and Badeshia also report the presence of $M_{23}C_6$ precipitates in the MMA deposited microstructure which are consistent with the slow cooling rate associated with MMA deposition and comparable to the conventionally cast microstructure reported by [106, 123]. Electron diffraction from the M_7C_3 phase revealed the presence of streaks which are reported to be the boundaries between different orientations of domains of orthorhombic structure [126].

In contrast to cast Stellite 6, the powder HIPed microstructure is almost entirely composed of a uniform distribution of micron sized M_7C_3 (Cr-rich) carbides that are surrounded by an fcc Co-based matrix [7, 123, 127] (Fig. 2.15). Image analysis performed by Yu et al. [123] suggests that HIPed Stellite 6 is composed of 17.9 ± 1.7 vol.% M_7C_3 and 82.1 ± 1.7 vol.% Co-based matrix. HR-EBSD studies conducted by Zhao et al. suggest that HIPed Stellite 6 has 86.3 vol.% fcc Co-based matrix, 13.6 vol.% M_7C_3 Cr-based carbide and 0.1 vol.% hcp Co-based matrix. Similarly, XRD conducted by Ashworth et al [127] also indicates the presence of a very small fraction of the hcp allotrope in HIPed Stellite 6. Unlike the cast microstructure W-rich carbides are not found within the HIPed microstructure. It has been suggested that this could be attributed to the very short time for diffusion associated with gas atomisation which prevents the segregation of W-rich zones. Subsequently, the large atomic radius of tungsten prohibits significant tungsten diffusion during HIPing and therefore it exhibits a near homogeneous distribution throughout the HIPed alloy. Gas atomisation followed by HIPing reportedly enables the complete suppression of W-rich carbides within the alloy [123].

2.4.4. Deformation behaviour of Stellite alloys

It is often argued that one of the principal factors governing the wear characteristics of Stellite alloys is the high work hardening ability of the Co-based solid solution matrix phase [29, 128]. When a Co-alloy exhibits the metastable fcc allotrope (i.e. Stellite alloys), the fcc \rightarrow hcp transformation can be induced via straining at temperatures below the equilibrium fcc \rightarrow hcp transformation temperature as a result

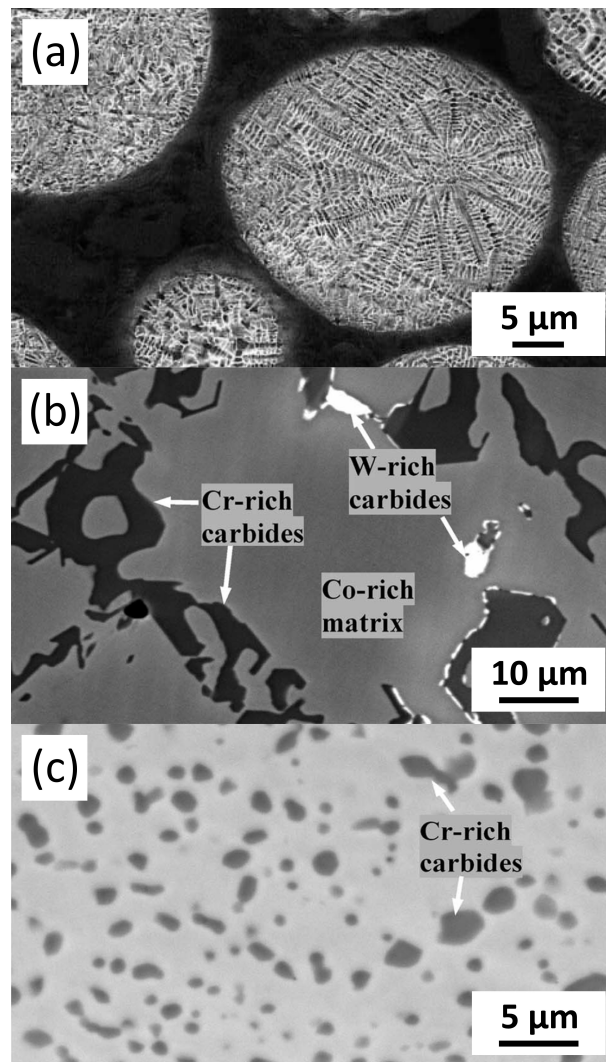


Figure 2.15: (a) Secondary electron image of etched Stellite 6 powder [121]. (b) BSE micrograph of the typical cast microstructure of Stellite 6 [123]. (c) BSE micrograph of the typical HIPed microstructure of Stellite 6 [123].

of a mechanism involving the coalescence of an ordered array of stacking faults. The inherently low stacking fault energy of cobalt ($15\text{--}50\text{ mJ/m}^2$ [129, 130]) means so called perfect dislocations can readily decompose into partial dislocations thus giving rise to a stacking fault which can be regarded as the embryo for $\text{fcc}\rightarrow\text{hcp}$ transformation. In other words, the low stacking fault energy matrix of Stellite alloys means plastic deformation via dislocation cross slip or climb is less energetically favourable relative to plastic deformation via the generation of stacking faults and subsequently transformation. This deformation mechanism is responsible for the rapid work hardening observed in Stellite alloys [110, 113, 116, 127].

Smith [131] performed in situ uni-axial thermomechanical synchrotron mea-

measurements on HIPed Stellite 6 and suggest that Stellite 6 exhibits a large work hardening and less ductility at room temperature and 350 °C relative to testing at 700 and 825 °C. This observation was rationalised by an observable increase in defect generation and transformation during room temperature and 350 °C testing compared to testing at 700 and 825 °C. With respect to room temperature and 350 °C testing, Smith [131] suggests that plastic deformation at low strains is initially accommodated by defect generation within the γ -Co matrix phase resulting in work hardening. At larger strains ($\sim 2.5\%$ and $\sim 3.5\%$ for room temperature and 350 °C testing respectively) plastic deformation is accompanied by the fcc \rightarrow hcp transformation.

In their cyclic three point bending studies at low strains (5.3% after loading), Zhao et al. [7] suggest that HIPED Stellite 6 accommodates plastic deformation principally via heterogeneous slip. It has been suggested that intergranular carbides play a key role in slip activation and development in Stellite 6 whereby slip bands change direction or new slip systems are activated at the sites of intergranular carbides. This work reports a diffuse and homogeneous strain distribution in the deformed matrix and suggest that the effective work hardening exhibited by Stellite 6 could be the reasoning for this phenomenon. Zhao et al. [7] propose that early slip system activation and the subsequent work hardening promotes slip system activation in previously undeformed grains driven by a local change in stress state.

Various studies exist which investigate the deformation structures of cobalt alloys for example references [130,132]. Regardless, it is well known that the stacking fault energy (SFE) of a cobalt solid solutions heavily influences the mechanisms through which plastic deformation is accommodated (Fig. 2.16). Additionally, these such works illustrate the temperature and compositional dependent nature of the SFE in Co-based solid solutions.

2.4.5. Degradation of Stellite in a PWR environment

The following two sections aim to provide an overview of the limited number of studies which assess the degradation of Stellite hardfacings specifically within a

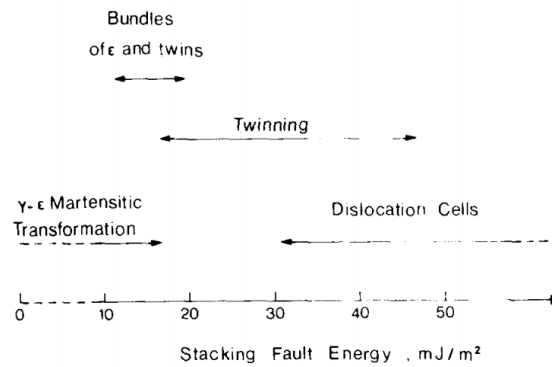


Figure 2.16: Deformation structures observed in Co-Ni-Cr-Mo alloys near room temperature as a function of stacking fault energy [130].

primary coolant system PWR environment.

2.4.5.1. Aqueous corrosion and oxidation of Stellite

Several authors have investigated the corrosion behaviour of Stellite 6 in a simulated primary coolant system environment at temperatures up to 300 °C in water containing LiOH or a combination of LiOH and H₃BO₃ [133–137]. These studies observed the presence of Cr-enriched Co-depleted oxide films which reportedly develop as a result of solid state diffusion and preferential dissolution of cobalt from the oxide-solution interface. Hocking and Lister [137] also suggest that the oxide layers principally form on the cobalt matrix phase as opposed to the Cr-based M₇C₃ carbide phase present within Stellite 6. X-ray photoelectron spectroscopy (XPS) studies after both long- and short-term exposure to simulated primary system PWR conditions suggest that Cr₂O₃ and CoO are typically found in the uppermost surfaces of the oxide layers which form on Stellite 6 [133,134,136]. Karimi et al. [138] performed long term exposure tests on Stellite 3 and observed preferential interfacial corrosion between the Co-based solid solution matrix and the Cr-rich carbide phase which they attributed to an electro chemical effect. Obviously, the corrosion rate and mechanisms of corrosion for Stellite alloys are significantly influenced by temperature and water chemistry. Interestingly, during their work on cobalt alloys subjected to lithiated PWR conditions, Taylor and Armson [133] reported a ten-fold increase in the release rate of cobalt as a result of increasing the temperature from 180 °C to 250 °C. However, this work also reports

a relatively small difference in the cobalt release rate between 250 °C and 290 °C.

2.4.5.2. Tribocorrosion of Stellite in PWR conditions

It has been proposed that Stellite alloys are susceptible to tribocorrosion within a PWR environment whereby material loss is principally attributed to the repeated growth and mechanical removal of passive oxide layers [139,140]. With reference to PWR control rod drive mechanisms, Lemaire and Calvar [141] provided evidence which strongly suggests that Stellite 6 is susceptible to tribocorrosion and propose that wear increases with the number of depassivation events and time for material dissolution before repassivation. Xu et al. [142] performed electrochemical measurements before and after sliding wear in a simulated PWR environment on an alloy analogous to Stellite 6 (UNS R30006) in an effort to investigate the effects of wear on corrosion rate. After applying mechanical stimulation to disrupt the oxide layers at the interface, it was observed that the corrosion rate did not notably increase after wear at low temperatures (25-65 °C). However, at elevated temperatures (150-250 °C), the increase in corrosion rate was up to eight times greater in comparison to the corrosion rate prior to the wear event (depending on the specific experimental conditions). Moreover, it took ~ 20 min before the corrosion rate returned to the same lower levels prior to the application of the mechanical stimulus. More recent work conducted by Ratia et al. [143,144] investigated the sliding wear behaviour of self-mated HIPed Stellite 6 and 3 in lithiated water as a function of temperature. This work attributed tribocorrosion to a notable increase in wear following testing at temperatures above 150 °C. It was proposed that the rate of oxidation increases with respect to increasing temperature for Stellite alloys and that the repeated mechanical removal of this oxide product from the surface accounts for the increase in wear with respect to temperature.

2.4.6. Related wear and degradation studies on Stellite and other Co-based alloys

2.4.6.1. The tribological importance of oxidation during in air sliding wear of Stellite alloys

The importance of the oxide layer on Stellite 6 and 21 under room temperature dry sliding conditions has been highlighted by Persson [145] who suggests that an oxide layer predominantly comprising Cr_2O_3 and CoO greatly reduces the extent of surface damage and wear. However, Persson's work suggests that the presence of an oxide layer has only a marginal effect on the coefficient of friction under dry sliding testing conducted at room temperature and attributes the room temperature performance of Stellite predominantly to the alignment of the basal planes parallel to the direction of shear.

In their elevated temperature metal-to-metal dry sliding wear tests on cobalt-chromium alloys in air, Crook and Li [146] observed the formation of a protective oxide glaze layer at temperatures in excess of $250\text{ }^\circ\text{C}$. They also suggested that in these alloys, stacking fault energy increases with increasing temperature (resulting in higher wear rates), however the effect of the protective oxide dominates tribological degradation as the temperature was increased above $250\text{ }^\circ\text{C}$. Additionally, the self-mated dry sliding wear testing of Stellite 31 in air performed by Scott et al. [147] reported similar results to Crook and Li [146]. At temperatures in excess of $250\text{ }^\circ\text{C}$, a stable thermally softened oxide glaze layer formed which acted to retard the rate of wear [147]. Although a glaze layer was not explicitly observed, Conceição et al. [148] reported similar findings for Stellite 1 in air under dry sliding wear conditions. At a temperature of $700\text{ }^\circ\text{C}$, rapid tribolayer formation occurred as a result of the compaction of oxidised debris. This work concluded that at $700\text{ }^\circ\text{C}$ the oxide film becomes stabilised and reduces both the wear rate and coefficient of friction. Birol [149] also reported the formation of a glazed layer on Stellite 6 during ball-on-disk wear tests conducted in air at an elevated temperature of $750\text{ }^\circ\text{C}$. This work attributed the superior elevated temperature ($750\text{ }^\circ\text{C}$) wear resistance of Stellite 6 to an adherent and relatively highly plastic film that forms on the surface of Stellite 6. It is reported that this film is capable of sustaining the action of sliding wear without spalling.

2.4.6.2. Tribocorrosion of Stellite type alloys in alternative environments

Guadalupe Maldonado et al. [150] studied the tribocorrosion behaviour of Stellite 21 (CoCrMo type alloy with low C) in sulphuric acid at ambient temperature under a range of different conditions and suggest that wear increases by an order of magnitude when a passive film forms on the surface. This work suggests that wear accelerated corrosion and mechanical wear are the two mechanisms which contribute to material degradation. The formation of a passive film reportedly increases the wear rate of Stellite 21 due to: (i) corrosion enhanced wear and the repeated removal of the passive film; and (ii) an increase in subsurface deformation when the oxide film is present.

To date, a large volume of literature exists, for example in references [80–82], which investigate the tribocorrosion phenomenon that occur in the CoCrMo type alloys used in joint replacement prostheses. These studies discuss the importance of the nanochemical tribocorrosion phenomenon whereby a nanocrystalline layer is generated in response to the application of mechanical sliding loads. Büscher et al. concluded that material removal occurs as a result of either (i) the tearing of nanocrystals resulting in globular debris (< 80 nm), or (ii) the fracture of ϵ -martensite resulting in needle-shaped debris. It was proposed by Büscher and Fischer [80] that dynamic recrystallisation resulting in the nanocrystalline layer is a result of two mechanisms, more specifically (i) the rotation of clusters of atoms at the mating surface, and (ii) the shearing of cells which are generated by stacking faults and ϵ -martensite needles. Büscher and Fischer [80] concluded that a low stacking fault energy and discrete planar sliding in response to plastic deformation are essential material attributes which enable the steady increase in strength towards the surface without generating defect structures which may increase wear rate.

2.4.6.3. The temperature dependent nature of stacking fault energy

Crook and Lee [146] investigated the in air sliding wear performance of cobalt-chromium alloys and suggested that with increasing temperature up to 250 °C a decrease in wear resistance could be linked to a temperature dependent increase in stacking fault energy. This observation is in agreement with the work of Bhansali and Miller [151] who studied the role of stacking fault energy on the tribological performance of a range of different Co-, Fe- and Ni-based alloys. This work concluded that materials with low stacking fault energies and high stacking fault densities are capable of rapid strain hardening and therefore exhibit the highest resistance to galling and sliding wear.

2.4.6.4. Crystallographic texture in Stellite as a result of sliding contact

The work of Persson et al. [145, 152, 153] on both Stellite 6 and 21 suggests that under dry sliding conditions a preferentially oriented superficial layer of transformed (hcp structure) material forms where the basal planes of the hcp structure become preferentially aligned parallel to the direction of shear (Fig. 2.17). This preferentially orientated layer reportedly has a maximum observed thickness of ~ 30 nm and is beneficial to the sliding wear resistance of Stellite alloys. Basal planes are the only easily activated slip planes in a hcp crystal structure, therefore the reoriented hcp layer can readily accommodate deformation. Persson et al. [145, 152, 153] concluded that the alignment of the basal plane parallel to the direction of shear is the crucial mechanism governing the low friction properties exhibited by the Stellite family of alloys.

The observations of Persson regarding the alignment of the basal planes in Stellite alloys are in line with the findings by Huppermann and Clegg [154] who noted a preferred orientation of the hcp basal planes parallel to the direction of shear in polycrystalline pure Co after sliding wear in air. A more fundamental study on the plastic deformation of Co single crystals without the added complexity of the wear of polycrystalline materials by Barquins and Courtel [155] showed

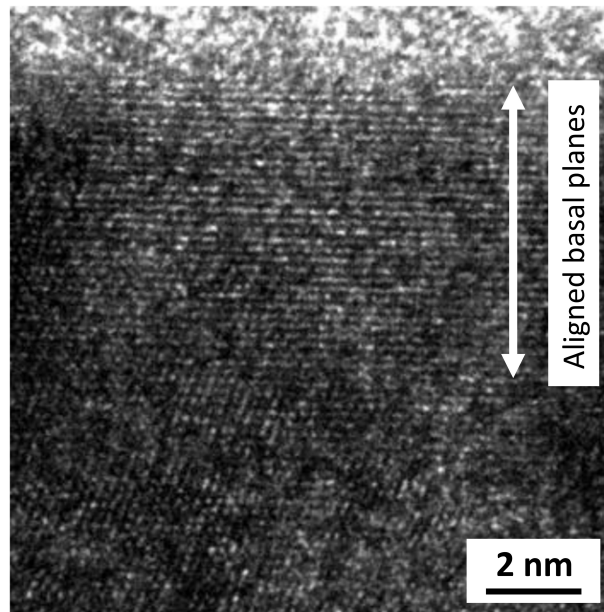


Figure 2.17: HR-TEM illustrating the alignment of the basal planes parallel to the direction of sliding induced shear in a Stellite alloy [145].

that the basal plane is the plane of lowest friction in hcp cobalt. Huppermann and Clegg [154] reported a reduction in coefficient of friction with increasing applied load for polycrystalline Co; they attributed this observation to increased plastic deformation resulting in an increase in the preferred basal orientation. This work is in agreement with the work of Wheeler and Buckley [156] who suggest that texturing in cobalt as a result of (in air) sliding is expected to be sensitive to loading due to the limited number of slip systems associated with the hcp allotrope of Co. Huppermann and Clegg [154] also illustrated the importance of the hcp structure through the alloying of Co with 8 wt% Fe to stabilise the fcc allotrope. This work showed that the stabilised polycrystalline fcc cobalt had over twice the coefficient of friction and initial wear rate of the polycrystalline hcp allotrope during sliding wear tests.

The findings of Buckley and Johnson [157] are in agreement with the above and conclude that the crystal structure influences both the adhesion and friction of polycrystalline and single crystal metals and that hcp metals exhibit notably lower coefficients of friction and adhesion in comparison the fcc and bcc crystal structures. With respect to crystallographic orientation, the coefficient of friction for hcp materials is highly anisotropic in nature whereby the preferred slip plane

exhibits the lowest friction coefficient when sliding is performed on that plane in the preferred slip direction. Finally, Buckley and Johnson [157] report that the friction properties of hexagonal materials are related to both the lattice parameters and the number of slip systems associated with deformation. Generally speaking, hexagonal material which exhibit near ideal atomic stacking ratios, e.g. Co ($c/a = 1.633$), will slip primarily on the basal planes. hcp metals which exhibit basal slip generally have the lowest coefficient of friction as illustrated in Fig. 2.18. There are however some exceptions to this generalisation, for example beryllium ($c/a = 1.587$) which slips on the basal plane. Fig. 2.18 illustrates the ratio of inter basal spacing to a rather than the c/a because some hexagonal rare earth metals exhibit more than a single set of basal planes within the unit cell.

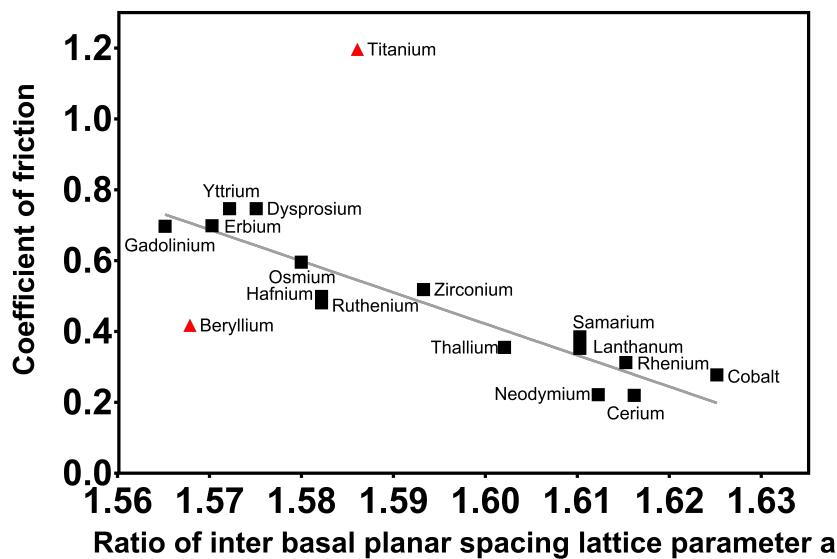


Figure 2.18: Data from the work of Buckley and Johnson [157] illustrating the coefficient of friction for various hcp metals sliding against 440C steel in a vacuum with a 100 g load and a sliding velocity of 2 m/s.

2.5. FE-BASED HARDFACING ALLOYS

2.5.1. Introduction to Fe-based hardfacing alloys

Ever since the first deployment of nuclear power plants for both commercial (Calder hall nuclear power station UK (1956)) and defence (USS Nautilus, S1W

reactor (1954)) applications, the safety critical nature of fission reactors has been much debated and rigorously regulated. One aspect of reactor design which is repeatedly questioned and scrutinised is the extensive use of Co-based Stellite hardfacings. Over the years a number of Fe-based hardfacings have been developed to address this issue, however a fully satisfactory Fe-based solution to this issue remains allusive. This is hardly surprising upon considering the metallurgical trade-off between alloy design for both corrosion and wear resistance. This problem is further convoluted by the fundamental lack of understanding concerning the metallurgy of hardfacings specifically designed for the operative wear mechanisms in nuclear systems, namely galling, tribocorrosion, and corrosion enhanced wear. In light of the above, this section aims to review the current literature on the metallurgy, deformation mechanisms, and tribology of Fe-based hardfacings with the aim of highlighting the fundamental gaps in our current understanding of Fe-based hardfacings for nuclear applications.

A plethora of well-established alloy design principals need to be considered prior to elaborating on the microstructure and metallurgy of Fe-based hardfacing alloys, more specifically: (i) Solid solution strengthening in the form of interstitial elements [158, 159], substitution elements [160], and substitutional-interstitial atomic complexes [161, 162]; (ii) Precipitate and dispersion strengthening, for example carbides and hard secondary intermetallic phases [27, 163]; (iii) Grain boundaries and polycrystalline strengthening whereby the grain size of polycrystalline materials can greatly influence both their strength and hardness such that grain size reduction is extensively exploited as a strengthening mechanism within engineering materials and hardfacings [164–174]; (iv) Dislocation interaction and stacking faults; and (v) Martensitic transformations. The vast majority of these alloy design principals are well reported in the literature and will not be discussed hereafter. However, the relative importance of dislocation interaction, stacking faults and martensitic transformations in Fe-based austenitic hardfacings cannot be overlooked with respect to their fundamental impact on the tribological performance of hardfacings. Additionally, these alloy design principals are less well understood in the context of Fe-based hardfacings and will therefore be discussed

in the following section.

2.5.2. Deformation structures in austenitic Fe-based alloys

In order to comprehensively evaluate the tribological performance of austenitic hardfacings, one must first consider the mechanisms which govern surface modification at a sliding interface. It is therefore important to evaluate the different deformation structures which have been observed in austenitic Fe-based alloys. To date, there are very few studies which assesses the deformation mechanisms of complex multiphase austenitic Fe-based hardfacings. Therefore, this section will principally focus on the extensive literature which details the deformation mechanisms and structures associated with austenitic stainless steels.

The deformation structures and subsequent work hardening behaviours of austenitic stainless steels are fundamentally dependent upon their stacking fault energy (SFE) which is influenced by both temperature and composition [175, 176]. As the SFE decreases, the plastic deformation mechanisms for austenitic steels shift from dislocation glide and climb (high SFE), to dislocation glide and climb plus mechanical twinning, to dislocation glide and climb plus martensitic transformation (low SFE) [175–182].

Two SFE dependent martensitic transformation mechanisms have been proposed in the literature [112, 183, 184], more specifically (i) a stress-assisted martensitic transformation via a pathway defined by $\gamma \rightarrow \epsilon \rightarrow \alpha'$, and (ii) a strain-assisted martensite transformation via a pathway defined by $\gamma \rightarrow \text{twinning} \rightarrow \alpha'$. Generally speaking, the martensitic transformation pathway is dependent on SFE whereby a low SFE ($< 18 \text{ mJm}^{-2}$) favours direct transformation whilst a higher SFE ($> 18 \text{ mJm}^{-2}$) favours transformation via $\gamma \rightarrow \text{twinning} \rightarrow \alpha'$ [179, 185, 186]

2.5.2.1. The formation of stacking faults and ϵ -martensite

A stacking fault is a planar defect in an otherwise perfect crystal structure which can be characterised by a disordering of crystallographic planes [187]. Face centred cubic (fcc) (ABCABC stacking sequence) and hexagonal close packed (hcp)(ABABAB stacking sequence) crystal structures differ only in their stacking

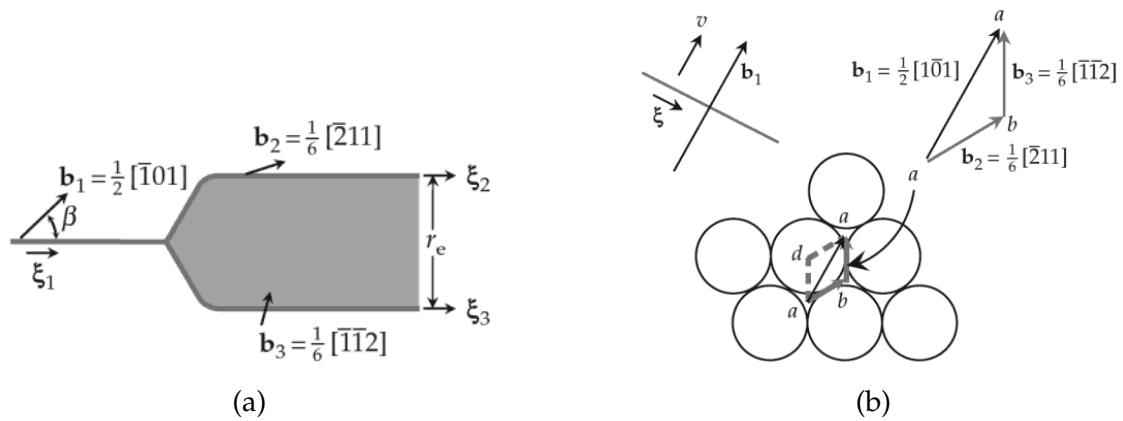


Figure 2.19: (a) Idealised schematic depicting the dissociation of a perfect dislocation b_1 into Shockley partials b_2 and b_3 [187]. (b) (lower) Hard sphere model of a close packed plane of atoms which resides just below a (111) glide plane with atoms situated just above the plane positioned at a sites [187]. (b) (upper left) glide of a perfect dislocation from the lower to the upper right of the figure with burgers vector b_1 and line sense ζ [187]. (b) (upper right) vector diagram illustrating a perfect dislocation b_1 and Shockley partial dislocations b_2 and b_3 [187].

sequence whereby both exhibit close packed planes with sixfold symmetry. Stacking faults can be subdivided into, (i) intrinsic stacking faults, (ii) extrinsic stacking faults, and (iii) high energy stacking faults [187]. Regardless, the intrinsic stacking fault Fig. 2.19(a) prevails in austenitic crystals because the extrinsic stacking fault has a higher fault and core energy than the intrinsic arrangement [187]. Additionally, the high energy type stacking fault has a prohibitively high energy [187].

Fig. 2.19(b) depicts a close packed layer of atoms situated just below the glide plane of a dislocation and the points defined by (a) denote the sites of the atoms just above the glide plane. The glide of the perfect dislocation $b_1 = \frac{1}{2}[\bar{1}01]$ from the one of the sites defined by a to the other site defined by a (Fig. 2.19b) clearly requires a larger dilation normal to the slip plane and hence a larger misfit energy relative to the indirect path defined by $a \rightarrow b \rightarrow a$. Therefore, the pathway defined by $a \rightarrow b \rightarrow a$ is more energetically favourable. The path from $a \rightarrow b$ as shown in Fig. 2.20 results in the creation of a stacking fault with relative shear displacement $b_2 = \frac{1}{6}[\bar{2}11]$. Similarly, the path from $a \rightarrow b$ requires a relative shear displacement of $b_3 = \frac{1}{6}[\bar{1}\bar{1}2]$. In other words, the glide of a partial dislocation $\frac{1}{6}[\bar{2}11]$ (Fig. 2.19b) results in the shearing of the crystal resulting in an intrinsic stacking fault Fig. 2.20

and the glide of the partial $\frac{1}{6}[\bar{1}\bar{1}2]$ removes the fault and restores the perfect lattice arrangement behind the dislocation [187]. Partial dislocations of the $\frac{1}{6} \langle \bar{1}\bar{1}2 \rangle$ type are glissile on the $\{111\}$ planes and are referred to as Shockley partials. Fig. 2.19a illustrates the dissociation of a perfect dislocation with Burgers vector b_1 into two Shockley partials with Burgers vector b_2 and b_3 respectively which enclose a stacking fault.

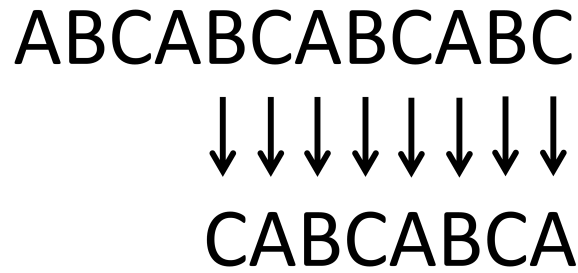


Figure 2.20: Schematic of an intrinsic stacking fault generated by shearing operations on the $\{111\}$ planes. In this instance, the B plane and all planes above it undergo a shear displacement $\frac{1}{6}[\bar{2}11]$ parallel to the B plane. Therefore, the B plane moves into the C position and each plane above it undergoes the transition $A \rightarrow B, B \rightarrow C$ or $C \rightarrow A$

The spacing between two Shockley partial dislocations is governed by the balance between the repulsive forces acting between the two partials (as a result of their interacting stress fields), and the attractive forces generated via the creation of a flawed region between the partials. The stacking fault energy per unit area of fault (λ) is expressed in Eq. (2.17), where n denotes the atomic planar thickness of the fault, ρ_A corresponds to the density of the atoms in the close packed plane (in moles per unit area), $\Delta G^{\gamma \rightarrow \epsilon}$ is the chemical free energy difference between austenite and ϵ -martensite, E^{str} is the strain energy, and $\sigma(n)$ is the free energy per unit area of the interface [112]. Fig. 2.21a schematically depicts the temperature dependent nature of the fault energy associated with the dissociation of defects of varying fault thickness [112]. At T_0^{coh} all the faults have the same energies 2σ , however the fault energies diverge as the temperature is decreased and the energy associated with thicker faults decreases more rapidly.

$$\lambda = n\rho_A(\Delta G^{\gamma \rightarrow \epsilon} + E^{str}) + 2\sigma(n) \quad (2.17)$$

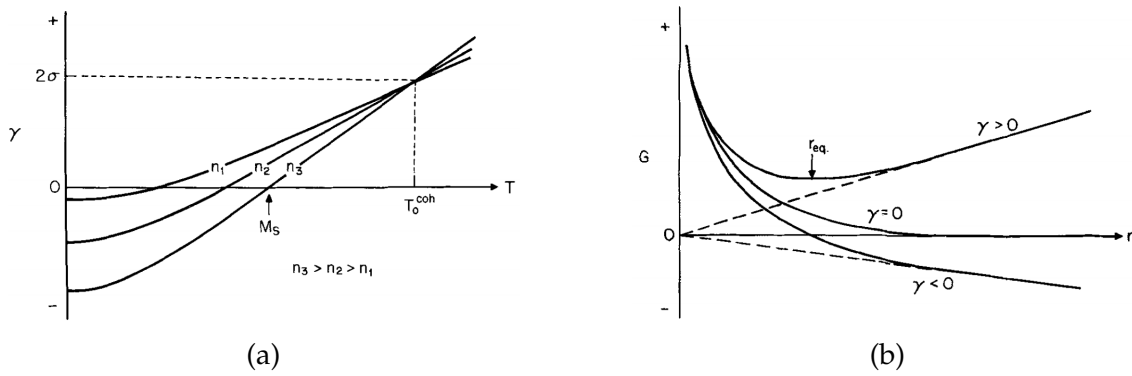


Figure 2.21: (a) Schematic depicting the temperature dependence of the fault energy (γ) for three faults of different thickness [112]. (b) Illustration depicting the total free energy (G) as a function of partial dislocation separation (r) for partial dislocations bounding a faulted region [112].

If one now considers the dissociation of a dislocation of infinite length which is separated by a distance r , the total free energy per unit length ($G(r)$) can be expressed as the summation of the dislocation energy ($E_{\perp}(r)$) and the fault energy (Eq. (2.18)) [112]. As the distance between two partial dislocations (r) increases, the dislocation energy ($E_{\perp}(r)$) monotonically decreases, therefore the restraining force for a stable partial dislocation separation arises from a positive stacking fault energy ($\gamma > 0$) Fig. 2.21b. When this criterion is met, there is an equilibrium partial dislocation separation (r_{eq}) where the total free energy is minimised and the dislocation repulsion is balanced by the attractive forces associated with the fault energy. When $\gamma < 0$ the fault is unstable with respect to the formation of a hcp martensitic embryo [112].

$$G(r) = E_{\perp}(r) + \gamma r \quad (2.18)$$

The $\gamma \rightarrow \epsilon$ transformation occurs via the coalescence of stacking faults on every two $(111)_{\gamma}$ planes by $\frac{a_{\gamma}}{6}$ [112] partial dislocations, where a_{γ} represents the lattice parameter of the parent γ -phase [112, 179, 181, 188–190]. Therefore, stacking faults can be regarded as an embryo or intermediate step in the $\gamma \rightarrow \epsilon$ transformation [189]. The $\gamma \rightarrow \epsilon$ transformation has been directly observed in austenitic stainless steels whereby plastic deformation yields the formation and growth of stacking faults which subsequently start to intersect, overlap, and

ultimately form bundles of stacking faults which permit the $\gamma \rightarrow \epsilon$ transformation [179, 189, 190]. Similar observations on Fe-based alloys have also been made in references [188, 191]. Additionally, the Shorji-Nishiyama [188] orientation relationship ($(111)_\gamma \parallel (0001)_\epsilon, [1\bar{1}0]_\gamma \parallel [11\bar{2}0]_\epsilon$) is known to exist between γ and ϵ phases [130, 179, 189]. Several authors discuss the formation behaviour of stacking faults and stacking fault bundles and it is generally accepted that this phenomenon often occurs at sites of crystallographic discontinuity, for example: (i) intersections between active slip planes of different families, (ii) grain and annealing twin boundaries, and (iii) interfaces between different phases and inclusions [179, 190].

Fujita and Ueda [190] suggest that the formation of ϵ occurs via an irregular overlapping process whereby stacking faults form irregularly at first on the $\{111\}$ slip planes after which further stacking faults are preferentially induced on nearby $\{111\}$ planes as this is more energetically favourable with regards to the minimisation of the bulk free energy and the total energy of the stacking faults. Therefore, stacking faults are usually arranged on every second slip plane such that the ϵ -martensite structure is formed. The nature of this irregular ϵ formation mechanism yields ϵ laths which are heavily faulted [190]. This is in agreement with several other works which also demonstrate that the ϵ -martensite laths have a heavily faulted structure when formed by overlapping stacking faults [179, 189, 190].

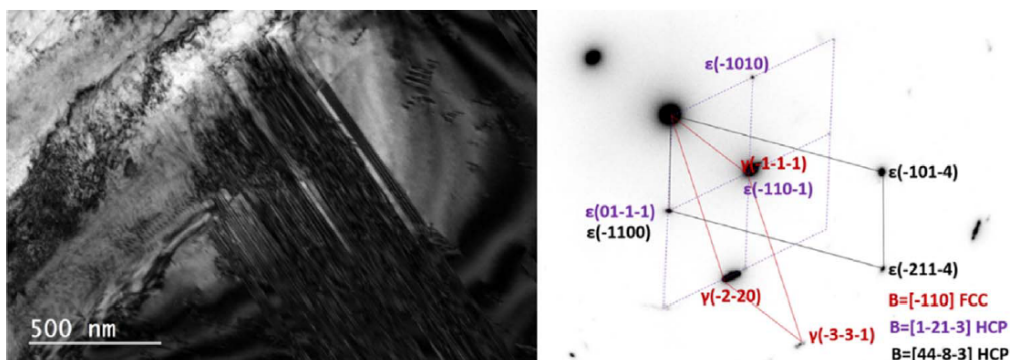


Figure 2.22: Bright field image and accompanying diffraction pattern illustrating the formation of ϵ -martensite shear bands which results from the so called bundling of stacking faults [179].

2.5.2.2. The formation of α' via the $\gamma \rightarrow \epsilon \rightarrow \alpha'$ transformation

ϵ -martensite often serves as an intermediary in the nucleation of α' -martensite in austenitic stainless steel (304) [179, 181, 186, 189, 192, 193]. Several studies on the martensitic structures present in 304 austenitic stainless steel report that the nucleation of α' -martensite is most frequently observed at the intersection of two ϵ -martensite laths on two different $\{111\}_\gamma$ planes (Fig. 2.23), or near regions where ϵ laths adjoin twin or grain boundaries (regions under compression) [181, 189]. In the early stages of nucleation the α' -martensite phase reportedly forms as needles along the $\langle 110 \rangle_\gamma$ direction which is the crystallographic direction defined by the intersecting ϵ laths [181, 189]. The subsequent growth of α' -martensite has been reported to occur at the expense of ϵ -martensite and conforms to a lath type morphology [181]. Nishiyama [194] theorized that the ϵ -martensite laths serve as nucleation centres for α' -martensite phase which subsequently grows directly into the γ -austenite. This theory was reportedly confirmed and observed in the in-situ TEM studies of Kaouni and Li [179].

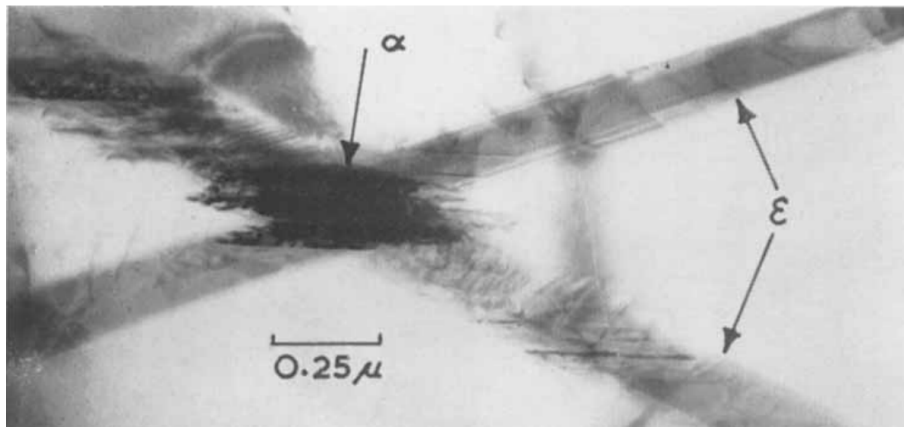


Figure 2.23: The formation of an α' needle at the intersection between two ϵ laths [189].

Mechanistically, the $\epsilon \rightarrow \alpha'$ transformation can be subdivided into two invariant-plane strains (Fig. 2.24): (i) a one-third of a twinning shear (denoted $\frac{T}{3}$) in the γ lattice with a displacement of $\frac{a_{fcc}}{18}\langle 112 \rangle$, and (ii) a one-half of a twinning shear (denoted $\frac{T}{2}$) in the γ lattice with a displacement which can be described by $\frac{a_{fcc}}{12}\langle 112 \rangle$ [195, 196]. The $\frac{T}{3}$ shear can be accomplished by an array of $\frac{a_{fcc}}{2}\langle 112 \rangle$ Shockley partials on every one third $\{111\}_\gamma$ slip plane whilst the $\frac{T}{2}$ shear can

be achieved by an array of Shockley partials averaging one over every second $\{111\}_\gamma$ plane. If $\frac{a_{fcc}}{18}\langle 112 \rangle$ partial dislocations piled up at the intersection, with the $\frac{T}{2}$ sheared structure, pass on these uniformly distorted planes, a perfect α' structure is generated [186, 195, 196] (Fig. 2.24).

Experimentally, α' -martensite is commonly observed to nucleate at the intersections between two ϵ -martensite laths Fig. 2.24 Fig. 2.25 [189, 195]. This observation accounts for the $\frac{T}{2}$ shear since only a small atomic rearrangement is needed to form a perfect $\frac{T}{2}$ shear from ϵ -martensite, however this is not the case for the $\frac{T}{3}$ shear. Olson and Cohen [196] therefore present two possibilities whereby the $\frac{T}{3}$ can exist: (i) the ϵ -martensite is heavily flawed and thus contains regions where the local average shear matches the shear of a $\frac{T}{3}$ partial dislocation array; and (ii) in the case of perfect ϵ -martensite laths, the $\frac{T}{3}$ shear can be achieved when one-third of the dislocations trying to pass the $\frac{T}{2}$ region remains at the interface between the intersecting laths. The TEM studies of Bracke et al. [195] have verified and validated the geometrical Olson-Cohen model [196] outlined above for the deformation induced $\gamma \rightarrow \epsilon \rightarrow \alpha'$ martensitic transformation Fig. 2.25.

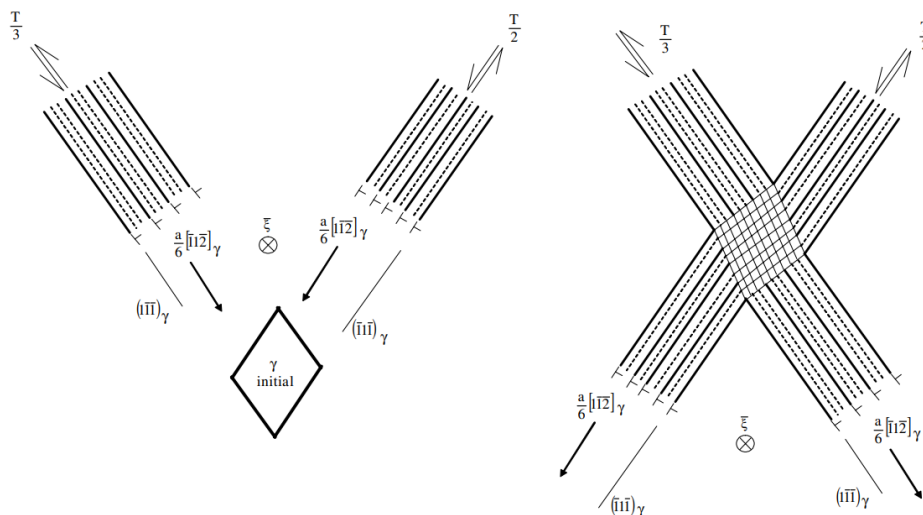


Figure 2.24: A schematic depicting the Olson and Cohen model [196] for the strain induced nucleation of α' -martensite [195]. The left and right images show a before and after schematic representation of the intersection of localised slip bands respectively.

Fig. 2.26a is a schematic taken from the work of Fujita and Katayama [193] which depicts the nucleation and growth of α' -martensite as a result of the inter-

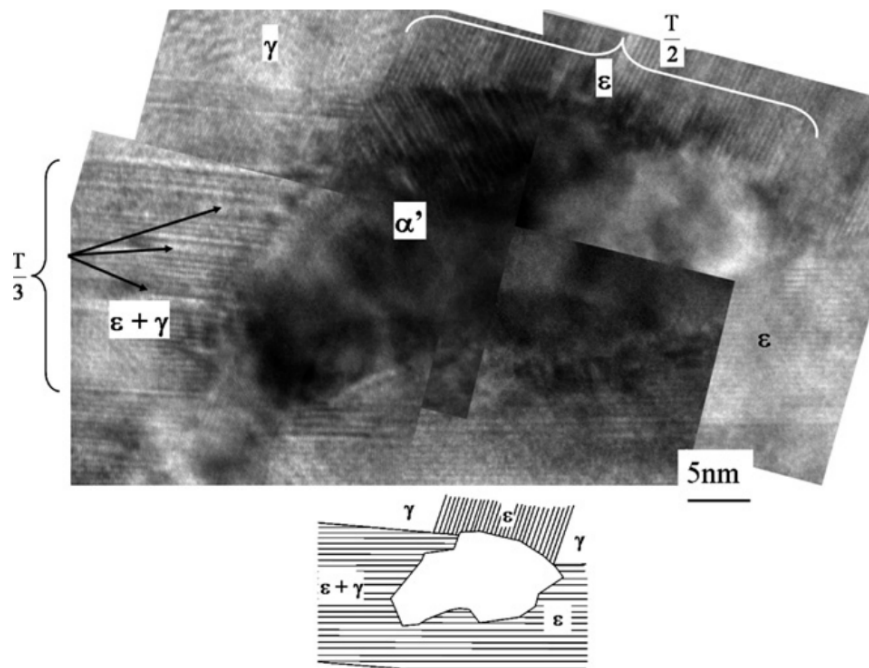


Figure 2.25: TEM micrograph depicting the intersection of two ϵ -martensite laths resulting in the formation of α' -martensite. It is clear that one of the ϵ -martensite laths contains regions of austenite [195].

section between two sets of ϵ -laths. In this case, the growth and nucleation of the α' -martensite along the primary slip plane (P_m) is assisted by the stair-rod type cross-slip of partial dislocations from the coplanar primary slip plane (P_c) onto the coplanar conjugate slip plane (S_c) (Fig. 2.26a). The α' -martensite grows in a downwards direction when the growth of the ϵ -crystal is suppressed on the S_c slip plane (Figs. 2.26a and 2.26b). As illustrated in Fig. 2.26b, the successive growth of α' -martensite crystals can occur via the coalescence of α' -crystalites [193].

Several authors report the observation of the Kurdjumov-Sachs orientation relationship ($(111)_\gamma \parallel (0001)_\epsilon \parallel (011)_{\alpha'}$) with respect to the $\gamma \rightarrow \epsilon \rightarrow \alpha'$ transformation [181, 189]. Additionally, the α' -martensite laths were observed by Venables [189] to have a $\{225\}_\gamma$ habit plane although occasionally plates were seen to have a $\{111\}_\gamma$ habit plane when they formed from thick ($\sim 1000\text{\AA}$) ϵ -martensite laths. Venables [189] and Mangonon and Thomas [181] never observe the independent nucleation of α' -martensite directly from the γ phase, therefore these studies suggest that ϵ -martensite is a true intermediary in the nucleation of α' -martensite and that the sequence of martensitic transformation in 304 stainless

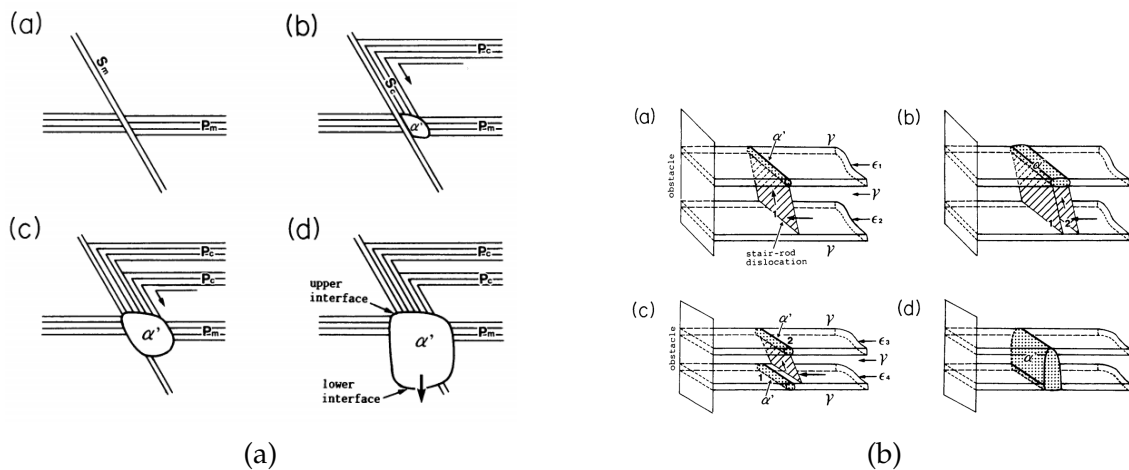


Figure 2.26: Schematics taken from the work of Fujita and Katayama [193]. (a) illustrates the nucleation and growth of α' -martensite via the aid of the stair-rod type cross slip of partial dislocations from the coplanar primary slip plane (P_c) to the coplanar conjugate slip plane (S_c). (b) depicts the growth of α' -martensite via the coalescence of several α' -crystallites which formed by localised $\epsilon \rightarrow \alpha'$ transformations.

steel is $\gamma \rightarrow \epsilon \rightarrow \alpha'$. In contrast, several authors suggest that this is not the only transformation sequence for the formation of α' -martensite and that α' -martensite can nucleate directly from within the γ phases during deformation [179, 186] (Section 2.5.2.1).

Twinning in austenite is akin to the $\gamma \rightarrow \epsilon$ (Section 2.5.2.1) since twinning simply requires the passage of Shockley partials on every close packed plane as opposed to on every second plane. Therefore, the nucleation of a γ -twin merely involves a denser array of dislocations in comparison to the $\gamma \rightarrow \epsilon$ transformation.

2.5.2.3. The direct formation of α' via the $\gamma \rightarrow \alpha'$ transformation

During their in-situ TEM studies on 304 stainless steel, Kaoumi and Liu [179] reportedly observed the direct $\gamma \rightarrow \alpha'$ transformation without the ϵ -martensite phase (Fig. 2.27). The nucleation of α' -martensite was observed at a grain boundary and proceeded to migrate into the γ phase as the γ was transformed into α' with further straining. Regardless, several authors [197–199] have shown that the $\gamma \rightarrow \alpha'$ transformation can occur without the need for ϵ -martensite as an intermediate. These works showed that α' -martensite can nucleate at intersecting slip bands from the γ phase when aided by pile up dislocations closely spaced on

the $\{111\}_\gamma$ planes. The general mechanism for the direct $\gamma \rightarrow \alpha'$ transformation is comprehensively discussed in the work of Olson and Cohen [184].

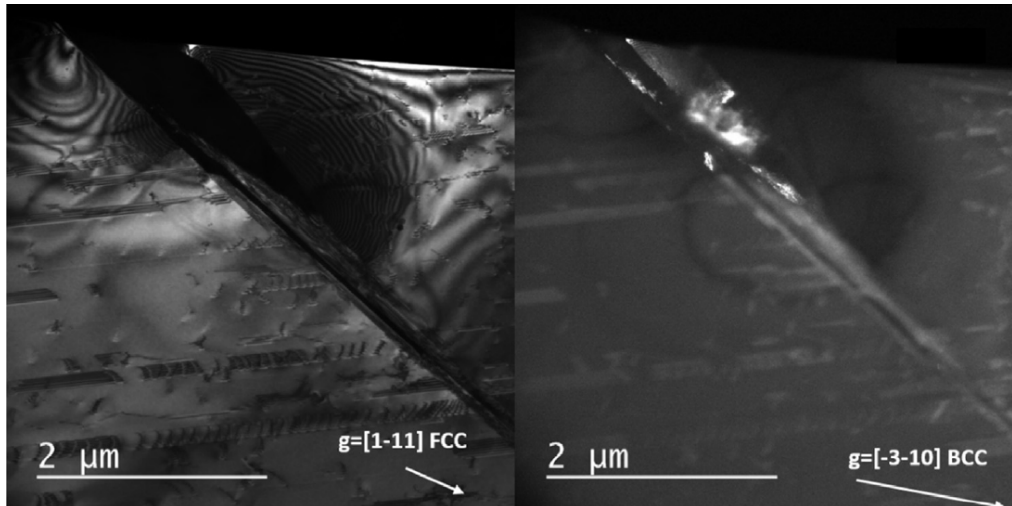


Figure 2.27: The direct nucleation of α' at a grain boundary in 304 stainless steel ($\gamma \rightarrow \alpha'$) [179].

Interestingly, several authors have reported the nucleation of α' -martensite at the intersections of twins (Fig. 2.28) which relates to a transformation sequence described by $\gamma \rightarrow \text{twinning} \rightarrow \alpha'$ [186, 193, 200, 201]. Fujita and Katayama [193] suggest that the direct $\gamma \rightarrow \alpha'$ transformation occurs by at least two sets of shear displacement. In this instance, the primary shear displacement is given by γ -twins and second shear displacement is provided by the formation of stacking faults. Fujita and Katayama [193] suggest that the direct $\gamma \rightarrow \alpha'$ transformation can happen via two types of transformation: (i) a slow Schiebung type transformation, and (ii) a rapid Umklapp type transformation. Generally speaking, the Schiebung type transformation is preferred in γ -crystals oriented for a single slip system whilst the Umklapp type transformation is preferred in γ -crystals oriented for multiple slip systems. In both of these cases, the direct $\gamma \rightarrow \alpha'$ transformation starts in regions of high stress concentrations [193].

Fig. 2.29 is a schematic of the $\gamma \rightarrow \alpha'$ transformation observed in the in-situ TEM studies performed by Fujita and Katayama [193]. This illustration shows both a solid and dotted vertical line on the left-hand side of the image which shows the boundary of a γ -grain before and after a γ -twin deformation respectively. Additionally, the chain line denoted T illustrates the local shear

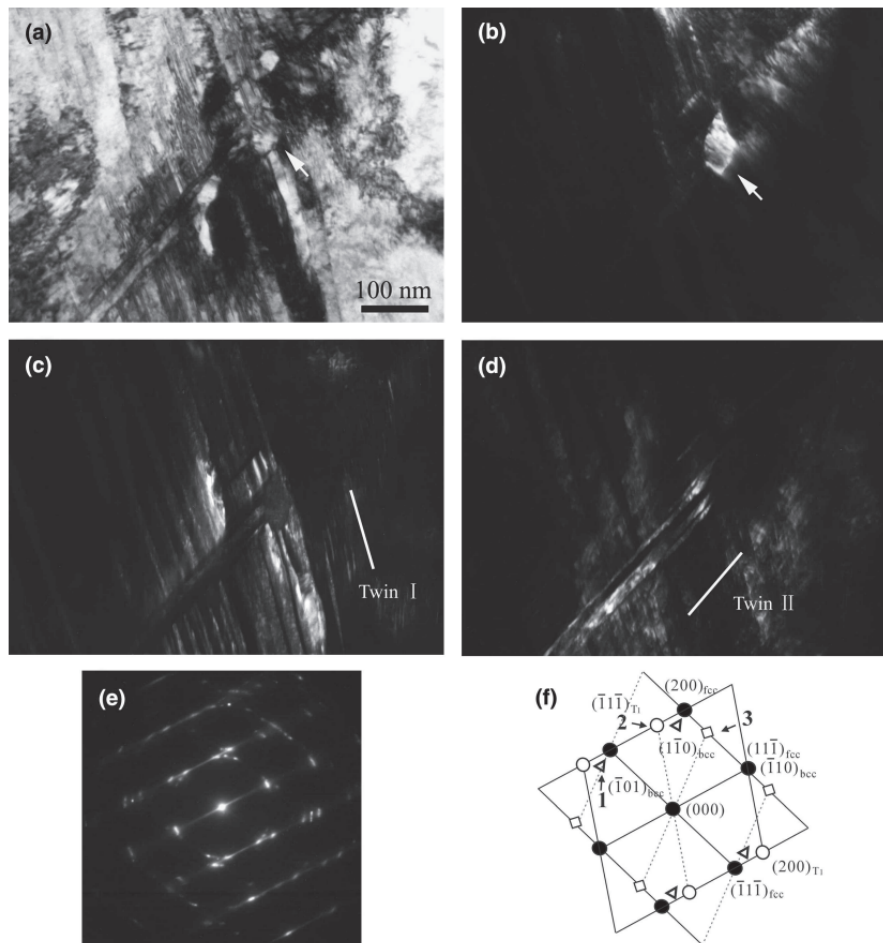


Figure 2.28: TEM micrographs taken from the work of Huang et al. [200] illustrating the nucleation of α' -martensite at the intersection of deformation twins. (a) Bright-field TEM micrograph. (b) Dark-field image of α' -martensite taken from the diffraction spot 1 in (e,f). (c) and (d) correspond to dark field images of deformation twins taken from the diffraction spots 2 and 3 in (e,f) respectively. (e) depicts a SAD pattern of (a) with zone axis $[011]_{\gamma} \parallel [111]_{\alpha'}$. (f) is an indexed pattern corresponding to (e). The regions of α' -martensite are marked by arrows in (a) and (b).

displacement which arises as a result of the γ -twin. It is clear that there is an abrupt increase in tensile stress at the boundary as the thickness of the twinned region increases, therefore a secondary shear displacement occurs on the conjugate slip planes in order to alleviate this localised tensile stress state [193]. As previously discussed, this secondary shear displacement satisfies the criterion for the $\gamma \rightarrow \alpha'$ transformation, thus the $\gamma \rightarrow \alpha'$ transformation occurs in the vicinity of the grain boundary. In other words, the work of Fujita and Katayama [193] suggests that the elastic strain energy induced in the vicinity of a γ grain boundary promotes

the $\gamma \rightarrow \alpha'$ transformation. The double shear displacement required for the $\gamma \rightarrow \alpha'$ transformation is satisfied at the interface of the α' -phase and thus grows due to the coherent strain arising from the structural differences between the γ and α' phases (Fig. 2.29) [193]. This mechanism seemingly accounts for the direct $\gamma \rightarrow \alpha'$ transformation observed at a grain boundary in the work of Kaoumi and Liu [179].

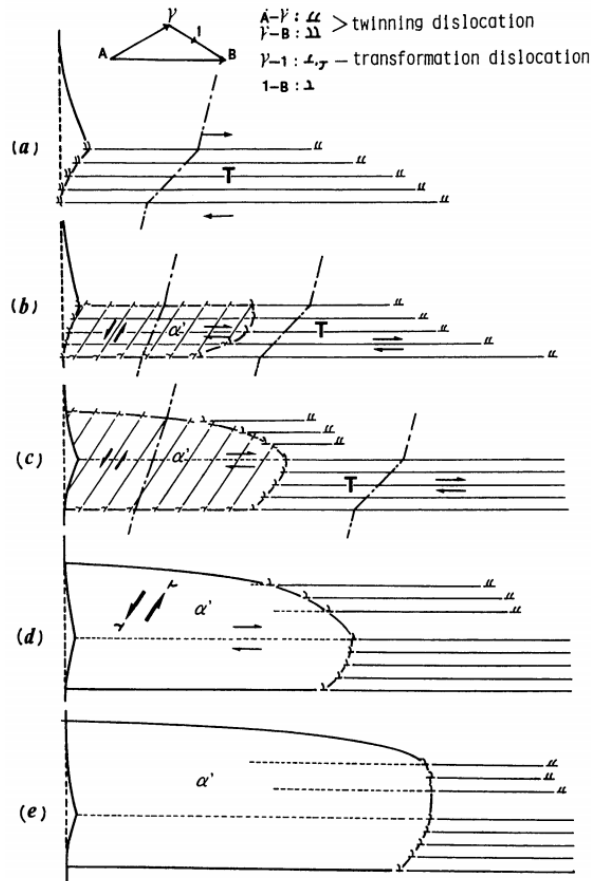


Figure 2.29: Illustration taken from the work of Fujita and Katayama [193] depicting the direct $\gamma \rightarrow \alpha'$ at a γ -grain boundary.

2.5.3. Evolution and development of Fe-based hardfacings

The following section aims to elaborate on the metallurgical trends, microstructures and tribological traits observed in Fe-based hardfacing alloys. Therefore, this section will discuss the evolution and design rational for a selection of notably important Fe-based hardfacing alloys which are reported in Table 2.6. It should also be noted that this table (Table 2.6) highlights the fact that there has been a recent influx of interest in the design of Fe-based hardfacings for nuclear

applications [24, 29, 163, 202, 203].

Table 2.6: Table of a selection of hardfacing alloys and wear resistant stainless steels.

Alloy	Date	Fe	C	Cr	Cu	Element wt%						
						Mn	Mo	Ni	Nb	N	Si	Ti
Nitronic 60 [22]	1975	bal.	0.05-0.10	15.00-17.00	0.50 max	7.50-8.50	0.50 max	6.00-10.00	-	0.10-0.20	3.70-4.20	-
Gall Tough [25]	1989	bal.	0.25 max	12.00-20.00	3.00 max	2.00-7.00	3.00 max	2.00-7.75	-	0.35 max	1.00-5.00	-
Norem [27]	1989	bal.	0.85-1.40	18.00-27.00	-	5.00-13.00	6.00 max	4.00-12.00	-	0.10-0.30	1.50-5.50	-
Norem 02 [28]	1989	bal.	1.10-1.35	22.50-26.00	-	4.00-5.00	1.80-2.20	3.70-4.20	-	0.02-0.18	3.00-3.50	-
Nitromaxx [29]	2015	bal.	0.90-1.30	21.00-27.00	-	3.00-7.00	1.00-5.00	2.00-6.00	-	0.30-0.60	1.50-4.00	-
Tristelle 5183 [6, 23]	1987	bal.	1.90	21.00	-	-	-	10.00	7.50	-	5.00	-
RR2450 [24]	1997	bal.	1.70-2.00	19.00-22.00	-	-	-	8.5-10.50	8.00-9.00	-	5.25-5.75	0.30-0.50

2.5.3.1. Nitronic 60 (1975)

Although Nitronic 60 [22] (Table 2.7) was not specifically designed as a hardfacing alloy, its composition has been used extensively as a precursor in the development of Fe-based hardfacings. In actual fact, Nitronic 60 was designed by the Armco steel corporation as a bulk sliding/galling wear resistant austenitic stainless steel which exhibits improved tribological performance in sliding compared to 304 and 316 type stainless steels. However, it forms the basis of the matrix composition in many Fe-based hardfacings. Schumacher [204, 205] attributes the sliding wear resistance of Nitronic 60 to a high rate of work-hardening and the alloys ability to generate lubricating oxide layers at contacting surfaces. The performance of this alloy is reported to be critically dependent on silicon content for two specific reasons. Firstly, Si is believed to be a substitutional solute atom within the lattice of a rapidly forming easily sheared surface oxide film; this reportedly imparts improved oxide adherence and stability. Secondly, Si is believed to favourably influence the work hardening rate of Nitronic 60. Ni principally acts as an austenite stabiliser in Nitronic 60 and it is added in direct proportion to Si that otherwise acts to stabilise ferrite. The alloying addition of Ni in Nitronic 60 [22] has the adverse effect of slightly lowering the work hardening rate. However, the net effect of the additions of both Ni and Si is to increase the rate of work hardening. Mn is well known to be a weak stabiliser of austenite but its addition is limited as it acts to reduce the general corrosion resistance of the alloy. Therefore, Mn is added to Nitronic 60 to both stabilise austenite and to keep nitrogen in solution. Nitrogen

is a powerful stabiliser of austenite and additionally acts to both strengthen and increase the work hardening ability of austenite phase in Nitronic 60 [22]. In the case of Nitronic 60, carbon is present as an impurity and has an adverse effect on the alloy's corrosion resistance.

Table 2.7: Nominal composition of Nitronic 60 in wt% [22].

Element wt%						
Fe	C	Cr	Mn	Ni	N	Si
Bal.	0.05-0.1	15.0-17.0	7.5-8.5	6.0-10.0	0.1-0.2	3.7-4.2

Nitronic 60 was designed for use in its wrought, solution-annealed form whereby the alloy is typically solution-annealed at ~ 1000 °C followed by rapid cooling in an effort to generate a predominantly austenitic microstructure [206,207]. However, the precipitation of δ -ferrite is possible. During the annealing of Nitronic 60 at temperatures between 600-900 °C intermetallic and carbide phases precipitate out from both the Fe-based phases [206,208]. A higher fraction of δ -ferrite can be achieved through the manipulation of the alloys chemistry, namely increasing the δ -ferrite stabilising elements such as Cr, Si and Mo etc. The precipitation of δ -ferrite reportedly acts to impede grain growth which alters the mechanical properties of the alloy through an increase in the effective barriers to dislocation motion.

2.5.3.2. GallTough (1989)

GallTough [25] (Table 2.8) was developed by Carpenter Technology Corporation in response to a need for an austenitic stainless steel with comparable mechanical and corrosion resistant properties to Nitronic 60 [22] but with reportedly improved galling resistance. GallTough can be described as a duplex stainless steel predominantly comprising of austenite and a small fraction of ferrite [25,209]. In order to retain a largely austenitic microstructure and provide the required galling resistance, the alloying additions of silicon, nickel and manganese must conform to a critical balance (Eqs. (2.19) and (2.20)). A minimum C plus N content is specified (Eq. (2.21)) as these alloying additions reportedly contribute to the

galling resistance of GallTough ([25]).

$$\%Ni + \frac{1}{2}(\%Mn) \geq 6 \quad (2.19)$$

$$\%Ni + \frac{1}{2}(\%Mn) \leq \frac{1}{8}(11(\%Si) + 42) \quad (2.20)$$

$$\%C + \%N \geq 0.15\% \quad (2.21)$$

In addition to the above, both the ferrite and austenite forming elements must be balanced such that in its annealed condition the alloy contains no more than 10% ferrite in order to achieve its galling resistance. Despite contributing to the galling resistance of the alloy, the addition of silicon is limited to about 5 wt% as silicon acts as a ferrite former and also reduces the solubility of nitrogen in the alloy ([25,210]). Nickel is principally added to GallTough as it promotes the formation of austenite and also stabilises the alloy against martensitic transformation. Additionally, nickel also acts to improve the general corrosion resistance of GallTough when subjected to acids for example hydrochloric acid. The addition of nickel is limited to a maximum of approximately 7.75 wt% as it adversely affects the galling resistance of GallTough ([25]). According to the patent [25], GallTough is alloyed with manganese as it, (i) increases the solubility of nitrogen in the alloy, (ii) stabilises the desired austenitic microstructure, and (iii) stabilises the alloy against martensitic transformation. However, the addition of manganese reportedly has a negative effect on the galling resistance of GallTough. Chromium is principally added to GallTough for improved corrosion resistance and to improve the solubility of nitrogen in the alloy. The addition of chromium is limited to about 20% as chromium is a strong ferrite stabiliser. Both carbon and nitrogen are strong austenite stabilisers which also prevent martensitic transformation and contribute to galling resistance. Additionally, nitrogen contributes to both the tensile and yield strength of GallTough.

GallTough reportedly has a threshold galling stress of 104 MPa in a standard ASTM test [26]. However, there is little in the way of published literature

Table 2.8: Nominal composition of GallTough in wt% [25].

Element wt%								
Fe	C	Cu	Cr	Mn	Mo	Ni	N	Si
Bal.	> 0.25	> 3.0	12.0-20.0	2.0-7.0	> 3.0	2.0-7.75	> 0.35	1.0-5.0

which comprehensively assesses the tribological performance of GallTough. An additional galling resistant alloy designated GallTough plus [26] has also been developed by the Carpenter Technology Corporation. The design objective behind GallTough plus was to develop an alloy which possesses a superior combination of both galling and chloride corrosion resistance compared to alloys, for example GallTough and Nitronic 60 [26]. GallTough plus was specifically developed for situations requiring chloride corrosion resistance and will therefore not be discussed here after.

2.5.3.3. Norem (1989)

The Norem family of alloys [27, 211] (Table 2.9) was developed by the Electrical Power Research Institute (EPRI) in response to the need to reduce the use of Co-based hardfacing alloys in the primary system of PWR's. To date, there exists a number of commercially available variants of Norem that of which have been designated 01, 02, 02A, 03A, 03B, 04A, 04B, 05A, 05B [4]. The general composition for the Norem series of alloys (Table 2.9) evolved from two working hypotheses [205], more specifically (i) the alloy should have a low deformation induced M_s temperature, and (ii) the alloy's SFE should be minimised. However, it was recognised during alloy design that these two criteria are somewhat metallurgically mutually exclusive whereby common alloying elements for example Ni, Mn and C act to lower the M_s temperature but also undesirably act to increase the SFE [205]. It should also be noted that the Norem series of hardfacing alloys were originally designed for application to substrate surfaces via weld deposition methods. In light of the above, the following paragraph aims to provide some commentary on the metallurgical design rational behind the Norem family of alloys.

The work of Schramm and Reed [212] has demonstrated that nitrogen acts

to both stabilise austenite and decrease the stacking fault energy of austenitic stainless steels. Therefore, nitrogen was considered beneficial to the tribological performance of the Norem family of alloys. In contrast, Schumacher [213] suggests that increasing the nitrogen content from 0.18 to 0.43 wt% in a Fe-18Cr-13Mn-9Ni-0.03C stainless steel does not act to improve the alloys tribological performance. This work additionally proposed that a nitrogen content of 0.1 wt% provided the best tribological performance. In light of the above, nitrogen was added to the Norem family of alloys in the range of 0.1-0.3 wt% to encourage some nitrogen to remain in solution whilst accepting its partial segregation to the carbide phases [205]. Carbon is added in the range of 0.85-1.40 wt% in an effort to yield a carbide fraction similar to that present in the Stellite family of alloys [205]. However, carbon undesirably (and unavoidably) acts to increase the SFE of the austenitic matrix. A silicon content between 1.5-5.5 wt% is desirable as it (i) provides solid solution strengthening to the matrix, and (ii) increases wear resistance by reportedly forming adherent oxides which favour mild oxidative wear [205, 214]. Chromium (18-27 wt%) is an essential alloying element in the Norem family of alloys as it is required for passive behaviour (~ 18 wt% Cr in the matrix [205]) and carbide precipitation. Molybdenum (0-6 wt%) is also added to impart improved corrosion resistance [205]. Manganese (5-13 wt%) is considered to be an important alternative austenite stabiliser to nickel in the Norem series of alloys as it is reportedly not as detrimental to the tribological performance of the alloy [205]. Finally, nickel (0-12 wt%) is a mandatory alloying element which is required in addition to manganese to stabilise the austenite matrix phase despite it reportedly being detrimental to the tribological performance of austenitic stainless steels.

Table 2.9: Compositional ranges for the major alloying elements of the Norem family of alloys in wt% [27].

Element wt%							
Fe	C	Cr	Mn	Mo	Ni	N	Si
Bal.	0.85-1.4	18.0-27.0	5.0-13.0	0.0-6.0	4.0-12.0	0.1-0.3	1.5-5.5

In the interests of providing an example, the following sections aim to give a

more detailed overview of Norem 02 despite the fact a large volume of literature exists which discusses the other Norem variants, for example references [2, 13]. Fig. 2.30 depicts the microstructure of Norem 02 deposited onto 316L type stainless steel via PTA welding. This complex microstructure is comprised predominantly of austenitic dendrites which engulf δ -ferrite islands. The interdendritic regions are principally occupied by an M_7C_3 and austenite eutectic in addition to other precipitate phases, namely ferrite, $M_{23}C_6$ and/or M_3C [215, 216]. Beaurin et al. [215] report the presence of distinct orientation relationships between the δ -ferrite islands and austenite dendrites which indicates that the growth of austenite is not random, but rather there is a germination of austenite variants on δ -ferrite during cooling. This is in agreement with the work of Cockeram et al. [216] and suggests that the δ -ferrite phases is the primary phase to nucleate within the liquid phase as a result of the large undercooling post PTA deposition. The subsequent recalescence arising from the rapid release of the heat of fusion presumably permits the nucleation of austenite on the δ -ferrite phase. Based on its presence in the interdendritic regions, the next significant phase to precipitate out on continued cooling is the M_7C_3 Cr-based carbide. Other phases which precipitate out in the latter regions to solidify include, ferrite, $M_{23}C_6$ and or M_3C .

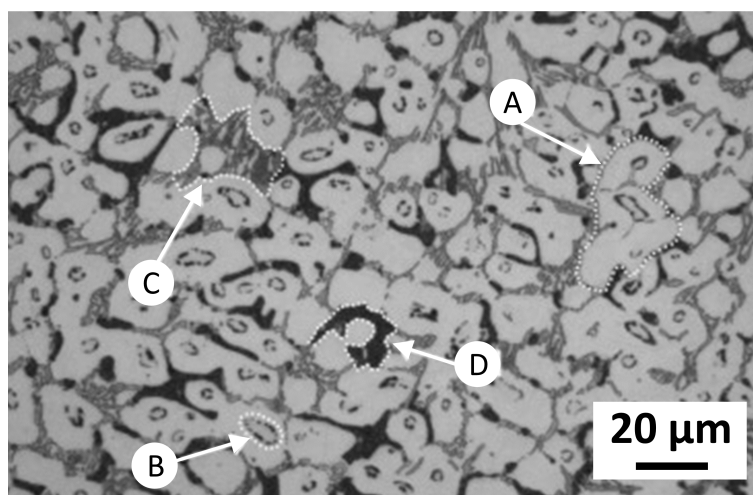


Figure 2.30: Optical micrograph depicting the microstructure of Norem 02 deposited via PTA welding. The regions denote the following: (A) austenite dendrites, (B) ferrite islands, (C) interdendritic eutectic region principally comprised of a M_7C_3 type carbide and austenite eutectic and (D) precipitate regions, namely $M_{23}C_6$ and or M_3C carbides and ferrite [215].

With respect to PTA weld deposited Norem 02, Cockeram et al. [216] suggest that the fraction of δ -Fe present within in the γ -Fe dendrites has a significant effect on the tribological performance of the dendritic regions. This work concludes that adhesive damage is initiated in the dendritic regions of the microstructure and that a high fraction of δ -ferrite improves the tribological performance of the alloy. Norem 02 can reportedly contain an optimised fraction of δ -ferrite whereby there is a sufficient fraction of δ -ferrite for good tribological performance whilst the δ -ferrite content is sufficiently low that it does not compromise the fracture toughness of the alloy [216]. In light of the above, it is clear that both the PTA weld parameters and thermal history during processing of the alloy must be controlled in order to achieve the fraction of δ -ferrite content required for a hardfacing with both optimised wear resistance and damage tolerance [216].

Smith et al. [29] investigated the temperature dependent nature of the mechanically induced $\gamma \rightarrow \alpha'$ transformation in HIPed (1050 °C, 100 MPa, 2h), quenched and austenised (1000 °C) Norem 02 via the use of in situ synchrotron X-ray diffraction Fig. 2.31. This work suggests that at room temperature the $\gamma \rightarrow \alpha'$ transformation commences at $< 0.5\%$ strain after which the α' peak width abruptly increases in the 0.5-1 % strain regime and then subsequently remains constant. This plateau in the α' peak width with respect to increasing strain indicates that the defect accumulation in the α' phase became saturated. In contrast, at 350 °C Norem 02 did not display the $\gamma \rightarrow \alpha'$ transformation and the defect accumulation resulting in the broadening of the γ reflection was relatively modest. Fig. 2.31 also shows that the stress strain response of Norem 02 at room temperature and at 350 °C diverge from one another as the γ peak widths for the different test temperatures also diverge. In light of the above, the work hardenability of Norem 02 is greatly reduced with respect to increasing temperature moreover, the $\gamma \rightarrow \alpha'$ strain induced transformation was not present and the defect accumulation was also greatly reduced at 350 °C compared to room temperature.

The temperature dependent deformation and strain hardening mechanisms of Norem 02 discussed above [29] are in agreement with the observations made in references [28, 218] on the temperature dependent tribological performance

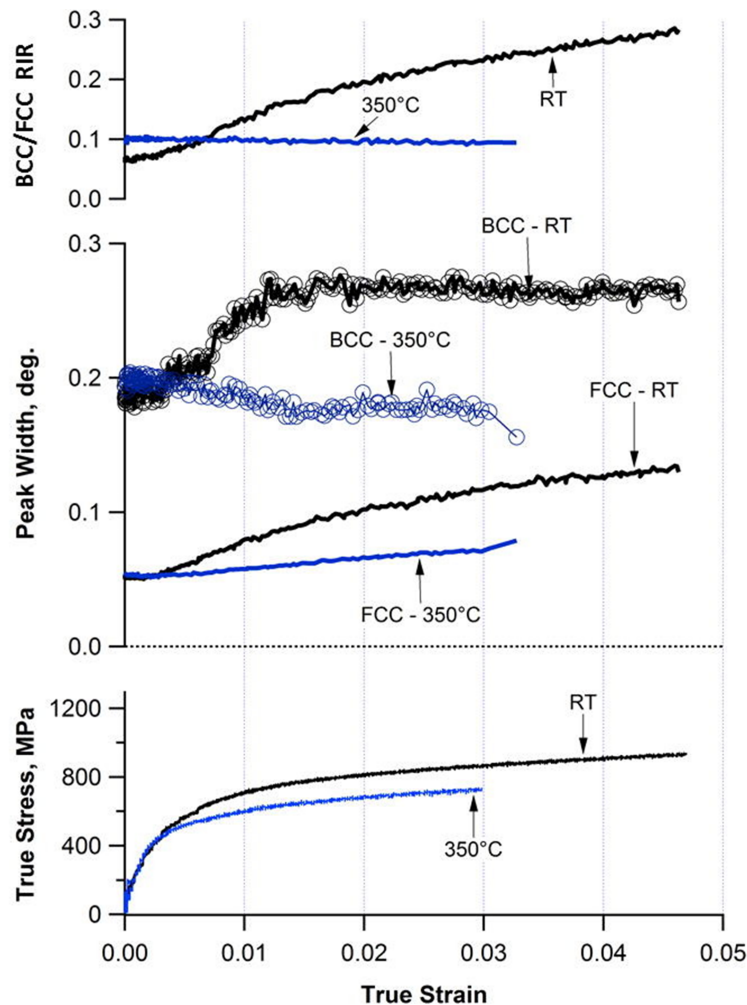


Figure 2.31: Summary data taken from the work of Smith et al. [29] illustrating the dependence of the relative α'/γ ratio [217], the γ and α peak width, and the true stress on both true strain and test temperature.

of Norem 02 deposited by gas tungsten arc welding (GTAW). Kim and Kim [28] performed self-mated reciprocating (9 mm stroke 100 cycles) high contact stress (103 MPa) block-on-block type wear tests in air at both room temperature and 300 °C. This work (Fig. 2.32a) reported an abrupt change in the sliding wear behaviour of Norem 02 at temperatures in excess of 180 °C whereby the mass loss increased significantly with respect to temperature up to 200 °C where galling occurred. This degradation in sliding wear performance of Norem 02 with respect to increasing temperature above 180 °C is reportedly a result of an abrupt decrease in the materials ability to effectively work harden Fig. 2.32b. Kim and Kim suggest that the absence of the $\gamma \rightarrow \alpha'$ strain induced transformation is one of the principal reasons

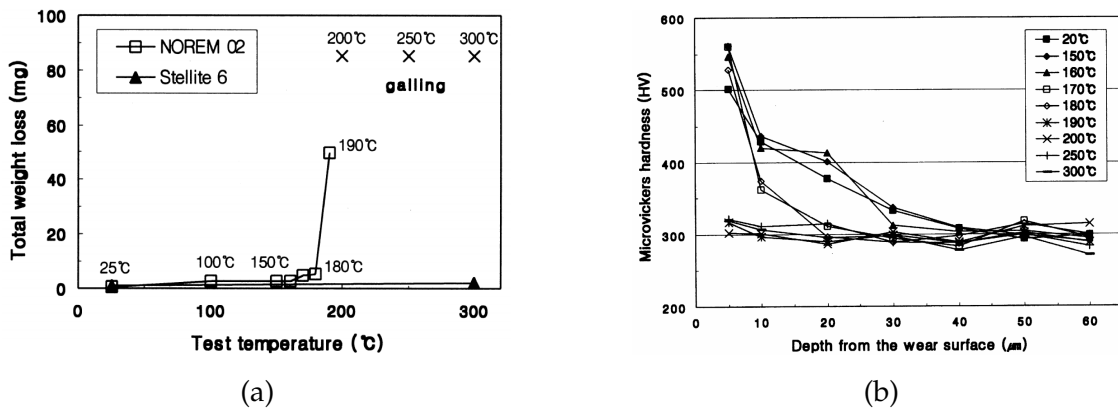


Figure 2.32: Graphs taken from the work of Kim and Kim [28]. (a) Mass loss measurements of Norem 02 and Stellite 6 as a function of test temperature after reciprocating self-mated sliding wear testing in air for 100 cycles (9 mm stroke) with a contact stress of 103 MPa. (b) Microhardness profiles beneath the worn surface of Norem 02 tested at different temperatures.

for the sudden loss of work hardening ability and wear resistance associated with Norem 02 at temperatures above 190 °C. This has been ascribed to the hypothesis that the M_d temperature for Norem 02 is located between 180 and 190 °C, thus the strain induced $\gamma \rightarrow \alpha'$ transformation is not possible above 190 °C. Lee et al. [218] report almost identical findings for self-mated reciprocating (9 mm stroke 100 cycles) high contact stress (103 MPa) block-on-block type wear tests conducted in distilled water at elevated temperatures and pressures. This work suggests that under these testing conditions Norem 02 displays a notable increase in mass loss at 455 K followed by galling at temperatures above 475 K.

In their TEM studies of the worn surface of Norem 02, Kim and Kim [28] investigated the effects of temperature on deformation mechanisms. This work reports on the direct observation of lath-type α' martensite after testing at room temperature (Fig. 2.33a) and 180 °C (Fig. 2.33b). It was reported that stacking faults and dislocations were rarely observed at these testing temperatures despite that fact that the width and amount of lath-type α' martensite decreased with respect to increasing temperature from room temperature to 180 °C (Fig. 2.33b). At 190 °C only dislocations were observed in the worn surface Fig. 2.33c. However, the location from which the TEM samples were taken relative to the worn surface remains unclear in the paper.

In a similar study, Persson et al. [219] performed in air self-mated sliding

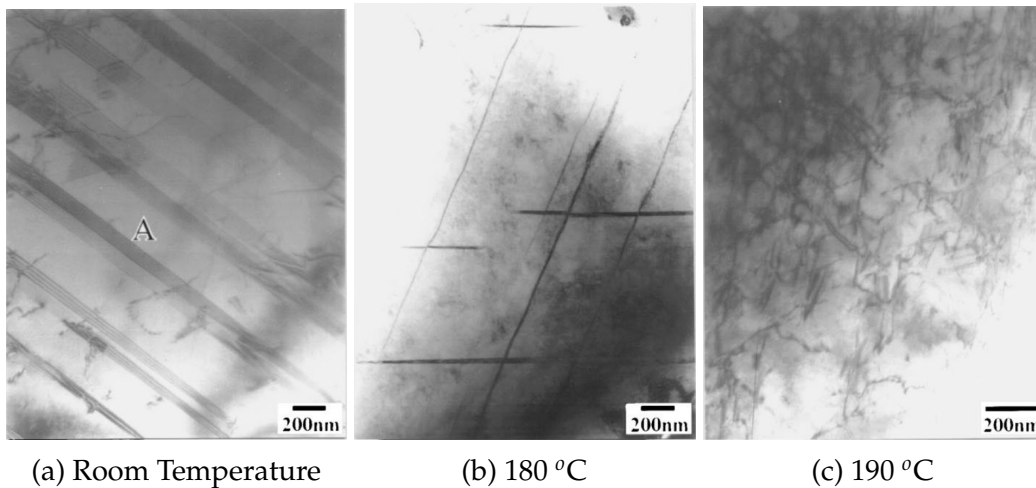


Figure 2.33: TEM brightfield micrographs of the worn surfaces of Norem 02 taken from the work of Kim and Kim [28].

wear tests at room and elevated temperature on laser clad Norem 02 using a testing procedure described in detail by Hogmark et al. [220]. This work reported almost identical findings to the work of Kim and Kim [28] whereby a significant degradation in the sliding performance of Norem 02 was observed at temperatures at and in excess of 150 °C. This temperature dependent degradation was described as galling and was accompanied by a notable increase in the coefficient of friction to 0.5-0.7 in comparison to a value of ~ 0.25 during testing at room temperature.

2.5.3.4. Nitromaxx (2015)

The design approach of Nitromaxx (Table 2.10) was to modify the existing hardfacing, Norem 02, so that strain localisation is suppressed [202]. This design approach was rationalised based on the observation that galling and plasticity-dominated wear are associated with localised subsurface shear deformation [29,46,202]. Therefore, the following strategies were employed in the design of Nitromaxx [202]: (i) increase the fraction of secondary hard phases which act to arrest shear localisation; (ii) increase the flow strength of the matrix phase such that the plastic asperity size and the dimensions of localisation events are reduced; and (iii) increase the strain hardening exponent of the matrix which acts to diffuse localised strain.

In Nitromaxx, the mechanisms governing the plastic deformation and thus strain hardening of the alloy were altered through lowering the SFE of the austenitic

Table 2.10: Nominal composition of Nitromaxx in wt% [29].

Fe	C	Cr	Element wt%				
			Mn	Mo	Ni	N	Si
Bal.	0.9-1.3	21.0-27.0	3.0-7.0	1.0-5.0	2.0-6.0	0.3-0.6	1.5-4.0

matrix by super-saturation with nitrogen [202]. Nitromaxx also contains a high volume fraction (~ 50 vol %) of hard secondary phases in the form of both carbides ($M_{23}C_6$) and nitrides (Cr_2N) (Fig. 2.34).

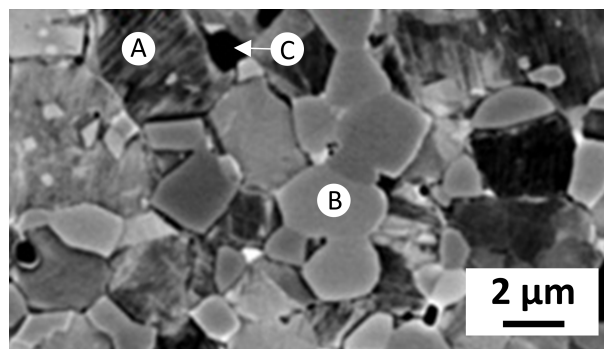


Figure 2.34: Microstructure of HIPed and solution annealed Nitromaxx where region (A) γ -Fe matrix phase, (B) $M_{23}C_6$ type carbide, and (C) Cr_2N type nitride [202].

The tribological performance and microstructure of Nitromaxx are critically dependent on processing whereby the alloy has been designed to be manufactured by a combination of powder HIPing (1050 °C) and a specific solution annealing heat treatment (at 1100 °C for 2 h) to generate an optimised microstructure [29, 202]. Additionally, the implementation of a specific powder processing method is reportedly key to increasing the nitrogen content of the melt ($\sim 0/5$ wt%) prior to gas atomisation [202]. Based on both elevated temperature XRD and CALPHAD thermodynamic modelling (Fig. 2.35), Smith et al. [202] suggest that the fraction of nitrogen in γ -Fe can be increased by annealing Nitromaxx at the highest possible temperature. Additionally, the complex phase equilibria between the carbide and nitride species present in the alloy could be the result of nitrogen supersaturation in the matrix after annealing at 1100 °C.

Nitromaxx supposedly maintains flow strength and sufficient levels of strain hardening independent of temperature between 150 and 350 °C [202]. Upon

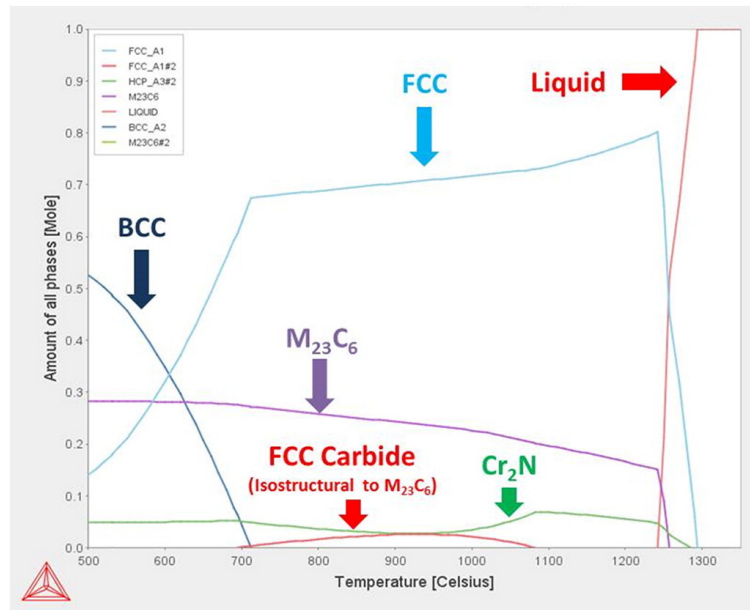


Figure 2.35: Computationally predicted equilibrium phase fraction diagram for Nitromaxx [202].

comparing the tribological performance of Nitromaxx with Norem02, Smith et al. [202] concluded that the use of hard secondary phases without matrix nitrogen modification in Norem 02 does not achieve the required tribological performance at 350 °C and that matrix nitrogen modification is essential for elevated temperature wear performance. The constant flow stress exhibited by Nitromaxx between 150 and 350 °C has been attributed to deformation twinning by Smith et al. [202]. This work rationalises the observation of deformation twinning between 150-350 °C to the reduction of the matrix stacking fault energy (achieved through matrix nitrogen modification). As in the case of TWIP steels, the presence of deformation twinning in Nitromaxx acts to increase the alloys strain hardenability [221].

2.5.3.5. *Tristelle 5183 (1987)*

Tristelle 5183 [6,23] is a patented austenitic stainless steel hardfacing alloy specifically designed by the Cabot Corporation for use in the nuclear industry (Table 2.11). In accord the patent filed by Crook et al. [6], Tristelle 5183 is principally alloyed with Cr in order to provide an adequate degree of corrosion resistance (> 15 wt%), however if added in excess the ductility of the alloy is significantly compromised (< 25 wt%). As expected, Ni is utilised as an austenite stabiliser in Tristelle 5183

(> 5 wt%), however too much significantly alters the deformation and fracture characteristics of the alloy through its influence on the matrix stacking fault energy (SFE) (< 15 wt%). Tristelle 5183 was designed to be processed from the liquid state, therefore it is alloyed with silicon in the range of 2.7 - 5.5 wt%. to provide the alloy with sufficient fluidity. Silicon additions in excess of 5.5 wt% reportedly [6] promote the formation of excessive intermetallic phases within the matrix. Carbon enables the precipitation of carbides and is added in the range of 1-3 wt%, however excessive amounts of carbon may result in unacceptable alloy brittleness. Key to the design of Tristelle 5183 is the addition of Nb (plus vanadium). These alloying additions have a high affinity for C, therefore they promote the precipitation of Nb/V-based carbides in preference to Cr-based carbides. This partially enables the retention of Cr within the matrix solution and reportedly prevents the degradation of the chemical and mechanical properties of the matrix [6].

Table 2.11: Nominal composition of Tristelle 5183 in wt% [6,23].

Element wt%					
Fe	C	Cr	Nb	Ni	Si
Bal.	1.9	21.0	7.5	10.0	5.0

Powder HIPed Tristelle 5183 has a Fe-based austenitic matrix which surrounds secondary hard phases precipitates and a smaller fraction of ferrite, a silicide phase, and/or $M_{23}C_6$ [7, 222]. The approximate phase fractions of Tristelle 5183 have been evaluated by Zhao et al. [7] and Bowden [222] and are reported in Table 2.12. Zhao et al. [7] suggest that HIPed Tristelle 5183 has a wide overall grain size distribution with an average grain size of $\sim 8 \mu\text{m}$. Both chromium-based M_7C_3 type and niobium-based MC type carbides are found consistently throughout the microstructure [7, 222]. It has been reported that the M_7C_3 type Cr-based carbide is homogeneously distributed throughout the microstructure and is no bigger than approximately $3 \mu\text{m}$ in size. The MC type niobium-based carbide phase is believed to conform to a multimodal type distribution which evolves significantly throughout the processing history of the alloy [7, 222]. There currently appears to be some discrepancy concerning the presence of an intermetallic silicide phase in

HIPed Tristelle 5183 [163]. Bowden suggests that the silicide phase is seemingly abundant within HIPed Tristelle 5183 with a phase fraction of ~ 8 wt% [222]. In contrast, Zhao et al. do not report the presence of any silicide phase in HIPed Tristelle 5183, however a very small fraction of Cr-based $M_{23}C_6$ type carbide has identified [7].

Table 2.12: Approximate phase fractions in HIPed Tristelle 5183 as evaluated by Bowden [222] and Zhao et al. [7] by Rietveld and EBSD respectively.

	Austenite	M_7C_3	MX	Ferrite	π -ferrosilicide	Carbides
Bowden (wt%)	58	13	8	8	13	-
Zhao et al. (vol%)	72.6	-	-	8.8	-	18.6

2.5.3.6. RR2450 (1997)

RR2450 (Table 2.13) evolved from the commercially available stainless steel Tristelle 5183 which was modified principally by the addition of titanium (0.3-0.5 wt%) as well as further increasing the amount of niobium (8.0-9.0 wt%) and silicon (5.25-5.75 wt%) [24]. These alloying additions significantly alter the HIPed matrix phase make-up of RR2450 relative to Tristelle 5183 whereby the matrix of RR2450 is triplex in nature and comprised of austenite, ferrite and a π -ferrosilicide [163, 223]. HIPed RR2450 also contains an MX phase (niobium and titanium containing carbonitride) and an M_7C_3 Cr-based carbide. The working principal behind the design of RR2450 is that secondary hardening can also be achieved via the precipitation of a π -ferrosilicide phase in addition to carbide phases [163]. RR2450 is reportedly a high-performance silicide-strengthened stainless steel which utilises a somewhat novel Fe-Cr-Ni silicide phase designated π -ferrosilicide to supposedly enhance tribological performance [163].

Powder HIPing is the preferred manufacturing route of choice for RR2450 as it enables the manufacture of near net shape components which exhibit a homogenous microstructure [91, 163, 224]. Bowden et al. [163, 222] suggest that production sized RR2450 powder contains: austenite (~ 38 wt%), π -ferrosilicide (~ 26 wt%), ferrite (~ 20 wt%), MX carbonitride (~ 14 wt%), and M_7C_3 (~ 2 wt%).

Table 2.13: Nominal composition of RR2450 in wt% [24].

Element wt%						
Fe	C	Cr	Nb	Ni	Si	Ti
Bal.	1.7-2.0	19.0-22.0	8.0-9.0	8.5-10.5	5.25-5.75	0.3-0.5

Following HIPing, RR2450 reportedly has an equiaxed triplex matrix microstructure which contains: austenite (27 wt%), ferrite (29 wt%) and π ferrosilicide (23 wt%) [7, 163, 222]. This matrix surrounds two secondary hard phase precipitates, namely M₇C₃ (13 wt%), and (Nb,Ti)CN (13 wt%) [7, 163, 222]. Zhao et al. [7] suggest that HIPed RR2450 has an average grain size of $\sim 8 \mu\text{m}$.

2.5.4. Related studies on the tribological degradation of stainless steels

One might argue that 304 [179] and 316 type stainless steels readily undergo a strain induced transformation yet still exhibit exceptionally poor tribological characteristics [11]. Hsu et al. [225] highlight the fact that 304 and 316 are also prone to galling despite undergoing a strain induced transformation. With respect to the tribological performance of austenitic stainless steels, this work questions the importance of strain induced transformation and emphasises the fact that work-hardening rate and hardness are not infallible indicators of galling and wear resistance [11, 27]. Hsu et al. [225] also highlight the importance of segregating galling tendency from wear resistance despite the fact a both these materials characteristics are in part dependent on material deformation.

Hsu et al. [225] performed block on ring un-lubricated sliding wear experiments on 304 stainless steel, 316 stainless steel, and Nitronic 60 blocks sliding against AISI 440C stainless steel (R_c 58-62) rings in both air and inert (argon) environments. The relevant findings from this work can be summarised by the following points: (i) both the friction and wear behaviour of austenitic stainless steels are dependent on the stability of the γ phase with respect to martensitic transformation to ϵ and α' ; (ii) wear rates increase as the fraction of α' increases; (iii) α' was present in all alloys post wear testing, however the fraction of α' was dependent on alloy

stability; (iv) the γ phase stability is heavily dependent on composition whereby composition can affect the amount and morphology of the ϵ and α' phases [226]; (v) the relative hardness of the γ , ϵ and α' phases in addition to the depth of the hard transformed region and gradient of hardness in the near surface region significantly influence the wear rate and galling tendency of austenitic stainless steel. In the case of the austenitic stainless steels investigated by Hsu et al. [225], if the generation of a hard surface layer is unsupported by a notably softer bulk, the alloy is reported to exhibit poor tribological properties due to the following: (i) the hard surface regions are left vulnerable to fracture, (ii) the hard material will damage the counter surface, and (iii) plastic deformation will propagate deep into the bulk resulting in increased galling tendencies.

Baressanelli and Moskowitz [227] suggest that martensite formation during the plastic deformation of metastable austenitic stainless steels can inhibit necking. Therefore, the formation of martensite acts to reduce localised plastic flow and thus distributes deformation over a larger volume. With specific reference to galling and seizure, Hsu et al. [225] argue that this is not beneficial for good tribological performance, moreover, they suggest that it is preferable to localise shear in the surface layers and prevent the development of a structure which leads to continued plastic deformation deep below the worn surface. This work proposes two main approaches to localise shear: (i) alloying additions which promote the formation of a low shear strength surface layer (e.g bearing bronze); and (ii) the addition of elements which impede dislocation motion, for example nitrogen or elements which promote the formation of fine precipitates. It is argued that fine precipitates will strengthen the base material whilst they are not large enough to significantly increase the nucleation and growth of cracks. In light of the above, Hsu et al. [225] propose that stainless steels which readily generate strain induce α' -Fe are the most susceptible to galling. They suggest that factors which reduce the hardness gradient between the transformed and supporting base material would act to improve the galling resistance of stainless steel. Examples include, softer martensite in the transformed region, grain size refinement, pinning of dislocations, and the addition of precipitates in the bulk material. This could

be the reasoning for the improved galling wear resistance reported for Nitronic 60 [225] relative to 316 and 304 stainless steels.

Nitronic 60 has a lower martensite start temperature compared to 304 stainless steel [205,225] and reportedly possesses a superior galling resistance [22]. This suggests that stainless steel alloys which possess low stacking fault energies potentially exhibit a higher galling wear resistance [205]. This observation gives rise to the following design criterion for Fe-based hardfacing design: (i) the alloy should have a low deformation induced M_s temperature such that the austenitic matrix should be stable with respect to the α' phase, and (ii) the alloy should be designed with the lowest possible stacking fault energy [205]. Unfortunately, these alloy design requirements are mutually exclusive from a compositional point of view, for example Ni and C are known to lower the M_s temperature of stainless steels however these alloying additions act to increase the stacking fault energy [212,228]. On the other hand, Cr and Si are known to reduce the stacking fault energy and the M_s temperature of austenitic stainless steels [212, 228, 229], however these alloying additions are strong ferrite stabilisers. The alloying addition of Mn in austenitic stainless steels acts to decrease both the stacking fault energy and M_s temperature [212,228,229] in addition to stabilising the γ phase, however it significantly impinges on the corrosion resistance of stainless steels in an elevated temperature aqueous environment. Nitrogen modified austenitic stainless steels are believed to be an attractive solution to improving the galling resistance of austenitic stainless steels as N is an austenite stabiliser that decreases both the stacking fault energy and M_s temperature without significantly compromising the corrosion resistance of the austenitic stainless steel within an elevated temperature aqueous environment [202].

2.6. SUMMARY

Rolls-Royce plc currently clad/hardface primary cooling system PWR components with Co-based Stellite alloys and where applicable Tristelle 5183. Tristelle 5183 is only utilised in comparably mild sliding contact scenarios due to its inferior tribological performance relative to Stellite alloys and its inability to meet the in-service

requirements when subjected to highly loaded sliding contacts (Galling). In light of the above, Tristelle 5183 and Stellite 6 will be the alloys of principal interest in the current work. It has been made clear in Section 2.5 that the current state of the literature concerning the metallurgy, microstructural characterisation, and tribology of Fe-based hardfacing alloys, in particular Tristelle 5183, is unfathomably limited. Although Tristelle 5183 is by no means a suitable replacement for Stellite alloys, it warrants further investigation as it is important that the metallurgy, microstructural characterisation and tribology of existing Fe-based hardfacing alloys systems are comprehensively understood prior to the development of new Fe-based alloy systems.

The metallurgical and microstructural advantages of HIPed and HIP-bonded hardfacings have been made clear in Section 2.3.2, however little is known regarding the variability which potentially arises in HIPed and HIP-bonded hardfacings as a result of the broad powder particle size range ($< 500 \mu\text{m}$) which is typically employed in the powder HIPing process [230]. Given the safety critical nature of components use in PWR's, this is of significant concern as there exists no work which assess both the phase and microstructural fluctuations in gas atomised powders as a function of cooling rate, i.e. particle diameter. The large range of cooling rates ($10^4 - 10^6$ [97, 231–233]) and deep undercoolings subjected to powder particles during gas atomisation may significantly effect microstructural formation in complex multiphase alloys for example Tristelle 5183. Upon considering the solid-state nature of HIP processing, the different microstructures and combinations of equilibrium and non-equilibrium phases which may form during atomisation has the potential to significantly compromise the tribological performance of HIPed and HIP-bonded hardfacings. In light of this clear gap in the literature, the present work aims to investigate phase and microstructural formation in different size ranges of commercially available nitrogen gas atomized Tristelle 5183 powder in order to better understand phase selection during solidification and ultimately asses the suitability of the powder currently being used for HIP processing. Such work naturally leads onto the characterisation of HIPed and HIP-bonded Tristelle 5183 about which there is also very little in the way of published literature.

Given the industrial and regulatory pressures associated with the urgent need to reduce the use of Co-based hardfacings in nuclear systems, most of the published literature on the tribological performance of Fe-based hardfacings principally focuses on the in service performance analysis of hardfacings in the form of pass or fail type testing. Such testing methods are favoured by industry due to the rapid way in which the suitability of complex hardfacing alloys can be assessed. These types of studies have failed to recognise the importance of developing a mechanistic understanding of the tribological performance and degradation of hardfacing alloys. Section 2.5 has highlighted a limited number of studies which attempt to describe the wear mechanisms of Fe-based hardfacings subjected to sliding contact. However, there exists no work which provides a description of the wear mechanisms of Fe-based hardfacings subjected to sliding contact in a primary cooling system PWR environment. Therefore, providing a description of the wear mechanisms of Tristelle 5183 subjected to sliding in a PWR environment is one of the principal aims of this work. If one obtains an exhaustive understanding of the mechanisms dictating the tribological degradation of Tristelle 5183 within a primary cooling system PWR environment, one may then be able to identify the metallurgical and microstructural characteristics which need to be developed in future iterations of Fe-based hardfacing design. Stellite 6 will also be investigated in this study as little in autoclave work exist for this alloy and it acts as a baseline alloy against which Tristelle 5183 can be directly compared and evaluated.

EXPERIMENTAL METHODOLOGY

3.1. MATERIALS AND HEAT TREATMENTS

3.1.1. Nitrogen gas atomised Tristelle 5183

The Tristelle 5183 powder investigated in this study was supplied by LSN Diffusion Ltd. (Ammanford, SA18 3GY, UK). The powder was manufactured using nitrogen gas atomisation to give a near-spherical powder particle morphology with a particle size typically $< 500 \mu\text{m}$. A melt temperature of approximately 1500°C was used in the atomisation of Tristelle 5183. In order to investigate both phase selection and powder microstructure as a function of cooling rate (i.e powder size), a laboratory shaker sieve was used to separate the as-received powder into the following size fractions: < 20 , $20 - 38$, $38 - 45$, $45 - 53$, $53 - 63$, $63 - 75$ and $75 - 106 \mu\text{m}$.

Nitrogen gas atomised Tristelle 5183 powder was broadly classified prior to HIPing into a so-called "production sized" powder fraction ($60 - 150 \mu\text{m}$ sized powder particles). The chemical composition of this production sized Tristelle 5183 powder is reported in Table 3.1 and was measured at LSN Diffusion Ltd. Further chemical analysis (Table 3.1) was also performed on the < 20 and $63 - 75 \mu\text{m}$ sieved powder size fractions at AMG Analytical Services (Fullerton Road, Rotherham, S60 1D1, UK). All the chemical analysis was performed using inductively coupled plasma (ICP) spectrometry and Leco combustion analysis for the assessment of nitrogen and carbon.

3.1.2. HIPed and HIP bonded Tristelle 5183

Production sized ($60 - 150 \mu\text{m}$) Tristelle 5183 powder was HIPed into bar form ($30 \text{ mm } \varnothing \times 200 \text{ mm}$) at Bodycote HIP Ltd (Carlisle Close, Sheffield Road, Sheep-

Table 3.1: Chemical compositions of powder Tristelle 5183 as determined by chemical analysis.

Powder Fraction		Element %							
		Fe	Cr	Ni	Nb	Si	C	N	Other
60 - 150 μm	wt%	Bal.	21.72	10.39	6.90	4.67	2.08	0.05	0.73
	at%	Bal.	21.07	8.93	3.75	8.40	8.75	0.17	0.63
< 20 μm	wt%	Bal.	21.38	10.46	5.34	4.52	1.71	0.03	1.11
	at%	Bal.	20.72	8.98	2.90	8.11	7.17	0.11	1.21
63 - 75 μm	wt%	Bal.	19.90	10.02	6.52	4.27	1.87	0.04	1.01
	at%	Bal.	19.33	8.62	3.54	7.68	7.86	0.13	1.10

bridge, Chesterfield, S41 9ED). The chemical composition of this production sized powder fraction is reported in Table 3.1. Powder was initially canned in mild steel canisters prior to HIPing. HIPing was carried out at $1120\text{ }^{\circ}\text{C} \pm 10\text{ K}$ and $103\text{ MPa} \pm 5\text{ MPa}$ with a dwell time of 240-270 min and a cooling rate of 3.4-5.5 K/min (certificate of conformity in accordance to EN 10204: 2004 3.1) (parameters defined by Rolls-Royce plc in order to achieve a fully dense bar with an optimised microstructure). After HIPing, the mild steel canisters were machined away by LSN Diffusion Ltd (Ammanford, SA18 3GY, UK). Disks for wear testing and metallurgical examination were machined from the HIPed bars using electrical discharge machining (EDM) and subsequently ground on the flat faces to remove any recast layer associated with the EDM machining. In component manufacture, hardfacing inserts are HIP-bonded to stainless steel components. Therefore, a number of Tristelle 5183 disks were further heat treated at $1050\text{ }^{\circ}\text{C}$ for 132 min with a heating and cooling rate $< 10\text{ K/min}$ to simulate this thermal cycle.

3.1.3. Cast Tristelle 5183

A conventionally cast sample of Tristelle 5183 was obtained from the melt in the crucible just prior to gas atomisation. The alloy was poured from a ladle into a small regular hexagonal prism-shaped ceramic shell mould and cooled in air with no forced cooling to room temperature. The composition of the cast alloy is given in Table 3.2. The apothem of both regular hexagonal faces of the cast

sample measured 15 mm in length and both parallel hexagonally shaped faces were separated by a distance of 12 mm.

The chemical composition reported in Table 3.2 was determined by inductively coupled plasma (ICP) spectrometry and LECO combustion analysis for the measurement of carbon and nitrogen. This chemical analysis was performed externally by AMG Analytical Services (Fullerton Road, Rotherham, S60 1D1, UK). Unlike the HIPed and powder Tristelle 5183 samples used in this work (both from the same production batch), the cast sample was obtained from a separate production run.

Table 3.2: Chemical composition of cast Tristelle 5183 as determined by chemical analysis.

	Element %							
	Fe	Cr	Ni	Nb	Si	C	N	Other
wt%	Bal.	20.65	10.35	5.73	4.58	1.92	0.03	1.05
at%	Bal.	19.88	8.83	3.09	8.16	8.00	0.10	1.28

3.1.4. HIPed Stellite 6

Commercially available nitrogen gas atomised Stellite 6 powder was consolidated into bar form by HIPing and supplied by LSN Diffusion Ltd (Ammanford, SA18 3GY, UK). HIPing of Stellite 6 powder was conducted at 1200 °C and 100 MPa with a dwell time of 4 h. The chemical composition of HIPed Stellite 6 reported in (Table 3.3) was conducted by AMG Analytical Services (Fullerton Road, Rotherham, S60 1D1, UK) and determined by inductively coupled plasma (ICP) spectrometry and Leco combustion analysis for the measurement of carbon and nitrogen. Disks for wear testing and metallurgical examination were machined from the HIPed bars using electrical discharge machining (EDM) and subsequently ground on the flat faces to remove any recast layer associated with the EDM machining.

3.2. X-RAY DIFFRACTION AND RIETVELD ANALYSIS

Table 3.3: Chemical composition of HIPed Stellite 6 as determined by chemical analysis.

	Element %							
	Co	Cr	W	Si	C	Ni	Fe	Other
wt%	Bal.	27.08	5.01	1.47	0.96	0.87	0.73	0.07
at%	Bal.	29.06	1.52	2.92	4.46	0.83	0.73	0.07

3.2.1. Principles of XRD

3.2.1.1. *The interaction of X-rays with matter*

An incident X-ray beam is principally scattered by the electrons of an atom, more specifically by either Thomson (coherent) or Compton (incoherent) scattering. It is well known that if an electromagnetic wave is incident upon a charged particle, for example an electron, the electromagnetic wave exerts a Lorentz force on the charged particle. The oscillatory electric field associated with an X-ray beam forces any electron it encounters into an oscillatory motion about its mean position. An oscillating electron is continually accelerating and decelerating during its motion, and thus emits an electromagnetic wave. This is regarded as the Thomson (or elastic) scattering of an X-rays by an electron. The scattered X-ray beam has the same frequency and wavelength as the incident X-ray beam and can be regarded as coherent as there is a phase relationship between the incident and scattered X-ray beams. Compton scattering involves the deflection of the incident X-ray photon as a result of its interaction with a loosely bound or free electron. This electron is ejected from its orbital position in the form of a Compton recoil electron and the X-ray photon incurs an energy loss because of the interaction. As some of the energy associated with the incident X-ray photon is used in providing kinetic energy to the electron, the so called scattered X-ray has an increased wavelength and reduced energy relative to the incident photon. This type of X-ray scattering is known as Compton modified radiation and it is important to note that there is no fixed phase relationship between the scattered and incident X-ray beam. This type of radiation can be regarded as incoherent radiation that cannot be avoided and acts to increase the background in diffraction patterns. The interaction of X-rays

with matter also yields the emission of fluorescent X-rays, heat and electrons in the form of photoelectrons, Auger electrons and Compton recoil electrons.

3.2.1.2. Bragg's Law

Fig. 3.1 illustrates a small section of a crystal with its atoms arranged on three planes all equally spaced a distance of d' apart. It is assumed that the incident X-rays are parallel and monochromatic with a wavelength λ . These X-rays are incident at an angle θ known as the Bragg angle which can be defined as the angle between the incident X-rays and the crystal planes under investigation (Fig. 3.1). The atoms within a crystal scatter the incident X-rays in all directions, however in particular directions the scattered X-rays are completely in phase with one another. These in phase X-rays reinforce one another to form a diffracted beam (Fig. 3.1). In other words, a diffracted X-ray beam can be described as a large number of scattered X-rays that are mutually reinforcing one another. The reinforcing effect of scattered X-ray's is satisfied when the diffracted beam forms a reflected angle identical to that of the incident Bragg angle (θ). These scattered X-rays that reinforce one another have satisfied what is known as the Bragg condition. A derivation of Bragg's law can be found in references [234–236]. This relationship is expressed in Eq. (3.1)

$$\lambda = 2d_{hkl} \sin(\theta) \quad \text{where:} \quad d_{hkl} = \frac{d'}{n} \quad (3.1)$$

(Eq. (3.1)) is more commonly known as Bragg's law where n is a whole number which represents the order of reflection and λ is the wavelength of the X-ray source used. The order of reflection is equal to the number of wavelengths which sum to equal the path difference for X-rays which have been scattered by different planes of atoms. If one now considers fixed values for both λ and d' , there may be several incident angles at which diffraction occurs - moreover, these angles correspond to the different orders of reflection ($n=1,2,3\dots$). The first order reflection ($n=1$) is the result of constructive X-rays which differ in path length by one complete wavelength, for example X-rays following paths 1' and 2' in Fig. 3.1. Similarly, the second order reflection is the result of X-rays that differ in path length by two

complete wavelengths, for example X-rays following paths $1'$ and $3'$ in Fig. 3.1. This relationship between the crystal structure and order of reflection carries on throughout the crystal.

When the incident X-ray source is applied to a crystal at a diffraction angle the scattered X-rays that satisfy the Bragg condition are completely in phase with one another. This results in the constructive interference of these diffracted X-rays thus yielding a diffracted beam. When the incident X-ray source is applied to a crystal at angles which do not coincide with diffraction angles the scattered X-rays are out of phase with one another and this results in destructive interference. Obviously, the above derivation applies to materials which exhibit periodically spaced structures i.e. are crystalline. In the case of a material where atoms are arranged randomly in space (i.e. are amorphous) the scattering of X-rays occurs in all directions.

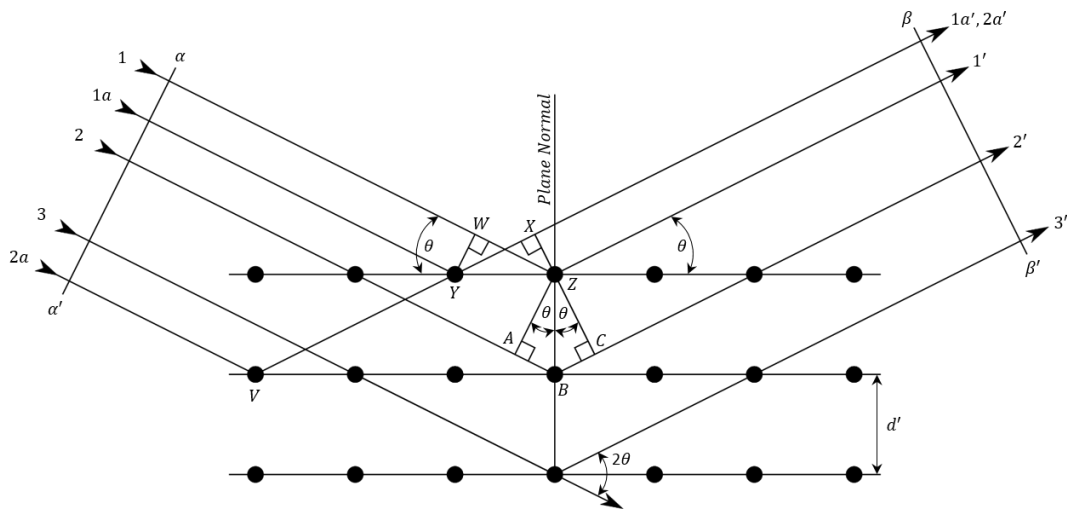


Figure 3.1: Diffraction of X-rays by a crystal.

3.2.1.3. Structure Factor

The peak intensities for a given phase are determined by: (i) the atoms contained within the unit cell and their xyz positions, (ii) the site occupancy of a given atom, (iii) the relative scattering strength of a given atom (scattering factor), and (iv) the thermal parameter of a given atom. The structure factor (F_{hkl}) is a mathematical function that describes both the amplitude and phase of a wave diffracted from

crystal lattice planes with Miller indices hkl . In other words, the structure factor is the sum of all the scattered waves from each of the individual atoms which make up the unit cell. Structure factors are of significant importance in XRD as they describe how the atomic arrangement within the unit cell (defined by uvw for each atom) influences the scattered beam. If the unit cell is comprised of $1, 2, \dots, N$ atoms with fractional coordinates $u_1v_1w_1, u_2v_2w_2, \dots, u_nv_nw_n$ the structure factor for the hkl reflection is given by Eq. (3.2) ([234]).

$$F_{hkl} = \sum_{i=1}^N f_n e^{2\pi i(hu_n + kv_n + lw_n)} \quad (3.2)$$

Where f is the atomic scattering factor which is a measure of scattering efficiency of an isolated atom. If one now considers the model presented in Fig. 3.1 with the addition of a second atom in the unit cell as shown in Fig. 3.2. It is clear that each of the original atoms is accompanied by an adjacent atom which is offset by a vector designated r_1 . These adjacent atoms also scatter X-rays and will additionally diffract the incident X-ray beam. However, X-rays scattered from the original and new set of atoms are out of phase by a phase difference denoted by ϕ_1 (Fig. 3.2).

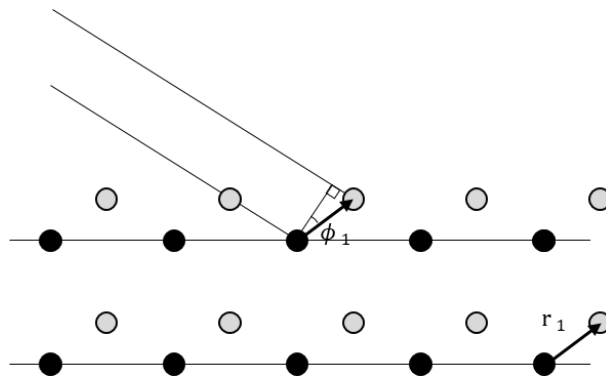


Figure 3.2: X-ray scattering from two planes in a primitive crystal.

In the case of Fig. 3.2, the simple vector diagram presented in Fig. 3.3 illustrates the resultant wave which is scattered from the two sets of atoms which make up the unit cell. The amplitudes of the individual waves are proportional to the atomic scattering factors f_1 and f_2 and the phases differ by angle ϕ_1 (Fig. 3.2). The resultant vector represents the structure factor of the two atom unit cell with

amplitude F_{hkl} and phase ϕ . ϕ represents the phase difference arising from the offset in position between the two sets of different diffracting atoms. Fig. 3.4 illustrates a vector diagram for a unit cell which is comprised of five atoms and shows that the resultant diffracted wave is acquired from the linear superposition of all the scattered wave vectors from all the atoms within the unit cell.

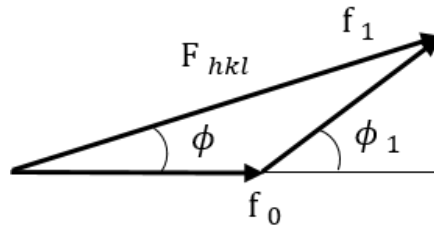


Figure 3.3: Vector phase diagram illustrating the superposition of two waves diffracted from two different atoms which make up a simple unit cell.

Eq. (3.2) is of significant importance in X-ray crystallography as it allows one to determine the intensity of a given hkl reflection based on the atomic positions of the atoms which make up the unit cell. The intensity of the diffracted beam by all the atoms of a unit cell (in a direction predicted by Bragg's law) is proportional to $|F|^2$ (the square of the amplitude of the resultant beam). This is why reflections only occur for certain (hkl) values in a particular crystal structure.

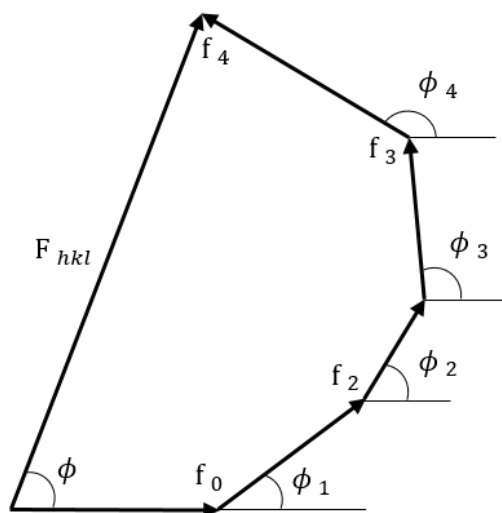


Figure 3.4: Vector phase diagram illustrating the superposition of 5 waves diffracted waves scattered from a primitive unit cell.

3.2.2. Laboratory X-ray diffractometers

3.2.2.1. *Bruker D500*

A Bragg-Brentano configured Bruker D500 X-ray diffractometer employing Cu K- α radiation was utilised in the acquisition of diffractograms. This diffractometer is equipped with a vertical $\theta - 2\theta$ goniometer, a scintillation-counting (0D) X-ray detector, and a diffracted beam (post-sample) graphite monochromator. This diffracted beam graphite monochromator acts to narrow the wavelength distribution of the diffracted beam, eliminate signal arising from Cu K- β radiation, and reduce fluorescence effects arising from the irradiation of both Co and Fe samples by Cu K- α radiation. The working voltage and current used during laboratory XRD were 40 kV and 25 mA respectively.

3.2.2.2. *Bruker D8 Advanced*

Diffractograms were also recorded using a Bruker D8 advanced powder diffractometer in Bragg-Brentano geometry employing Cu K- α radiation and a vertical $\theta - \theta$ goniometer. This diffractometer is equipped with a LYNXEYE XE-T position sensitive (1D) energy discriminating detector that facilitates the filtering of both fluorescence and K- β radiation. This machine is also equipped with a variable anti-scatter screen, variable divergent slits, and a variable detector window. The machine was operated with a working voltage and current of 40 kV and 40 mA respectively.

3.2.3. Sample Preparation

XRD was performed directly on inert gas atomised powder samples with no prior sample preparation. The powder samples were placed in a powder sample holder and levelled prior to analysis. The preparation of HIPed and cast samples for XRD required considerable care in order to remove any deformation induced martensitic transformation generated during the stages of sample preparation. Following sectioning, these samples were ground, diamond polished to a 1 μm finish, and subsequently given a final polish using 0.06 μm colloidal silica prior to

XRD analysis. Despite the variation in X-ray penetration depth with respect to 2θ , it is well known that the majority of the X-ray intensity contributing to the diffracted signal comes from within $\sim 10 \mu\text{m}$ of the analysed surface [234]. Therefore, this procedure was essential to minimise sub-surface mechanical damage and enable the acquisition of X-ray diffractograms that are representative of the as-received un-deformed alloys.

3.2.4. Principles of Rietveld

Rietveld refinements [237] were performed using Topas V6 software in order to quantitatively evaluate X-ray diffractograms. The empirical (classical), semi-empirical and fundamental approaches to Rietveld refinement were employed in the present study and the specific approach for any given problem was chosen on a case by case basis. The Rietveld method uses least-squares minimisation to refine crystallographic information by minimising the residual function (s_y) between experimentally determined diffraction data and a computationally calculated pattern based on hypothesised crystal structures and instrumental parameters. The residual function is reported in Eq. (3.3) where y_i is the observed gross intensity at step i , $w_i = \frac{1}{y_i}$, and y_{ci} is the calculated intensity at step i . In order to minimise the residual function a selection of parameters which describe the calculated intensity are refined, for example the structural model.

$$s_y = \sum_i w_i (y_i - y_{ci})^2 \quad (3.3)$$

The least squares minimisation process generates a set of normal equations which concern the derivatives of the calculated intensities with respect to the refined parameters. The elements of the normal matrix, M_{jk} , can be expressed in terms of Eq. (3.4) where x_j and x_k are adjustable parameters. These normal equations make up the normal matrix which is solvable through its inversion.

$$M_{jk} = - \sum_i 2w \left[(y_i - y_{ci}) \frac{\partial^2 y_{ci}}{\partial x_j \partial x_k} - \left(\frac{\partial y_{ci}}{\partial x_j} \right) \left(\frac{\partial y_{ci}}{\partial x_k} \right) \right] \quad (3.4)$$

The normal matrix is m by m in size where m is the number of parameters

being refined. However, as the residual function is non-linear, the solution must be found by an iterative procedure. The non-linear relationship between the adjustable parameters and the intensities means the starting model must be close to the correct solution otherwise the non-linear least squares procedure will not refine to the global minimum. An inappropriate starting model will diverge or lead to a false minimum if the starting point is in its domain during the non-linear least squares procedure.

A wide range of phase specific and global parameters may be refined simultaneously during Rietveld refinement. The phase specific (structural model) parameters which may be refined include: atomic position coordinates (x_j , y_j and z_j for the j^{th} atom in the unit cell), isotropic thermal parameters (B_j for the j^{th} atom in the unit cell), site-occupancy multipliers (N_j for the j^{th} atom in the unit cell), the scale factor, specimen-profile breadth parameters, lattice parameters, the overall temperature factor, individual anisotropic thermal parameters and crystallite size and microstrain. The parameters which may be refined globally include: the 2θ -zero position, the instrumental profile, the profile asymmetry, the background, the wavelength, the specimen displacement, and absorption.

At any arbitrary point within an x-ray diffractogram the observed intensity (y_i) is composed of contributions from many Bragg reflections. X-ray diffractograms may be modelled as a collection of individual peak profiles which have a peak height, a peak position, a peak width, tails which decay with increasing distance from the peak position, and an integrated area which is proportional to the Bragg intensity. It is known that the Bragg intensity is proportional to the absolute value of the structure factor squared ($|F_K|^2$). $|F_K|^2$ values can be calculated from the structural models, therefore the calculated intensities (y_{ci}) may be evaluated by summing the calculated contributions from neighbouring Bragg reflections plus a background as shown in Eq. (3.5) for the classical approach. In this equation, S is the scale factor; K represents the hkl Miller indices of a Bragg reflection; L_k contains the Lorentz, polarisation and multiplicity factors; ϕ is the (empirical) reflection profile function (Gauss, Lorentz and modified Thompson-Cox-Hastings pseudo-Voigt etc.); P_K is a preferred orientation function; A is an absorption factor;

F_K is the structure factor for the K^{th} Bragg reflection; and y_{bi} is the background intensity at the i^{th} step [237].

$$y_{ci} = \sum_{J=1}^{N_{\text{phases}}} S_J \sum_{K=1}^{M_{\text{peaks}}} L_K |F_{K,J}|^2 \phi(2\theta_i - 2\theta_{K,J}) P_{K,J} A_J + y_{bi} \quad (3.5)$$

The reflection profile function, ϕ , approximates the effects of several factors including instrumental features (including peak-profile asymmetry) and specimen effects, for example sample broadening by crystallite-size and microstrain effects. By way of example, the modified Thompson-Cox-Hastings pseudo-Vigot function [237,238] (*TCHZ*), shown in Eq. (3.6), is an analytical reflection profile function which has been used frequently throughout the present work. In this equation, Γ is the full width half maximum (FWHM) and η is a mixing parameter.

$$\begin{aligned} TCHZ = & \left(\frac{2\eta}{\pi\Gamma} \right) \left[1 + 4 \left(\frac{2\theta_i - 2\theta_K}{\Gamma} \right)^2 \right]^{-1} + \\ & (1 - \eta) \left(\frac{2}{\Gamma} \right) \left(\frac{\ln(2)}{\pi} \right)^{\frac{1}{2}} \exp \left[-4 \ln(2) \left(\frac{2\theta_i - 2\theta_K}{\Gamma} \right)^2 \right] \end{aligned} \quad (3.6)$$

The mixing parameter (η) relates to the FWHM's of the individual Lorentzian (Γ_L) and Gaussian (Γ_G) components and can be expressed in terms of a series expansion as shown in Eq. (3.7).

$$\eta = 1.36603 \left(\frac{\Gamma_L}{\Gamma} \right) - 0.47719 \left(\frac{\Gamma_L}{\Gamma} \right)^2 + 0.11116 \left(\frac{\Gamma_L}{\Gamma} \right)^3 \quad (3.7)$$

As opposed to using η and Γ as refinable parameters in the least squares procedure, it is convenient to use Γ_L and Γ_G directly as these can readily be identified with particle size effects, instrumental resolution and strain broadening. Γ can be approximated in terms of Γ_L and Γ_G via a simple series expansion as

shown in Eq. (3.8).

$$\Gamma = \left(\Gamma_G^5 + 2.69269\Gamma_G^4\Gamma_L + 2.42843\Gamma_G^3\Gamma_L^2 + 4.47163\Gamma_G^2\Gamma_L^3 + 0.07842\Gamma_G\Gamma_L^4 + \Gamma_L^5 \right)^{\frac{1}{5}} \quad (3.8)$$

where the Gauss (Γ_G) and Lorentz (Γ_L) FWHM components are given by Eq. (3.9) and Eq. (3.10) respectively. In these equations, U, V, W, X, Y and Z are the refinable parameters.

$$\Gamma_G = \left(U \tan^2(\theta) + V \tan(\theta) + W + \frac{Z}{\cos^2 \theta} \right)^{\frac{1}{2}} \quad (3.9)$$

$$\Gamma_L = X \tan \theta + \frac{Y}{\cos \theta} \quad (3.10)$$

The fundamental parameters approach [239,240] is a convolution approach to line profile fitting whereby the final line profile can be built up from instrumental and sample aberrations which are convoluted with the emission profile. This approach to line profile fitting uses physically based models to generate the line profile shapes. Therefore the refined parameters are determined by the diffractometer configuration and thus, parameters which can often be directly measured. In the case of a divergent beam diffractometer these parameters include: the angular aperture of the divergent slit, the width and axial length of the receiving slit, the angular apertures of the axial and Soller slits, the length and projected width of the x-ray source, the absorption coefficient, and the axial length of the sample. The instrumental profile shape $K(2\theta)$ is initially evaluated by convoluting the geometrical instrument function $J(2\theta)$ with the emission/wavelength profile $W(2\theta)$ at a given Bragg angle (Eq. (3.11)).

$$K(2\theta) = \int W(2\theta - 2\varphi)J(2\varphi)d2\varphi = W(2\theta) \otimes J(2\theta) \quad (3.11)$$

The geometric instrument function $J(2\theta)$ is a convolution of numerous instru-

ment aberration functions related to diffractometer as shown in Eq. (3.12).

$$J(2\theta) = J_1(2\theta) \otimes J_2(2\theta) \otimes \dots \otimes J_i(2\theta) \dots \otimes J_N(2\theta) \quad (3.12)$$

The specimen broadening function $B(2\theta)$ is convoluted with the instrumental profile function $K(2\theta)$ to give an overall profile function $I(2\theta)$.

$$I(2\theta) = K(2\theta) \otimes B(2\theta) \quad (3.13)$$

In summary, the aim of a Rietveld refinement is to minimise the difference between a measured and a calculated diffractogram which is generated from structural models. However, Rietveld refinements require an accurate description of peak profiles. In the case of the classical (empirical) approach, peak profiles are described via the use of an empirical peak profile function. In contrast, in the fundamental parameters approach, line profiles are described by a convolution of a sample broadening function with an instrumental profile function which is defined by the diffractometer configuration. In the case of the semi-empirical approach, the instrument is defined with an empirical function which is convoluted with a sample broadening function in order to generate a mathematical description of peak profiles.

3.3. OPTICAL AND SCANNING ELECTRON

MICROSCOPY (SEM)

3.3.1. Principles of scanning electron microscopy (SEM)

3.3.1.1. Scanning electron microscope operation

A scanning electron microscope (SEM) enables both the imaging and analysis of bulk samples using a highly focused beam of electrons contained within a vacuum chamber. Electrons are generated through the use of either a thermionic, Schottky or field-emission type cathode and are subsequently accelerated due to a potential difference applied between the anode and cathode of the electron gun. The higher gun brightness and smaller electron virtual source associated with a field emission

gun (FEG) electron source permits higher resolution imaging relative to thermionic type filament instruments.

After leaving the anode of the electron gun, the electron beam is controlled and focused using both electron optics and mechanical apertures. Electron optics exploit the axial magnetic field with rotational symmetry of an electron through the use of a magnetic flux produced by a pole piece lens. A pole piece lens is effectively an electromagnet designed such that the magnetic field is concentrated within a small gap to enable the focusing of electrons. Focusing is achieved due to magnetic field interactions between electrons that are passed through the centre of the lens and the magnetic field associated with the pole piece lens. The focus is controlled by varying the current that is passed through the lens whereby a greater current results in a shorter focal length. The electron beam is condensed using condenser lenses before being finely focused onto the specimen surface using objective lenses. Mechanical apertures are used in conjunction with electromagnetic lenses and are primarily used to limit the diameter of the electron beam and remove scattered electrons.

Situated within the objective lens is a set of scan coils; these coils carry a varying voltage such that the resulting magnetic field deflects electrons back and forth across the sample. The incident electrons that strike the sample surface interact with both the nuclei and the electrons of the sample and result in the emission of electrons, X-rays, heat, and light (cathodoluminescence). These secondary signals can be analysed to gain a wealth of knowledge about the sample.

3.3.1.2. The interaction of electrons with matter

The interactions that occur between the incident electrons and the atoms within the sample can be categorised as either elastic or inelastic. Elastic interactions occur between the sample nuclei and the incident electrons and typically involve large deflection angles and small incident electron energy losses. On the other hand, inelastic interactions are the result of collisions between incident electrons and the orbital electrons associated with the atoms of the sample. Inelastic interactions can be characterised by small deflection angles and large incident electrons energy

losses.

The interaction volume (Fig. 3.5) can be defined as the volume within the sample that is affected by incident electron interactions. The atomic number of the sample influences the size of the interaction volume whereby higher atomic number materials dissipate the energy from incident electrons more effectively than samples which have lower atomic numbers. In other words, the interaction volume within the sample is inversely related to the mean atomic number of the region of the sample examined. Additionally, the size of the interaction volume is also related to the accelerating voltage and angle of the incident electron beam. With special reference to the materials examined in this thesis, the typical interaction volume has a depth of $\sim 3 \mu\text{m}$ and a diameter of $\sim 2 \mu\text{m}$ (as evaluated by Monte Carlo simulations).

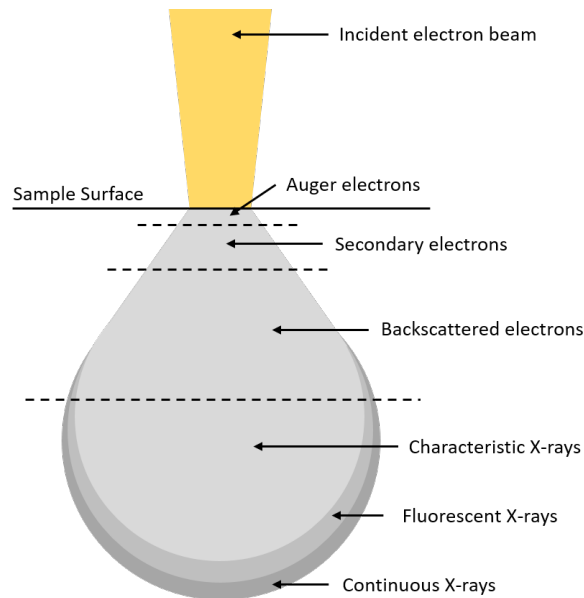


Figure 3.5: Schematic illustration of interaction volume between an incident electron beam and matter.

The energy spectrum (Fig. 3.6) of electrons which are emitted from a sample is comprised of contributions from secondary, backscattered and Auger electrons.

3.3.1.3. Secondary electrons (SE)

Secondary electrons (SE) are characteristically low in energy, typically $\lesssim 50 \text{ eV}$ (Fig. 3.6), and are generated as the result of inelastic collisions between incident

electrons and the loosely bonded conduction band electrons in the sample. Excited secondary electrons with energies in excess of the surface work function are able to escape the sample surface. The work function can be defined as the minimum thermodynamic work required in order for an electron to be removed from the sample surface. Secondary electrons only have a very short mean free path length due to their inherently low energies, therefore only the secondary electrons which originate from very near the sample surface have the required energy to escape the sample. The shallow depth of detectable secondary electrons makes the analysis of secondary electrons very sensitive to a sample's surface topography and enables a resolution ranging between $\sim 0.5 - 5$ nm depending on the emission source and microscope configuration.

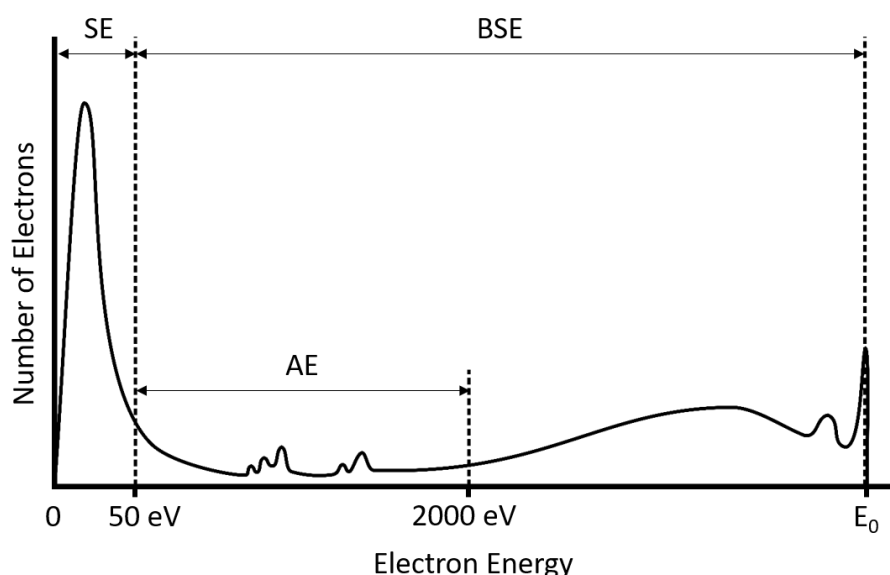


Figure 3.6: Schematic of the energy spectrum of electrons emitted from the sample surface. SE, BSE, AE and E_0 respectively represent secondary electrons, backscattered electrons, Auger electrons and the electron energy of the primary incident electron beam.

3.3.1.4. Backscattered electrons (BSE)

Backscattered electrons are primary (incident) electrons that re-emerge from the sample surface predominantly due to elastic interactions with the sample's nuclei. When compared to inelastic interactions the energy lost by a primary electron during an elastic interaction is negligible. However, the broad energy spectrum

over which backscattered electrons are produced (Fig. 3.5) is expected as the re-emergence of primary electrons can occur as a result of a varying number of interactions. Typically speaking, a plethora of large angle elastic scattering events is required in order for an electron to be deflected such that it is capable of leaving the sample surface. Hence, as the probability of multiple scattering events increases into the sample, the emission of backscattered electrons is more likely to be the result of deeper penetrating primary electrons. The inherently high energies associated with backscattered electrons mean they are not easily absorbed by the sample, therefore a relatively large proportion of backscattered electrons are able to escape the sample surface. The maximum depth (and width) of penetration into the sample that a re-emerging backscattered electron can achieve is inversely related to the mean atomic number of the irradiated region. The probability of an elastic interaction occurring is higher in regions which exhibit high mean atomic numbers because larger atoms have a larger effective cross-sectional area.

Back scattered electron (BSE) images are produced from a combination of both Rutherford and Mott scattered electrons. If a BSE image is acquired at a large working distance Rutherford scattered electrons dominate the detector signal and the micrograph exhibits preferential mean atomic number contrast (Z-contrast). In contrast, if the working distance is reduced a notable proportion of the signal arises from singly elastically scattered electrons that carry mainly crystallographic contrast. This is known as channelling contrast and arises from the Mott scattering of electrons in accord with Bragg's law.

3.3.1.5. X-ray emission and Auger electrons

When an atom becomes ionised due to the removal of an inner shell electron an electron from a higher energy level subsequently occupies the electron vacancy; this results in a release of energy otherwise known as the de-excitation energy. More often than not, this energy is released through the emission of an X-ray photon. Sometimes however, the de-excitation energy is transferred to another electron that leaves the atom in the form of an Auger electron (Figs. 3.5 and 3.6). Auger electrons can be generated either by primary incident electrons

or by backscattered electrons. As with secondary electrons, Auger electrons are very susceptible to inelastic scattering and only leave the specimen from the near surface regions. The wavelengths or energies of the X-rays which are emitted due to electron de-excitation can be analysed and used to determine the elemental composition of the sample. Likewise, the energies of the Auger electrons can also be used to determine the chemical composition of the sample in the near surface regions. Characteristic X-rays arise from within the entire excitation volume, so the resolution is limited to $\sim 1 - 2 \mu\text{m}$.

3.3.1.6. Energy dispersive X-ray spectroscopy (EDS)

The elemental composition of a region can be determined by measuring the energy associated with the X-rays produced as a result of the de-excitation that occurs when a low energy electron vacancy is occupied by an electron from a higher energy level. As previously mentioned, these electron vacancies exist due to the inelastic interactions that result in the emission of secondary electrons. The energy and wavelength associated with the X-ray emission is characterised by: the element, the energy level of the shell vacancy and the number of orbital shell jumps made in order to fill the vacant shell. The energy criterion needed to remove an electron from a given shell is known as the critical excitation energy. Therefore, if the incident electron beam has sufficient energy to remove an electron from a given shell, a characteristic X-ray will be produced due to electron de-excitation. The differences in the critical excitation energy between different elements gives rise to variations in the spatial resolution when analysing different elements. Non-characteristic X-rays are also produced due to the deceleration of electrons as they enter the coulombic field of an atom and are often referred to as background, continuum or bremsstrahlung X-rays.

A collimator, electron trap, window, semiconductor crystal detector and a field effect crystal transistor make up the main constituent components of an EDS detector. The collimator ensures that only X-rays which have been generated due to interactions between the electron beam and sample enter the detector. Preceding the collimator is an electron trap which is aptly named as it prevents the entry of

electrons into the detector. The window is simply fitted to the detector to act as a barrier and isolate the semiconductor crystal detector from the chamber of the microscope. However, the window limits the ability to detect low atomic number elements. The semiconductor crystal detector is kept under a high vacuum cold environment and converts incident X-rays into measurable short voltage pulses. This is achieved by applying a large bias voltage across a lithium drifted silicon semiconductor to create a region depleted in electrons. When an X-ray passes through this depleted region a series of electron hole pairs are created; these charge carriers migrate to opposing electrodes thus generating a charge signal. This signal is added to the applied bias voltage and is proportional to the energy of the original X-ray. The voltage pulse from the detector requires amplification and this is partly achieved using a field effect transistor.

3.3.1.7. Electron backscatter diffraction (EBSD)

Electron backscatter diffraction (EBSD) enables the acquisition of crystallographic information from a highly polished planar sample in an SEM. In order to perform EBSD the sample is tilted such that it is at a shallow angle of 20° relative to the incident electron beam. This configuration results in a sample tilt of 70° relative to the phosphor screen of an orthogonally mounted EBSD detector (Fig. 3.7). The incident beam interacts with the crystal lattice of the sample such that backscattered electrons with low energy loss are channelled. These channelled electrons are subject to path differences that give rise to constructive and destructive interference. In other words, scattered electrons which incur only small energy losses due to elastic interactions may travel through the crystal lattice in such a way that their energy and direction satisfy the Bragg condition for a given crystal structure and thus undergo diffraction. The diffraction of electrons due to a regular crystal lattice results in constructive and destructive interference, therefore diffraction cones are formed which relate to each family of lattice planes Fig. 3.8.

When the phosphor screen of the EBSD detector is placed in close proximity to the sample, the phosphor screen is illuminated due to its intersection with the diffraction cones and fluoresces due to excitation via electron collision Fig. 3.8.

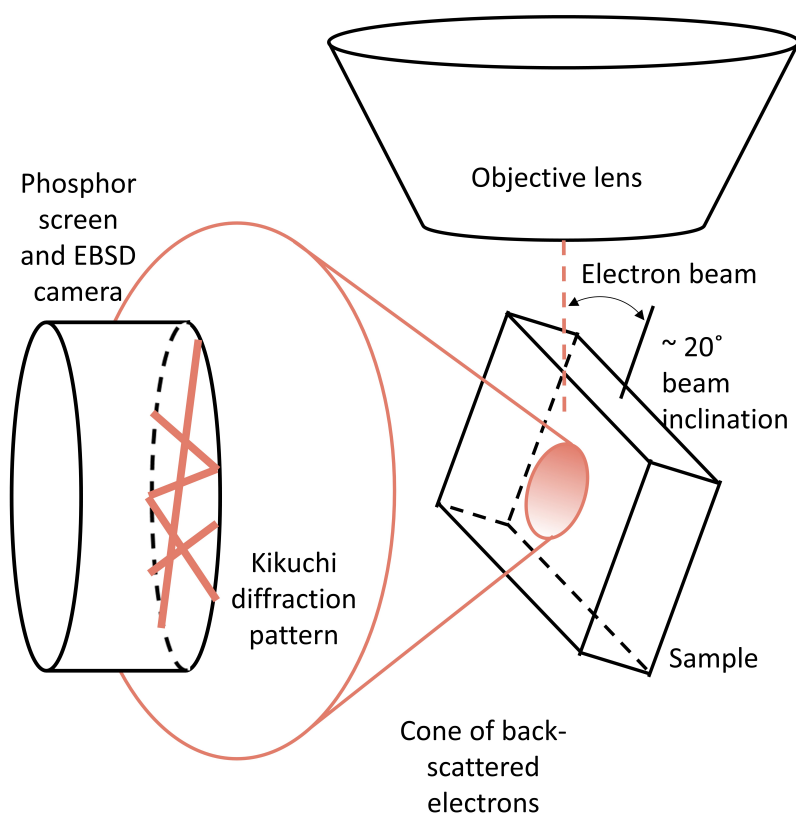


Figure 3.7: Schematic illustrating the geometric set-up of an EBSD measurement system.

The presence of the phosphor screen enables the diffraction pattern to be recorded by a charged-coupled device (CCD) camera. This diffraction pattern is referred to as a Kikuchi pattern and is uniquely defined by: the crystal irradiated by the incident beam, the orientation of the crystal in space, the wavelength of the incident electron beam, and the proximity of the detector in relation to the sample. A Kikuchi pattern is composed of Kikuchi lines which appear almost straight due to the shallow nature of the diffraction cones Fig. 3.8. The Bragg angle is of the order of only a few degrees due to the relative size of the electron wavelength and dimensions of the unit cell. A Kikuchi pattern also contains a background which is predominantly the result of low energy electrons that have undergone inelastic interactions. The constituent Kikuchi bands which make up the Kikuchi diffraction pattern can be computationally analysed and indexed through the use of an optimised Hough transform and a crystallographic database [241].

A Kikuchi pattern can be regarded as a gnomonic projection of the lattice

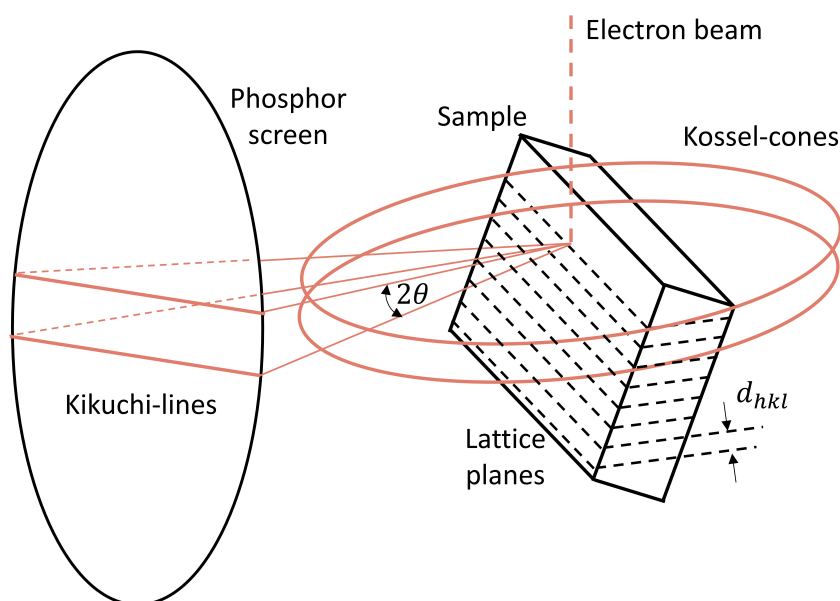


Figure 3.8: Schematic illustrating the formation of an electron backscatter pattern (EBSP).

onto the phosphor detector. The band width of a Kikuchi line pair corresponds to the Bragg angle. The centreline of a Kikuchi band represents what can be described as an imaginary section line between a set of diffraction lattice planes and the phosphor detector screen. The centreline positions of a Kikuchi band correspond to a crystal's interplanar angles. Therefore, the positions and widths of a number of Kikuchi bands from within a pattern provide sufficient information for phase identification and the determination of a crystal's orientation. The direct interpretation of a Kikuchi pattern is inherently difficult via computational methods, therefore a Hough space transform is employed in the computational analysis of Kikuchi patterns. The Hough transformation is used as part of an image processing algorithm which permits the detection of lines within an image. A line in the form of a Kikuchi band in the image space is transformed via the Hough transformation into a spot in the Hough space. These spots can be quantified computationally and this enables the computational identification of phases and crystal orientations when indexed to existing crystallographic information.

3.3.2. Laboratory scanning electron microscopy

The scanning electron microscopy (SEM) presented in this thesis was performed using two microscopes: (i) a tungsten filament type FEI Quanta 600, and (ii) a Jeol 7100F equipped with a field emission gun-type (FEG) electron source. The working parameters of these microscopes were optimised on a case by case basis depending on the type of analysis required. The Quanta 600 is equipped with two Bruker XFlash silicon drift detectors whilst the Jeol 7100F is fitted with an Oxford Instruments Nordlys Nano EBSD detector and an Oxford instruments X-Max silicone drift detector. When using the Quanta 600, EDX data was acquired using Bruker's ESPRIT software. The EBSD and EDX acquired with the Jeol 7100F was performed using Oxford Instruments Aztec software.

3.3.3. Metallurgical sample preparation for microscopy

In order to perform microstructural analysis in the SEM, highly polished planar samples had to be produced. If required, metallurgical samples were initially mounted in a conductive hot mounting compound named Conducto-Mount which was supplied by MetPrep Ltd. Samples were subsequently ground, diamond polished to a 1 μm finish and then given a final polish using 0.06 μm colloidal silica.

Powder samples were initially mixed with finely ground Conducto-mount resin prior to hot mounting in an effort to aid the retention of the powder during metallurgical preparation and to promote a uniform distribution of powder across the mounted sample. Bulk HIPed and HIP bonded samples were cut to the required size by either electrical discharge machining (EDM) or a cubic boron nitride cut off wheel prior to mounting. These samples were taken from a central region of the bar and from distance > 20 mm from the bar end. The cast Tristelle 5183 samples were cut from approximately the central region of the casting using a cubic boron nitride cut-off wheel. After mounting, all metallurgical samples were prepared in accordance to the procedure outlined above.

3.3.4. Optical microscopy and metallurgical sample preparation

The optical micrographs presented in this thesis were acquired using a Nikon Eclipse LV100ND equipped with five objective lenses offering objective magnifications of 5x, 10x, 20x, 50x and 100x optical zoom. The digital acquisition of optical micrographs was made using a Nikon DS-Ri1 high resolution microscopy camera. When appropriate, polished Tristelle 5183 samples (Section 3.3.3) were chemically etched for optical microscopy in an effort to highlight the general microstructure of the alloy. Tristelle 5183 was etched using a mixture of 10 ml nitric acid, 10 ml acetic acid, 15 ml hydrochloric acid and 2-5 drops of glycerol.

3.4. TRANSMISSION ELECTRON MICROSCOPY (TEM)

3.4.1. Principles of TEM

3.4.1.1. Electron optics

In TEM an electron transparent sample is inserted into the path of a high energy beam of electrons. The resulting interactions between the electron beam and sample can be used for imaging, chemical analysis and crystallographic studies. In its simplest configuration, a TEM takes the form of a columnar vacuum chamber which contains: an electron source, a series of pre and post sample electromagnetic lenses, apertures, and detectors as shown schematically in Fig. 3.9.

The electron gun and condenser lenses are the principal components which make up the illumination system in a TEM. The illumination system channels the electrons from the source to the sample and can be operated in either parallel beam or convergent beam modes. Two types of electron source are used in TEMs: (i) thermal emission sources which rely on the thermionic emission of electrons from a gun cathode via heating, and (ii) field emission sources where electrons are emitted as a result of a large potential difference which is applied between the anode and cathode of the electron gun. The electron beam passes through a set of condenser lenses which control and condition the electron beam prior to its interaction with the sample. The first condenser lens forms an image of the gun crossover. The second condenser lens and condenser-objective lens

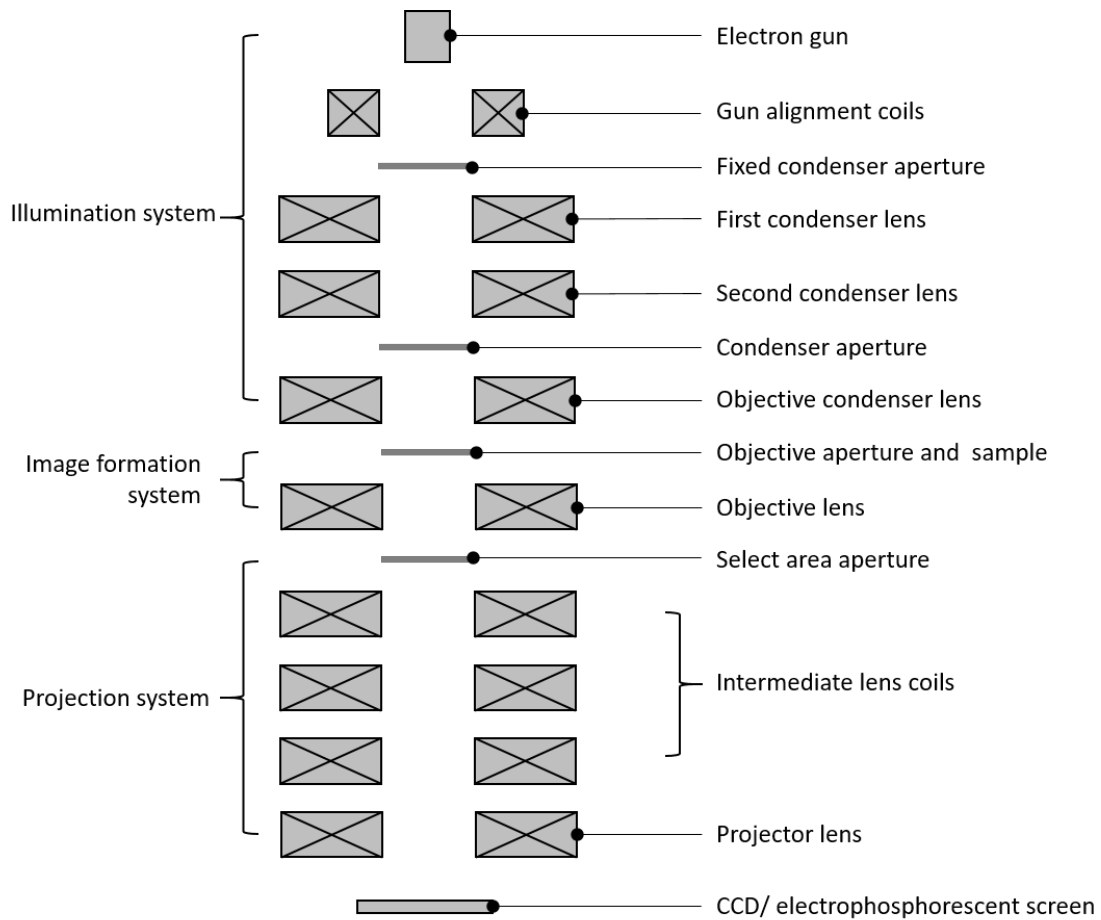


Figure 3.9: Schematic of the optical components in a basic TEM.

are additionally adjusted such that the electron beam irradiates the sample in a convergent or parallel manner. The “condenser apertures” include a fixed aperture and a movable aperture. The fixed aperture is inserted into the first condenser lens and arrests electrons travelling at large angles relative to the optical axis. The second condenser aperture consists of a series of interchangeable movable apertures inserted into the second condenser lens and control both the divergence angle and the dose of the incident beam. The condenser apertures also act to reduce spherical aberration.

The specimen/sample stage and objective lens form the heart of the TEM and is the region within a TEM where all the beam-sample interactions take place. All the lenses which lie below the sample in the TEM column act to magnify the image of the specimen. The first intermediate image is formed by the objective lens and a magnification of 20 - 50 times is achieved depending on the ratio of the distances

between both the object plane and the image plane. The quality of the objective lens is paramount as this lens determines the quality of all the information that can be acquired about the specimen. In other words, a quality objective lens has both a small spherical aberration coefficient and small chromatic aberration coefficient. The objective aperture is inserted into the back focal plane of the objective lens and acts to cut off peripheral electrons and thus improve diffraction contrast. Select area diffraction (SAD) apertures of various sizes (10 - 100 μm) can be inserted into the image plane of the objective lens in order to isolate small areas for diffraction analysis.

The beam subsequently passes through an intermediate lens (usually comprised of three lenses) which is positioned in-between the objective and projector lens. The intermediate lens changes the focusing position of either the initial image formed by the objective lens, or a diffraction pattern formed in the back focal plane of the objective lens. In other words, the excitation of the first intermediate lens determines whether a diffraction pattern or TEM image is produced. Generally speaking, the intermediate lens consists of three constituent parts: an initial part which selects the focusing position, a second part which magnifies the diffraction pattern or image, and a third part which enables a rotation-free image or diffraction pattern. The combined magnification of the intermediate lens can vary between $\sim 0.5\text{x}$ and $\sim 100\text{x}$.

The final lens in the TEM column is the projector lens (or set of lenses) which has a fixed magnification at a value of $\sim 150\text{x}$. The projector lens further magnifies the image produced by the intermediate lens and projects this magnified image onto an electron detecting device, for example a charged coupled device (CCD) camera with a yttrium aluminium garnet single crystal. A more detailed description of the working principals of a TEM can be found in references [235, 242].

3.4.1.2. Select area diffraction (SAD) and convergent beam electron diffraction (CBED)

A select area diffraction pattern (SADP) is obtained by illuminating a localised region of the sample with a parallel beam (plane wave traveling in one direction).

This localised region is selected through the use of a select area diffraction aperture which is inserted into the image plane of the objective lens. The diffraction pattern is formed by focusing the imaging lenses to the back focal plane of the objective lens [242]. The spatial regions which can be investigated via SAD are often large (> 100 nm) in comparison to the dimensions of the crystalline features of interest; this clearly limits the diffraction studies that can be performed using SAD. However, this can be overcome by the use of convergent beam electron diffraction (CBED). In CBED a conical shaped convergent electron beam is focused onto a small area of the sample with a diameter of 10 nm or less. As in the case of SAD, the CBED pattern is formed on the back focal plane of the objective lens and is subsequently magnified by the imaging lenses.

3.4.1.3. Bright field and dark field imaging

A bright field image is acquired by illuminating the entire area of interest simultaneously using a parallel electron beam. The image is produced by the transmitted wave (the wave that does not undergo diffraction), and image contrast arises from the combination of both diffraction and absorption. In other words, strongly diffracting regions within the sample appear dark in a bright field image, whereas regions that strongly transmit electrons appear bright. A bright field image is produced on the back focal plane of the objective lens through the use of the objective aperture. The sample can be tilted to change the relative angle between the incident beam and crystal planes to vary the diffraction contrast of the image.

In contrast, a dark field image is produced by excluding the directly transmitted wave using the objective aperture such that the image is produced by scattered electrons, for example a particular diffracted beam or a certain region of a diffraction ring. In other words, a dark field image is an image that is produced by one diffracted wave of a diffraction pattern formed on the back focal plane of the objective lens through the use of the objective aperture. Dark field imaging is typically used for confirming the source of specific diffraction events and is therefore useful when studying crystal defects and imaging crystallographic phases.

3.4.1.4. High resolution transmission electron microscopy

(HRTEM)

High resolution transmission electron microscopy (HRTEM) is a particularly useful tool when analysing crystal structures, lattice defects, and interface structures in the TEM. A HRTEM image can be described as an interference pattern between both the forward scattered and diffracted electron waves from the sample (phase contrast). In other words, the contrast in a HRTEM image emerges from the interference in the image plane between the electron wave and itself.

3.4.1.5. Scanning transmission electron microscopy (STEM)

In scanning transmission electron microscopy (STEM), a finely focused beam of electrons scans across the sample in a raster pattern. One of the key advantages of STEM over TEM is that other signals, for example secondary electrons, scattered beam electrons, characteristic X-rays, and electron energy loss can be spatially resolved. The interactions which occur between a finely focused electron beam and the sample generate a signal stream. This signal is subsequently related to the beam signal position to generate an image by attributing a gray level to the signal level at a given location in the sample. A bright field STEM (BF-STEM) image is formed by electrons scattered through low angles, therefore contrast is the result of a weakening of the direct beam due to its interactions with the sample. In contrast, transmitted beam electrons which have been scattered through relatively large angles (inelastically scattered or thermal diffuse scattered electrons) may be detected via an annular dark field detector. A high-angle annular dark field (HAADF) image exhibits atomic number based contrast (Z-contrast) because Rutherford-scattering effects are minimised and diffraction-contrast effects are smoothed out. As characteristic X-rays can be spatially resolved when operating a TEM in STEM mode, EDX mapping can be performed (TEM-EDX). Because the sample is thin, beam spreading is limited and the resolution of TEM-EDX is similar to the probe size unlike in SEM.

3.4.2. Sample preparation using a focused ion beam (FIB)

The electron transparent TEM lamellae presented in this thesis were prepared using a focused ion beam (FIB) instrument. The lift out procedure used in the current work involved the site specific deposition of platinum over a thin region approximately $15\ \mu\text{m} \times 2\ \mu\text{m} \times 2\ \mu\text{m}$ in length, width and depth respectively. Platinum was deposited via the use of both a gas injection system (GIS) and an ion beam (Fig. 3.10). In addition to bulk samples, TEM lamellae were also taken directly from the tribologically affected surfaces of wear test samples. These TEM lamellae were taken parallel to the direction of shear. The sensitive nature of both the top surface and subsurface regions of these samples required Pt to be deposited using an electron beam and GIS prior to ion beam Pt deposition. This additional sample preparation step was performed in an effort to minimise the extent of ion induced damage during FIB Pt deposition.

Following Pt deposition, two large trenches approximately $15\ \mu\text{m} \times 12\ \mu\text{m} \times 6\ \mu\text{m}$ in length, width and depth respectively were milled either side of the Pt strip via Ga^+ bombardment (Fig. 3.10). These trenches were positioned such that the $15\ \mu\text{m}$ dimension lies parallel to the Pt strip. An ion debulk cleaning operation was then performed along the top and bottom faces of the sample either side of the Pt strip to produce a level sample with minimised ion induced surface damage. A U-shaped cut was then milled around the extremities of the sample such that the lamella was attached to the bulk sample by only a small volume of material directly adjacent to one side of the Pt strip. The sample was subsequently attached to the probe of a nanomanipulator via the deposition of FIB Pt (Fig. 3.10). The final section of material holding the TEM lamella to the bulk sample was then removed via ion milling and the TEM lamella was attached to a Cu TEM grid via Pt deposition. The probe was detached from the sample via ion milling and then fully retracted. Final thinning was laterally performed at a $1\text{-}2^\circ$ tilt either side of the sample in a stepwise fashion whereby the beam current was reduced incrementally during the thinning stages until the sample reached the required electron-transparent thickness. Final ion cleaning operations were performed at reduced working voltages and currents on both faces of the lamella at tilts ranging

from $3\text{-}6^\circ$ into the sample. A final sample thickness of the order of 150 nm was achieved Fig. 3.10.

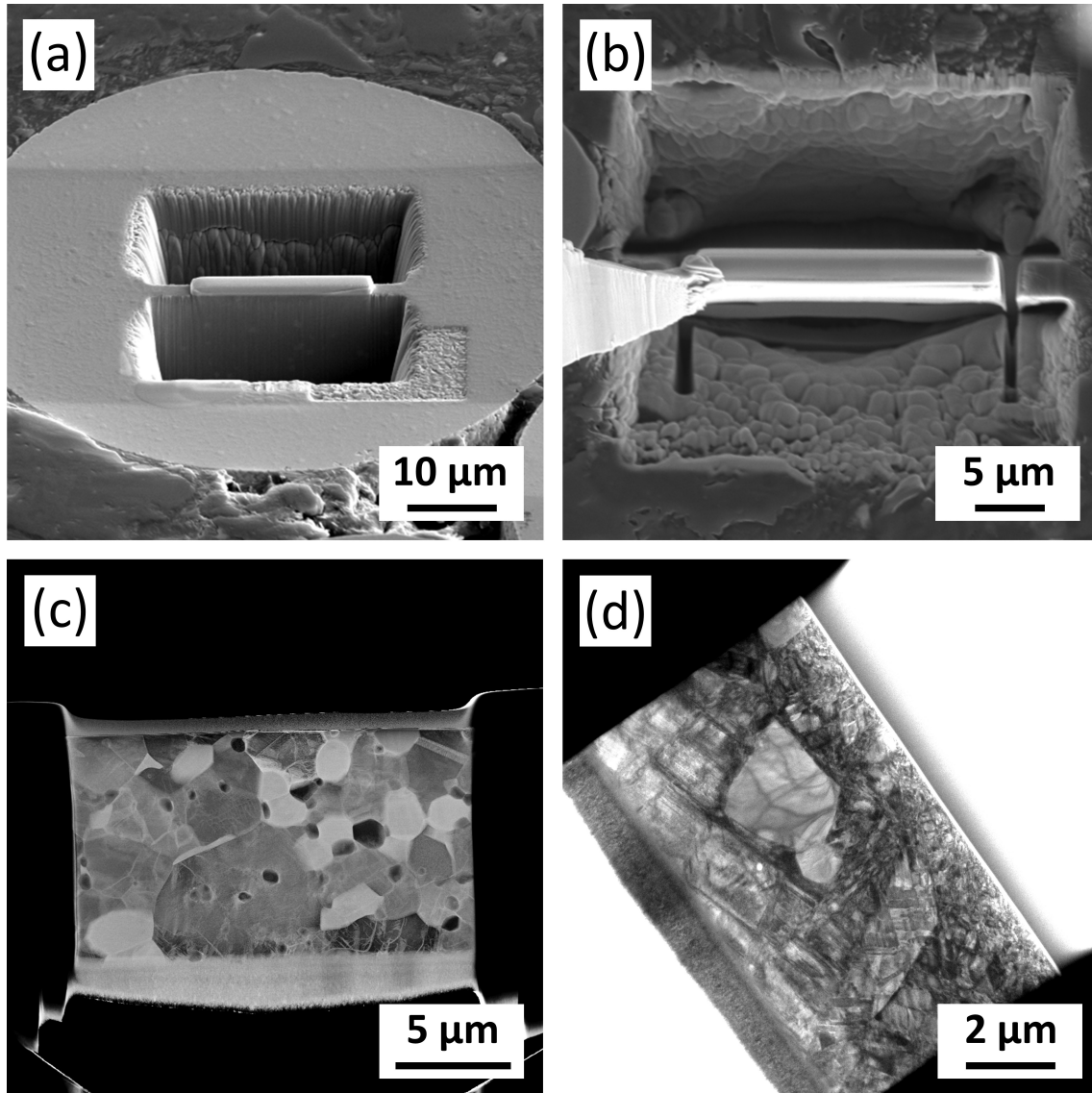


Figure 3.10: (a) Secondary electron image depicting a Tristelle 5183 powder particle with a platinum strip which has trenches ion milled on either side. (b) secondary electron image of the nanomanipulator performing the lift-out on a Tristelle 5183 powder particle. (c) HAADF-STEM image of a bulk HIP and HIP bond Tristelle 5183 lamella after final thinning and cleaning. (d) BF-TEM image of a Tristelle 5183 wear track lamella after final thinning and cleaning.

Sample re-thinning and cleaning was performed in some cases to permit HRTEM analysis and further diffraction studies. These operations were performed at the lowest possible accelerating voltage and current in order to minimise the ion induced damage to the sample surface. In an effort to produce the best quality

TEM lamellae the re-thinning and cleaning operations were performed diagonally across the sample surface and not in the direction of the original FIB thinning and cleaning operations. The final sample thickness post re-thinning was between 80-100 *nm*.

3.4.3. Laboratory TEM and Dual beam instrumentation

3.4.3.1. Laboratory TEM

The TEM presented in this was performed on three microscopes: (i) a Jeol 2100F equipped with a field emission gun (FEG)(NMRC University of Nottingham), (ii) a FEG source FEI Talos F200X (WMG University of Warwick), and (iii) a JEOL 2100+ (NMRC University of Nottingham). All these microscopes were aligned such that an operating voltage of 200 kV could be employed. The FEI Talos F200X is equipped with a FEI Super-X integrated EDS system which employs four silicon drift detectors (SDD). Additionally, both Jeol microscopes were equipped with a Oxford instruments X-Max SDD.

3.4.3.2. Laboratory dual beam (FIB)

Two dual beam microscopes were used in the preparation of the FIB lamellae used in the current work. An FEI Scios DualBeam (WMG University of Warwick) was principally employed for the preparation of site specific TEM lift out samples; this dual beam microscope is equipped with an FEI SidewinderTM ion column, an FEI NiColTM electron column and an FEI EasyLiftTM nanomanipulator. An FEI Quanta 200 3D DualBeam FIB/SEM (NMRC University of Nottingham) was also employed in this work; this dual beam microscope is equipped with an FEI MagnumTM ion column and a conventional tungsten filament thermal emission electron source.

3.5. MECHANICAL TESTING

3.5.1. Hardness testing

Both macro-scale and micro-scale hardness testing have been utilised throughout the course of this work. Macro-hardness measurements were used to assess the hardness of polished bulk materials and these measurements were made with a Vickers hardness tester employing a 20 kgf load (ISO 6507). Micro-hardness measurements were performed using a Buehler MMT-7 Digital Micro-Hardness tester employing a Knoop indenter and a 25 gf load. This instrument was used to measure the subsurface hardness of polished perpendicular cross sections taken from the wear tracks of autoclave wear test samples. These hardness measurements were taken from matrix regions at equispaced intervals beneath the samples worn surface and diagonally displaced relative to one another.

3.5.2. Wear Testing

Wear testing was conducted using a bespoke autoclave pin-on-disk tribometer which allowed testing to be conducted over a range of temperatures up to 250 °C within an aqueous environment. The pin and disks were machined via EDM from the same HIPed material stock and surface grinding was employed on the testing (contacting) surfaces of both the pin and disk ($R_a \sim 0.4 \mu\text{m}$). The cylindrical pins were machined to a 10 mm diameter and a 50 mm radius spherical end cap was ground onto the testing surface, whereas the disks were 30 mm in diameter with parallel ground end faces (Fig. 3.11). The disk was secured in a rotating sample holder and the pin was uniaxially loaded against the rotating disk through the application of a 4 kg dead load (Fig. 3.11). A free moving load stabilising mechanism prevented all lateral and rotation movement of the pin such that the pin and dead load assembly could only move in the direction normal to the plane defined by the test surface of the disk. The centre of the pin was loaded against the rotating disk at a position of 10 mm from the disk's axis of rotation; this resulted in a mean wear track diameter of 20 mm.

In order to simulate a primary system PWR environment, the wear test apparatus was immersed in deoxygenated deionised water with the addition of 8.5 mg LiOH per litre which results in a solution of $\text{pH} \sim 10.5$ at room temperature

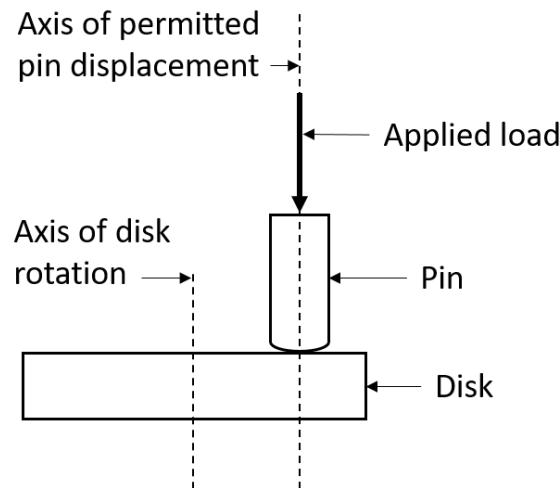


Figure 3.11: Simplified schematic of a pin on disk wear test apertures.

when prepared. Boric acid is added to the primary system of a PWR as it acts as a neutron absorber. However, the addition of boric acid was omitted in these tests as its concentration varies under normal PWR operating conditions and the current work aims to provide baseline measurements. Elevated temperature testing was achieved through the application of band heaters which surround the autoclave and a thermowell positioned inside the autoclave enabled the measurement of the test temperature. The autoclave was pressurised autogenously and no external pressurisation was employed. Therefore, the test pressure varies with respect to test temperature; for example a pressure of 50 bar was maintained during testing at 250 °C, whereas at 20 °C the autoclave pressure was 1 bar. A constant rotational speed of 200 rpm was applied to the disk which results in a sliding speed of 0.21 ms⁻¹ at the centre of the wear track. Wear testing was performed for a 5 h duration which results in a total mean sliding distance of ~ 3770 m with respect to the centre of the wear track. Testing was typically performed at 20 °C, 150 °C, 200 °C, and 250 °C and normally a minimum of three repetitions were performed at each temperature. These testing temperatures were selected in an effort to best understand the evolution in the operative wearing mechanisms between 20 °C and 250 °C (representative of primary system PWR conditions). The extent of wear was quantified by mass loss from the pin and the disk using a balance with a 0.1 mg precision.

In order to determine the mass change of a material as a result of corrosion

only, a disk was immersed at 250 °C for 5 h in the same wear apparatus without the application of any mechanical stimuli. These corrosion measurements provide a baseline for correcting the overall mass loss following wear testing. This can be expressed by the following equation:

$$\Delta m_w = \Delta m_T - \Delta m_{cor} \quad (3.14)$$

Where Δm_T is the mass change during the wear test and Δm_{cor} is the mass change of disk due to corrosion/oxidation. Δm_w is the mass change due to corrosion enhanced wear in the wear track. Corrosion tests found Δm_{cor} to be negligible relative to Δm_T for all the materials tested, therefore the effects of corrosion could be neglected. For clarity, it should be noted that a positive and negative mass change represents a mass gain and loss respectively.

For the purposes of being able to compare this work with other studies, the subsurface Hertzian contact stresses for a point contact along the contacts axis of symmetry were evaluated and presented in Fig. 3.12 (a) and (b) for Stellite 6 and Tristelle 5183 respectively [11]. In accord with the wear test configuration, these stresses were calculated for a 50 mm radius sphere in contact with a flat plate under a 39.24 N load. These stresses were evaluating using a Poisson's ratio of 0.3 and an elastic modulus of 237 GPa and 210 GPa for Stellite and Tristelle 5183 respectively [7]. σ_r , σ_θ and σ_z are the principal stresses, τ_1 and τ_2 are the principal shear stresses, and σ_{VM} is the Von Mises stress. The maximum shear stresses (τ_{max}) were 115.35 MPa (108 μm beneath the contact) and 106.41 MPa (112 μm beneath the contact) for Stellite and Tristelle 5183 respectively. The circular contact area diameters were 449 μm and 467 μm for Stellite and Tristelle 5183 respectively.

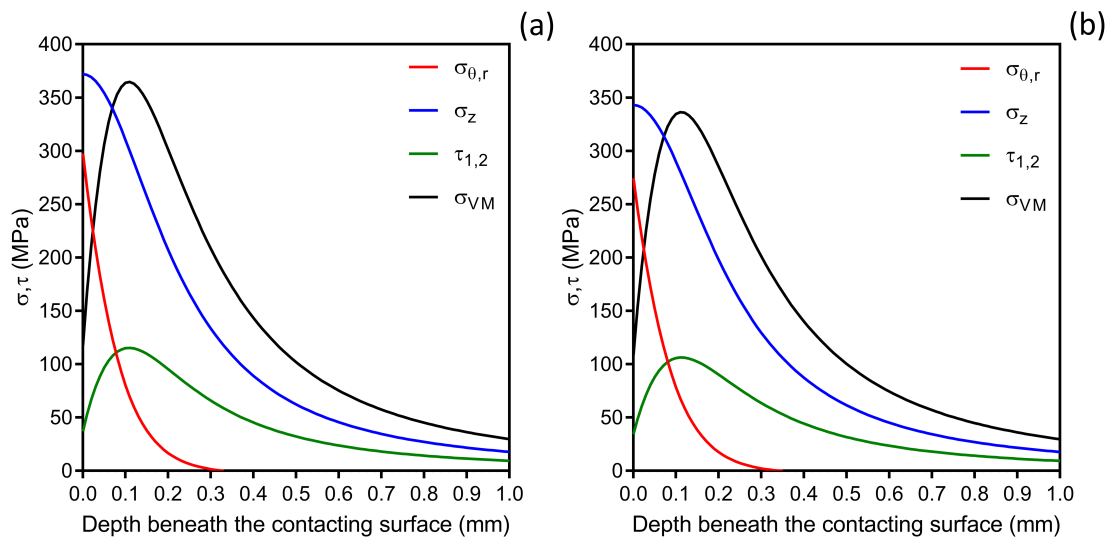


Figure 3.12: Subsurface Hertzian contact stresses for a point contact along the contacts axis of symmetry for Stellite 6 (a) and Tristelle 5183 (b). σ_r (red), σ_θ (red) and σ_z (blue) are the principal stresses, τ_1 (green) and τ_2 (green) are the principal shear stresses, and σ_{VM} is the Von Mises stress. These stresses were calculated for a 50 mm radius sphere in contact with a flat plate under a 39.24 N load.

MICROSTRUCTURAL EVOLUTION AND FORMATION IN GAS ATOMISED TRISTELLE 5183 POWDER

4.1. INTRODUCTION

The main aim of this chapter is to investigate the phase and microstructure formation in different size ranges of commercially available nitrogen gas atomized Tristelle 5183 powder in order to better understand phase selection during solidification by comparing the rapidly solidified microstructures with that of a conventionally cast alloy sample. Whilst the importance of ensuring that Tristelle 5183 powder contains minimal undesirable inclusions is reviewed in reference [224], there is, to date, no work which investigates powder microstructure as a function of cooling rate, i.e. particle diameter. This topic is important because a wide powder particle size range, e.g. diameters below 500 μm , is typically employed in the powder HIPing process [243]. It is well known that gas atomized powder particles of different diameters cool at different rates, typically in the range 10^4 to 10^6 K/s [97, 231–233]. However, it is currently not clear how cooling rate affects microstructure formation in the complex alloy under investigation in this study. At high cooling rates, different combinations of equilibrium and non-equilibrium phases may well form in powder particles of different sizes. This needs to be understood in order to properly select the powder size range used in HIP consolidation. A detailed investigation of the effect of cooling rate on microstructure formation in powder particles is crucial because a variation in the powder microstructure could affect the uniformity of the HIP consolidated product [230] and potentially give rise to undesirable property variations in a component.

4.2. RESULTS

4.2.1. Phase identification of gas atomised Tristelle 5183 powder using XRD

Fig. 4.1 shows representative XRD patterns for the different powder size fractions normalised to the peak of maximum intensity on each diffractogram. All patterns show peaks which correspond to fcc γ -iron (austenite) at $2\theta \sim 43.5^\circ$, 51° and 75° . Additionally, the patterns also have peaks at $2\theta \sim 45^\circ$, 65° and 82.5° which index to bcc α -iron (ferrite). The relative intensities of both the bcc α -iron and fcc γ -iron reflections are significantly dependent on the powder size fraction; the α -iron reflections exhibit a relative increase in intensity as the powder size decreases and the γ -iron reflections show a significant relative decrease in intensity with decreasing powder size.

All patterns show the presence of a B1 (Fm3m) NaCl-type, fcc MX carbonitride (M metal atom, X = C,N) with a lattice parameter close to that of NbC (ICDD file #01-070-8416 for NbC). The reflections consistent with this phase are clearly complex and can be interpreted as coming from three distinct populations of MX-type particles referred to as MX-1, MX-2 and MX-3. The evidence for these three distinct populations can be most clearly seen in the relatively low angle $\{111\}$ ($2\theta \sim 34-37^\circ$) and $\{200\}$ ($2\theta \sim 39.5-42.5^\circ$) reflections, which, for clarity have been marked on Fig. 4.1. The MX-3 population (at the higher 2θ values in the range of interest) has the smallest lattice parameter of the three MX populations and is consistent with the broad reflections that are most easily visible in the smaller powder size fractions. We interpret the remaining asymmetric reflections consistent with the MX carbonitride (at slightly lower 2θ values than the MX-3 peaks) as a convolution of reflections from the MX-1 and MX-2 populations. The asymmetry is a result of two effects: first, a population of particles, MX-2, that are compositionally non-uniform; and secondly, a population of particles, MX-1, that are microstructurally sparse and equilibrated, giving rise to peak height ratios that deviate from the ICDD database values for NbC. This analysis, based around an assumption of three populations, is justified by and entirely consistent with the

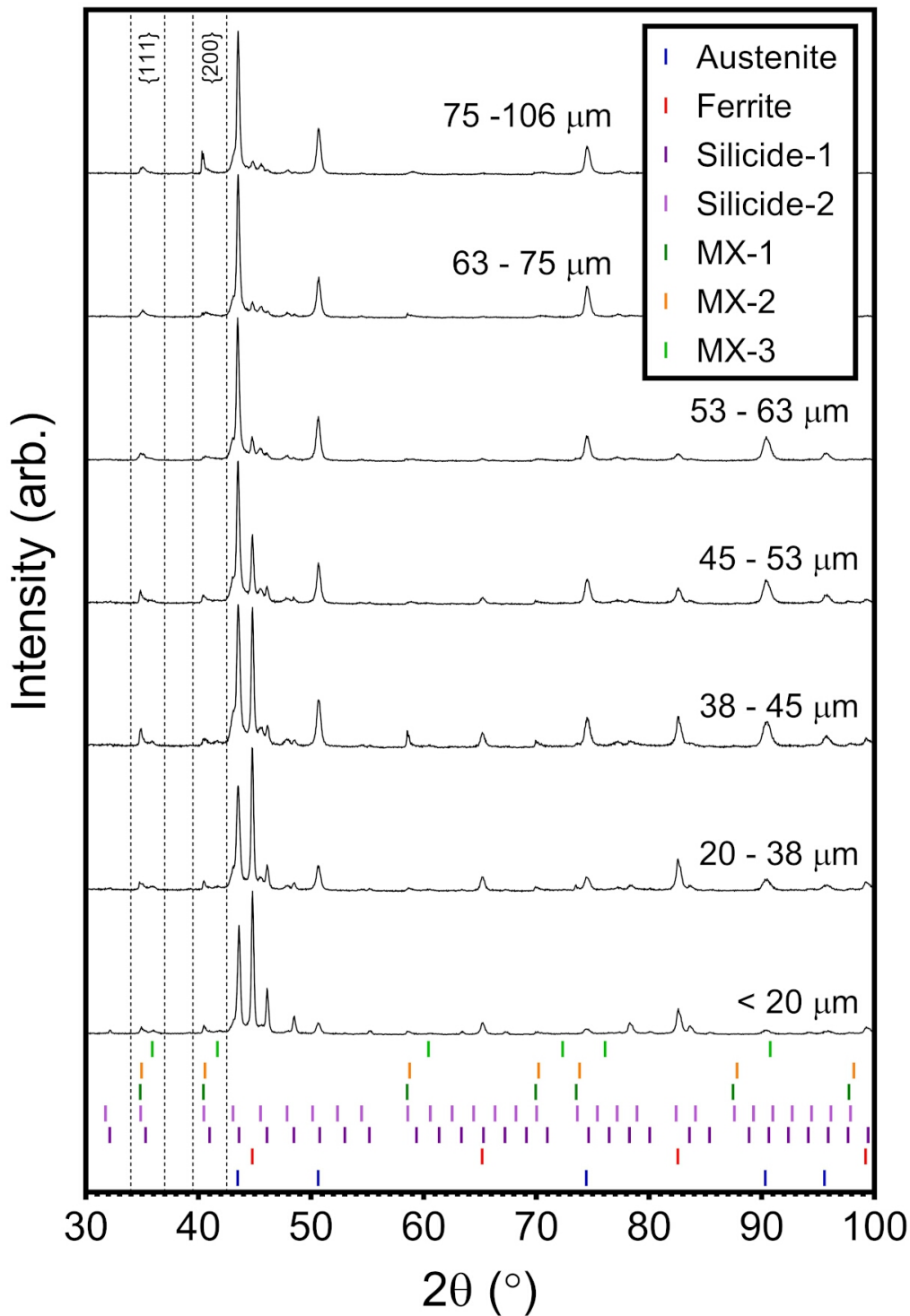


Figure 4.1: XRD patterns obtained from the different powder size fractions of gas atomised Tristelle 5183. The vertical markers indicate the Bragg peak positions for the different phases.

microstructural observations on Nb(C,N) set out in sections 4.2.2 and 4.2.3.

An additional two sets of reflections, consistent with an intermetallic silicide

phase, are seen in all the diffraction patterns. This phase is cubic and isostructural to $\text{Fe}_5\text{Ni}_3\text{Si}_2$ and $\text{Cr}_3\text{Ni}_5\text{Si}_2$ [163, 244, 245]. These two sets of intermetallic silicide reflections are referred to as silicide-1 and silicide-2. The presence of two different sets of silicide reflections is most clearly illustrated by the two reflections situated at 2θ angles between 48° and 49° . The relative intensity of the silicide phase with the larger 2θ values (that designated silicide-1) clearly increases as the powder size decreases therefore, suggesting that this phase is present in a higher fraction in the smaller powder particles. The refined values of the lattice parameters of the silicide phases are reported in Table 4.1. The values differ significantly from the values reported in references [245, 246] but this is not surprising as in the present study the silicides formed under non-equilibrium conditions involving rapid growth from the melt whereas in previous studies solid state equilibrated systems were examined.

Table 4.1: Comparison of measured and literature values for the lattice parameters of the silicide phases.

Sample	Phase	Lattice parameter (nm)
< 20 μm powder	Silicide-1	0.6224
	Silicide-2	0.6298
63-75 μm powder	Silicide-1	0.6222
	Silicide-2	0.6302
Ackerbauer et al. [245]	$\text{Fe}_5\text{Ni}_3\text{Si}_2$	0.6146-0.6124
Gladyshevskii et al. [246]	$\text{Cr}_3\text{Ni}_5\text{Si}_2$	0.6120

Overall, it is clear that there are broad similarities between the XRD patterns for 53-63, 63-75 and 75-106 μm powder size fractions. However, as the powder size decreases the diffraction patterns show more prominent α -Fe and silicide reflections. In light of the above, further analysis of XRD patterns was conducted on only two powder size fractions. These have been chosen as they are representative of the significant differences that are observed. The size fractions selected were the 63-75 μm size fraction (representative of the larger powder particles) and the < 20 μm fraction (the smallest size range in the study). The Rietveld refinement method employing a fundamental parameters approach was applied

to obtain quantitative estimates for phase fraction values as well as to determine refined lattice parameters. Fig. 4.2 shows full pattern fitting for these two powder size fractions; it is noted that the small difference between the calculated and experimental diffraction patterns illustrates that a sensible refinement has been achieved. The calculated phase fractions are reported in Fig. 4.3(a). The larger size powder comprises approximately 58% γ -Fe, 30% silicide, 7% α -Fe and 5% MX (in wt%) whereas the $< 20 \mu\text{m}$ powder fraction shows significantly different phase proportions with approximately 13% γ -Fe, 50% silicide 32% α -Fe and 5% MX (in wt%). Fig. 3(b) shows the refined lattice parameters of the MX-1, MX-2 and MX-3 populations in the different size fractions. It is apparent that the lattice parameter of the MX-1 and MX-2 populations changes very little with varying size fraction whereas that of MX-3 decreases as the powder size decreases. The refined value of the MX-1 population is close to the value 0.4469 nm given in the International Center for Diffraction Data file (#01-070-8416) for NbC suggesting that only this carbide formed under conditions close to stoichiometry.

In the section that follows, detailed microstructural observations are reported for the 63-75 μm and $< 20 \mu\text{m}$ powder size ranges to complement the detailed XRD analysis of these two size fractions.

4.2.2. Microstructure of 63-75 μm sized powder

Backscattered electron (BSE) images of a powder cross-section are shown in Fig. 4.4(a) and (b). The bright contrast features, which EDS showed to be a Nb-rich phase, are the MX populations identified by XRD. The single, large $\sim 10 \mu\text{m}$ -sized Nb(C,N) particle in Fig. 4.4(a) will be termed a pre-existing carbide. From its size and rounded morphology, it seems probable that this large particle was present in the alloy melt prior to atomisation. The approximately micron-sized Nb(C,N) particles in Fig. 4.4(a) and (b) will be referred to as primary carbonitrides. These form a fine scale distribution of faceted crystals throughout the powder particle and are largely entrained within a dendritic network, Fig. 4.4(b). Nanoscale Nb(C,N) particles are also evident in the interdendritic regions (Fig. 4.4(b)) and will be termed secondary carbonitrides. The interdendritic phase region could

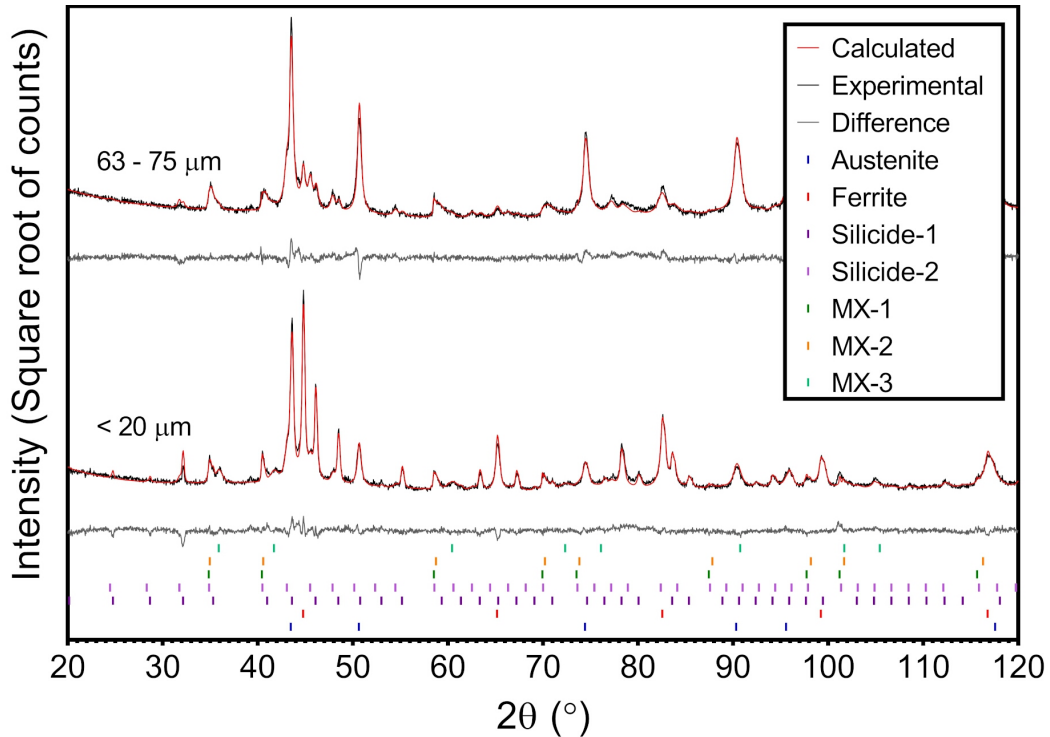


Figure 4.2: Experimental XRD patterns (black) for the $< 20 \mu\text{m}$ and $63\text{-}75 \mu\text{m}$ powder size fractions. Calculated patterns determined via Rietveld refinement are indicated in red and the difference between experimental and calculated diffraction patterns is presented in grey. The vertical markers indicate the refined Bragg peak positions (based on the $< 20 \mu\text{m}$ powder fraction).

not be definitively characterised by SEM-EDS but most likely corresponds to the silicide phase, isostructural to $\text{Fe}_5\text{Ni}_3\text{Si}_2$, detected by XRD.

Fig. 4.4(c) and (d) show an inverse pole figure (IPF) orientation map and a phase distribution map respectively, derived from EBSD analysis of a particle cross-section. A number of dendritic grains of $\gamma\text{-Fe}$ are present which formed during the rapid solidification inherent in gas atomisation. A distribution of the micron-sized primary $\text{Nb}(\text{C},\text{N})$ particles is also evident. The phase map (Fig. 4.4(d)) clearly shows that the interdendritic phase is a silicide isostructural with $\text{Fe}_5\text{Ni}_3\text{Si}_2$. The small fraction of material that could not be indexed is shown in black.

In order to gain further insight into the powder microstructure, STEM was performed on FIB lamellae prepared from the powder. The STEM bright field image, Fig. 4.5(a), shows dendritic features that are Ni-rich and Cr depleted compared to the interdendritic phase (Fig. 4.5(b) and (c)). The dendrites are

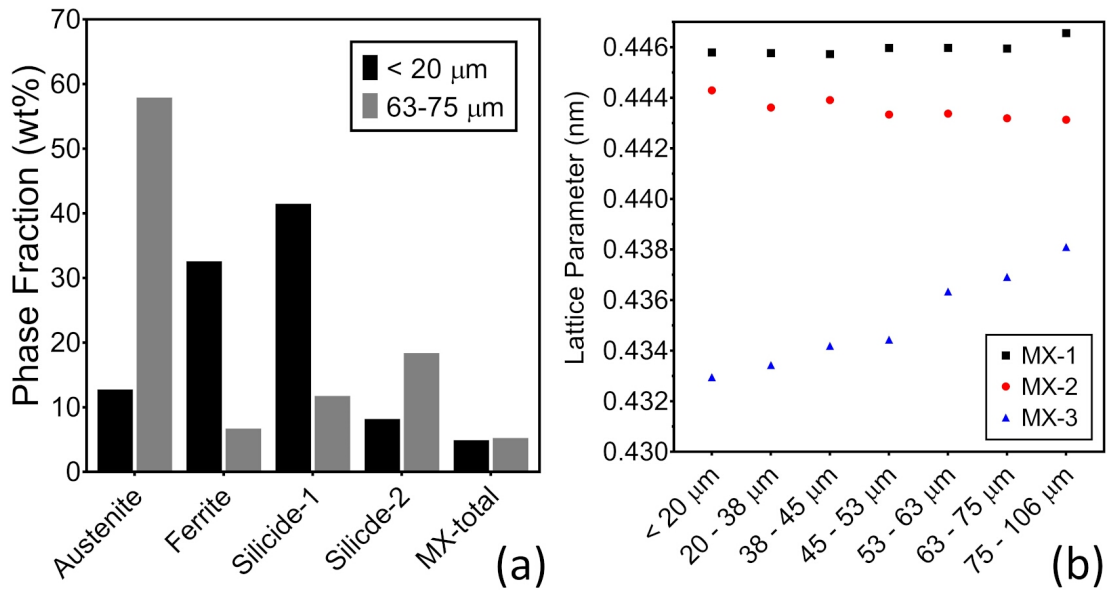


Figure 4.3: (a) Depicts a bar chart showing the proportions of phases in the $< 20 \mu\text{m}</math> and $63-75 \mu\text{m}</math> powder size fractions from Rietveld refinements of XRD data. (b) shows a plot of refined lattice parameters for MX-1, MX-2 and MX-3 against powder size fraction obtained by Rietveld refinement.$$

confirmed to be $\gamma\text{-Fe}$ through the SADP in Fig. 4.5(d) (region marked (d) in Fig. 4.5(a)). The composition of a typical dendritic region, given in Table 4.2, shows significant Si in the $\gamma\text{-Fe}$. The SADP of Fig. 4.5(e) confirms that region marked (e) in Fig. 4.5(a) is a phase isostructural with $\text{Fe}_5\text{Ni}_3\text{Si}_2$ and the composition of typical silicide regions, also given in Table 4.2, shows that the Cr level is almost twice that of austenite. Finally, the EDS map of Fig. 4.5(f) confirms that the nanoscale interdendritic carbides, seen in the BSE image of Fig. 4.4(b), are indeed Nb rich. Both the primary and secondary Nb-based carbonitrides are distinctly visible in Fig. 4.5(a) and (f). An example of a primary particle which is entrained within the dendritic network is highlighted by the larger of the two white circles in Fig. 4.5(a) and (f). Similarly, a secondary carbonitride residing within the interdendritic region is highlighted by the smaller of the two white circles in Fig. 4.5(a) and (f).

4.2.3. Microstructure of $< 20 \mu\text{m}</math> sized powder$

Backscattered electron (BSE) images of powder cross-sections are shown in Fig. 4.6(a) and (b). The bright contrast approximately micron-sized features are the Nb-rich

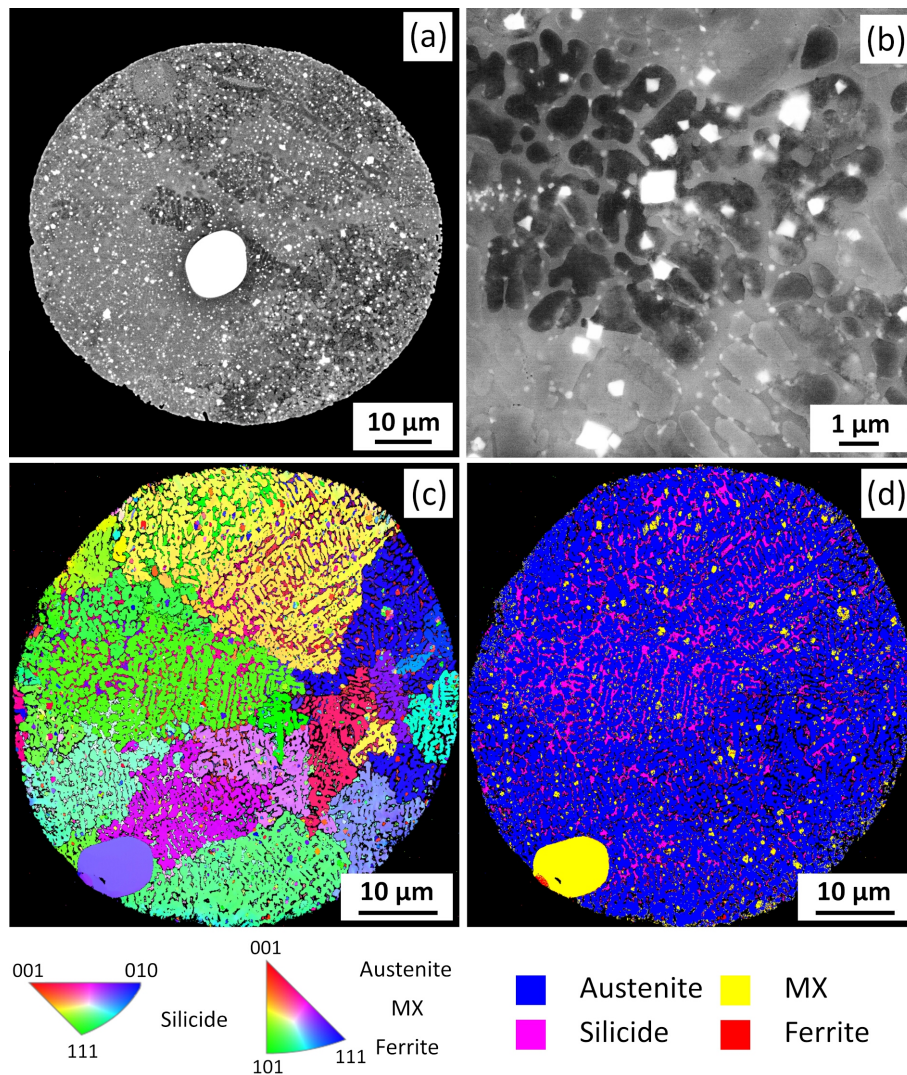


Figure 4.4: (a) and (b) show SEM images of a cross section through powder particles consistent with the 63-75 μm powder size fraction. (a) is a low magnification BSE image showing a bright contrast rounded pre-existing Nb(C,N) particle and uniformly distributed primary Nb(C,N) particles. (b) is a high magnification BSE image showing the micron-sized primary Nb(C,N) particles within a dendritic matrix and secondary, nanoscale Nb(C,N) particles in the interdendritic regions. (c) and (d) respectively depict EBSD derived IPFZ orientation phase distribution maps. The colours of the grains in (c) correspond to the crystallographic axes in the relevant stereographic triangles, the corresponding phases can be identified in (d).

MX phase previously identified by XRD and will be referred to as primary carbonitrides. The matrix microstructure is highly variable and exhibits irregular type dendritic features of varying contrast. Light grey contrast matrix regions where dendritic features are absent are also observed within this powder size

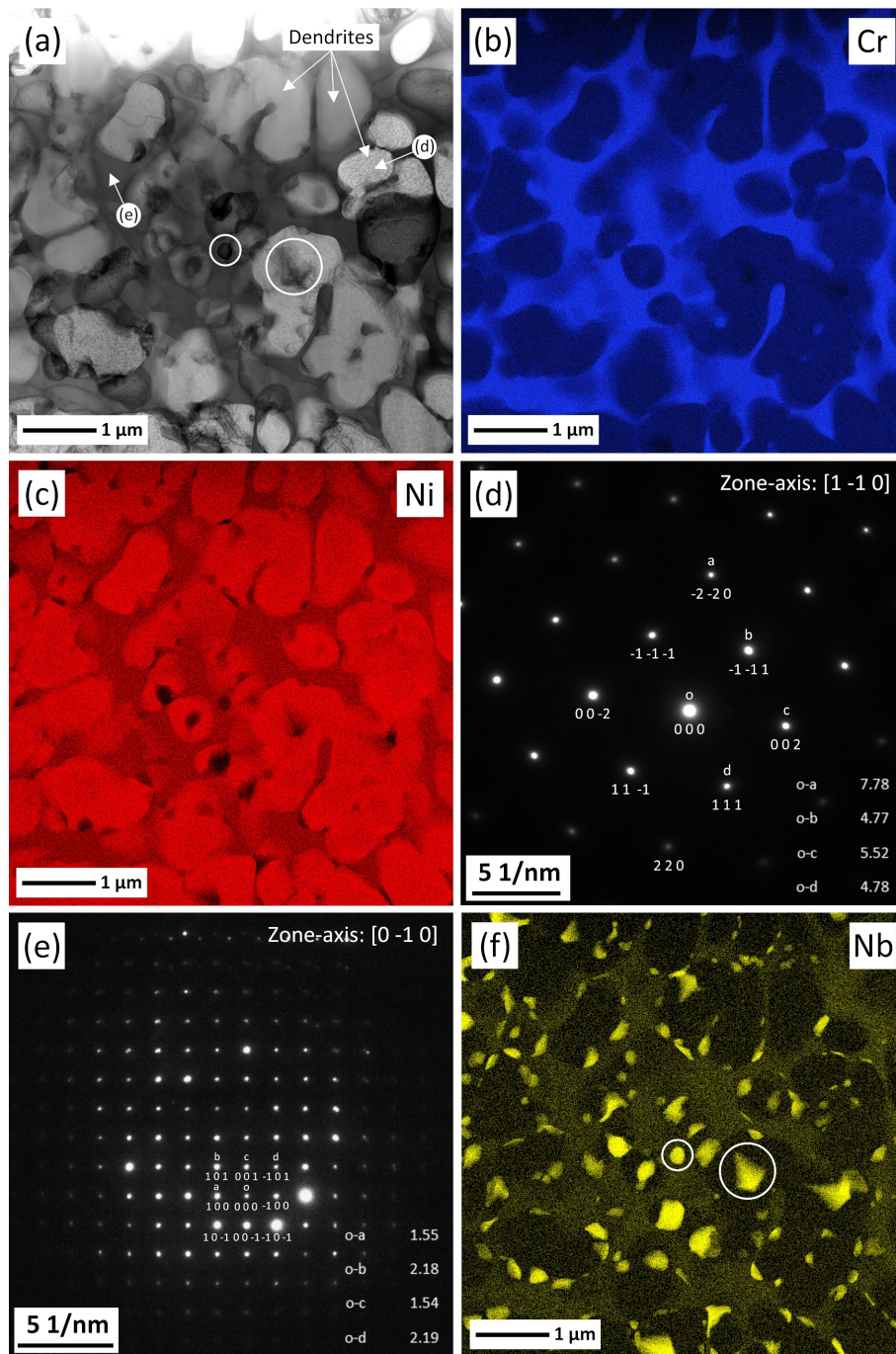


Figure 4.5: Representative microstructure of a powder particle from the 63-75 μm size fraction. (a) is a bright field STEM image showing a dendritic matrix, an interdendritic phase as well as primary and secondary Nb(C,N) structures. (b), (c) and (f) show X-ray maps of the same region depicted in (a) and correspond to maps for Cr, Ni and Nb respectively. (d) and (e) show SAD patterns from the areas marked as e and d in (a). (d) shows an SADP indexed to fcc γ -Fe [1 - 10] zone axis and the pattern in (e) is indexed to a [0 - 10] zone axis of a phase isostructural to $\text{Fe}_5\text{Ni}_3\text{Si}_2$. (f) clearly shows the locations of the Nb-rich particles.

Table 4.2: Compositions in at.% (excluding carbon) of phases present in gas atomised powder from different size ranges obtained by EDS in the TEM.

Powder size range	Phase	Element				
		Fe	Cr	Ni	Si	Nb
< 20 μm	α -Fe dendrites	60.8 \pm 0.3	15.3 \pm 0.2	11.2 \pm 0.3	10.1 \pm 0.2	0.2 \pm 0.1
	Cellular silicide	54.3 \pm 0.1	22.0 \pm 0.1	9.7 \pm 0.1	10.6 \pm 0.1	1.0 \pm 0.1
63-75 μm	γ -Fe dendrites	59.2 \pm 0.6	17.1 \pm 0.2	10.6 \pm 0.2	10.5 \pm 0.4	0.3 \pm 0.1
	Interdendritic Silicide	43.7 \pm 0.3	33.4 \pm 0.5	7.1 \pm 0.1	11.0 \pm 0.3	1.9 \pm 0.1

fraction, however the microstructural detail of these regions cannot be resolved by BSE-SEM.

Fig. 4.6(d) and (c) show an inverse pole figure (IPF) orientation map and a phase distribution map respectively derived from SEM/EBSD analysis of a powder particle cross section. The ferrite (α -Fe) and the silicide phases both occur as essentially single grains occupying approximately half the cross-section (Fig. 4.6(d)). The ferritic phase appears to conform to an irregular type dendritic morphology; this is particularly evident at the irregular dendritic front which separates the ferrite from the silicide, thus suggesting that the ferrite nucleated and grew first into the melt before its growth was terminated by impingement with the silicide phase. Micron-sized, Nb(C,N) particles are clearly distinguished in the phase map (Fig. 4.6(c)) and are dispersed in both the α -Fe and the $\text{Fe}_5\text{Ni}_3\text{Si}_2$ -type silicide phases.

To gain further insight into the microstructure, STEM and HRTEM were performed on a FIB lamella taken from a powder particle from the < 20 μm size fraction. The bright field image, Fig. 4.7(a), reveals a predominantly cellular structure with a small dendritic region labelled b in the top left as well as faceted particles, one of which is labelled c. Fig. 4.7(b) and (c) are the SADPs from regions labelled b and c respectively which confirm that these features are ferrite and fcc NaCl-type Nb(C,N) respectively. SADPs from the cellular-type matrix region, labelled d, and intercellular regions, such as e, both have the $\text{Fe}_5\text{Ni}_3\text{Si}_2$ silicide phase crystallography, despite showing different STEM contrast. The compositions of representative ferrite and cellular silicide regions, obtained by TEM-EDS, are given in Table 4.2. The two phases have similar Si and Ni contents but there is

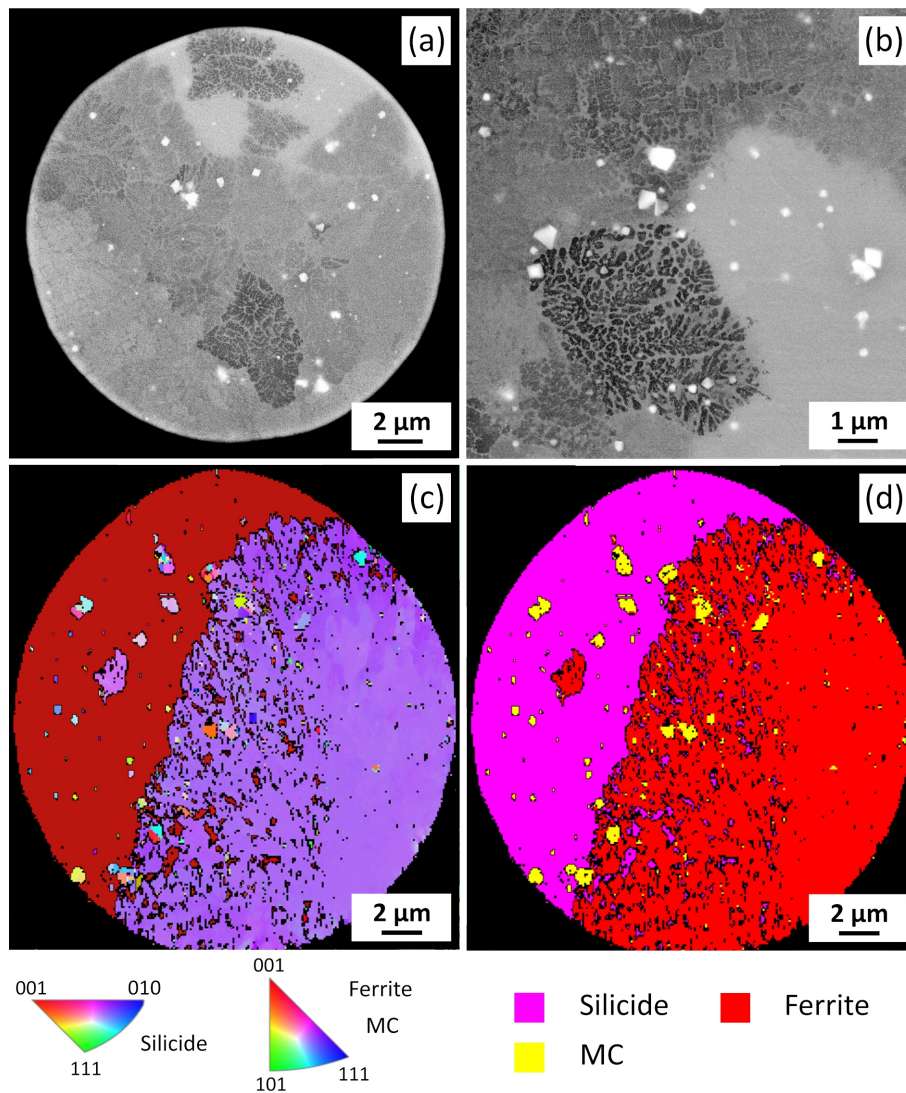


Figure 4.6: (a) and (b) show representative BSE-SEM micrographs of powder cross sections consistent with the $< 20 \mu\text{m}$ powder size fraction. (c) and (d) respectively show EBSD derived IPFX orientation and phase distribution maps of a powder cross section consistent with the $< 20 \mu\text{m}$ powder size fraction. The colours of the grains in (d) correspond to the crystallographic axes in the relevant stereographic triangles, the corresponding phases can be identified in (c).

a significantly higher Cr content in the silicide phase.

Fine nanoscale precipitates are seen to be almost entirely present at the intercellular boundary silicide regions (circled in Fig. 4.7(a)) and are shown in more detail in the STEM bright field image, Fig. 4.8(a). The EDS map for Nb, Fig. 4.8(b), reveals that they are Nb rich. The HRTEM image and corresponding FFT diffraction pattern, Fig. 4.8(c) and (d), confirm that they are nanoscale Nb(C,N) particles with, in the case of this precipitate, a lattice parameter $\sim 0.42 \text{ nm}$.

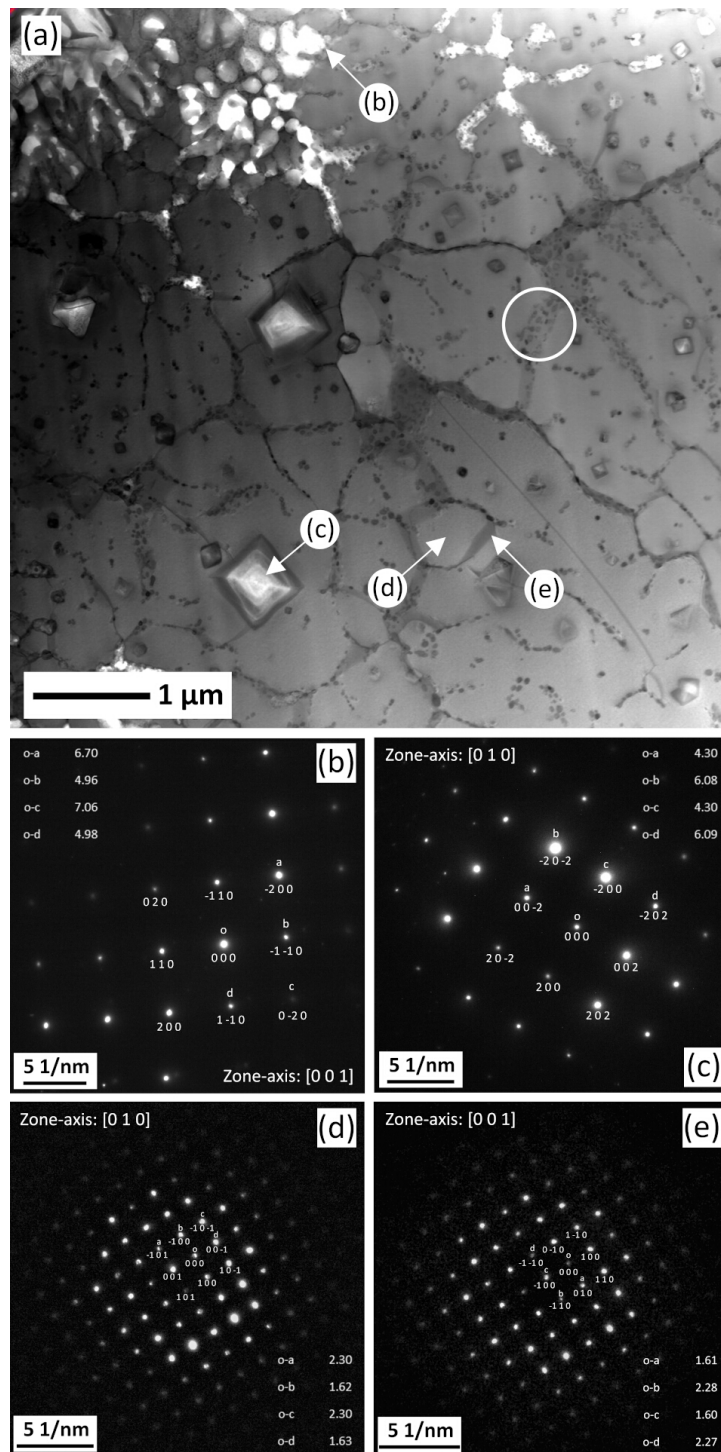


Figure 4.7: Representative microstructure of a powder particle from the $< 20 \mu\text{m}$ size fraction. (a) depicts an STEM bright field image where the regions marked (a), (b), (c) and (d) correspond to the respective SADP's. (a) shows a dendritic region (b), an angular particle (c), a matrix phase with a cellular structure (d) and a cellular boundary region (e). (b) is indexed to $\alpha\text{-Fe}$ [001], (c) is $\text{Nb}(\text{C},\text{N})$ [010], (d) and (e) exhibit the zone axes [010] and [001] of a phase isostructural to $\text{Fe}_5\text{Ni}_3\text{Si}_2$.

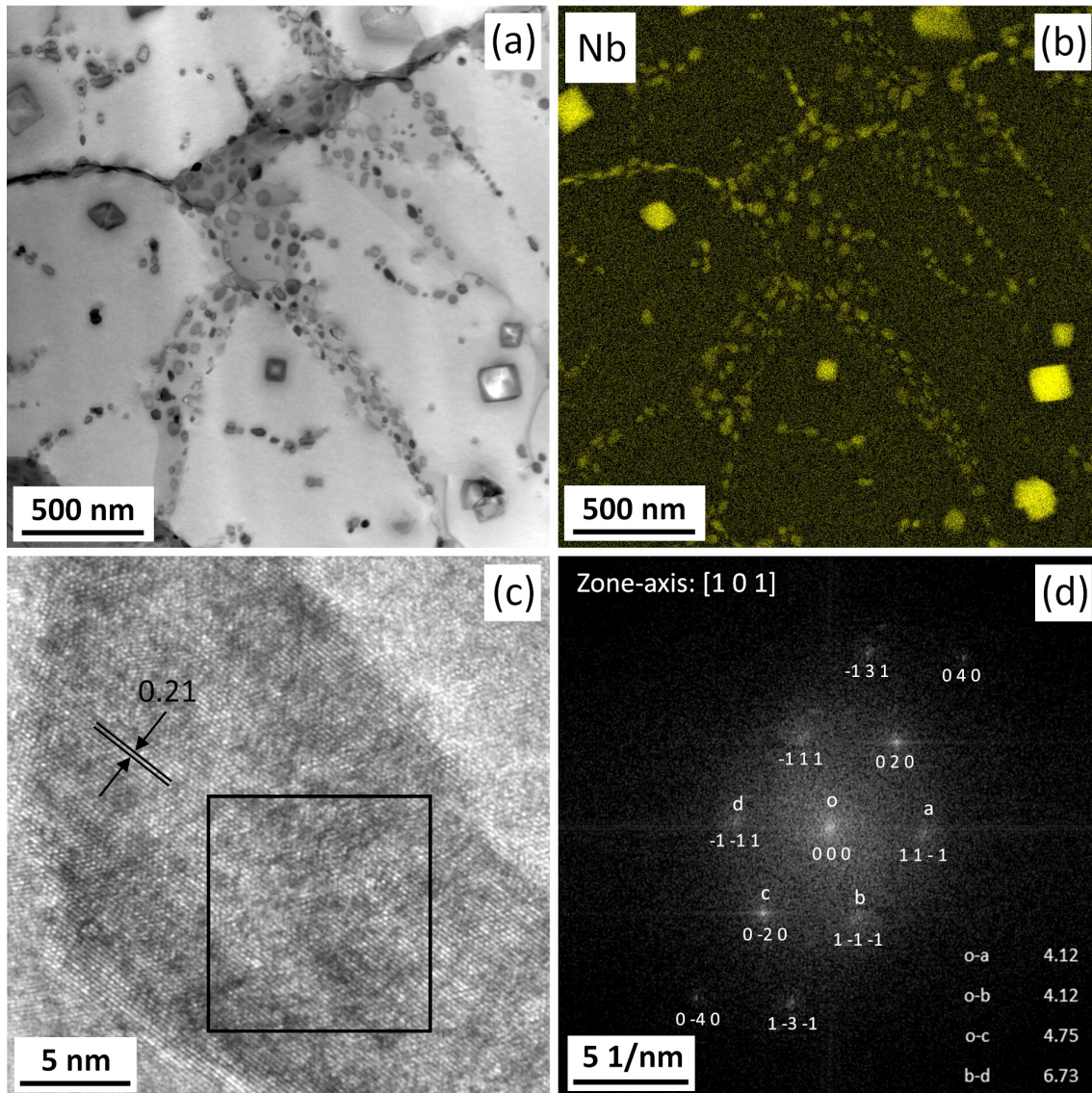


Figure 4.8: Microstructure of the intercellular region of a particle consistent with the $< 20 \mu\text{m}$ size fraction. (a) illustrates a STEM bright field image which shows nanoscale particles in the silicide matrix. (b) illustrates a Nb EDS map of the region depicted in (a). (c) shows a HRTEM micrograph of a Nb-rich precipitate and (d) shows the corresponding FFT diffraction pattern from the box region depicted in (c), indexed to Nb(C,N) [101] zone axis.

4.2.4. Microstructural characterisation of cast Tristelle 5183

Fig. 4.9(a) shows an overlaid, EBSD-derived phase and band contrast distribution map of a representative section from the as-cast alloy. Fig. 4.9(b) shows an inverse pole figure (IPF) orientation map of the same section as Fig. 4.9(a)(c) and (d) are Nb and Si EDS maps of the same areas. Large scale (20-100 μm) Nb(C,N) particles

are present, some of which show a dendritic morphology, whilst others are clusters of crystals with different orientations. These Nb(C,N) crystals are dispersed in a dendritic matrix which is austenite (γ -Fe), shown as the band contrast (light grey background) region of Fig. 4.9(a). Four phases occur in the last regions to solidify (interdendritic regions) which are: M_7C_3 ; bcc α -Fe (ferrite); a fine scale Nb(C,N) phase (Nb-rich and with a script morphology); and a silicide phase, based on the crystallography of $Fe_5Ni_3Si_2$. The silicide phase is generally found next to the α -Fe. The IPF map, Fig. 4.9(b) shows that the austenitic dendritic grain size is large, several hundred microns, consistent with slow cooling in conventional casting. The EDS map for Si (Fig. 4.9(d)) shows that it is preferentially segregated to the α -Fe and silicide regions. The proportions of the different phases in the cast structure, obtained from the EBSD data, are given in Table 4.3.

Table 4.3: Proportions of phases in cast Tristelle 5183 from EBSD-derived data (unindexed indicates fraction of analysed area which could not be assigned to a phase).

Phase	γ	Cr_7C_7	Nb(C,N)	α -Fe	Silicide	Unindexed
Vol%	76	10	7	4	2	1

4.3. DISCUSSION

4.3.1. Mould cast Tristelle 5183

This mould cast sample was obtained by pouring a small melt sample into a ceramic shell mould just prior to melt atomisation. To compare the cooling rate of the mould cast sample with that of the 63-75 μ m powder fraction the secondary dendrite arm spacings of the γ -Fe dendrites were measured. Using Eq. (4.1) below, that relates secondary dendrite arm spacing, λ_s , to cooling rate, $\frac{dT}{dt}$, where K is a constant for the alloy [247]:

$$\lambda_s = K \left(\frac{dT}{dt} \right)^{-0.33} \quad (4.1)$$

It is found that the cooling rate of the mould cast sample is $\sim 10^{-5}$ times that

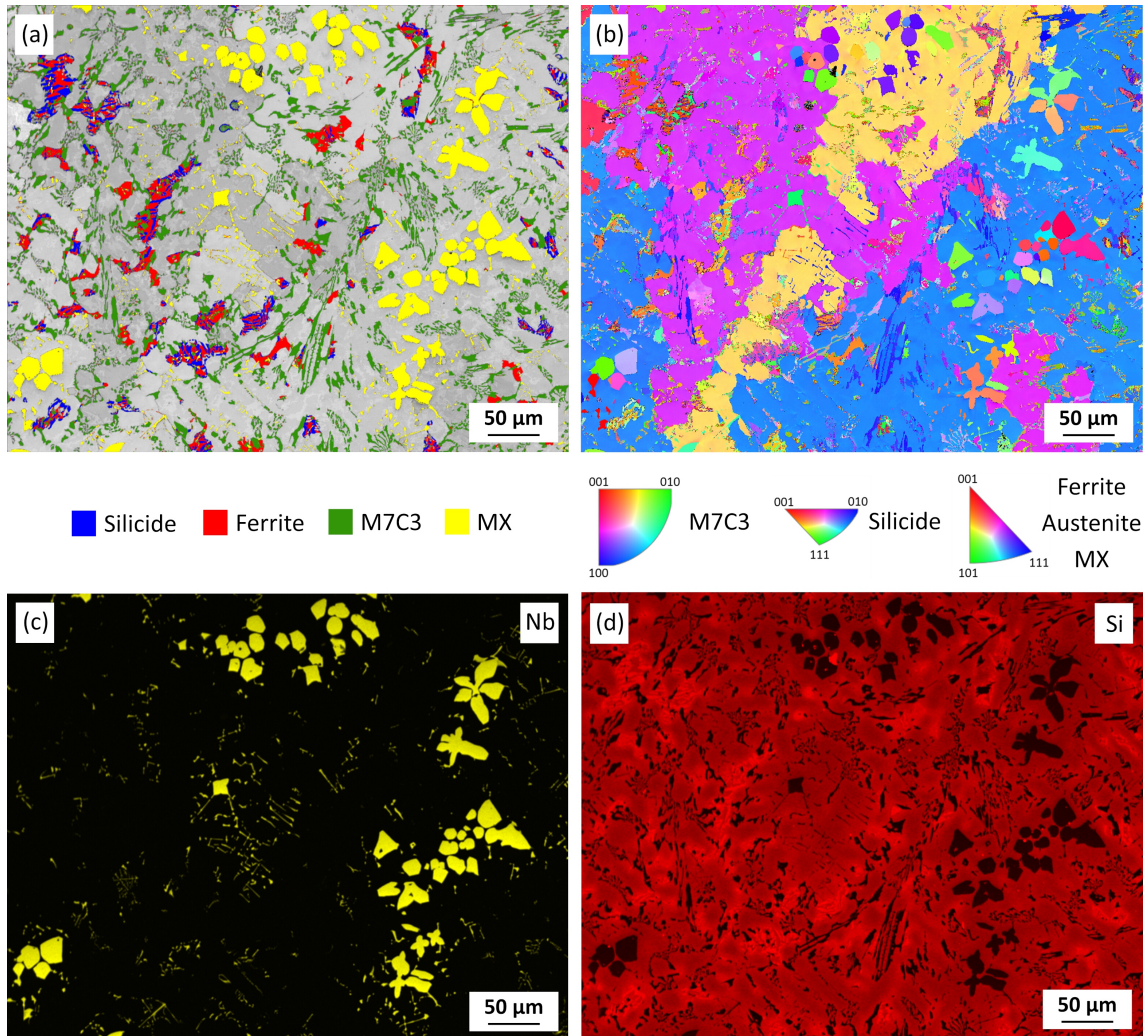
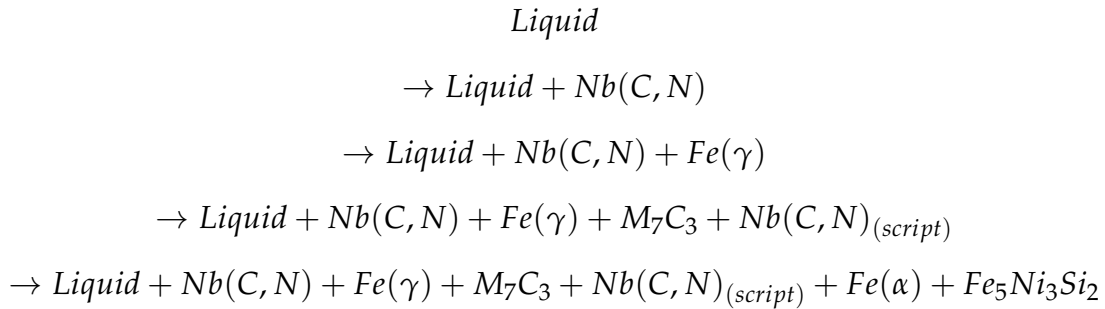


Figure 4.9: Typical microstructure of cast Tristelle 5183 alloy. (a) Shows a phase distribution map overlaid onto a band contrast map derived from EBSD data showing large Nb(C,N) crystals in a γ -Fe dendritic matrix (grey) with interdendritic Cr_7C_3 , Nb(C,N), bcc α -Fe and a phase isostructural to $\text{Fe}_5\text{Ni}_3\text{Si}_2$. (b) shows a IPFY orientation map, where the colours of the grains correspond to the crystallographic axes in the stereographic triangle for each phase. (c) and (d) are EDS maps of Nb and Si respectively confirming that the large crystals are Nb-rich and that Si is preferentially segregated to the interdendritic α -Fe and silicide phases.

of the 63-75 μm powder, i.e. around 0.8 K/s. By careful interpretation of the cast microstructure, the following solidification sequence can be proposed for Tristelle 5183 alloy under slow cooling conditions:



The above sequence implies that the alloy can be regarded as hypereutectic and that the Nb(C,N) phase is the first to solidify (primary phase) with a faceted or, in some cases, dendritic morphology. These coarse Nb(C,N) particles are in some cases up to 100 μm in size and some agglomerates are seen. This could be because the alloy charge in the atomisation crucible was below the liquidus temperature (i.e. in the L + Nb(C,N) phase field) when the sample was taken for casting. In order to assess the feasibility of this interpretation, the liquidus temperature of Tristelle 5183 was calculated using ThermoCalc [248] and the TCFE7 steels database (Fig. 4.10). The liquidus temperature of the alloy, i.e. the temperature for the reaction $L \rightarrow L + \text{Nb}(\text{C}, \text{N})$, is found to be $\sim 1700^\circ\text{C}$ (Fig. 4.10). This is above the probable processing temperature of the melt in the crucible and therefore supports the hypothesis that some large carbides pre-existed in the alloy charge prior to gas atomisation and could well have agglomerated during the holding time.

Under the slow cooling conditions of mould casting it is evident that solidification continues with the nucleation and growth of dendritic γ -Fe phase. From the EBSD inverse pole figure (IPF) map, Fig. 4.9, it is evident that the γ -Fe grain size is large, i.e. there are relatively few nucleation events, suggesting that Nb(C,N) particles do not act as potent nucleation sites for the γ -Fe phase. However, the coarse Nb(C,N) particles are not apparently pushed by the solidifying dendrites into interdendritic regions but instead the γ -Fe dendrites engulf the Nb(C,N) as they grow.

It is apparent from the microstructure that the M_7C_3 phase is the next significant

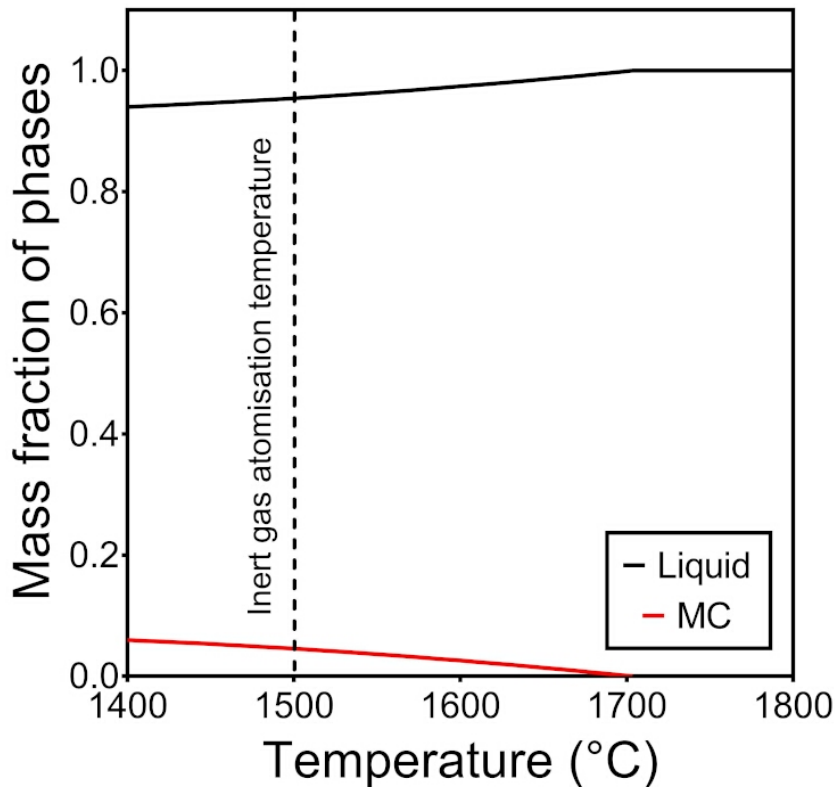


Figure 4.10: Phase fraction diagram for Tristelle 5183 calculated using ThermoCalc [248] and the TcFe7 database.

phase to precipitate out on continued cooling as it is located in the interdendritic regions and has a volume fraction (Table 4.3) of almost 10 vol%. Other phases which are observed in the latter regions to solidify are Nb(C,N) (with a Chinese script-shaped morphology), α -Fe, and a silicide phase isostructural with $\text{Fe}_5\text{Ni}_3\text{Si}_2$ but whose precise composition is uncertain. The morphology of the interdendritic Nb(C,N) clearly indicates that it formed by solidification. However, it is currently unclear whether α -Fe and $\text{Fe}_5\text{Ni}_3\text{Si}_2$ both form by solidification or whether α -Fe forms from the melt and $\text{Fe}_5\text{Ni}_3\text{Si}_2$ forms subsequently by a solid state transformation at a lower temperature.

4.3.2. Phase selection and microstructure formation in gas atomised Tristelle 5183 powder particles

4.3.2.1. Cooling rate considerations

As described by Yule and Dunkley [97], the cooling rate, $\frac{dT_d}{dt}$, of a liquid droplet in the gas atomisation process, prior to the onset of solidification, can be estimated from the well-known heat flow equations as follows, providing a number of simplifying assumptions are made as discussed in 4.3.3:

$$\frac{dT_d}{dt} = - \left(\frac{6h}{D\rho_d c_{p_d}} \right) (T_d - T_g) \quad (4.2)$$

where h is the heat transfer coefficient between the droplet and the atomising gas (h is a function of the dimensionless Nusselt number), T_d is the droplet temperature, T_g is the gas temperature, D is the droplet diameter, ρ_d is the density of the droplet and c_{p_d} is the specific heat of the liquid droplet ($Jkg^{-1}K^{-1}$). Details of the assumptions and thermophysical parameters employed for nitrogen gas-atomised Tristelle 5183 are given in 4.3.3. The calculations set out in section 4.3.3 reveal that the cooling rate of a 20 μm droplet is $\sim 7 \times 10^5$ K/s and that of a 75 μm droplet is $\sim 8 \times 10^4$ K/s assuming relative gas velocity of 40 m/s. However, the dominating factor is droplet diameter and clearly the two size fractions examined in detail in this work ($< 20 \mu m$ and 63-75 μm) have cooling rates that differ by approximately an order of magnitude, with this difference being relatively insensitive to other assumptions including that of relative gas velocity and gas temperature.

4.3.2.2. MX formation

It is evident from the XRD patterns, Fig. 4.1, that the MX phase is present in all powder size fractions. Furthermore, the detailed microstructural examination of powder cross-sections from the < 20 and 63-75 μm size fractions confirmed the presence of Nb(C,N) particles of significantly different sizes. This is strong evidence that the MX populations identified by XRD correlate directly with the Nb(C,N) particles identified by microscopy and EDX analysis.

In, for example, the 63-75 μm powder fraction, large pre-existing Nb(C,N) particles are clearly observed in a number of particle cross sections (Fig. 4.4(a) and (d)). The size and, in some cases, rounded morphology of such particles strongly

suggests that they did not form during the rapid solidification conditions imposed by gas atomisation. It seems more likely that they were present in the melt prior to gas atomisation as explained in 4.3.1 for the mould cast sample. Subsequently, we refer to these particles as pre-existing Nb(C,N). These pre-existing particles can be seen in all the powder size fractions but are more frequently observed in the larger powder size fractions. This further supports the hypothesis that large Nb(C,N) particles pre-existed in the alloy charge prior to atomisation as, during atomisation, there is a greater statistical likelihood of small powder particles being free from large Nb(C,N) particles.

Finer scale (both micron and nano-scale) Nb(C,N) particles are also evident in all the powder particles investigated through electron microscopy. It seems most likely that these nucleated from the melt and remained small due to the limited time available for growth during the atomisation process. A more detailed interpretation of the formation of these fine scale carbides, termed primary and secondary Nb(C,N) is discussed below.

XRD (Fig. 4.1) has allowed the identification of three different MX-type carbonitride populations, all of which are crystallographically consistent with Nb(C,N). We now argue that the MX populations are related to the three Nb(C,N) particle populations observed by SEM/TEM in the powder, namely (i) the pre-existing Nb(C,N), (ii) the micron-sized primary Nb(C,N), and (iii) the nano-scale secondary Nb(C,N). The sharp peak shapes and preferred orientation associated with the MX-1 population are indicative of a carbonitride that is both equilibrated and microstructurally sparse. The MX-1 population exhibits a lattice parameter of ~ 0.446 nm that is close to the value of 0.447 nm reported by Storms et al. [249] for stoichiometric NbC. Therefore, the XRD peak contributions identified as MX-1 are most likely to result from the pre-existing Nb(C,N) population that formed under near equilibrium conditions. The broad and somewhat asymmetric nature of the XRD peaks identified as MX-2 are characteristic of a population that has precipitated out and grown during solidification; it is expected that both the composition and lattice parameter increasingly deviate away from equilibrium due to compositional segregation effects during growth. The MX-2 population has an

averaged approximate lattice parameter of ~ 0.444 nm which, in accord with the work of Storms et al. [249], is typical of a niobium carbide which has formed under conditions which notably deviate from equilibrium. In light of the above, the MX-2 population is attributed to the primary micron-sized Nb(C,N) (identified through electron microscopy) that precipitated directly from the melt prior to iron-matrix phase nucleation. The lattice parameter of the MX-3 population decreases with increasing cooling rate and is significantly smaller than those of the other two MX populations; notably, it decreases from ~ 0.438 to ~ 0.432 nm as the powder size decreases i.e. as the cooling rate increases. The increasing deviation from the equilibrium value would indicate that this MX-3 population formed far from equilibrium during droplet solidification and crystals are carbon deficient with respect to the stoichiometric NbC formula [249]. The sensitivity to cooling rate and high deviation from equilibrium could suggest that the MX-3 population is consistent with the nano-scale Nb(C,N) particles which precipitate out in the very last stages of solidification.

4.3.2.3. Effect of powder particle size on solidification behaviour

The solidification path taken by Tristelle 5183 is clearly different for different powder size fractions as has been revealed by the variation in the XRD patterns presented in Fig. 4.1 and further supported by the more detailed microstructural examination of the < 20 and $63\text{-}75$ μm powder size fractions. There are two important phenomena to consider before discussing the detail of microstructural evolution. First, there is the well-known increase in cooling rate during gas atomisation with decreasing droplet diameter [97, 231]. Secondly, the sub-division of the melt during atomisation leads to finer droplets being less likely to contain potent heterogeneous nuclei. The combined effect is that finer droplets are more likely to achieve larger undercoolings before solid phase nucleation occurs and so are more likely to solidify directly to metastable phases rather than forming equilibrium phases on cooling.

It is apparent from Fig. 4.1 that powder size fractions of $53\text{-}63$ μm and above form predominantly γ -Fe with smaller amounts of MX, γ -Fe, and silicide phases.

It is evident that the solidification pathway is markedly different from that of the mould cast sample as M_7C_3 formation has been wholly suppressed. Under the constraint of either slow nucleation or growth kinetics, stable phases may be suppressed at higher cooling rates and metastable equilibria may develop [250]. The suppression of M_7C_3 is believed to be due to its slow nucleation and growth kinetics as it has a complex crystal structure. Additionally, the dendrite arm spacing is significantly refined compared to the mould cast sample with an average value $\sim 0.7 \mu\text{m}$ (Fig. 4.4(c-d)) compared with $\sim 18 \mu\text{m}$ (Fig. 4.9) in the mould cast sample. It is also notable that in Fig. 4.4 a clear distinction between pre-existing Nb(C,N) (up to $20 \mu\text{m}$) and primary Nb(C,N) (micron sized) can be seen, with the latter presumably nucleating from the melt during cooling. Fig. 4.4(b) shows the entrainment of primary Nb(C,N) within the γ -Fe dendrites due to the high initial growth rate of the latter immediately following nucleation. Solute elements Cr, Nb, Si and C are all rejected from the γ -phase dendrites during solidification into the interdendritic liquid which must then solidify in the post-recalescence stage of droplet cooling [231]. This leads to the formation of the nanoscale interdendritic particles seen in Fig. 4.4(b) and which TEM (Fig. 4.5) shows to be Nb(C,N) and which we refer to as secondary Nb(C,N). These particles are surrounded by an additional (distinct) interdendritic phase which has the crystallography of $\text{Fe}_5\text{Ni}_3\text{Si}_2$ but which contains significant Cr. This interdendritic silicide phase is seen to be significantly Cr-enriched compared with the γ -Fe dendrites and this can be attributed to the Cr rejection from the γ -phase dendrites.

In the case of powder size fractions below the 45-53 μm range, it is clear from Fig. 4.1 that increasing quantities of bcc α -Fe and silicide phase form with decreasing powder particle size range. This is confirmed by the quantitative Rietveld analysis data shown in Fig. 4.3. In general, it is through that the deep undercooling of the liquid during atomisation makes it possible to access the formation of one or more metastable phases [250–252], this is clearly possible in this alloy system for sufficiently high cooling rates of droplets. The formation of α -Fe directly from the melt in the present alloy is consistent with previous work involving fine powder particles of binary or ternary austenitic iron-based

alloys which were gas atomised and rapidly cooled [253, 254]. Both of these groups have reported the formation of bcc or α -Fe as the crystallization phase in the smaller powder (more rapidly cooled) particles whilst fcc or γ -Fe was the crystallization phase in larger diameter (more slowly cooled) particles. Typically, after one metastable phase nucleates, the rapid release of the heat of fusion causes droplet recalescence and this can allow the nucleation of another metastable phase at a somewhat higher temperature [250–252]. This phenomenon is revealed by the microstructure shown Fig. 4.6 (a cross section of a particle from the $< 20 \mu\text{m}$ size range) where it would appear that α -Fe nucleated at a deep undercooling but its growth into the liquid was terminated by the nucleation and growth of the silicide phase from another location in the droplet. However, micron-sized Nb(C,N) particles are still evident in the microstructure suggesting that the cooling rate was not sufficiently rapid to suppress the formation of this stable phase. The detailed microstructure in a particle such as this is shown in the TEM images, Figs. 4.7 and 4.8, where it can also be seen that fine scale Nb(C,N) particles also form. Primary angular Nb(C,N) particles appear to have been engulfed by the silicide phase whilst much finer 20 to 50 nm sized secondary Nb(C,N) particles are seen (Fig. 4.8) in the last to solidify cell boundaries. The silicide phase (Table 4.3) is close in composition to that reported by Bowden [163].

In the gas atomisation process a liquid metal stream is broken up into droplets by impinging gas jets [97]. The gas stream is turbulent, and this causes a stochastic dispersion of liquid droplets of different sizes to form. However, the cooling rate of a given size of droplet will depend not only on its diameter. The cooling rate will also be affected by the trajectory a droplet follows in the turbulent gas stream. The consequence of this is that, even in powder particles of similar diameters, different microstructures can be expected. XRD patterns, which arise from the collection of diffracted X-rays from large numbers of individual particles, obviously capture this stochastic variability in phase selection and represent average characteristics of a powder size fraction. In contrast, microscopy permits imaging of only limited numbers of individual particles and, indeed, planar sections through them.

Overall, it is evident that in this complex alloy system, metastable phases can

form in small diameter particles as a result of the high cooling rates to which they are subject. In the manufacture of critical components from HIP consolidated powder it is potentially important to avoid microstructural variability in the powder. The current study demonstrates, therefore, that the classification of atomised powder should be considered prior to HIPing in an effort to avoid the inclusion of particles containing the non-equilibrium microstructures that may degrade the performance of HIPed components.

4.3.3. Analytical droplet cooling rate model

The purpose of this section is to outline clearly the assumptions that have been made in the derivation of a simple model for droplet cooling rate. In the context of this work, the sole purpose of such a model is to establish an order of magnitude approximation for droplet cooling rate for a range of droplet sizes and relative velocities between the gas and droplets.

In practice, the flow pattern of the gas stream and entrained droplets is complex and inherently turbulent in nature. The precise details of the flow field are heavily dependent on the design and operational features of the gas atomiser. Important aspects of the flow field, the physics of break-up of the liquid stream and droplets, the interaction (or coupling) of momentum and energy between the gas and droplet flows have all been addressed in recent computational fluid dynamics studies [255,256]. These features are neglected by the simple heat flow model.

As molten droplets pass through the cooler gas stream, heat is lost via both convective and radiative heat transfer. Particles are assumed to remain spherical throughout atomisation moreover, this assumption has been widely verified in the case of gas atomisation with nitrogen, argon and helium. Additionally, the particle surface is assumed to be smooth and roughening effects, for example the dendritic surface roughness, have been ignored. The droplet size range of interest in the present study is approximately 1-100 μm . The mean relative velocity between droplets and the gas stream is likely to be in the range of a few tens to a few hundred m/s for the majority of particles [97]. The relative velocity will change with time but Clyne et al. [257] suggest this will have a relatively minor effect

on the rate of heat transfer from a particle. It has been shown in references [97] and [257] that, for typical gas atomiser operation, the convective heat transfer between the particles and the gas dominates such that radiative heat transfer can be safely ignored. A further significant assumption of the present model is that the gas temperature is taken to be constant (293 K). This assumption does not reflect actual operating conditions in that the atomising gas will heat up during production to an extent governed by the processing conditions.

As a result of the simplifying assumptions detailed above, the interaction between heat exchange and fluid flow can be understood in terms of the dimensionless groups listed in equations Eqs. (4.3) to (4.5) (symbols are defined in the nomenclature table (Table 4.5)).

$$Nu_d = \frac{hD}{k_g} \quad (4.3)$$

$$Re_D = \frac{\Delta U \rho_g D}{\mu_g} \quad (4.4)$$

$$Pr = \frac{c_{p_g} \mu_g}{k_g} \quad (4.5)$$

The heat transfer coefficient can be evaluated through its relationship with the Nusselt number (Nu_D). With respect to a spherical particle in a gas flow with a Reynolds number (Re_D) between $0 \leq Re_D \leq 103$, the work of Ranz and Marshall [258] has shown that:

$$Nu_d = 2 + 0.6Re_D^{0.5}Pr^{0.33} \quad (4.6)$$

The inherently low Prandtl number of nitrogen (on which the Nusselt number and heat transfer coefficient depend through Eq. (4.6)) and small droplet dimensions associated with gas atomisation suggest that the convective heat transfer within droplets is negligible and the cooling conditions are such that individual droplets can be assumed to be instantaneously isothermal (at least prior to the onset of solidification i.e. before the latent heat of fusion begins to be released).

This condition is satisfied when the Biot number (Eq. (4.7)) is < 0.1 .

$$Bi = \frac{hD}{k_p} \quad (4.7)$$

In the present situation, the Biot number for a $100 \mu\text{m}$ powder particle (i.e. the largest considered) ranges from 0.015 to 0.042 for gas velocities in the range 20 to 320 m/s. Hence the assumption of negligible thermal gradient within powder particles is valid. The heat transfer rate, which is assumed to be dominated by convection during gas atomisation, can be expressed in terms of the heat transfer coefficient as follows:

$$Q_c = \pi D^2 h (T_p - T_g) \quad (4.8)$$

The substitution and rearrangement of the above equations gives the following expression for the heat transfer coefficient:

$$h = \frac{2k_g}{D} + 0.6 \left(\frac{\Delta\rho_g}{D} \right)^{0.5} \mu_g^{-0.17} c_{p_g}^{0.33} k_g^{0.67} \quad (4.9)$$

The heat balance equation at the surface of a spherical droplet therefore leads to the following expression for the droplet cooling rate:

$$\frac{dT_p}{dt} = - \left(\frac{6h}{D\rho_p c_{p_p}} \right) (T_p - T_g) \quad (4.10)$$

Values of the thermophysical parameters used in the calculation of the cooling rate of droplets are given in Table 4.4. It is assumed that the thermophysical properties of Tristelle 5183 can be approximated by the 316 grade of austenitic stainless steel because the composition of 316 is similar to that of the iron matrix of Tristelle 5183. The cooling rates which have been calculated are for 316 stainless steel at its liquidus temperature (1660 K) and are displayed in Fig. 4.11.

The cooling rates reported in Fig. 4.11 are in line with those computed by an identical heat flow model in references [231, 259]. The latter considered an iron-based alloy and computed a cooling rate of 7×10^4 K/s for a $100 \mu\text{m}$ particle which is similar to that found here. In reference [259], aluminium droplets were

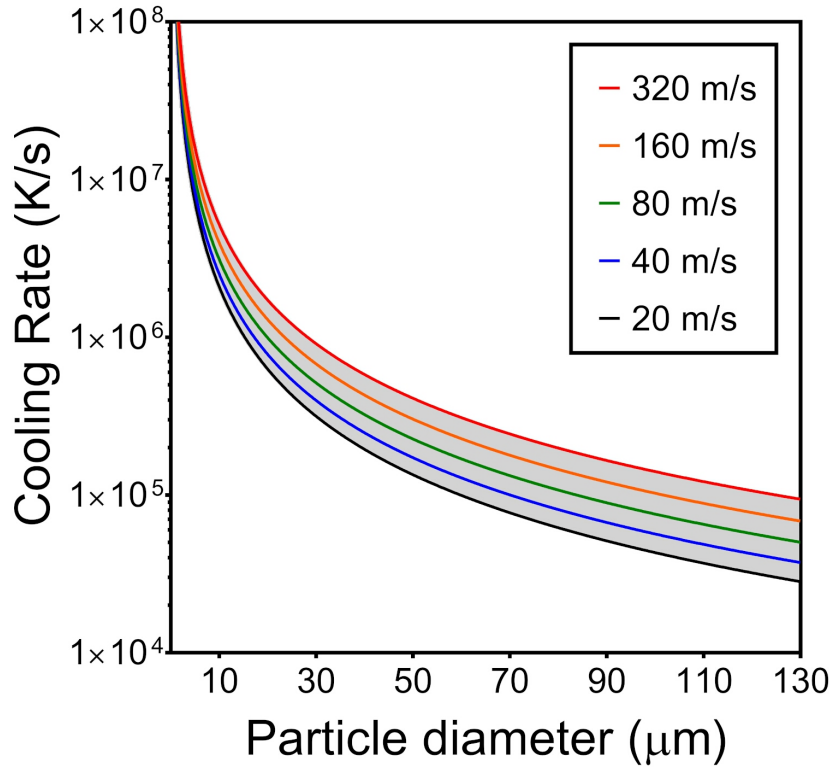


Figure 4.11: Plots of cooling rate versus particle diameter during nitrogen gas atomisation for different relative gas velocities. The cooling rate is calculated at the liquidus temperature of 316 stainless steel.

modelled (nitrogen atomising gas and a 100 m/s relative velocity) and a cooling rate of 1×10^5 K/s was calculated for a 100 μm droplet which is also consistent with the current approach allowing for the different thermophysical properties of aluminium. Measurements of droplet cooling rates are sparse and limited to estimates derived from secondary dendrite arm spacing measurements of the solidification microstructures. This measurement approach, which is thoroughly discussed in reference [233] in relation to Al-Cu alloys, has many limitations. However, Mullis et al. [233] conclude that cooling rates estimated by this method are at the low end of those predicted from analytical heat flow models and that low gas-particle relative velocities (ΔU) are the likely explanation. Therefore, the cooling rates we use in the paper are based on a 20 m/s value for ΔU .

Table 4.4: Data for heat transfer coefficient and cooling rate calculations for nitrogen gas atomisation Tristelle 5183 (1 atm pressure)

Symbol	Value	Name
c_{p_g}	$1040 \text{ Jkg}^{-1}\text{K}^{-1}$	Specific heat of nitrogen at NTP
c_{p_p}	$510 \text{ Jkg}^{-1}\text{K}^{-1}$	Specific heat of 316 stainless steel
ρ_g	1.165 kgm^{-3}	Density of nitrogen at NPT
ρ_p	7900 kgm^{-3}	Density of 316 stainless steel
μ_g	$1.75 \times 10^{-5} \text{ Nsm}^{-2}$	Dynamic viscosity of nitrogen at NPT
k_g	$0.026 \text{ Wm}^{-1}\text{K}^{-1}$	Thermal conductivity of nitrogen at NPT
T_g	293.15 K	Gas temperature

Table 4.5: Nomenclature defining the symbols used in the analytical droplet cooling rate model.

Symbol	Unit	Name
Bi	–	Biot number
c_{p_p}	$\text{Jkg}^{-1}\text{K}^{-1}$	Specific heat at constant pressure for the particle
c_{p_g}	$\text{Jkg}^{-1}\text{K}^{-1}$	Specific heat at constant pressure for the gas
D	m	Diameter of the particle
h	$\text{Wm}^{-2}\text{K}^{-1}$	Heat transfer coefficient
k_g	$\text{Wm}^{-1}\text{K}^{-1}$	Thermal conductivity of the gas
k_p	$\text{Wm}^{-1}\text{K}^{-1}$	Thermal conductivity of the particle
Nu_D	–	Nusselt number
Pr	–	Prandtl number
Q_c	W	Convective heat transfer rate
Re_D	–	Reynolds number
T_g	K	Temperature of gas
T_p	K	Temperature of particle
T_L	K	Liquidus temperature
t	s	Time
ΔU	ms^{-1}	relative velocity between the gas and particle
μ_g	$kg s^{-1} m^{-1}$	Dynamic viscosity of the gas
ρ_g	$kg m^{-3}$	Density of the gas
ρ_p	$kg m^{-3}$	Density of the particle

4.4. CONCLUSIONS

1. Gas atomised powders of Tristelle 5183 (Fe-21%Cr-10%Ni-7%Nb-5%Si-2%C in wt%) exhibit phase proportions which change with powder particle size

range i.e. cooling rate. Estimates of the cooling rate of liquid droplets indicate a change from approximately 8×10^4 to 7×10^5 K/s for droplet sizes of 75 and 20 μm respectively.

2. Particles of diameter greater than approximately 53 μm contain dendritic fcc $\gamma\text{-Fe}$ as the principal phase with smaller quantities of $\alpha\text{-Fe}$, an interdendritic silicide phase isostructural to $\text{Fe}_5\text{Ni}_3\text{Si}_2$ and $\sim 5\%$ Nb(C,N) . Particles $< 53 \mu\text{m}$ have increasing quantities of either dendritic $\alpha\text{-Fe}$ or cellular silicide phase with decreasing amounts of $\gamma\text{-Fe}$ as the particle size decreases, along with $\sim 5\%$ Nb(C,N) .
3. Coarse ($> 10 \mu\text{m}$) sized Nb(C,N) particles, seen in all powder size fractions, pre-existed in the melt prior to atomisation, whereas micron-sized Nb(C,N) that are found within $\alpha\text{-Fe}$, $\gamma\text{-Fe}$ or silicide are the primary solidification phase. Nanoscale Nb(C,N) also formed interdendritically, or in the cell boundaries of the silicide phase, in the last stages of solidification.
4. The Nb(C,N) XRD reflections from the gas atomised powders have been deconvoluted into three populations related to the three distinct Nb(C,N) morphologies. It is argued that one set of crystals consistent with the Nb(C,N) phase formed under near-equilibrium conditions whereas the other two populations formed under non-equilibrium conditions and appear to be carbon deficient with respect to stoichiometric Nb(C,N) .
5. The increasing quantities of $\alpha\text{-Fe}$ and silicide in smaller sized powder particles is consistent with increased undercooling prior to nucleation permitting metastable phase formation.
6. Rapid solidification processing significantly alters the solidification pathway of this alloy with the complete disappearance of an M_7C_3 phase which is found in significant quantities in a conventional mould cast sample which forms NbC , $\gamma\text{-Fe}$, M_7C_3 , $\alpha\text{-Fe}$ and silicide phase in the as-cast condition.

MICROSTRUCTURAL CHARACTERISATION OF HOT ISOSTATICALLY PRESSED TRISTELLE 5183

5.1. INTRODUCTION

This chapter aims to characterise the microstructure of commercially produced HIPed Tristelle 5183 and develop an understanding of the phase and microstructure evolution which take place during HIPing. Although HIPed Tristelle 5183 is used within the primary cooling systems of PWRs [10, 224], there currently exists very little published work which presents detailed alloy characterisation. To date, only two studies exist within the literature which attempt to provide a more detailed microstructural evaluation of HIPed Tristelle 5183 [7, 222], however, there appears to be some discrepancy in the identification of the minor intermetallic and/or carbide phases within the HIPed alloy. More in-depth characterisation of HIPed Tristelle 5183 is important as otherwise, without an overarching metallurgical and microstructural understanding of the existing Fe-based hardfacing alloys such as Tristelle 5183, the future development of new and improved Fe-based hardfacings is significantly hindered. Additionally, the in-depth characterisation of HIPed Tristelle 5183 is required prior to evaluating its tribological performance (Chapter 7).

5.2. RESULTS

HIPed Tristelle 5183 has a macrohardness of $350 \pm 1 \text{ Hv}_{20}$ ($n = 8$) and a density of $7504.9 \pm 5.0 \text{ kg/m}^3$ ($n = 3$). These values are reported as the mean \pm standard error of the mean.

5.2.1. Phase identification using XRD

Fig. 5.1 shows an X-ray diffractogram from the polished surface of as-received, HIPed Tristelle 5183. It has an fcc austenitic γ -Fe solid solution (Fm3m space group) as the major phase with smaller amounts of the following: orthorhombic M_7C_3 type carbide (basic structure in the Pmcn space group); MX type B1 phase (Fm3m space group with a lattice parameter extremely close to that of NbC); bcc ferritic α -Fe (Im3m space group) and traces of a cubic π -ferrosilicide phase, the crystallography of which has been reported by Bowden et al. [163] (P2₁3 space group). The phase fractions of as-received Tristelle and the lattice parameters of these phases were determined via Rietveld analysis and reported in Table 5.1.

Table 5.1: Phase fractions and lattice parameters of phases identified within Tristelle 5183 determined via Rietveld analysis.

	γ -Fe	M_7C_3	MX	α -Fe	π -ferrosilicide
wt%	76.1	12.7	9.9	1.0	0.3
vol%	75.1	14.0	9.6	1.0	0.3
		a = 0.4505			
Lattice Parameters (nm)	0.3582	b = 0.7002	0.4461	0.2859	0.6128
		c = 1.2130			

5.2.2. Microstructural characterisation - Optical microscopy

Fig. 5.2 shows an optical micrograph of a sample etched in a mixture of 10 ml nitric acid, 10 ml acetic acid, 15 ml hydrochloric acid and 2-5 drops of glycerol. Large ($\sim 5 - 20 \mu\text{m}$) and small micro-scale precipitates are prevalent throughout the microstructure and these features are presumably the carbide phases identified by XRD. The etching also reveals microstructural features known as prior particle boundaries (PPBs) which arise during the compaction of gas atomised powders. These PPBs are revealed by discontinuous chains of heavily etched sub-micron sized dark contrast features which could be either micro-scale pores and/or oxygen-based particles that form in response to HIPing of the original gas atomised powder [224]. Etching has also clearly revealed some matrix phase grain boundaries within individual powder particles .

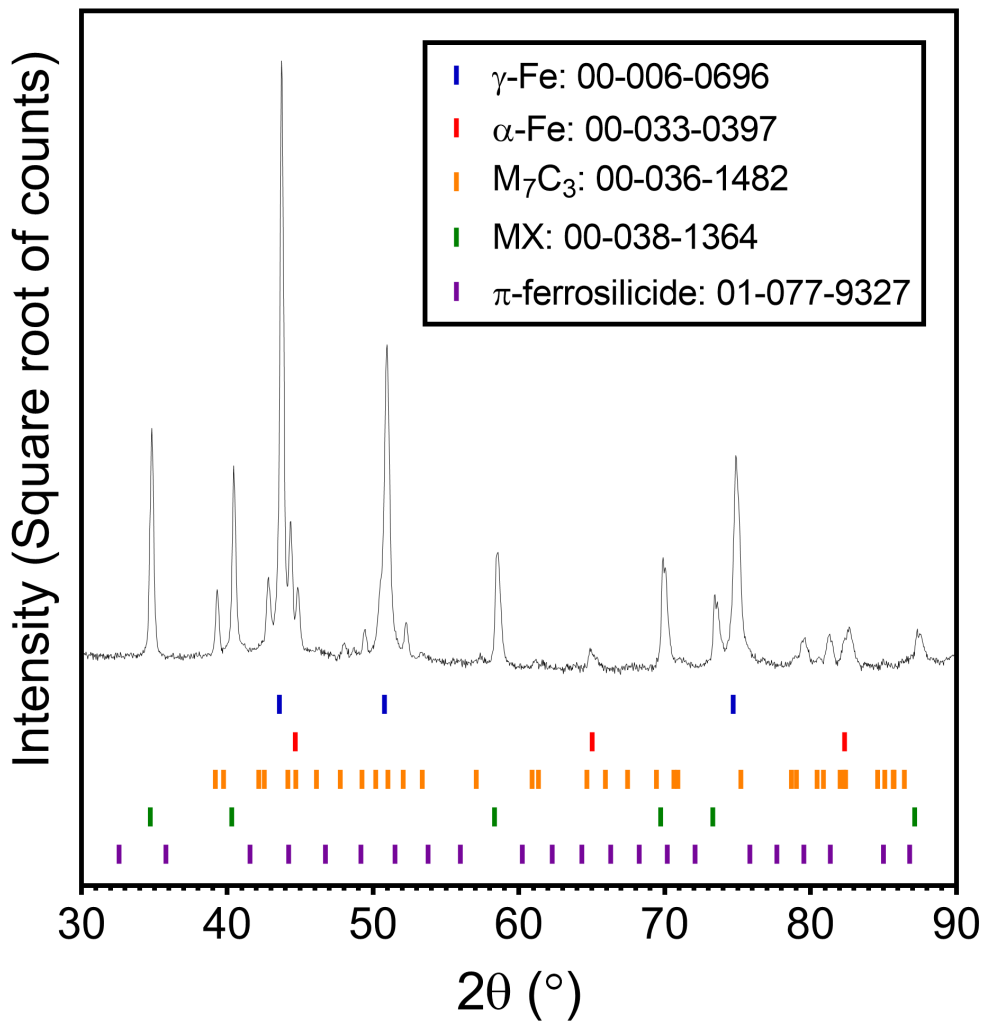


Figure 5.1: XRD pattern obtained from the polished surface of the as-received, HIPed Tristelle 5183. The ICDD database files used to index the diffractogram are shown in the legend. Tristelle 5183 exhibits reflections for γ -Fe (fcc), M_7C_3 , NbC (MX), α -Fe (bcc), and a trace of π -ferrosilicide.

5.2.3. Microstructural characterisation - SEM

Fig. 5.3 (a-c) show representative BSE-SEM micrographs of the HIPed microstructure. The EDX maps, Fig. 5.3 (d-h), are from the same region depicted in Fig. 5.3 (c). The matrix and carbide precipitate phases are clearly distinguishable and can be correlated with phases identified by XRD (Fig. 5.1). The bright-contrast features in the BSE micrographs (Fig. 5.3 (a-c)) are clearly Nb-rich (Fig. 5.3 (h)) and are thus consistent with the MX phase (Fig. 5.1). This phase has a bimodal size distribution and the majority of the precipitates are $< 2 \mu\text{m}$ in size and have a

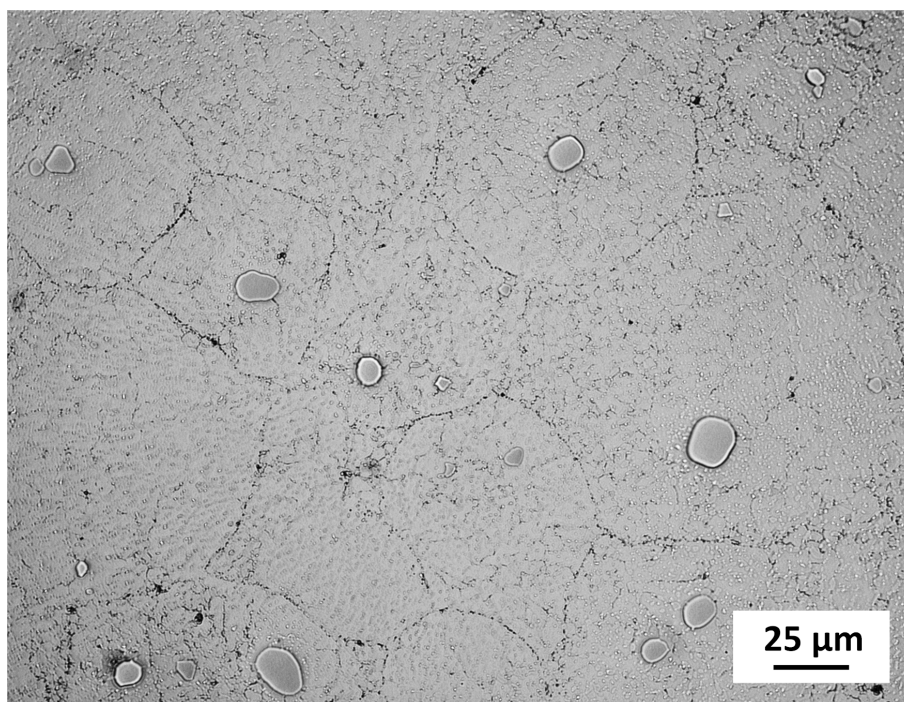


Figure 5.2: Optical micrograph of etched HIPed Tristelle 5183 revealing prior particle boundaries, carbide precipitates and matrix phase grain boundaries.

somewhat spheroidised morphology. However, a small fraction is significantly larger ranging in size between $\sim 5 - 20 \mu\text{m}$ and exhibit a combination of both globular and angular morphologies (Fig. 5.3 (a)). The larger MX (NbC) particles principally form in the melt stage prior to gas atomisation whereas the finer ones precipitate out during gas atomisation and HIPing [260] (Chapter 4). The dark contrast features ($\sim 1-5 \mu\text{m}$ in size) evident in Fig. 5.3 (b-c) are Cr-rich (Fig. 5.3 (e)) and correspond to the M_7C_3 phase. This phase is not observed in the gas atomised powder and must therefore precipitate out during HIPing. Based on the phase fractions identified in XRD, the grey contrast matrix is principally γ -Fe with contrast variation arising from channelling contrast as well as a small fraction of the α -Fe and π -ferrosilicide phases. Inspection of the BSE micrographs (Fig. 5.3 (a-c)) shows that the matrix grain size has a wide distribution, and whilst the average grain size is small, some grains are large relative to the other microstructural features within the HIPed alloy. The small fraction of the π -ferrosilicide phase can be identified in the EDX maps as Si (Fig. 5.3 (f)) and Cr (Fig. 5.3 (e)) rich, and Fe (Fig. 5.3 (d)) depleted relative to the surrounding matrix.

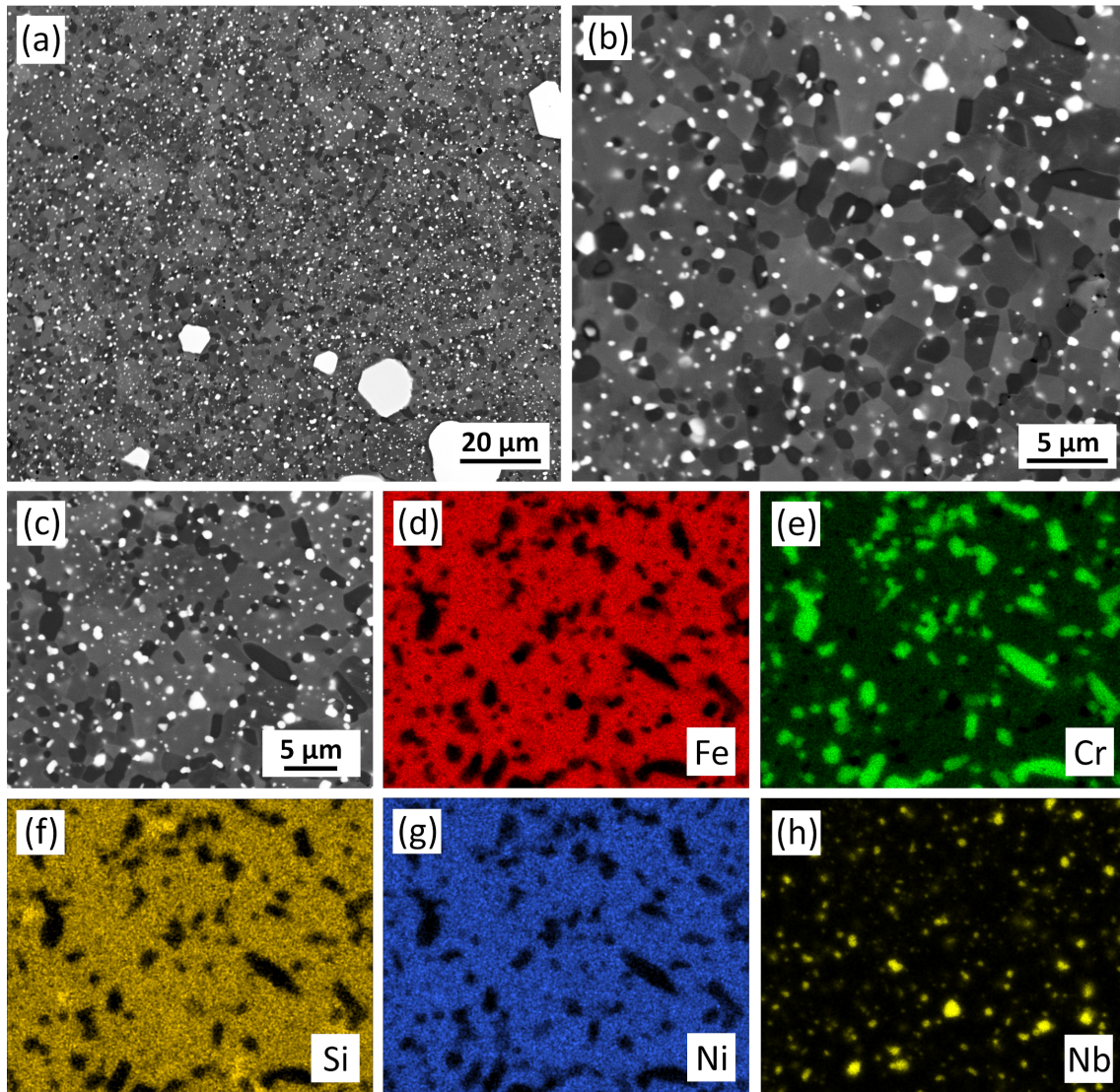


Figure 5.3: BSE-SEM micrographs (a-c) and EDX maps (d-h) depicting the microstructural detail of as-received HIPed Tristelle 5183. The BSE-SEM micrographs show MX precipitates (bright contrast), M_7C_3 carbides (darkest contrast) and matrix grains (varying grey contrast) which are principally γ -Fe. The EDX maps (d), (e), (f), (g) and (h) are from the same region shown in (c) and are maps for Fe, Cr, Si, Ni and Nb respectively.

Fig. 5.4 shows BSE-SEM micrographs exhibiting dark contrast features between ~ 0.1 and $0.3 \mu\text{m}$ in size, indicated by red arrows in Fig. 5.4 (b), which delineate the prior particle boundaries within the HIPed microstructure. These features are consistent with those identified by optical microscopy (Fig. 5.2), but in this case from unetched samples. Given the oxygen sensitivity of the alloy during thermal processing, it seems more probable that these particular features are networks of oxide inclusions rather than pores. Their dark contrast is in keeping with this

hypothesis and they clearly have a low mean atomic number which is consistent with the presence of oxide-rich inclusions.

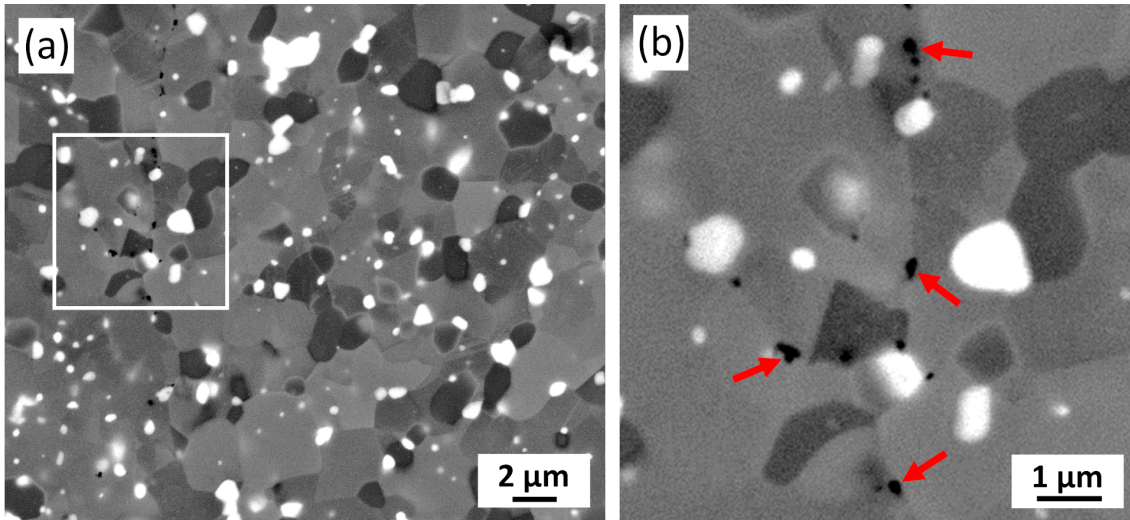


Figure 5.4: BSE-SEM micrographs depicting dark contrast (low mean atomic number) precipitates which reveal the prior particle boundaries within HIPed microstructure of Tristelle 5183. (b) shows the boxed region in (a) and the dark contrast precipitates are indicated by red arrows in (b).

Fig. 5.5 (a) and (b) show an EBSD-derived phase map and accompanying inverse pole figure (IPF) respectively of the same region. As previously identified by XRD and SEM, HIPed Tristelle 5183 (Fig. 5.5 (a)) is principally composed of a Fe-based austenitic (fcc) solid solution (blue) which surrounds both M_7C_3 (yellow) and Nb-based MX (green) precipitates. Smaller fractions of ferrite (red) and the π -ferrosilicide phase (pink) have been identified by EBSD and both these phases have a precipitate size typically $< 2 \mu\text{m}$. The compositions of numerous ($n = 6$) γ -Fe grains (identified by EBSD) were measured using EDX and the averaged composition is reported in Table 5.2.

The inverse pole figure orientation map (Fig. 5.5 (b)) shows that the γ -Fe matrix phase contains a large number of annealing twins which are prevalent within smaller grains. Fig. 5.5 (b) also confirms that the grain size of the γ -Fe matrix phase has a wide distribution. More specifically, several regions of distinctly different grain sizes and morphologies appear segregated by PPBs, and the averaged positions of these PPBs are indicated by the superimposed dashed white lines in Fig. 5.5 (b). A large number of γ -Fe grains, specifically larger grains,

exhibit intra-grain misorientations (Fig. 5.5 b). This was further investigated, and Fig. 5.6 depicts a kernel average misorientation (KAM) map of the same region shown in Fig. 5.5 showing the local orientation changes in the γ -Fe grains. This reveals subgrain substructures which are particularly prevalent in larger γ -Fe grains.

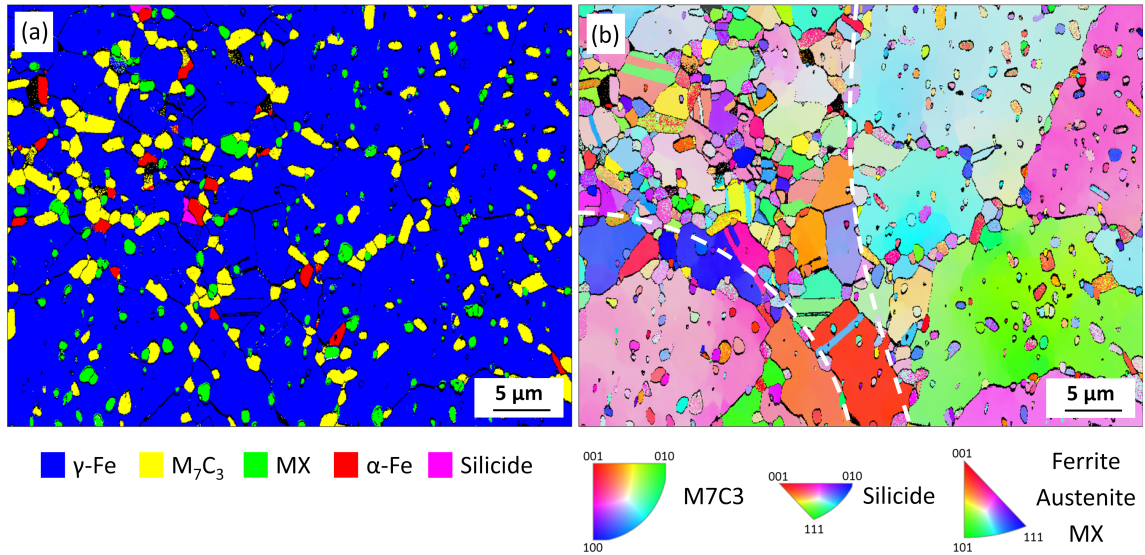


Figure 5.5: EBSD-derived phase and IPFZ orientation maps of the typical microstructure of HIPed Tristelle 5183. The superimposed dashed white lines indicate the averaged positions of prior particle boundaries.

Table 5.2: Composition of γ -Fe in HIPed Tristelle 5183 as determined by EDX-SEM. The results are presented as the mean \pm standard error of the mean (n=6).

	Fe	Cr	Ni	Si	Other
wt%	64.0 \pm 0.2	16.1 \pm 0.1	12.7 \pm 0.1	6.3 \pm 0.1	0.9 \pm 0.2
at%	60.0 \pm 0.2	16.2 \pm 0.1	11.3 \pm 0.1	11.6 \pm 0.1	0.9 \pm 0.2

5.2.4. Microstructural characterisation - TEM

The HAADF-STEM micrograph, Fig. 5.7 (a), shows the microstructural detail of HIPed Tristelle 5183 and Fig. 5.7 (b-f) show accompanying EDX-STEM maps from the same region. In Fig. 5.7 (a), the spheroidised dark contrast ($< 2 \mu\text{m}$) Nb-rich (Fig. 5.7 (f)) particles and bright contrast ($\sim 1 - 2 \mu\text{m}$) Cr-rich (Fig. 5.7 (c)) features

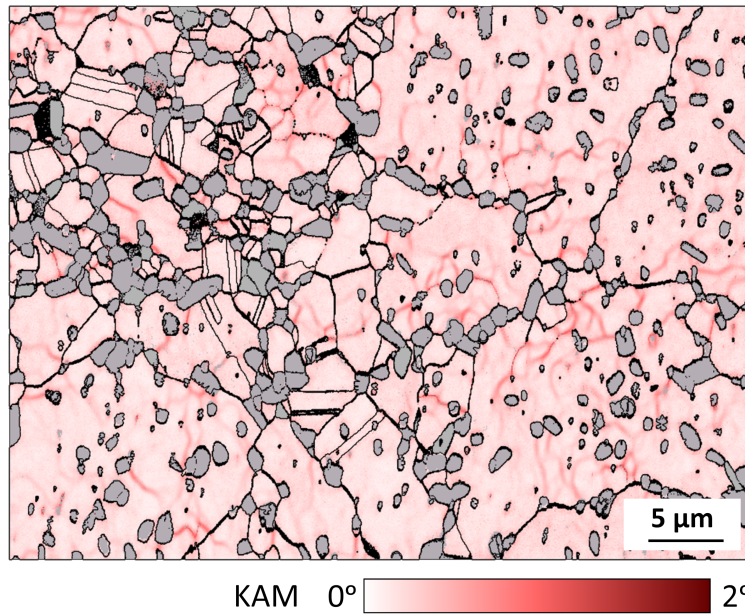


Figure 5.6: EBSD-derived kernel average misorientation (KAM) map of the γ -Fe grains with the HIPed microstructure of Tristelle 5183 revealing the intragrain localised orientation changes and thus subgrain structures. All the other phases within HIPed Tristelle 5183 are shown in grey.

are the MX type carbonitrides and M_7C_3 type carbides respectively, both of which have been confirmed by TEM-SAD and previously identified via XRD (Fig. 5.1), SEM (Fig. 5.3) and EBSD (Fig. 5.5). Fig. 5.7 (a) also reveals a small number of bright contrast features which are believed to be the π -ferrosilicide phase as they are rich in Si (Fig. 5.7 (e)) and Cr (Fig. 5.7 (c)) and depleted in Fe (Fig. 5.7 (b)) and Ni (Fig. 5.7 (d)) relative to the matrix. In this particular instance (Fig. 5.7), the remaining microstructural features are principally γ -Fe. The composition of the γ -Fe and π -ferrosilicide phases have been determined by EDX-STEM and reported in Table 5.3. The composition of the π -ferrosilicide phases is close to that reported by Bowden et al. [163].

Table 5.3: Composition in wt% of the γ -Fe and π -ferrosilicide phases in HIPed Tristelle 5183 as determined by EDX-STEM. The results are presented as the mean \pm standard error of the mean ($n_\gamma = 6$, $n_\pi = 1$).

Phase	Fe	Cr	Ni	Si
γ -Fe (wt%)	66.1 ± 0.3	15.8 ± 0.2	12.0 ± 0.2	6.1 ± 0.1
π -ferrosilicide (wt%)	54.7 ± 0.5	22.9 ± 0.4	11.5 ± 0.4	10.9 ± 0.4

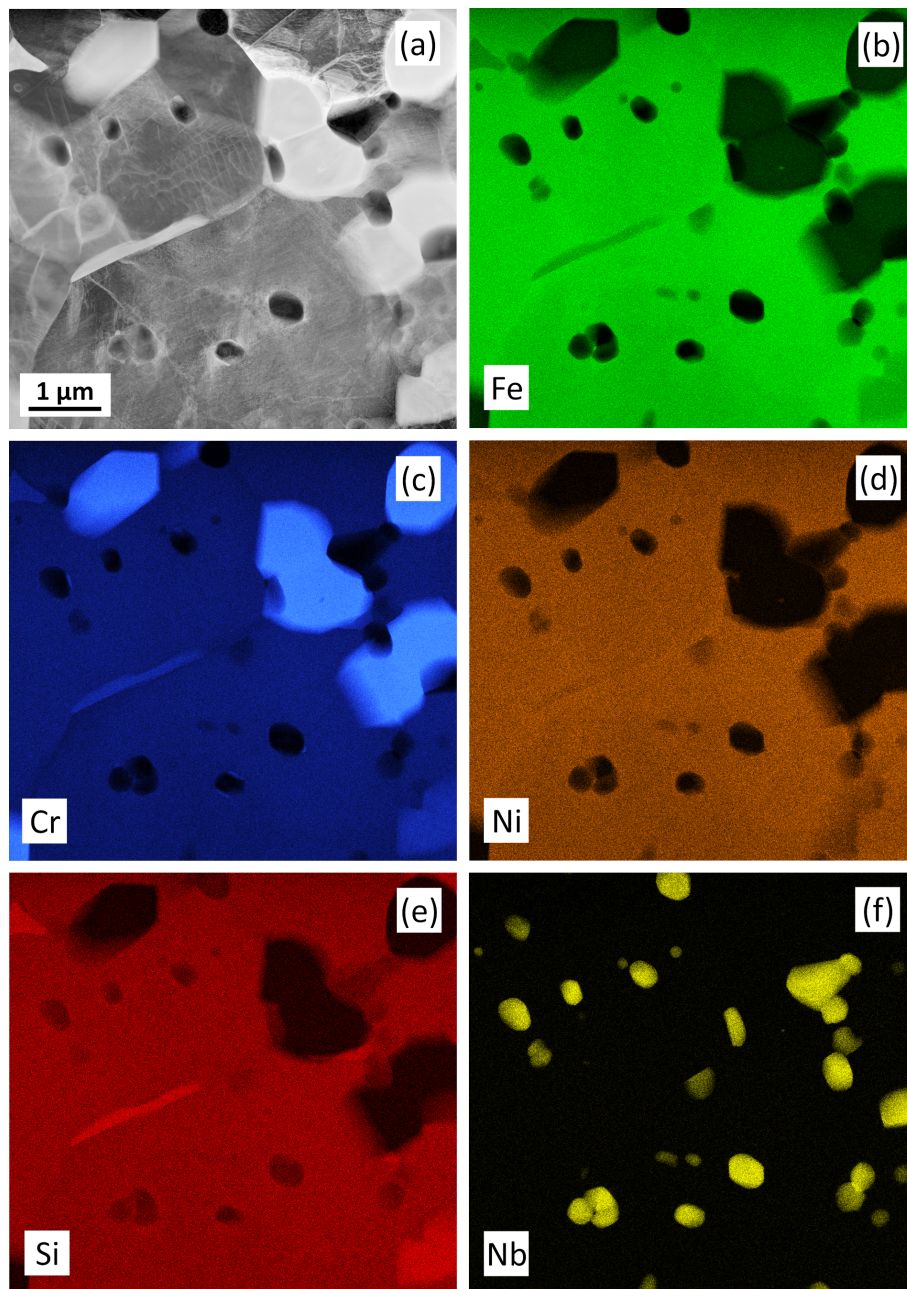


Figure 5.7: (a) depicts a HAADF-STEM micrograph of HIPed Tristelle and (b), (c), (d), (e) and (f) are corresponding EDX maps for Fe, Cr, Ni, Si and Nb respectively. (a) shows a grey contrast austenitic matrix with bright (Cr-rich (c)) and dark (Nb-rich (f)) contrast precipitates (M_7C_3 and MX carbonitride respectively) and (e) reveals the Si-rich π -ferrosilicide phase.

Fig. 5.8 (a) shows a BF-STEM micrograph of the microstructural detail of a typical M_7C_3 precipitate and Fig. 5.8(b) shows an accompanying Cr EDX map of this same region. This M_7C_3 precipitate exhibits parallel striations due to stacking faults and this heavily flawed microstructure is characteristic of all the M_7C_3

precipitates within Tristelle 5183 that were examined in this study. Fig. 5.8 (c) is a BF-TEM micrograph of the same precipitate shown in Fig. 5.8 (a) and the accompanying SADP (Fig. 5.8 (b)) confirms that this precipitate is Cr-based M_7C_3 (Zone axis: $[4\bar{1}\bar{1}]$). This SADP exhibits streaking due to stacking faults in the $\{110\}$ planes (with fault vectors $\pm\frac{1}{2}(a \pm b)$) and the high intensity maxima superimposed on these streaks corresponds to the diffraction spots for the basic orthorhombic structure. However the streaking is also somewhat continuous which is indicative of complete disorder in the stacking of polyatomic layers and additional spots are observed which are typical of volumetric planar disorder [261]. Therefore, it is suggested that this SADP arises from regions where there is a complete disorder in the stacking of layers and regions where there are blocks arranged in the basic orthorhombic sequence which are separated by planar faults. The compositions of numerous M_7C_3 precipitates were evaluated by EDX-TEM and the average atomic fractions of Cr and Fe which combine to form the M component of this phases were found to be 0.818 ± 0.04 and 0.182 ± 0.04 (mean \pm standard error of the mean ($n = 4$)) respectively ($\sim(0.82Cr0.18Fe)_7C_3$).

Fig. 5.9 (a-c) show BF-STEM micrographs of the different morphologies of the π -ferrosilicide precipitates (dark contrast) and it is clear that this phase has a tendency to reside at grain boundaries (as plate-like features) (Fig. 5.9 (a and b)) and triple junctions (Fig. 5.9 (c)). The plate-like morphology of the π -ferrosilicide phase shown in Fig. 5.9 (a and b) was confirmed by various tilting experiments. Fig. 5.9 (d) is a SADP from the triple junction π -ferrosilicide region shown in Fig. 5.9 (c) (at a different tilt) and confirms that the crystallography of this phase is consistent with the π -ferrosilicide identified by Bowden et al. [163].

5.3. DISCUSSION

Tristelle 5183 inert gas atomised powder (60 - 150 μm in size) was consolidated via HIPing in a mild steel canister which was sealed in argon prior to canister evacuation. HIPing was conducted at 1120 ± 10 °C and 103 ± 5 MPa with a dwell time of 240 - 270 min and a cooling rate of 3.4 - 5.5 K/min. The HIPed alloy was also given a subsequent simulated HIPed bond heat treatment under a vacuum at

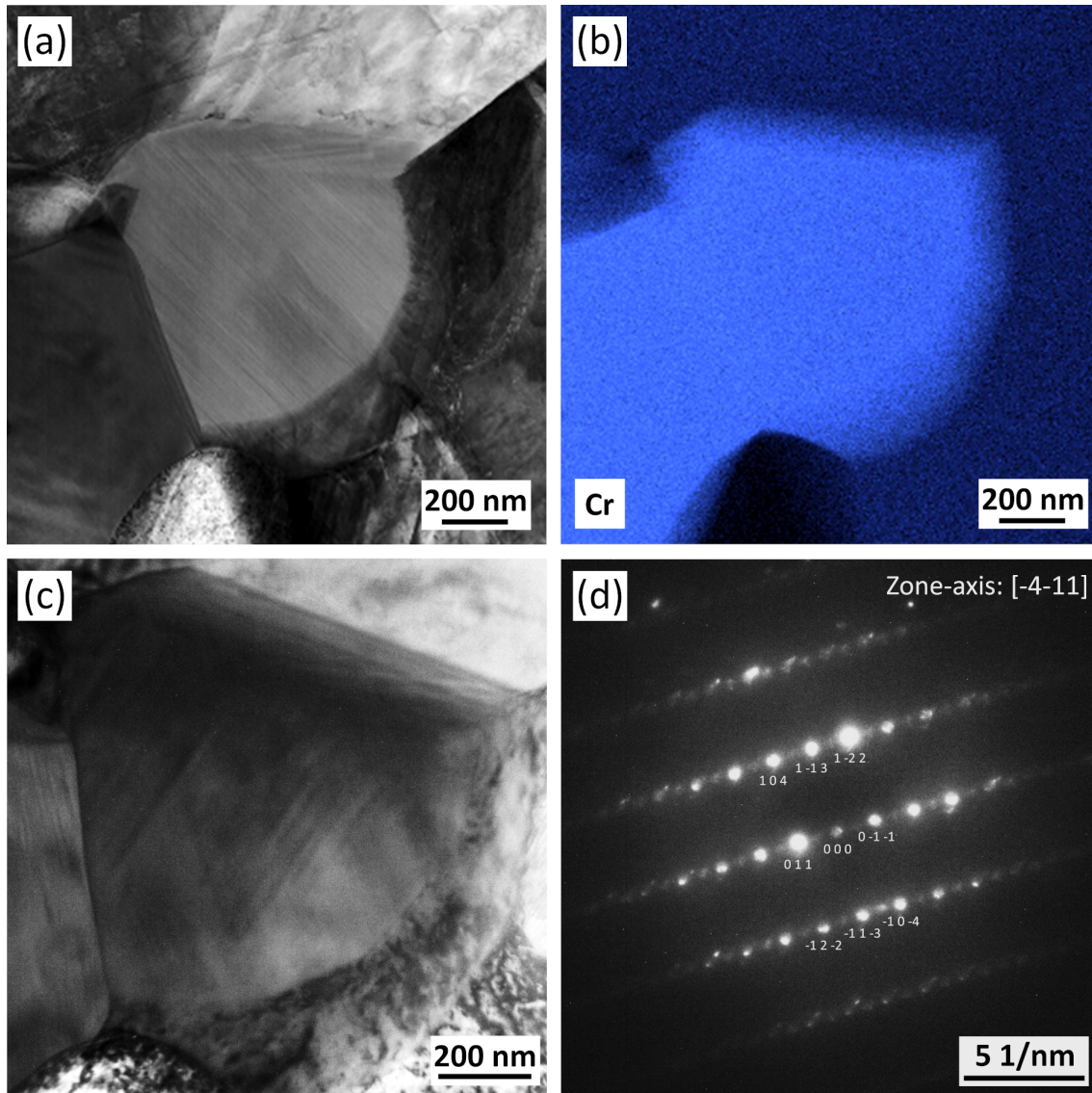


Figure 5.8: (a) depicts a representative BF-STEM micrograph showing the heavily flawed microstructure of the M_7C_3 precipitates within HIPed Tristelle 5183 and (b) shows an accompanying EDX Cr map of this same region. (c) shows a BF-TEM micrograph of the same precipitate shown in (a) and (d) is the SADP corresponding to (c).

1050 °C for 132 min with a heating and cooling rate < 10 K/min.

Table 5.4 shows a comparison between the phase fractions of HIPed material and two different powder size fractions of Tristelle 5183. It is evident HIPing largely homogenises the microstructure (at a temperature between 1100 and 1200 °C) and a large fraction of the metastable phases which form in response to the deep undercoolings and droplet recalescence during gas atomisation are decomposed during HIPing (Table 5.4). The formation of the different phases and the

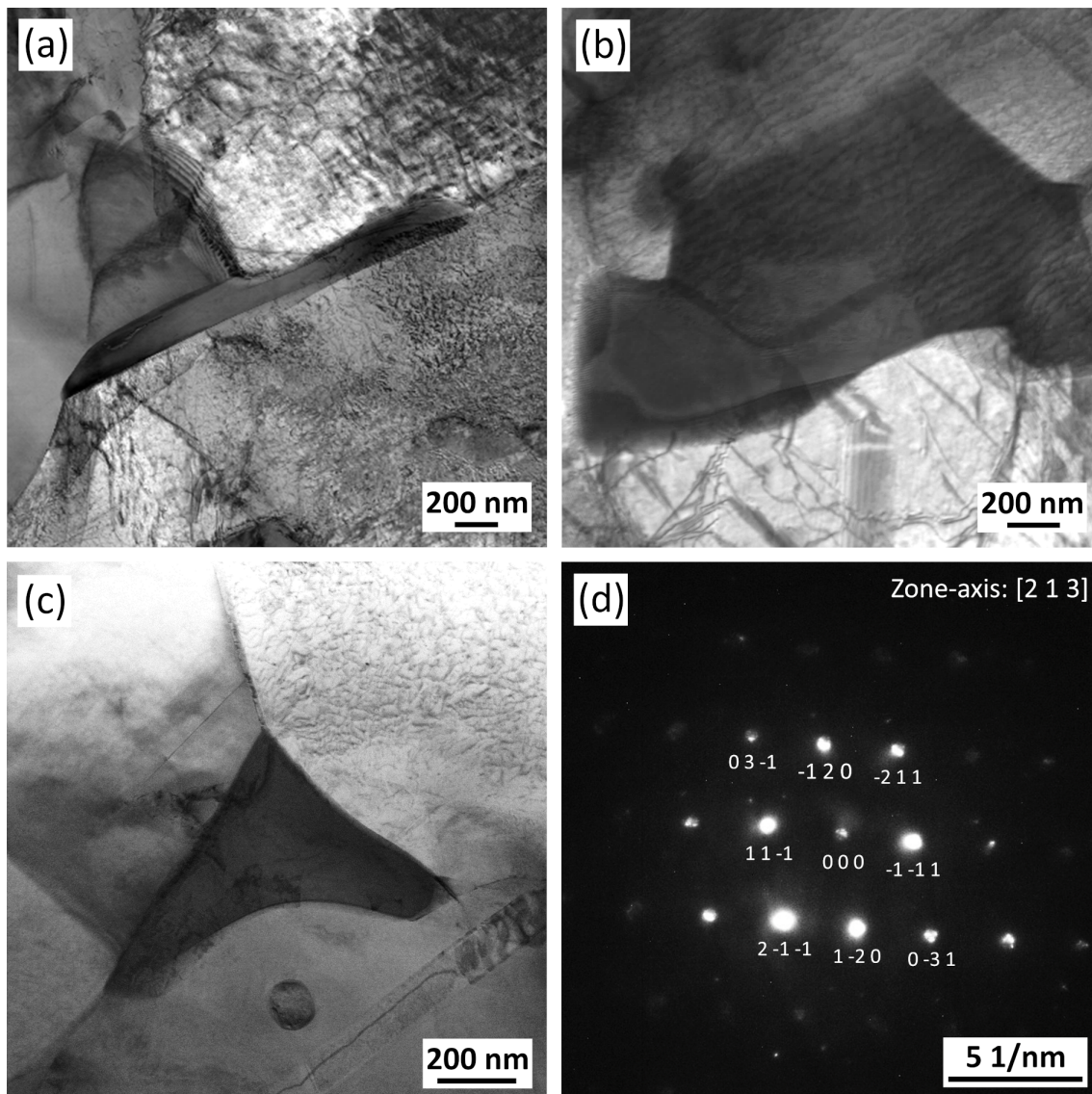


Figure 5.9: (a), (b) and (c) show BF-TEM micrographs depicting the morphologies of several different π -ferrosilicide regions of dark contrast within the HIPed microstructure of Tristelle 5183. (a) and (b) show plate-like grains whereas (c) depicts a π -ferrosilicide grain which forms at the triple junction. (d) shows a SADP from the triple junction π -ferrosilicide phase (at a different tilt to (c)) indexed to a $[213]$ zone axis of the π -ferrosilicide phase identified by Bowden et al. [163].

microstructural evolution will now be considered.

5.3.1. Matrix evolution during HIPing

Fig. 5.5 shows a series of large γ -Fe grains which are confined within certain powder particles; the morphologies of these larger grains are not typically equiaxed

Table 5.4: Phase fractions (wt%) of HIPed Tristelle 5183 and two different size fractions of gas atomised powder determined by Rietveld analysis.

	γ -Fe	M_7C_3	MX-Total	α -Fe	Ferrosilicide-Total
HIPed (wt%)	76.1	12.7	9.9	1.0	0.3
Powder < 20 μm (wt%)	12.8	-	4.9	32.6	49.7
Powder 63 - 75 μm (wt%)	57.9	-	5.2	6.7	30.2

and retain a phase and microstructural lineage with the dendritic structures observed in the gas atomised powders (Chapter 4) [260]. These larger grains have also been shown to contain notable in-grain misorientations and substructures (Fig. 5.6), and similar intra-grain misorientations can also be observed in the gas atomised powders (Chapter 4). The smaller γ -Fe grains observed within the HIPed microstructure (Fig. 5.5) are generally contained within what appear to be more highly deformed powder particles; these grains are typically more equiaxed, free from internal misorientations and substructures (Fig. 5.6), and generally contain annealing twins. TEM (Fig. 5.7) has also shown that a large number of the small equiaxed grains are largely defect free, which is entirely consistent with the absence of any significant internal misorientations within these grains (Fig. 5.6). The development of these matrix features can be explained by the nature of heating/cooling of the material combined with the mechanical deformation that occurs during the HIPing process.

During the initial stages of HIPing, plastic deformation dominates densification as the contact stresses between neighbouring particles are high enough for them to plastically yield. As pores close up, the contact stresses are reduced, isolated pores are formed, and densification in the latter stages of HIPing is dominated by creep and both bulk and grain boundary diffusion. The inhomogeneous plastic deformation incurred by a given powder particle in the initial stages of HIPing is known to be dependent on particle size, and smaller powder particles are generally plastically deformed more than larger ones [243,262–265] (Fig. 5.2). This can be rationalised on the basis that the fraction of contact area to the available surface area is higher for smaller powder particles compared to larger powder particles. However, the phase makeup and microstructures of individual powder particles

(which are dependent on powder particle size (Chapter 4) [260]) will also alter the local particle deformation characteristics. For example, the microstructural scale of the matrix phase dendrites and/or cells shifts by approximately an order of magnitude between particles $< 20 \mu\text{m}$ in size and powder particles between $63 - 75 \mu\text{m}$ in size (Chapter 4) [260].

Dynamic recrystallization occurs during the elevated temperature deformation of low to medium stacking fault energy materials such as Tristelle 5183 [266,267]. Therefore, the presence of annealing twins (Fig. 5.5), typically within the grains of what were smaller powder particles, indicates the regions which have been subject to dynamic recrystallization. Likewise, the largely equiaxed and defect free nature of these grains (Figs. 5.5 and 5.7) is also indicative that these regions have been subject to dynamic recrystallisation. In contrast, regions where annealing twins are absent have probably not been completely recrystallised; these regions are typically composed of larger grains within larger powder particles which have only been subject to relatively limited plastic deformation during HIPing.

It is hypothesised that the sub-structures exhibited within the austenitic grains (Figs. 5.5 and 5.6) are principally a result of two factors: (i) artifacts of the fine scale cellular and dendritic microstructures exhibited within the rapidly solidified gas atomised powders (Chapter 4) [260], and (ii) deformation structures generated during HIPing. These features are retained within the HIPed microstructure as a consequence of an insufficient homogenisation of the microstructure during HIPing and the inability of certain powder particles to undergo dynamic recrystallisation.

In light of the above, it is hypothesised that the ability of a powder particle (and/or region) to undergo complete recrystallisation during HIPing is principally governed by two aspects: (i) the degree of (inhomogeneous) plastic deformation incurred by a powder particle in the initial stages of HIPing (Figs. 5.5 and 5.6), and (ii) the phase makeup and metastable nature of powder particles prior to HIPing. The deep undercoolings and droplet recalescence that powder particles are subjected to during inert gas atomisation means a notable fraction of powder particles contain non-equilibrium metastable phases (Chapter 4) [260] (Table 5.4).

Smaller powder particles thus contain a larger fraction of metastable phases and therefore have a greater stored energy for recrystallisation during HIPing. The presence of lightly deformed (typically larger) powder particles which have not been subject to dynamic recrystallisation (Fig. 5.5) shows that the as-received powder particles do not generally have enough stored energy to recrystallise without significant deformation. Therefore, the stored energy generated due to plastic deformation in the initial stages of HIPing is believed to be a prerequisite for dynamic recrystallisation in the later stages of HIPing. As smaller powder particles are often subjected to a larger degree of plastic deformation and contain larger fractions of metastable phases, the smaller powder particles are statistically more likely to undergo complete (and/or partial) (dynamic) recrystallization during HIPing.

It is postulated that the wide distribution in the γ -Fe matrix grain size is a consequence of two factors, namely (i) the presence of both recrystallised and non-recrystallised regions, and (ii) the initial broad powder size range (60 - 150 μm) (and thus the large variability in powder phase makeup and microstructures) used for HIPing (Chapter 4) [260]. Therefore, the microstructures generated during gas atomisation can directly influence the final HIPed microstructure of Tristelle 5183. A significant fraction of the microstructure is not completely recrystallised during HIPing (Figs. 5.3 and 5.5) and as larger powder particles are less likely to undergo the required plastic deformation for dynamic recrystallisation, the microstructures of larger powder particles are more likely to be partially retained within the HIPed microstructure. The above hypothesis concurs with the findings of Irukuvarghula et al. [262] who studied the HIPed microstructure of 316L and also explains the broad γ -Fe grain size distribution within HIPed Tristelle 5183 reported by Zhao et al. [7].

To summarise, plastic deformation in the early stages of HIPing is a prerequisite for recrystallisation because the as-received powder does not generally have enough stored energy to recrystallise without deformation. The plastic deformation incurred by a given powder particle is dependent on its size therefore, the particle size distribution has a profound influence of the HIPed microstruc-

ture [262]. The plastic deformation undergone by a large fraction of powder particles in the early stages of HIPing is insufficient to permit dynamic recrystallisation during HIPing. The metastable nature of powder particles prior to atomisation can significantly influence recrystallisation during HIPing. Hence, it is clear that powder characteristics play a critical role in the development of the final microstructure post HIPing.

5.3.2. Phase evolution during HIPing

5.3.2.1. M_7C_3 precipitation

The HIPed microstructure of Tristelle contains ~ 14.0 vol% M_7C_3 , whereas the formation of this phase is wholly suppressed in the gas atomised powder (Table 5.4). It is postulated that the M_7C_3 phase precipitates only during HIPing because its complex crystal structure means its nucleation and growth kinetics are slow. Fig. 5.8 (d) shows that the M_7C_3 phase has a “basic” orthorhombic structure (Pmcn space group) but it is extensively flawed with $\{110\}$ planar defects. This concurs with the observations of Kowalski [261] and Morniroli et al. [126] and it is clear that the ideal stacking of polyatomic layers only extends over very small distances (Fig. 5.8 (a)). In accord with Kowalski [261], it is suggested that the greater part of the M_7C_3 crystal may be arranged differently whereby disordered and ordered polytypic structures may be present in M_7C_3 which precipitate out during HIPing. As shown in Fig. 5.8 (d), the disorder in the stacking sequence is due to stacking faults in the $\{110\}$ planes. However, in ordered polytypic structures, regions which differ from the basic arrangement of polyatomic layers due to $\{110\}$ faulting are periodically repeated over large regions of the M_7C_3 crystal. Twinning is also reportedly prevalent in M_7C_3 crystals which involve three kinds of orthorhombic regions rotated through an angle of 120° around the c axis [126] - however, this has not been directly observed in the present study.

5.3.2.2. MX phase evolution

The total phase fraction of the (Nb-based) MX (X=C,N) phase increases as a result of HIPing (Table 5.4) and it is clear, based on the phase and microstructural characterisation of HIPed and gas atomised Tristelle 5183 (Chapter 4) [260], that the MX type precipitates significantly evolve during HIPing. XRD (Fig. 5.1) shows that the HIPed alloy contains a single crystallographic population of the MX phase which exhibits sharp reflections, unlike the three distinctly different populations of MX phase which are observed within the gas atomised powder (Chapter 4) [260]. The lattice parameter of the MX phase in HIPed Tristelle 5183 is 0.4461 nm (as determined by Rietveld analysis (Table 5.1) which is close to the value of 0.4469 nm given in the International Centre for Diffraction Data file (# 01-070-8416) for stoichiometric NbC. Therefore, during HIPing the Nb-based MX phase appears to be equilibrated and chemically homogenised even though this phase exhibits morphological variability within the HIPed microstructure (Figs. 5.2, 5.3 and 5.5).

In the HIPed alloy, the MX precipitates exhibit a bimodal size distribution and conforms to two distinctly different morphologies, namely (i) $< 2 \mu\text{m}$ sized somewhat spheroidised precipitates (Figs. 5.3, 5.5 and 5.7), and (ii) large 5 - 20 μm sized crystals which evolve from the melt processing stage prior to gas atomisation (Figs. 5.2 and 5.3) [260]. In contrast, three morphologically different MX precipitates are observed in the gas atomised powder: (i) nanoscale particles contained within the interdendritic and intracellular regions of powder particles, (ii) $< 2 \mu\text{m}$ sized faceted crystals distributed throughout powder particles and (iii) large 5 - 20 μm sized crystals. The large 5 - 20 μm MX crystals are retained within the microstructure following HIPing and may possibly grow and spheroidise due to the prolonged period of time spent at elevated temperatures (1100 - 1200 °C) (Figs. 5.2 and 5.3). It is proposed that the faceted and nanoscale precipitates present within the gas atomised powders evolve into the $< 2 \mu\text{m}$ somewhat spheroidised precipitates during HIPing and this evolution is principally governed by two factors. Firstly, further MX phase precipitation occurs from the matrix which is supersaturated with Nb and C and the decomposition of Nb and C containing metastable phases (interdendritic and cellular silicides). Secondly, due to the

time spent at elevated temperature, the faceted and nanoscale MX precipitates spheroidise and coarsen. Coarsening is driven by the interfacial energy between matrix and MX particles. A widely accepted theory for coarsening of precipitates, controlled by diffusion, is given by the Lifshitz, Slyozov and Wagner (LSW) theory which reveals the dependence of coarsening rate on the temperature dependent diffusion coefficient (in this case of Nb) and on the time available.

5.3.2.3. *Silicide and ferrite evolution*

Fig. 5.5 shows that numerous grains within the HIPed microstructure are not completely recrystallised and retain a strong phase and microstructural lineage with the gas atomised powder particles prior to HIPing. Section 5.3.1 has shown that these grains are statistically more likely to be generated from larger powder particles which are principally composed of austenitic dendrites. However, following HIPing, the interdendritic silicide phase within the austenitic dendrites in the gas atomised powder has clearly been decomposed. This interdendritic phase is rich in Cr, Nb, Si and C solute elements (Chapter 4) and therefore, in accord with Fig. 5.5, it is suggested that this phase ultimately decomposes and transforms into M_7C_3 , austenite and (Nb-based) MX during the complete HIPing cycle. Retained features of these once-dendritic powder microstructures are seen as in-grain misorientations (Fig. 5.6).

A similar phase evolution is believed to take place within the grains/regions which are subject to dynamic recrystallization, however, these regions contain a larger fraction of ferrite and π -ferrosilicide (Figs. 5.5 and 5.7) precipitates. These precipitates reside at grain boundaries and triple junctions (often adjacent to one another) and are both typically $< 2 \mu\text{m}$ in size (Figs. 5.5 and 5.7). It is speculated that these phases are most probably solid-state precipitates which form during the cool down period of HIPing. Therefore, they are statistically more likely to nucleate and grow in the recrystallised regions because (i) there are a larger fraction of grain boundaries which are energetically favourable nucleation sites, and (ii) the larger fraction of grain boundaries favours growth permitting diffusion.

5.3.3. Oxide inclusions and prior particle boundaries (PPBs)

Optical microscopy (Fig. 5.2) and SEM (Fig. 5.4) have revealed fine discontinuous networks of submicron dark contrast features which reveal the PPBs within the HIPed microstructure of Tristelle 5183. Whilst these features most probably encompass micro-pores, oxide inclusions and a combination of the two, it is believed that these features are principally ($\sim 0.1 - 0.3 \mu\text{m}$ sized) oxide-based inclusions (Fig. 5.4), given the oxygen sensitive nature and chromia forming behaviour exhibited by Tristelle 5183. Oxide formation can occur during inert gas atomisation, powder storage and HIPing [224]. Whilst oxidation may occur throughout processing, the formation of the oxide inclusions within the HIPed microstructure (Figs. 5.2 and 5.4) must evolve during HIPing as these oxide-based features are not observed on the surfaces of gas atomised powders (Chapter 4) [260].

Gas atomised powders with compositions analogous to the austenitic matrix of Tristelle 5183 are known to exhibit homogenous nanoscale ($< 10 \text{ nm}$) oxide surface layers [268,269]. It is postulated that these continuous oxide layers prevent metal to metal contact and thus bonding between powder particles in the incipient stages of deformation during HIPing. With continued deformation, metal to metal contacts are established and the once-continuous oxide layers surrounding powder particles are disrupted. In accord with Irukuvarghula et al. [270], it is believed that these disrupted oxide layers coalesce to form oxide inclusions at the PPBs in order to minimise the interfacial energy between the metal and oxide layers. The growth of oxide inclusions has previously been reported during the recrystallization of 316 stainless steel and both Ni-Cr and Cu-Si alloy systems [270–272]. Therefore, it is further postulated that the possible growth (coarsening) of these oxide-based inclusions during HIPing may be assisted by diffusion and/or further coalescence [270]. Whilst the presence of oxide inclusions is principally confined to the PPBs it is clear that that some recrystallized grains are able to grow past the PPBs (Fig. 5.4). The oxide inclusions mostly reside at grain boundaries and in some instances appear to have been shifted about the PPBs; this indicates that the oxide inclusions may be pushed/dragged small distances ($< 2 \mu\text{m}$) by the moving grain boundaries during recrystallization.

5.4. CONCLUSIONS

1. HIPed Tristelle 5183 is principally composed of an austenitic Fe-based solid solution matrix which surrounds Cr-based M_7C_3 (~ 14 vol%) and Nb-based MX (~ 9.6 vol%) secondary hard phase precipitates. Smaller fractions of ferrite (~ 1.0 vol%) and a π -ferrosilicide phase (~ 0.3 vol%) are also observed within the alloy.
2. As received HIPed Tristelle 5183 contains oxide inclusions ($\sim 0.1 - 0.3 \mu\text{m}$ in size) which indicate the prior particle boundaries (PPBs) within the alloy. These oxide inclusions form during HIPing by the breakdown and coalescence of the nanoscale oxide films which are present on the gas atomised powder.
3. The γ -Fe grain size in HIPed Tristelle 5183 is highly varied as the microstructure has not been completely recrystallised during HIPing and some regions within the microstructure retain a strong morphological and crystallographic relationship with the inert gas atomised powder. Inert gas atomised Tristelle 5183 powder does not generally have enough stored energy to dynamically recrystallise without significant plastic deformation in the initial stages of HIPing. The degree of plastic deformation and therefore ability of a powder particle to recrystallise is dependent on powder size. The highly varied metastable nature of powder particles influences recrystallisation during HIPing.
4. The phase and microstructural characteristics of inert gas atomised Tristelle 5183 play a critical role in the development of the final microstructure post HIPing.
5. M_7C_3 carbides are not present in the gas atomised powder and precipitate out during HIPing with a basic orthorhombic crystal structure (Pmcn space group) that is largely flawed with $\{110\}$ planar crystallographic defects. The basic ideal stacking of polyatomic layers only extends over very small distances and the greater part of M_7C_3 precipitates may be arranged differently

and exhibit both disordered and polytypic structures.

6. Two distinctly different morphologies of Nb-based precipitate exist within the HIPed alloy; coarse 5-20 μm sized precipitates which evolve from the melt prior to inert gas atomisation and $< 2 \mu\text{m}$ spheroidised precipitates which evolve during gas atomisation and HIPing. The evolution of the MX precipitates during HIPing is governed by chemical homogenisation, equilibration, further growth via precipitation, coalescence and spheroidisation.
7. A π -ferrosilicide phase exists within Tristelle 5183 in trace amounts and principally resides at grain boundaries (as plates) or at triple junctions. This phase is closely related to the small fraction of ferrite also present within the HIPed alloy.

TRIBOLOGICAL ASSESSMENT OF SELF-MATED HIPED STELLITE 6 SUBJECTED TO SLIDING IN LITHIATED WATER

6.1. INTRODUCTION

This chapter aims to comprehensively assess the tribological performance of HIPed Stellite 6 during sliding in lithiated water at 20 and 250 °C. Despite the shortcoming of Stellite 6 when employed in a PWR environment, it has been found that its exceptional combination of wear and corrosion resistance cannot be readily replicated in other Co-free alloy systems. For these reasons, Stellite 6 is often regarded as the benchmark alloy against which the performance of other hardfacing alloys is assessed. However, a fundamental mechanistic understanding of why Stellite 6 exhibits such excellent tribological performance within a PWR environment remains somewhat fragmented and incomplete. The primary circuit operating environment of deoxygenated, lithiated water at up to 300 °C is known to play a critical role in the mechanisms of material loss, but there are relatively few reports available which comprehensively address this issue [139–142, 150, 273, 274]. In broad terms, it is generally accepted that tribocorrosion is unquestionably significant to the degradation of Stellite 6 during sliding in lithiated water. However, there is a paucity of information in the literature concerning the mechanisms of tribocorrosion leading to material removal during the sliding of self-mated Stellite 6 in a PWR environment.

Clearly, the degradation of Stellite 6 in a PWR needs to be better understood. Tribocorrosion is known to be influenced by a combination of both complex mechanical and chemical phenomena [150,275], so the main aim of the present chapter is to report the sub-surface nano-scale and micro-scale features of Stellite 6 follow-

ing self-mated sliding contact in lithiated water. HIPed Stellite 6 was tested at 20 °C and 250 °C and investigated by a combination of X-ray diffraction, scanning electron microscopy and transmission electron microscopy. An improved knowledge of the contacting surface and the sub-surface micro-scale and nano-scale structural evolution as a result of sliding is fundamental to understanding the mechanisms of tribocorrosion. Additionally, a better understanding of the tribological performance of Stellite 6 is of paramount importance in the development of new and improved cobalt-free alloys for future applications within PWRs.

6.2. RESULTS

6.2.1. As-received HIPed Stellite 6: Phases and microstructures

Fig. 6.1 shows an X-ray diffractogram from the polished surface of as-received HIPed Stellite 6. Stellite 6 is principally composed of an (fcc) γ -Co solid solution (Fm3m space group) with a smaller fraction of an orthorhombic M_7C_3 carbide phase (Pmcm space group) and a very small amount of an (hcp) ϵ -Co solid solution (P63/mmc space group). The phase fractions of as-received Stellite 6 were approximated via Rietveld analysis as reported in Table 6.1.

Table 6.1: Phase fractions of as-received Stellite 6 determined via Rietveld analysis.

	γ -Co	M_7C_3	ϵ -Co
wt %	88.7	10.9	0.4
vol %	86.3	13.3	0.4

SEM-BSE micrographs of Stellite 6 are shown in Fig. 6.2 and reveal dark-contrast, equiaxed chromium-rich precipitates (M_7C_3), ranging in size between ~ 1 and $4 \mu\text{m}$, in a Co-rich matrix where grain and annealing twin boundaries are clearly visible due to channelling contrast. At higher magnification (Fig. 6.2 (b)), there is evidence of deformation banding in the matrix around the M_7C_3 precipitates; this presumably results from the thermal mismatch between the two phases during the cooling period of the HIP cycle.

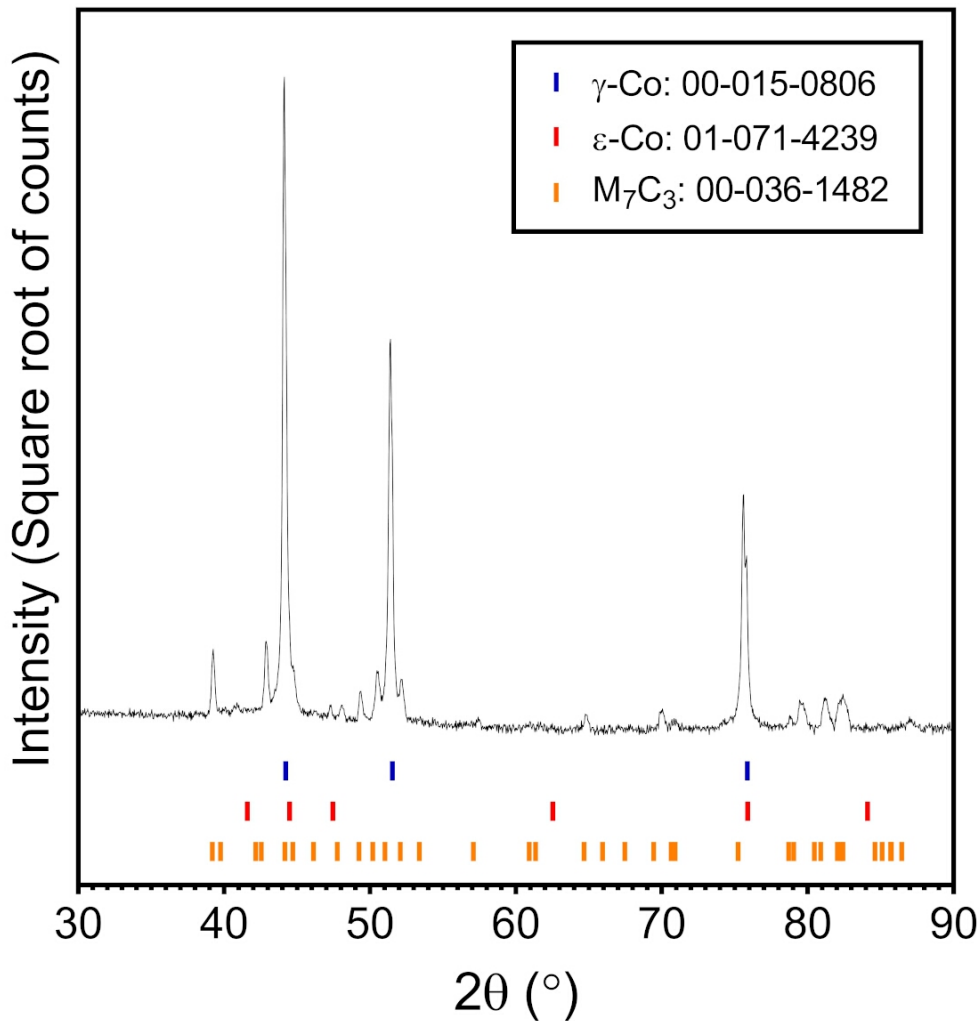


Figure 6.1: XRD pattern obtained from the polished surface of the as-received, HIPed Stellite 6. The ICDD database files used to index the diffractogram is shown in the legend. Stellite 6 exhibits reflections for γ -Co (fcc), M_7C_3 and a very small fraction of ϵ -Co (hcp).

Fig. 6.3 (a) and (b) show an EBSD-derived phase map of HIPed Stellite 6 and accompanying inverse pole figure (IPF) respectively. As previously identified via XRD and SEM, HIPed Stellite 6 (Fig. 6.3 (a)) is principally composed of a Co-rich solid solution matrix (blue) which surrounds an M_7C_3 type carbide phase (yellow). EBSD (Fig. 6.3 (a)) has identified several small grains which are crystallographically consistent with the ϵ -Co phase previously identified by XRD. The inverse pole figure (Fig. 6.3 (b)) clearly illustrates the high angle annealing twins and grain boundaries within the Co-based solid solution matrix.

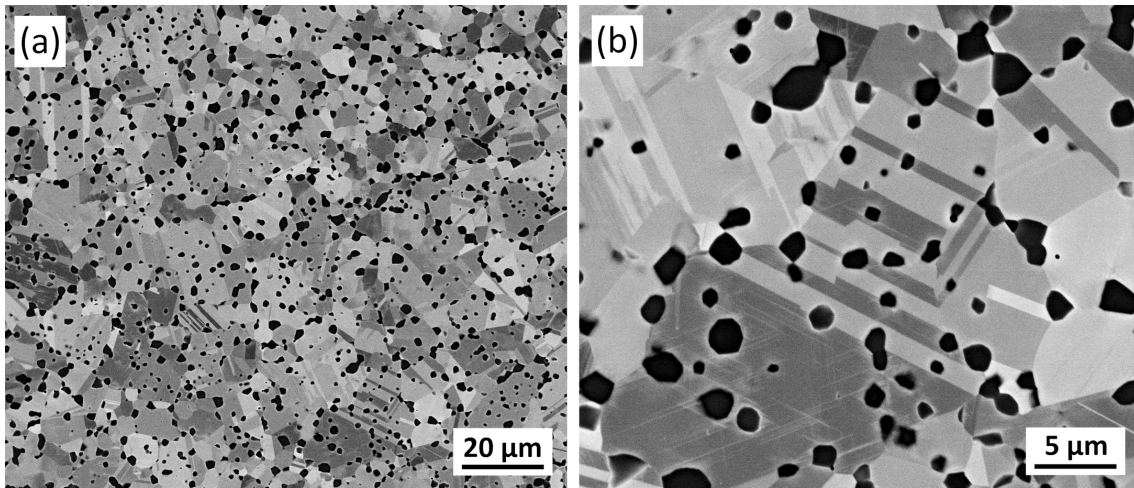


Figure 6.2: BSE-SEM channelling contrast micrographs of HIPed Stellite 6 showing M_7C_3 carbides (darkest contrast) and cobalt-based matrix grains with annealing twins.

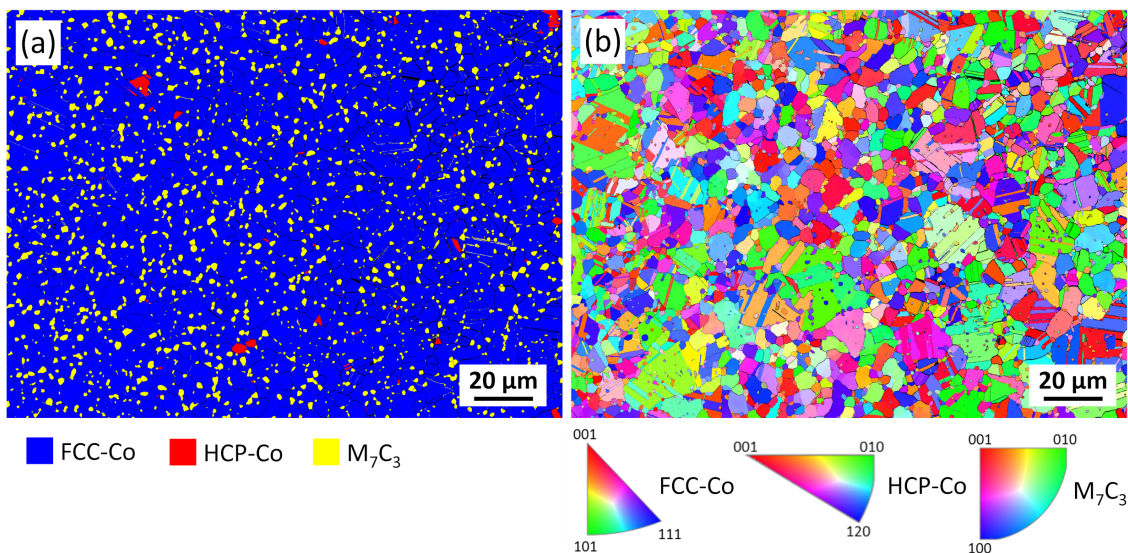


Figure 6.3: EBSD-derived phase and IPFZ orientation maps of the typical microstructure of HIPed Stellite 6.

6.2.2. Autoclave sliding contact test results - mass and volume loss

The combined pin and disk mass and volume losses for Stellite 6 after 5 h, 4 kg dead load sliding contact tests at 20 and 250 °C within an autoclave environment are shown in Fig. 6.4. The volume loss measurements were derived from mass loss values and converted to volume loss using a measured density of 8370 ± 1 kg/m³ (as evaluated by gas displacement pycnometry). The average volume loss

values equate to an average total specific wear rate of $1.17 \times 10^{-6} \text{ mm}^3 \text{ m}^{-1} \text{ N}^{-1}$ and $2.99 \times 10^{-5} \text{ mm}^3 \text{ m}^{-1} \text{ N}^{-1}$ for testing at 20 °C and 250 °C respectively. The combined pin and disk volume and mass loss increased by a factor of between ~ 16.5 and ~ 38.7 when the test temperature was raised from 20 to 250 °C. Table 6.2 shows a breakdown of the individual pin and disk mass losses following autoclave testing at 20 and 250 °C. Any general corrosion of the sample surface (outside the sliding contact zone) will also contribute to the mass change that is measured during testing. However, measurements made on corrosion samples in lithiated water at 250 °C (in the absence of sliding contact) showed that the mass change due to corrosion alone is negligible over the time frame of the sliding contact experiments ($< 0.2 \text{ mg}$).

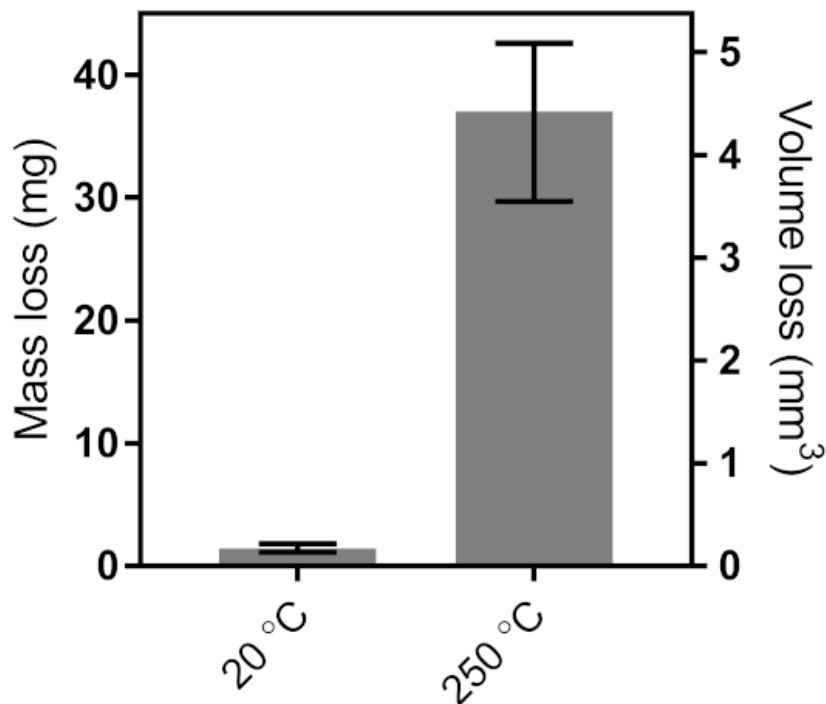


Figure 6.4: Graph showing the effect of autoclave test temperature on the mass and volume loss following 5 h sliding contact testing with a 4 kg dead load. The bars represent mean values and the error bars represent the minimum and maximum values of combined pin and disk wear ($n_{20}=3$, $n_{250}=6$).

Table 6.2: The effect of test temperature on the individual components of pin and disk mass loss of Stellite 6 following 5 h autoclave sliding contact testing with a dead load of 4 kg. The errors have been reported as the standard error of the mean ($n_{20}=3$, $n_{250}=6$).

Test temperature (°C)	Pin mass loss (mg)	Disk mass loss (mg)	Total mass loss (mg)
20	0.45±0.05	1.00±0.30	1.45±0.35
250	17.65±2.83	19.38±3.87	37.03±1.88

6.2.3. Microstructural characterisation of the contacting surfaces - surface topography

Fig. 6.5 shows low magnification optical stereoscope micrographs of Stellite 6 disk (Fig. 6.5 (a) and (b)) and pin (Fig. 6.5 (c) and (d)) samples after sliding contact tests at 20 (Fig. 6.5 (a) and (c)) and 250 °C (Fig. 6.5 (b) and (d)). These micrographs confirm the trends observed in the volume and mass loss measurements presented in Fig. 6.4 and clearly show that the amount of material removed increases with increasing temperature. Fig. 6.5 shows that the wear track becomes significantly wider and the contact area is much greater at the higher temperature. The disk wear tracks measure ~ 1.7 mm and ~ 6.3 mm in width following testing at 20 and 250 °C respectfully.

Plan view BSE-SEM micrographs taken from central regions within the wear tracks of Stellite 6 disks are shown in Fig. 6.6 (sliding direction horizontal). The worn surfaces appear remarkably similar despite the material loss being between ~ 16.5 and ~ 38.7 times greater at the higher temperature. At both temperatures, the surface features can principally be characterised by scoring and scratching and there is no evidence of any notable large-scale plastic transfer of material. There is little evidence for decohesion of the carbide from the matrix although occasionally carbide pull-out is observed, as indicated by the red arrows in Fig. 6.6 (a) and (b). Additionally, the fracture of carbides is also occasionally observed at the contacting surface. Depressions and discontinuities in the worn surface appear to accumulate dark contrast material which is possibly oxidised material. There is no evidence for preferential wear/corrosive attack on the carbide, the matrix, or at the carbide-matrix interface within the resolution of the SEM. Additionally, the matrix

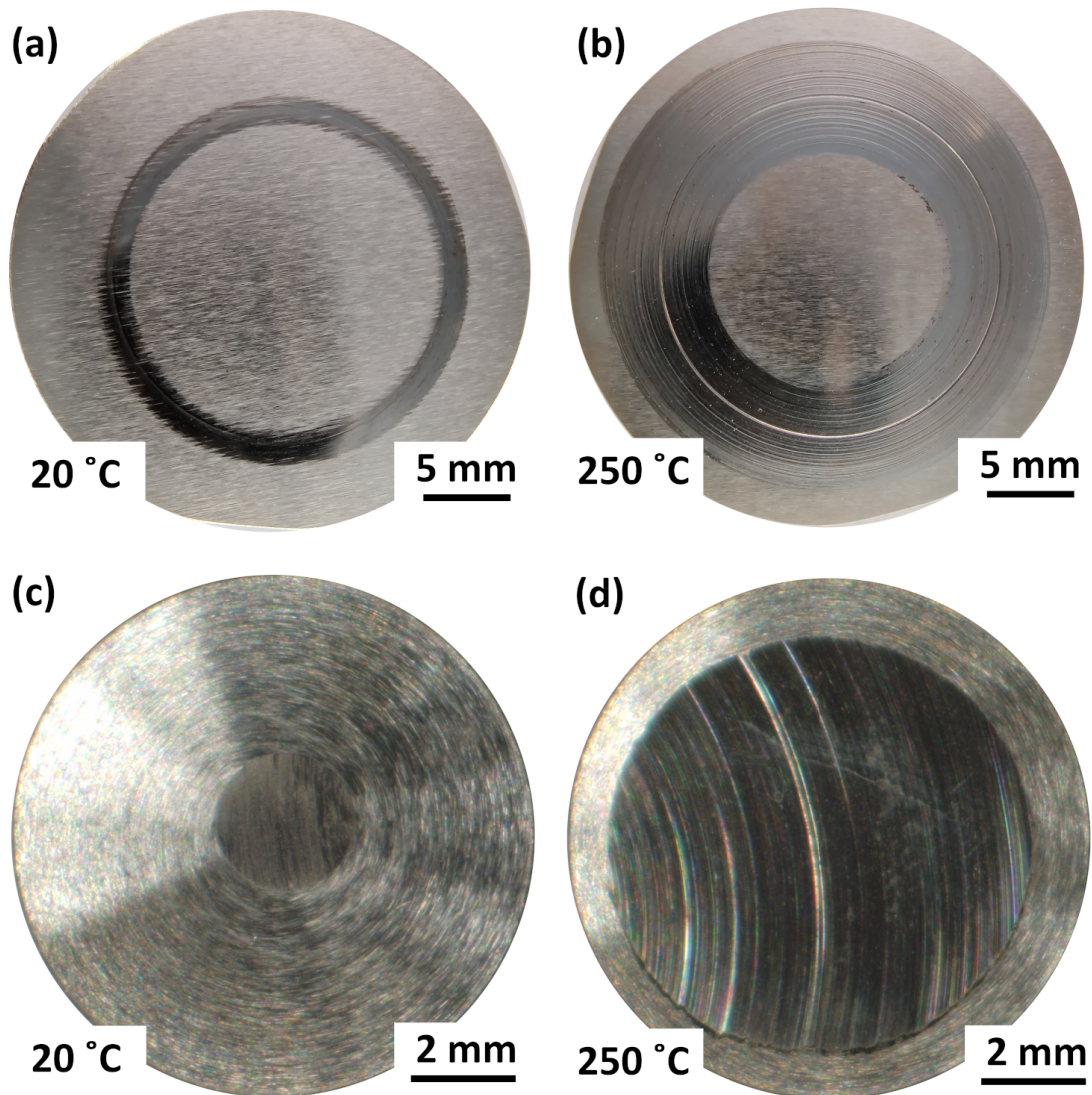


Figure 6.5: Stereoscope optical micrographs of Stellite 6 disk ((a) and (b)) and pin ((c) and (d)) tribologically affected surfaces following sliding contact autoclave tests at 20 ((a) and (c)) and 250 °C ((b) and (d)).

and carbide phases apparently recede (wear/corrode) evenly in conjunction with one another. These observations are based on the lack contrast variation due to topological features consistent with preferential wear/corrosive attack, the absence of z-contrast variation due to localised corrosion, and the presence of continuous scratches across adjacent carbide and matrix regions. Comparison of Fig. 6.6 (c) and (d) show only subtle differences in features on the contacting surfaces. Firstly, the scoring and scratching along the sliding direction is more frequent and deeper in the sample tested at 250 °C; secondly, there is also a more noticeable mottled contrast on the matrix surface at 250 °C than at 20 °C. This mottled

contrast is possibly related to oxidation and/or mixing at the contacting surface during sliding. Some contrast variation is also observed over the M_7C_3 phase. In summary, the worn surface features strongly suggest that the mechanisms of material removal are essentially the same at the different temperatures, which is entirely consistent with previous studies [143,144].

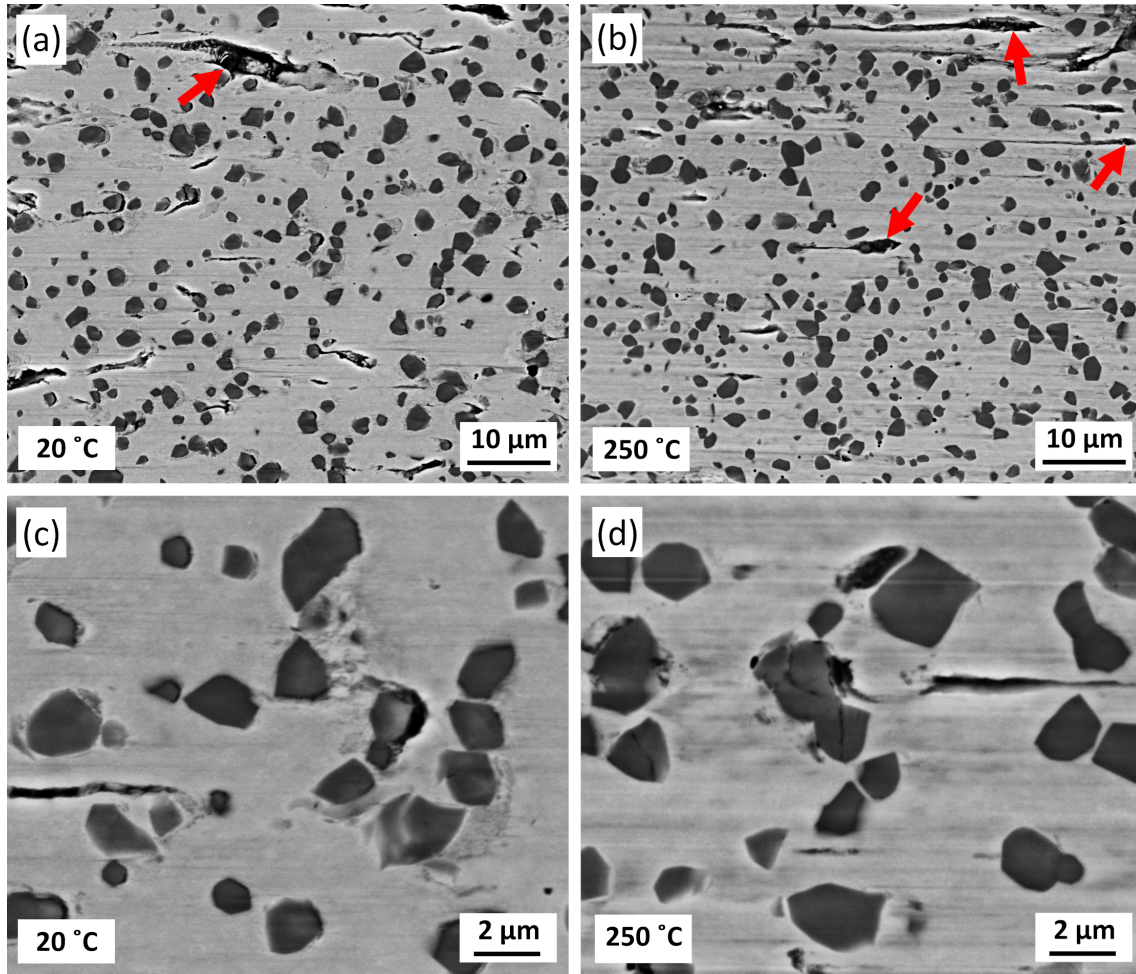


Figure 6.6: Plan view BSE-SEM micrographs showing the microstructure of the tribologically affected surface of Stellite 6 disk samples after sliding contact tests in an autoclave environment at 20 °C (a and c) and 250 °C (b and d) for 5 hours. Sliding direction was horizontal on the image.

6.2.4. X-ray diffraction from the worn surface

The X-ray diffractograms shown in Fig. 6.7 were obtained from the as-received HIPed material and exclusively from within the wear tracks following testing at 25 and 250 °C. As expected, all the phases observed in the as-received HIPed

material are still present following autoclave testing at both temperatures. However, autoclave testing has clearly had a profound effect on the peak shapes, peak shift, max peak intensities and peak asymmetry of the matrix phase reflections relative to the polished surface of Stellite 6. This change in peak shape is a result of crystallographic faulting and crystallite size and strain broadening effects induced by autoclave sliding contact. Large reflections that are consistent with hcp ϵ -Co are also observed in the XRD patterns from within the wear track and are due to strain induced martensitic (SIM) transformation. A significant fraction of ϵ -Co is generated in response to autoclave sliding at both testing temperatures, however from the inspection of peak height ratios, the extent of this transformation is less at 250 °C than at 20 °C.

The extent of the $\gamma \rightarrow \epsilon$ transformation at the different test temperatures was quantitatively compared using the Rietveld method to analyse the XRD patterns. Even though the X-ray intensity contributing to the diffracted signal decreases exponentially with increasing depth into the sample [234], the average X-ray penetration depth contributing 99 % of the diffracted intensity was on average $\sim 5 \mu\text{m}$ over the range of 2θ values (35-120 °) used in the Rietveld refinements [234]. However, the samples are expected to have similar X-ray interaction volumes regardless of the test temperature and therefore a comparative quantitative assessment for the volume percent of fcc γ matrix transformed to ϵ -martensite can be made. At 20 °C and 250 °C, the volume percent of matrix transformed to ϵ -martensite from within the interaction volume contributing to the diffracted signal was $\sim 95 \%$ and $\sim 88 \%$ respectively.

6.2.5. Sub-surface microstructural characterisation of Stellite 6

BSE-SEM micrographs taken from within the wear track parallel to the sliding direction for Stellite 6 tested at 20 and 250 °C are shown in Fig. 6.8. In all cases, the (worn) contacting surfaces appear continuous and flat with no evidence for any preferential wear/corrosive attack of the carbide, the matrix or the carbide-matrix interface. There is also no evidence of any extensive plastically transferred material on the sliding surface when observed via SEM. At both test temperatures, the

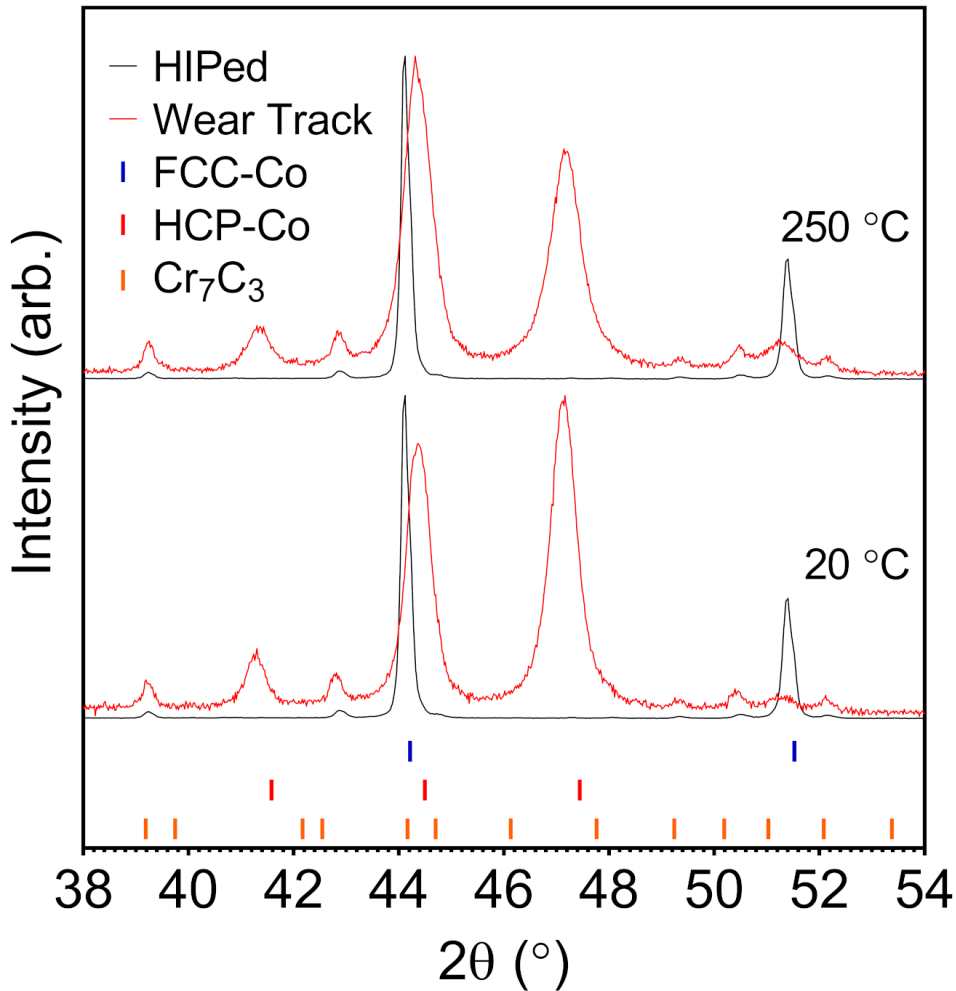


Figure 6.7: XRD patterns of Stellite 6 from the ground surface prior to testing and from within the wear track (following testing at 25 and 250 °C). Patterns normalised to the reflection of maximum intensity.

severe plastic deformation (due to the sliding contact) within the subsurface is observed to be accommodated by the generation of planar defects in the matrix which are visible due to channelling contrast. Within approximately the top 5 and 8 μm of the subsurface of the samples tested at 20 (Fig. 6.8 (a) and (c)) and 250 °C (Fig. 6.8 (b) and (d)) respectively, the extent of plastic deformation is sufficiently severe to make grain/cell boundaries almost indistinct. At both test temperatures, a deformation gradient is clearly generated from the loaded sliding contact; this is evident from the decrease in deformation features with increasing depth below the surface. The deformation structures appear largely the same irrespective of

test temperature (Fig. 6.8). However, the density of observable planar defects at any given depth from the contacting surface is larger following testing at 250 °C. This suggests that at 250 °C the subsurface is subjected to somewhat higher levels of strain during sliding and that the plastic deformed zone is deeper penetrating.

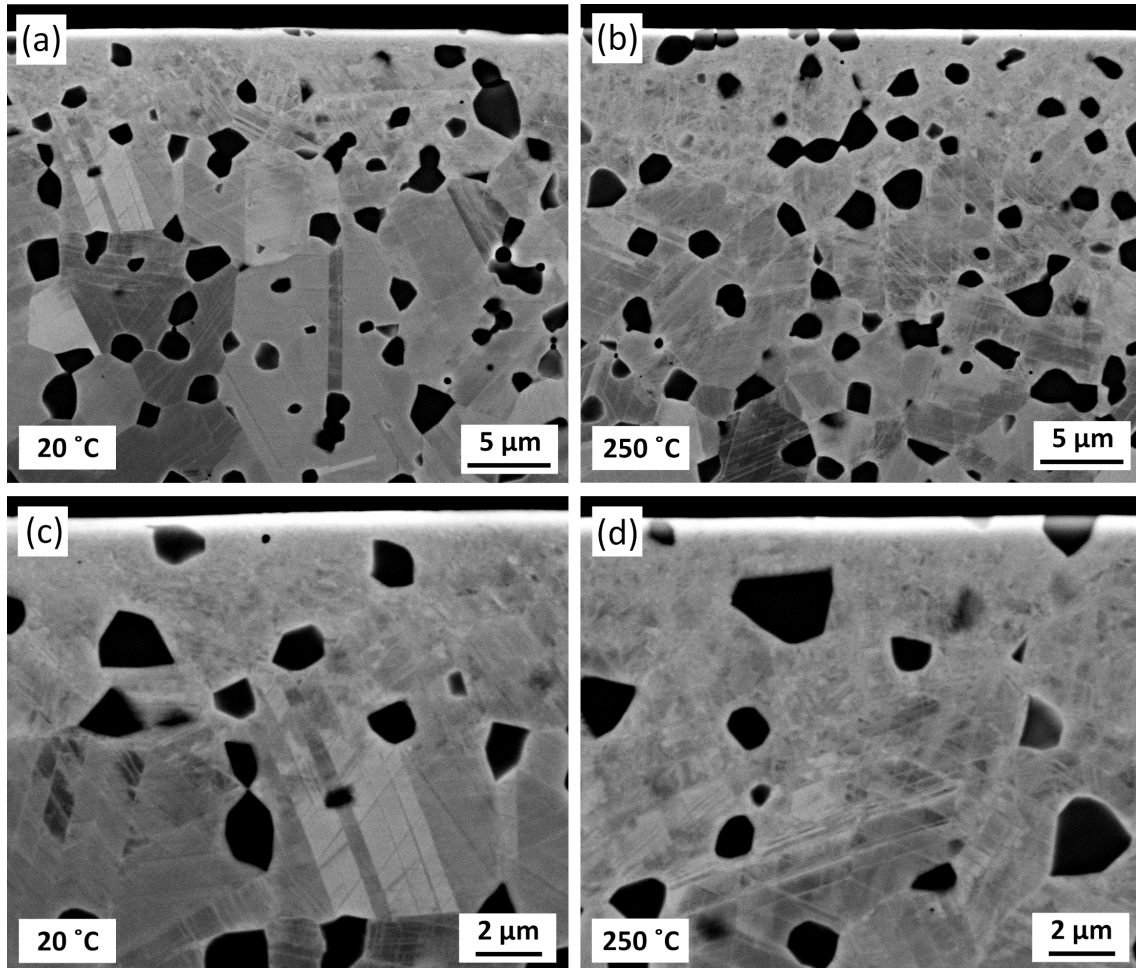


Figure 6.8: Cross-sectional BSE-SEM channelling contrast micrographs of Stellite 6 taken from within the wear track (parallel to the sliding direction) after testing at 20 °C (a, c) and 250 °C (b, d). M_7C_3 (dark contrast) carbides are distributed in Co-rich matrix with planar deformation structures.

Fig. 6.9 shows EBSD derived phase maps (Fig. 6.9 (a) and (b)), band contrast maps (Fig. 6.9 (c) and (d)) and inverse pole figures (Fig. 6.9 (e) and (f)) taken perpendicular to the sliding direction of Stellite 6 samples following autoclave sliding wear testing at 20 (Fig. 6.9 (a), (c) and (e)) and 250 °C (Fig. 6.9 (b), (d) and (f)). EBSD reveals three crystallographically distinguishable structures which are identical to those identified in XRD (Fig. 6.7) namely, (i) fcc γ -Co (blue), (ii) hcp ϵ -Co (red) and (iii) M_7C_3 carbide (yellow). Fig. 6.9 demonstrates that a large fraction

of the resolvable planar defects are laths of ϵ -Co which are presumably generated via the $\gamma \rightarrow \epsilon$ strain induced transformation previously identified by XRD (Fig. 6.7). Fig. 6.9 confirms the observations made via conventional SEM (Fig. 6.8) and shows a clear deformation gradient whereby the extent of deformation-induced microstructural refinement of the matrix increases towards the sliding surface. Additionally, the band contrast micrographs (Fig. 6.9 (d) and (d)) show a relative increase in the degree of subsurface deformation following testing at 250 °C. Despite the increase in subsurface deformation observed following testing at 250 °C (Fig. 6.8 and Fig. 6.9 (c) and (d)), the phase maps (Fig. 6.9 (a) and (b)) show that the extent of $\gamma \rightarrow \epsilon$ strain induced transformation is greater after sliding at 20 °C relative to 250 °C; this was also deduced from XRD (Fig. 6.7) patterns. Irrespective of test temperature, the phase maps (Fig. 6.9 (a) and (b)) suggest that the matrix at the contacting surfaces has completely transformed to ϵ -martensite.

Bright field (BF)-STEM micrographs of the subsurface microstructure obtained from cross-sectional FIB samples of Stellite 6 taken parallel to the direction of sliding are shown in Fig. 6.10 and allow sub-micron features to be revealed. Despite the fact that TEM micrographs of the contacting surface do not necessarily encompass the stochastic variability within the wear track, such studies offer valuable insight into the nanoscale modes of deformation and material removal within the top $\sim 2 \mu\text{m}$ which cannot otherwise be assessed via other lower resolution imaging techniques. After testing, the principal near surface microstructural features remain similar irrespective of test temperature with M_7C_3 particles embedded in a highly deformed Co-based matrix (Fig. 6.10 (a) and (b)). However, inspection of the effective grain size shows that at any given depth from the contacting surface the deformation induced matrix microstructural refinement is more extensive following testing at 250 °C than at 20 °C. This implies that higher subsurface strains are induced during sliding at 250 °C. By way of rough approximation, at a distance of $\geq 1 \mu\text{m}$ and $\geq 2 \mu\text{m}$ following testing at 20 and 250 °C respectively, the matrix nanostructure is principally composed of rhombic, trigonal and quadrilateral blocks which are generated via extensive deformation banding and SIM transformation (Fig. 6.10(a) and (b)). This matrix nanostructure

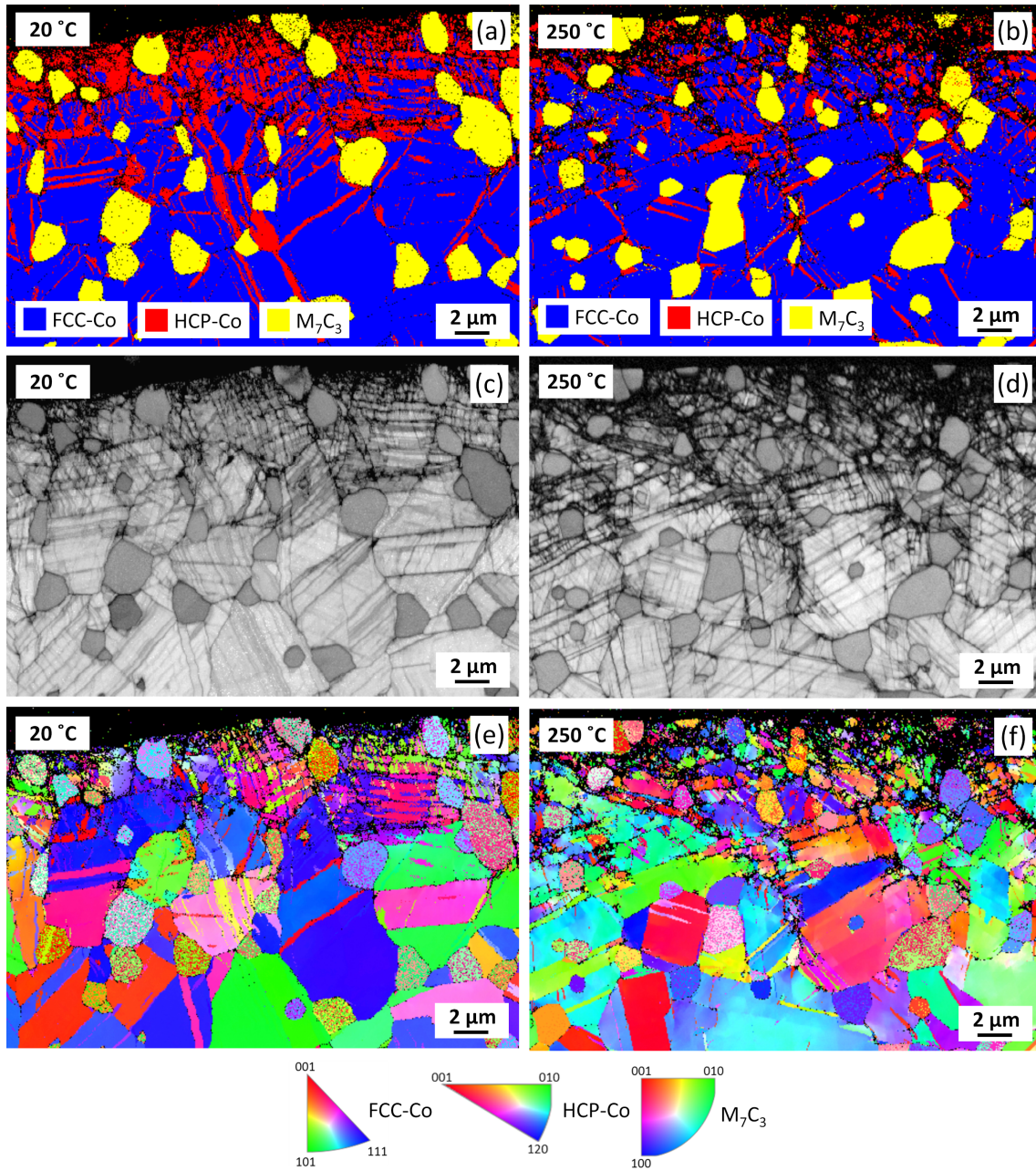


Figure 6.9: EBSD derived phase maps ((a) and (b)), band contrast maps ((c) and (d)) and inverse pole figures ((e) and (f)) taken perpendicular to the sliding direction of HIPed Stellite 6 following autoclave sliding wear testing at 20 ((a), (c) and (e)) and 250 °C ((b), (d) and (f)).

is also heavily flawed with stacking faults as indicated by the fine parallel striations contained within individual blocks (Fig. 6.10 (a) and (b)). At depths $\leq 1 \mu\text{m}$ and $\leq 2 \mu\text{m}$ beneath the contacting surface following testing at 20 (Fig. 6.10 (a) and (c)) and 250 °C (Fig. 6.10 (b) and (d)) respectively, there appears to be a shift in the principal deformation mode which appears to result in the generation of

fine equiaxed nanocrystals which exhibit a high degree of internal and boundary disorder.

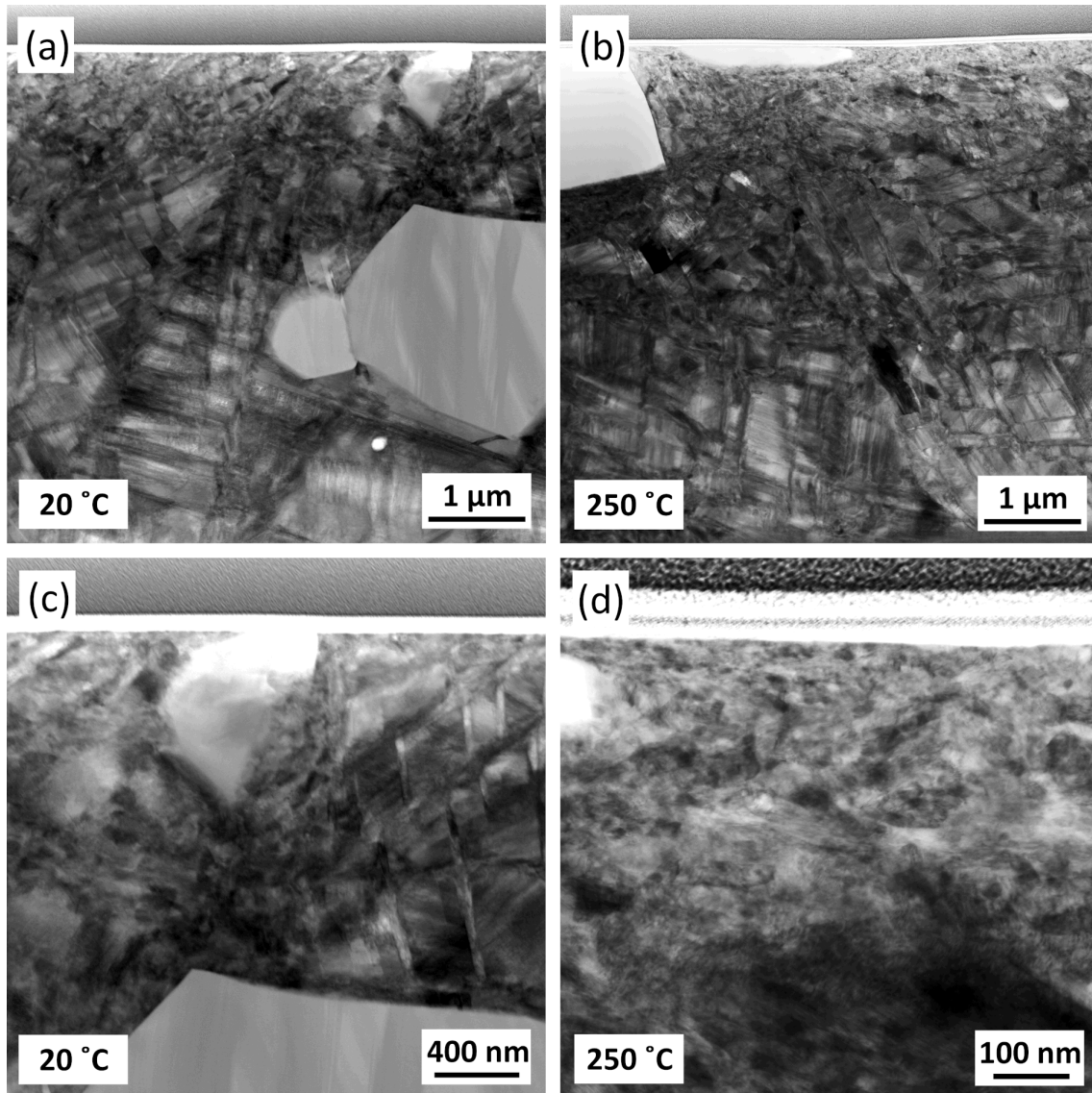


Figure 6.10: Representative BF-STEM micrographs of Stellite 6 taken from within the wear track (parallel to the sliding direction) after testing at 20 °C (a, c) and 250 °C (b, d).

The BF-TEM images (Fig. 6.11 (a) and (c)) reveal the microstructural detail of the most heavily deformed nanocrystalline region below the contacting surface following testing at 20 and 250 °C respectively. The selected area diffraction patterns (SADP) of these regions presented in Fig. 6.11 (b) and (d) (following testing at 20 and 250 °C respectively) confirm that these nanostructures are ϵ -Co (hcp). This supports the hypothesis that the matrix completely undergoes the SIM

($\gamma \rightarrow \epsilon$) transformation to ϵ -Co before being exposed to the contacting surface at both test temperatures. The diffraction rings are clearly more continuous following testing at 250 °C (Fig. 6.11 (f)) thus, showing that the effective grain size within the top ~ 300 nm is more heavily refined after testing at the higher temperature.

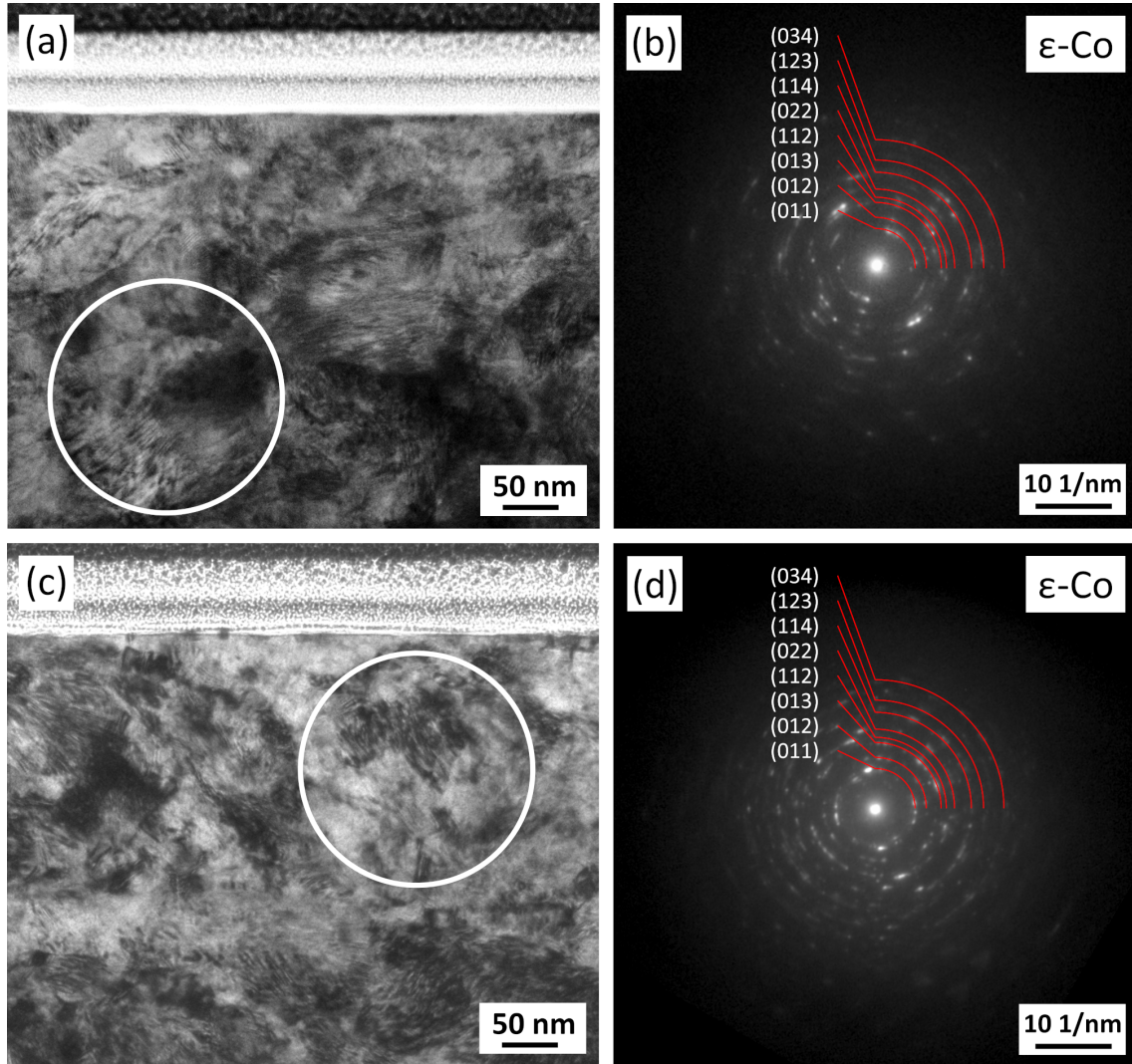


Figure 6.11: Representative BF-TEM micrographs ((a) and (c)) and SADPs ((b) and (d)) from samples taken parallel to the direction of shear, showing the deformation structures directly beneath the contacting surface of Stellite 6 after exposure to sliding contact at 20 °C ((a) and (b)) and 250 °C ((c) and (d)). The SADPs, (b) and (d), index to hcp ϵ -Co and have been recorded from the regions marked with circles in (a) and (c) respectively.

The BF-STEM micrograph and accompanying EDX maps (Fig. 6.12) show a $\lesssim 10$ nm thick oxygen-rich layer on the contacting surface following testing at 250 °C which is most probably a passive oxide layer. The passive nature of Stellite 6

in a high temperature (~ 300 °C) lithiated water environment has been reported previously [133,134,276].

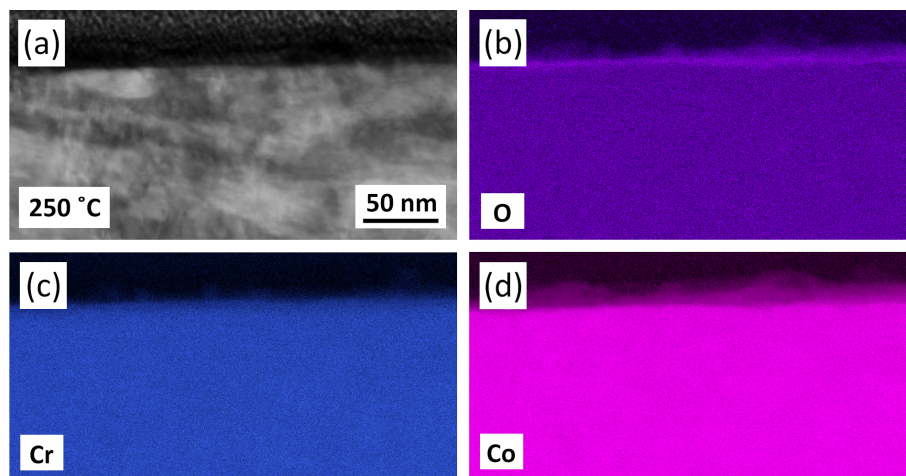


Figure 6.12: (a) BF-STEM micrograph of Stellite 6 taken parallel to the direction of shear following exposure to sliding contact at 250 °C. (b), (c) and (d) show EDX maps of the same region depicted in (a) and correspond to maps for O, Cr and Co respectively.

The HAAD-STEM micrograph (Fig. 6.13 (a)) and accompanying Co EDX map Fig. 6.13 (b) show the microstructural detail of the matrix surrounding a high aspect ratio M_7C_3 carbide previously shown at lower magnification in Fig. 6.10 (b) following testing at 250 °C. This particular M_7C_3 particle has clearly worn extensively during sliding as such high aspect ratio carbides are not observed in the as received material (Fig. 6.2 and Fig. 6.3). Fig. 6.13 (c) and (d) are higher magnification BF-TEM micrographs of this same carbide which show a thin nanolayer ~ 20 nm thick at the contacting surface (red arrows) which spans the entire length of the carbide (Fig. 6.13 (a)). The microstructural features within this nanolayer become increasingly finer across the length of the carbide (Fig. 6.13 (c)) and eventually become indistinguishable with no contrast variation (Fig. 6.13 (c) and (d)). Additionally, the Co content within this nanolayer decreases across the length of the carbide. Fig. 6.13 (d) shows what appears to be some discontinuity between the carbide and nanolayer in the form of a dark contrast hairline crack like feature. Fig. 6.14 depicts both BF-STEM (Fig. 6.14 (a)) and HAADF-STEM (Fig. 6.14 (b)) micrographs taken parallel to the sliding direction showing a thin ~ 100 nm thick fractured M_7C_3 carbide situated at the contacting surface of Stellite 6 following

testing at 20 °C. This high aspect ratio carbide morphology must be generated during sliding wear and is similar to the carbide also shown in Fig. 6.13.

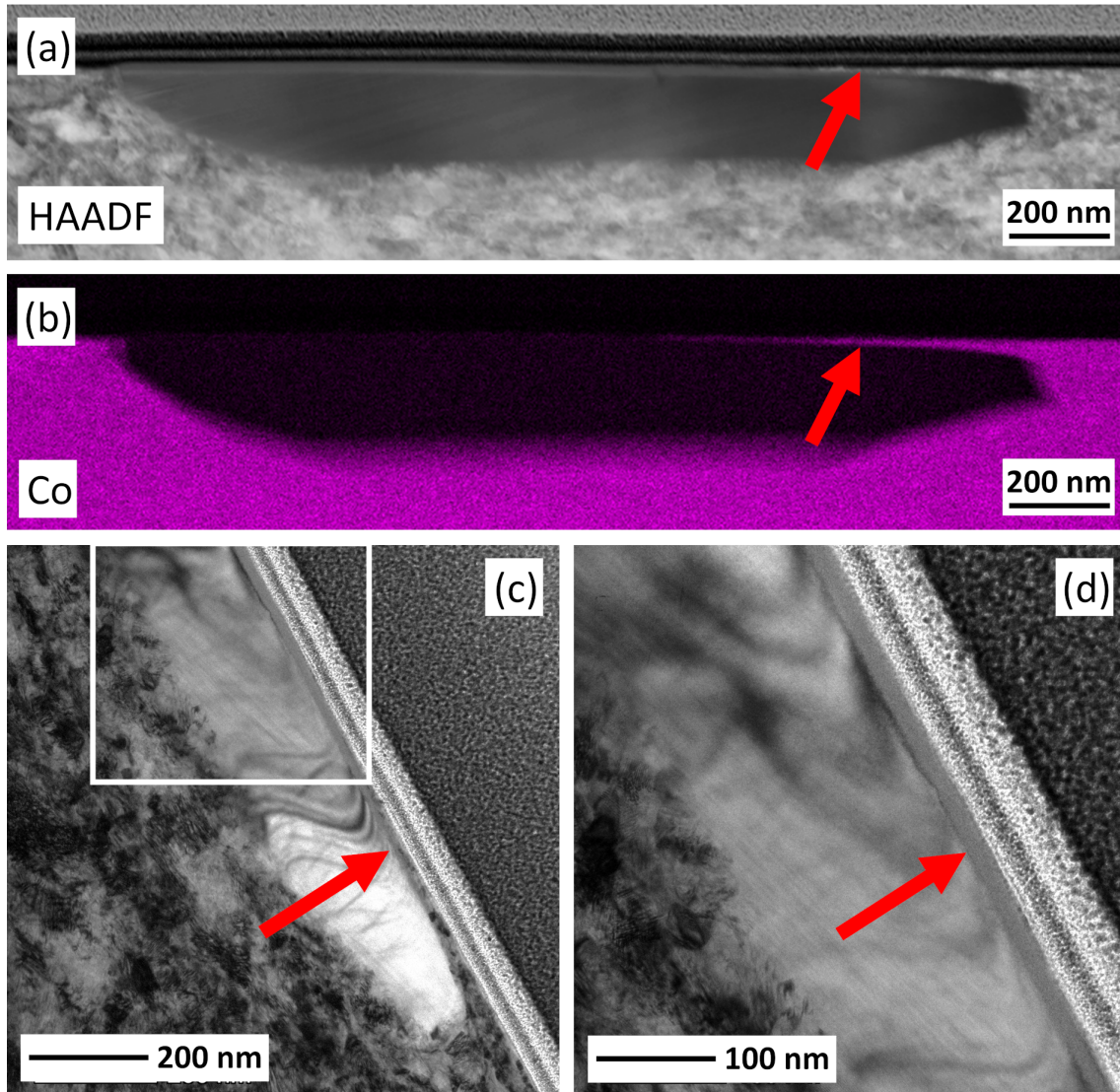


Figure 6.13: Micrographs taken parallel to the direction of sliding which show the formation of a mechanically mixed nanolayer over an M_7C_3 carbide positioned at the contacting surface of Stellite 6 following testing at 250 °C. (a) depicts a HAADF-STEM micrograph and (b) shows an accompanying Co map. (c) and (d) show higher magnification BF-TEM micrographs of this same carbide.

6.3. DISCUSSION

This study has shown that the combined pin and disk material loss from Stellite 6 during self-mated sliding contact in lithiated water is higher at 250 °C than at

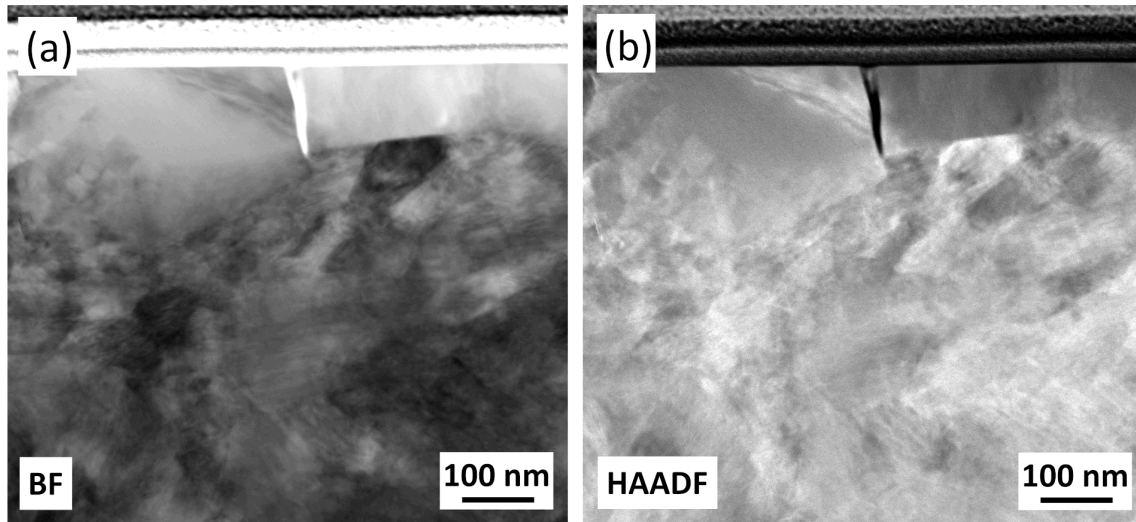


Figure 6.14: BF-STEM (a) and HAADF-STEM (b) micrographs taken parallel to the sliding direction showing a thin ~ 100 nm thick fractured M_7C_3 carbide situated at the contacting surface of Stellite 6 following testing at 20°C .

20°C , by a factor of between ~ 16.5 and ~ 38.7 when assessed through volume loss measurements. The most notable macro/microscopic difference between the two different test temperatures is the extent of scratching and scoring within the wear track. However, the site specific TEM study of the most heavily deformed regions (a few micron from the contacting surface) provides new insights into the sub-surface deformation behaviour and the tribological degradation mechanisms during sliding contact in lithiated water.

Stellite 6 remains highly corrosion resistant and exhibits passivating behaviour at both 20°C and 250°C [133,134,276] (as shown for 250°C in Fig. 6.12). Although there are differences in the depth to which subsurface deformation features are observed and the extent of strain induced martensite, the subsurface deformation structures and the phases present within the tribologically affected material (TAM) appear largely comparable irrespective of test temperature (Figs. 6.8 to 6.11). The following sections will consider the complex interaction of mechanical deformation and chemical degradation to better understand the mechanisms responsible for the wear behaviour of Stellite 6. Particular attention will be given to analysing the complex sub-surface deformation behaviour of the Co-base matrix under the high strain conditions imposed by the sliding contact.

6.3.1. Matrix deformation and role of the carbide phase during sliding contact

In comparing the tribologically affected material (TAM) at the two different test temperatures it should be noted that the nominal contact pressures are different due to differences in pin wear (although the local asperity contact pressures will be relatively unaffected [277]). In both cases the strain gradient from the sliding contact induces clearly observable deformation structures up to a depth of at least $\sim 30 \mu\text{m}$ from the sliding interface (Fig. 6.8 (a) and (b)) which, is consistent with previous related work [143, 144].

To simplify the following discussion, it is convenient to sub-divide the continuum of plastically deformed matrix material within the TAM into three layers as schematically illustrated in Fig. 6.15 The characteristics of each of these layers is summarised in Table 6.3. The deformation structures discussed in this section are representative of those observed following testing at both 20 and 250 °C

Table 6.3: Summary of the dominant mechanisms governing the subsurface microstructural evolution beneath the contacting surface of Stellite 6 in response to sliding in lithiated water.

Deformation layer	Relative strain	ϵ phase (hcp)	γ phase (fcc)
3	high	<ul style="list-style-type: none"> • Grain boundary sliding and rotation • Basal and prism plane alignment <ul style="list-style-type: none"> • Nanocrystal formation • Grain subdivision by dislocation activity • Basal ($\langle 11\bar{2}0 \rangle (0001)$) and prismatic dislocation slip ($\langle 11\bar{2}0 \rangle \{10\bar{1}0\}$) 	
2	medium	<ul style="list-style-type: none"> • Basal ($\langle 11\bar{2}0 \rangle (0001)$) and prismatic dislocation slip ($\langle 11\bar{2}0 \rangle \{10\bar{1}0\}$) <ul style="list-style-type: none"> • Twinning • Glide of (0001) stacking faults • Basal and pyramidal dislocations 	<ul style="list-style-type: none"> • $\gamma \rightarrow \epsilon$ Transformation (complete transformation)
1	low	<ul style="list-style-type: none"> • Twinning • Glide of (0001) stacking faults • Basal and pyramidal dislocations 	<ul style="list-style-type: none"> • $\gamma \rightarrow \epsilon$ Transformation <ul style="list-style-type: none"> • $\{111\}$ Twinning • Glide of 111 Stacking faults • Dislocation slip on the 111 planes

The undeformed microstructure away from the TAM comprises around 13 vol% of equiaxed M_7C_3 precipitates ($\sim 1\text{-}4 \mu\text{m}$ in size) in a Co-based solid solution matrix (fcc, γ -Co) which is made up of equiaxed grains with annealing twins (Fig. 6.1) and merges into layer 1 at around $30 \mu\text{m}$ from the surface.

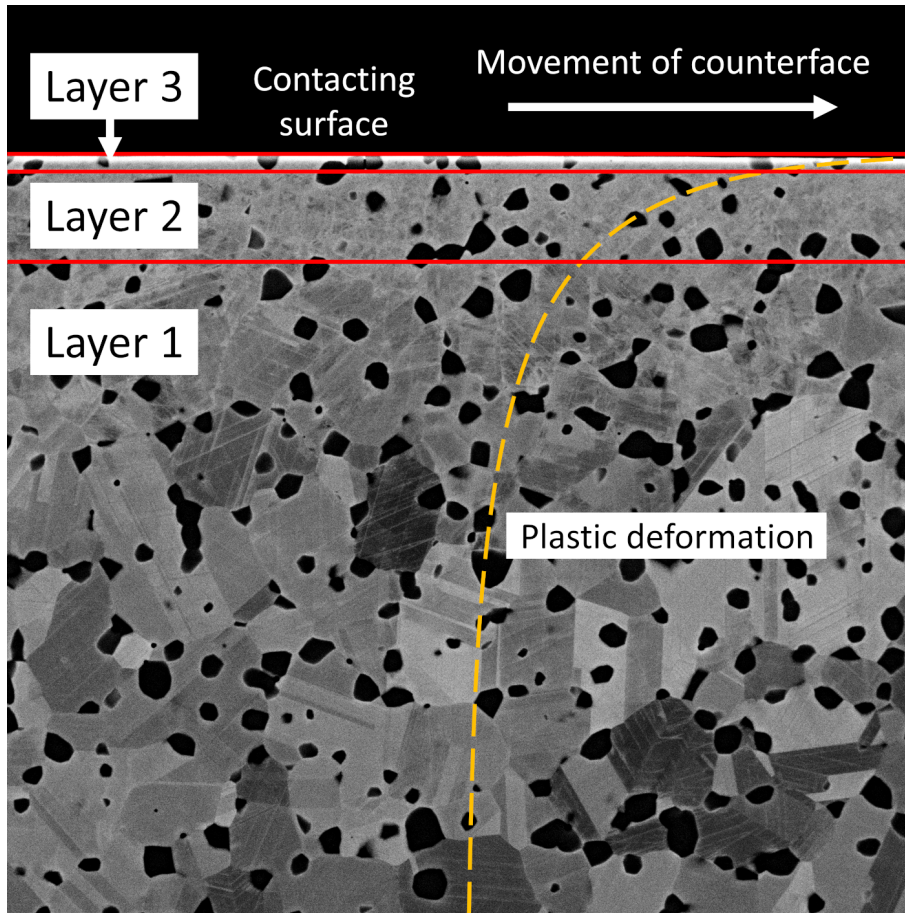


Figure 6.15: Schematic illustrating the different layers within the TAM used to describe the continuum of plastic deformation within the subsurface. The dashed line is an idealised representation of the extent of plastic flow within the subsurface (not to scale).

Layer 1 is the region of the TAM furthest from the sliding contact where the original grain and annealing twin boundaries are still distinguishable, and which is subjected to the lowest levels of strain. It occupies depths $\gtrsim 5$ and $8 \mu\text{m}$ following testing at 20 and 250°C respectively (Figs. 6.8 and 6.9) and grain refinement occurs principally via the formation of deformation bands (Figs. 6.8 and 6.9). These bands are the primary deformation mode in layer 1 and principally form as a result of the strain-induced martensitic transformation (SIMT) $\gamma(\text{fcc}) \rightarrow \epsilon(\text{hcp})$ (Fig. 6.9) which has been extensively observed in Stellite 6 and other related Co-based alloys [80, 108, 143, 144, 278–282]. The SIMT in Stellite 6 occurs via the glide of Shockley partials on every other close packed $\{111\}$ plane and is known to occur up to temperatures of $\sim 700^\circ\text{C}$ [29, 112, 190, 282]. Additionally, ϵ -martensite reportedly forms preferentially at annealing twin boundaries in the early stages of

transformation (Fig. 6.9) [283]. However, some studies suggest that a SIMT may not be the initial mode of deformation in low stacking fault energy (SFE) Co-based fcc alloys [278,279,284]. Therefore, it is possible that within the regions subjected to the very lowest strains (i.e. farthest from the interface), the fcc γ phase could accommodate initial plastic deformation via dislocation glide on the $\{111\}_{\gamma}$ planes, forming intersecting planar arrays of dislocations [279]. As the strain is increased (i.e. closer to the interface), it is suggested that the deformation mode changes first from dislocation slip to $\{111\}_{\gamma}$ twinning [279,285–287], and that further increasing the strain leads to the onset of the $\gamma \rightarrow \epsilon$ martensitic transformation which further refines the original grains by the formation of intragranular ϵ -martensite platelets and their intersection. Within layer 1, it is found that the density of intergranular deformation bands increases towards the contacting surface due to the increasing strain.

Layer 2 is a transition region of severe plastic deformation which shows increased microstructural refinement as the surface is approached (Figs. 6.8 to 6.10). It starts at depths $\gtrsim 1$ and $2 \mu\text{m}$ following testing at 20 and 250 °C respectively, and then merges into layer 1. The grain refinement in this region is so extensive that the original grain boundaries become indistinguishable (Figs. 6.8 to 6.10). Additionally, the high density of ϵ -martensite platelets and their intersection heavily refines the microstructure (Figs. 6.8 to 6.10). The ϵ -martensite phase is heavily flawed with (0001) stacking faults (Fig. 6.10 (observed as fine closely spaced parallel striations)) due to both the nature of the $\gamma \rightarrow \epsilon$ transformation and the extensive strain imposed by the sliding contact deformation [112,278,279]. It is likely that as the surface is approached the increasing strain is first accommodated by an increasing fraction of $\gamma \rightarrow \epsilon$ transformation. At this stage, the development of ϵ -martensite lamellae and networks makes the accommodation of strain particularly difficult in the ϵ -martensite phase therefore, it is likely that deformation is principally accommodated by further transformation of the γ -phase. However, at some point within layer 2, the γ -phase will have fully transformed to the hcp ϵ -phase (Fig. 6.9) and further strain will have to be accommodated by either the twinning and/or dislocation slip of this phase. Given the low SFE of the ϵ -martensite phase,

it is postulated that deformation will principally be accommodate by twinning (Fig. 6.10) which further reduces the effective grain size within this region of the TAM. Twinning is also extensively observed in pure hcp ϵ -cobalt during plastic deformation [279,288–290], even within nanoscale grains [279,290], due to its low stacking fault energy (27 ± 4 mJ/m²) [291,292].

Layer 3 is defined as the region of TAM within $\lesssim 1$ and $2 \mu\text{m}$ of the surface following testing at 20 and 250 °C respectively, and is characterized by predominantly equiaxed nanoscale grains composed entirely of ϵ -Co (as identified by the SAD (Fig. 6.11)) < 100 nm in size (Figs. 6.10 and 6.11). These nanocrystalline grains are heavily flawed with (0001) stacking faults of various orientations and moiré fringes are also observed (Fig. 6.11). In layer 3, it is probable that basal and prism dislocation slip become the dominant mechanism of strain accommodation within the ϵ -Co phase. It is postulated that further grain refinement is achieved via subdivision due to the slip of dislocations which permits the generation of a largely equiaxed nanocrystalline grain structure (Figs. 6.10 and 6.11). It is also suggested that the misorientation between subdivided grains is increased by further dislocation slip on these primary slip systems. There exists a high degree of grain boundary disorder, presumably due to dislocation activity as revealed by TEM (Figs. 6.10 and 6.11) and the lack of clearly defined grain boundaries suggests that grain boundary rotation and grain boundary sliding must be confined to the highest strained regions of layer 3 [279]. Grain boundary rotation and slip and the increased intergranular misorientation caused by dislocation slip could cause the alignment of the primary slip systems parallel to the direction of shear identified in XRD (Fig. 6.7). The alignment of these primary slip systems has previously been reported in pure cobalt [154–156] and Stellite type alloys [152,153,219]. These planes are the planes of lowest friction during siding and are believed to readily accommodate deformation through shear [152–156,219]. However, this preferred orientation may also be a result of the heavily flawed nature of the ϵ -Co phase. Dynamic recrystallisation is not believed to be operative as there appears to be no nucleation/growth period and layer 3 is not composed of defect-free grains with clearly defined boundaries typically observed in dynamically recrystallised

materials (Figs. 6.10 and 6.11). Nevertheless, a lineage with the previous deformation structures is retained during microstructural evolution; therefore, continuous dynamic recrystallization is believed to be operative. Similar observations have been made in a comparable Co-based alloy system [80].

Confirmation of the significant extent of ϵ -martensite formation throughout the layers comes from EBSD (Fig. 6.9) and XRD (Fig. 6.7). Rietveld analysis of these patterns indicates that ~ 95 and ~ 88 vol.% of the matrix was transformed to ϵ -martensite within the interaction volume contributing to the diffracted signal following testing at 20 and 250 °C respectively. Even though the X-ray intensity contributing to the diffracted signal decreases exponentially with increasing depth into the sample [234], the average X-ray penetration depth contributing 99 % of the diffracted intensity was on average $\sim 5 \mu\text{m}$ over the range of 2θ values (35-120°) used in Rietveld refinements. Therefore, the matrix within upper regions of layer 2 and layer 3 must be composed almost entirely of the ϵ -phase. This is in accord with EBSD (Fig. 6.9) and the SAD of layer 3 (Fig. 6.11) which confirms that the matrix phase within layer 3 is entirely composed of ϵ -martensite and that transformation must have occurred at lower strained regions within the deformation continuum and therefore within layer 2.

The transition between layer 2 and 3 can be regarded as the region within which dislocation slip replaces twinning of the ϵ phase as the principal mode of deformation. Dislocation activity has been observed in these regions via TEM (Figs. 6.10 and 6.11). Thus, in accord with various other studies [279, 290], it is hypothesised that dislocation slip becomes operative principally in the form of basal ($\langle 11\bar{2}0 \rangle (0001)$) and prismatic ($\langle 11\bar{2}0 \rangle \{10\bar{1}0\}$) slip. This concurs with Rietveld analysis which showed that the ϵ -phase had a c/a ratio ~ 1.615 which is close to ideal (1.633), so it is expected that both these primary slip systems are active [284, 293]. However, cracking or void formation is not generally apparent in the highly strained nanocrystalline region (Figs. 6.10 and 6.11) therefore, either twinning or $\langle c + a \rangle$ dislocation slip must also be operative in order to satisfy the von Mises requirement for homogenous deformation [284, 294]. It is proposed that the shift in the dominant deformation mechanism from twinning to dislocation

slip of the ϵ -martensite phase can be explained in terms of the reduction in the effective grain size as the sample surface is approached. The critical resolved shear stress for twinning is known to increase as the effective grain size is reduced [278, 279, 295, 296]. The transition in the dominant deformation mode occurs when the critical resolved shear stress for dislocation slip falls below that for twinning as a result of a refinement in the effective grain size [279]. This shift in the mechanisms of strain accommodation has been reported previously in several hcp materials [118, 297, 298].

Although the general microstructural features and deformation mechanisms of the three layers discussed above are representative of the observations made on samples tested at 20 and 250 °C, some differences are observed between the two test temperatures. For example, the extent of $\gamma \rightarrow \epsilon$ transformation observed in EBSD (Fig. 6.9) and XRD (Fig. 6.7) and the depths to which different deformation mechanisms operate beneath the contacting surface. One factor which may be responsible for some of the differences observed in matrix deformation behaviour with respect to temperature is the temperature dependent nature of the SFE of the γ - and ϵ -phases in Stellite 6. Several other studies attribute a temperature dependent reduction in the fraction of $\gamma \rightarrow \epsilon$ transformation during sliding experiments conducted in air on Stellite alloys to a change in the SFE [299, 300]. Whilst there currently exists no data on the SFE of the specific matrix phase compositions in Stellite 6, the temperature dependent nature of both γ - and ϵ -Co has been demonstrated in pure Co [291, 292] and other Co-based binary and tertiary alloys [292, 301]. It is therefore hypothesised that temperature dependence of the SFE both the γ - and ϵ -phases in Stellite 6 may affect the critical strains (and therefore subsurface locations) of the different deformation mechanisms as well as the fraction of $\gamma \rightarrow \epsilon$ SIMT.

A temperature dependent increase in wear has previously been reported in Stellite alloys during in air sliding over the temperature ranges investigated in this work (20-250 °C) [147, 299, 300]. In these instances, the increased wear with respect to increasing temperature over this temperature range was attributed to an increase in the SFE of the matrix and a reduction in the fraction of SIMT

and therefore work hardenability [299,300]. Whilst these studies agree with the general trends in material removal observed in this work, the $\sim 16.5 - 38.7$ times increase in volume loss during sliding in autoclave conditions far exceeds those observed during in air sliding. Although important, it is clear that the temperature dependent nature of SFE does not solely account for the observed increase in wear and therefore, other phenomena must also significantly influence the rate of material removal with increasing test temperature which is explored further in the section on corrosion.

In Stellite 6, detailed characterisation of the matrix-carbide interaction within the TAM has shown that the M_7C_3 precipitates effectively reduce plastic flow by acting as rigid bodies which constrain the matrix and homogenise deformation. The loading conditions imposed by sliding can be described by simple shear and compression, but the presence of the M_7C_3 phase assists in the generation of multiaxial stress states within the matrix. This promotes the activation of different crystallographic deformation systems (faulting on the (111) planes and slip system activation) thus promoting potent matrix work hardening. It is suggested that the M_7C_3 precipitates within the TAM can remain underpinned by the matrix regions subjected to lower strains such that they act to reduce and partially equalize/homogenise the strain gradient within the surrounding matrix closer to the contacting surface. This matrix-carbide interaction significantly stabilises the TAM, contributes to work hardening and helps confine severe plastic deformation within close proximity to the contacting surface.

6.3.2. Mechanical removal of material

Macro/micro-scale material transfer, adhesion and extrusion via ratchetting at the contacting surfaces are rarely observed at either of the test temperatures. By characterising the deformation microstructures beneath the contacting surface in such detail, significant insights have been gained into understanding why Stellite 6 remains so resistant to plasticity dominated wear, adhesion, and material transfer. In related alloys, micro/macro scale shear localisation phenomena and localised instabilities are generally believed to be precursors to material fracture

and transfer events during sliding [73, 202, 302–304]. However, the deformation structures observed at any given depth below the contacting surface of Stellite 6 appear to have resulted in a largely homogenous accommodation of strain on the micro/macro scale and any heterogeneous deformation features are largely retained within the top 2 μm (Figs. 6.10 and 6.11). This resistance to both the generation of inhomogeneous deformation structures and shear localisation phenomena could well be an important reason why material transfer events and extruded slivers of material are rarely observed at the contacting surface of Stellite 6. It should also be noted that the presence of a corrosion product at the contacting surface (Fig. 6.12) will also limit material transfer events.

The principal degradation mechanisms of Stellite 6 in the present self-mated contact conditions must occur via material removal on the nanoscale (often termed nanowear). Despite the differences observed between the two different test temperatures, the previous sections have shown that the subsurface deformation mechanisms and structures within the TAM are generally similar following testing at 20 and 250 °C. With the exception of the occasional carbide pull out (Fig. 6.6), detailed top-surface and cross-sectional investigations of the TAM have provided no evidence to suggest that macro/micro-scale wear mechanisms are the principal modes of degradation (Figs. 6.8 to 6.10). Any evidence of microscale subsurface localisation, microstructural instabilities, mechanical mixing, and the embedding of oxides was relatively infrequent and generally confined within the uppermost regions of layer 3 when investigated on the nanoscale via TEM at both testing temperatures. In light of the above, material detachment must be associated with the uppermost region of layer 3 and principally occur on the nanoscale via the direct removal of nano-sized elements from the sample surface and not typically by macro/micro-scale subsurface rupture as is hypothesised in more conventional wear theories [11]. The following sections aim to elaborate on the potential mechanisms of nanoscale material removal.

6.3.3. Oxidation and tribocorrosion in lithiated water

The previous sections have shown that degradation is principally confined to the nanoscale removal of material from uppermost region of the nano-crystalline layer. Therefore, the oxidative behaviour at the contacting surface of Stellite 6 and its temperature dependence must also be significant to degradation during sliding contact in lithiated water. In related Stellite alloys and tribochemical environments (e.g. 0.5M H₂SO₄), various studies exist which propose that tribocorrosion is the principal cause of degradation during sliding contact tests in different aqueous environments where passivating behaviour is observed [139–142,150,273,274,305]. Stellite 6 is known to exhibit passivating behaviour in lithiated water at both 20 and 250 °C and thin corrosion films composed of CoO and Cr₂O₃ are known to develop [133,134,276]. During self-mated sliding contact in a lithiated water environment at 20 and 250 °C, Ratia et al. [143,144] suggest that the principal factor governing degradation is the repeated removal and regrowth of a passive oxide film on Stellite 6 by the application of a mechanical stimulus (i.e. wear enhanced corrosion - the corrosion of depassivated metal). Tribocorrosion of the carbide phase, i.e. the amount of material removed during a sliding contact depassivation/passivation cycle, is potentially related to the mechanism and kinetics of oxide film formation over the carbide surface. Hocking et al. [134] have shown that in lithiated high temperature water an oxide film forms over the carbide but with a lower thickness than over the matrix (~ 40 %). This concurs with other studies which suggest that the Co-rich matrix corrodes faster than the carbide phase [138,306].

In the present work, the passivating behaviour of Stellite 6 was confirmed and TEM revealed a thin (10 - 20 nm) passive oxide layer at the contact surface which is principally composed of Co and a smaller fraction of Cr (Fig. 6.12) following testing at 250 °C. This observation agrees with various earlier studies [133,134,276]. For example, the X-ray photoelectron spectroscopy study by McIntyre et al. [276] who identified a 10 to 15 nm thick passive film involving primarily CoO and Cr₂O₃ when Stellite 6 was tested in water of pH 10 at 285 °C during short term exposure (168 h). It is important to note that the passive film observed in Fig. 6.12 could

be affected by the time spent in lithiated water at various temperatures during the autoclave cool down period following testing at 250 °C. Further growth of the passive film and/or metal dissolution is possible during this period; however it is likely that the extent of growth would be small as the kinetics must slow down as the temperature falls. Additionally, fast passive film growth is expected on a depassivated surface (wear induced) which subsequently slows once a stable film forms - especially at low temperatures.

6.3.4. Synergistic degradation effects in lithiated water

It is clear that the passivating behaviour of Stellite 6 is fundamentally important to degradation via tribocorrosion during sliding in lithiated water [143, 144, 150]. However, the mechanisms of tribocorrosion (corrosion enhanced wear and wear enhanced corrosion) leading to the nanoscale removal of material are less well understood, and the role of passivation needs to be integrated with subsurface mechanical deformation, mechanical mixing and three-body sliding abrasion effects when evaluating nanoscale material detachment. Based on the findings presented in this work, it seems likely that degradation involves a complex interaction of both mechanical deformation and chemical phenomena. These collectively result in the detachment of predominantly nanoscale particulates composed of oxidised material which may also contain a fraction of metallic and or mixed metal plus oxidised material at the point of detachment. Regardless, the wear enhanced corrosion mechanism (i.e. the corrosion of depassivated metal) which has previously been described in the literature still seems to be generally applicable to the self-mated sliding of Stellite 6 in lithiated water, despite the fact it is almost certainly an oversimplification of the tribocorrosion phenomena occurring in the present investigation [143, 144, 150].

Temperature dependent variation in the oxidative reactions and passivating behaviour occurring at the contacting surface of Stellite 6 are likely to influence the plastic strain accumulation and the deformation characteristics and microstructures within the subsurface (Figs. 6.8 to 6.11). It is postulated that the increase in the passive oxide thickness observed at 250 °C may lead to increased strain during

sliding. This is one factor which could account for the increased deformation observed at any given depth following testing at 250 °C (Figs. 6.8 to 6.11). This concurs with Maldonado et al. [150] who showed that increased passivation on Stellite type alloys increases the strain induced during sliding. In light of the above, it is suggested that the differences observed in the deformation induced subsurface microstructure between the different test temperatures (Figs. 6.8 to 6.11) will influence the passive behaviour at the contact. Likewise, the extent of passivation at a given temperature will influence the deformation mechanisms and subsurface strains. The rate of passivation and extent of subsurface deformation are closely coupled to one another and are both influenced by temperature; this interaction between chemical and mechanical phenomena may influence the rate of material removal from the surface.

It is possible that metal dissolution and passivation reactions at the contacting surface may enhance the wear of the nanocrystalline layer [74, 75, 78, 82, 150, 275]. Given the matrix deformation mechanisms identified within the nanocrystalline layer (Table 6.3), it is possible that oxidation/passivation, molecular absorption and or dissolution may influence near surface mechanical properties and intergranular bonding which will affect the removal of nanoscale particulates from the surface. Several studies [75, 150] suggest that passive films influence the deformation characteristics within nanocrystalline layers possibly by: (i) acting as a source of dislocations and or other deformation structures due to a potential mismatch in elastic properties between the passive film and underlying material, (ii) manipulating the composition and therefore SFE of the metallic material directly beneath the passive film which alters the critical strains for deformation, and (iii) obstructing the free surface therefore hindering dislocation annihilation. Increased defect densities due to the presence of a passive layer will promote increased continuous dynamic recrystallization and the generation of increasingly smaller grains beneath the subsurface (Figs. 6.10 and 6.11) which may influence the nanoscale removal of material. Grain boundary sliding and rotation has been highlighted as a possible deformation mode in the highest strained regions of the nanocrystalline layer; therefore the potential chemical manipulation/modification of grain

boundaries due to passivation may be significant in the removal of nanoscale particulates.

TEM has shown that nanolayers may develop at the contacting surface in the form of < 20 nm thick mechanically mixed nanolayer/tribofilm within which almost no microstructural features are clearly distinguishable (Fig. 6.13). In this particular instance, the tribofilm is generated as matrix material is forced to plastically flow over the top of an M_7C_3 carbide (Fig. 6.13). However, such features have also been observed over the matrix phase and do not cover the entirety of the contacting surface. Regardless, these nanolayers have clearly accommodated large strains. It is probable that nanoscale mechanical mixing within the autoclave environment causes a compositional change within the tribofilm (Fig. 6.13); this is most probably due to oxidation, metal dissolution and or oxide embedding. The formation of this tribofilm may account for the mottled variation in contrast that is observed across both the carbide and matrix phases (Fig. 6.6). It is hypothesised that this nanoscale mechanical mixing and interaction with the test environment may be partially responsible for material detachment and possibly contribute to the higher rates of wear at $250\text{ }^\circ\text{C}$. Moreover, a compromised ability to retain a tribofilm due to environmental changes including increased passivation at elevated temperature ($250\text{ }^\circ\text{C}$) may be a factor which contributes to the increased wear observed at $250\text{ }^\circ\text{C}$ as well as the difference in subsurface deformation. It is not definitively clear how these nanolayers become detached or degrade; however discontinuities have been observed at the interface between the nanolayer and the bulk material (Fig. 6.13) which suggests fracture after extrusion via plastic ratchetting may be important. Additionally, the extent of chemical degradation/oxidation during the mechanical mixing of these nanolayers prior to their detachment or degradation still remains much debated. Whilst the classical wear enhanced corrosion mechanism which involves the corrosion of de-passivated metal is still relevant [143, 144, 150], such mechanisms do not account for the formation of mechanically mixed nanolayers on the contacting surface. Thus, the term "corrosion enhanced nanowear" seems to be a more fitting way of describing degradation in the instance where nanolayers are present. These nanocrystalline

tribofilms readily accommodate high strains possibly by crystallographic slip or grain boundary slip and rotation. Therefore, the formation of such tribofilms may partially account for the preferred orientation of the primary slip systems observed in XRD (Fig. 6.7). These planes are reported to be the planes of lowest friction which readily accommodate deformation through shear [152–156,219].

The scratching and scoring observed on the contacting surface (Figs. 6.5 and 6.6) is likely to be influenced by debris particles/agglomerates partially retained within the sliding contact which induce a three-body sliding abrasion situation prior to their ejection [150]. The increased plastic disturbance and surface roughening caused by abrasive debris within the sliding contact unquestionably promotes nanoscale material removal, possibly by micro-cutting in some instances given that notable prow formation is not frequently observed (Fig. 6.6) [150]. One source of abrasive particles comes from the carbides, and several micro and nanoscale abrasion marks can be directly traced back to the locations where carbide pull-outs have occurred (Fig. 6.6). The M_7C_3 precipitates are largely equiaxed in as-received HIPed Stellite 6 (Figs. 6.2 and 6.3) therefore, the high aspect ratio carbides observed at the contacting surface (Figs. 6.10, 6.13 and 6.14) must be generated by the wear of carbides which are effectively constrained at the sliding interface by the surrounding matrix. It is postulated that carbide pull-out may occur when the carbide reaches a critical thickness where carbide fracture may occur (Figs. 6.6 and 6.14) and/or, the combined matrix-carbide interaction is no longer an effective barrier to extensive plastic flow (Fig. 6.6). For example, the vertical crack in the carbide shown in Fig. 6.14 most probably occurs when it is critically thinned to a point where it can no longer support the loads imposed during sliding.

The tribologically affected surface is considerably rougher following testing at 250 °C (Figs. 6.5 and 6.6) and estimates of the average maximum wear track depth have been calculated to be ~ 1.7 and $8.8 \mu\text{m}$ following testing at 20 and 250 °C respectively. This increase in surface roughness following elevated temperature testing can most probably be related to the average maximum wear depths and the scale of the microstructural features. The size of the M_7C_3 carbides are $\sim 1 - 4$

μm with an average spacing of $\sim 2 - 3 \mu\text{m}$ between them. Upon comparing the microstructural scale and distribution of the carbides with the average maximum wear depths, it is clear that a higher fraction of carbides (or fragments of carbides) will be released during testing at 250°C which subsequently generates a rougher surface.

Another source of nanoscale abrasive debris particles comes from the detachment of oxidised material and possibly work hardened matrix and/or mechanically mixed metal plus oxide. These nanoscale abrasive particles may oxidise further and agglomerate during sliding. The debris particles and agglomerates reportedly get bigger with increasing test temperature [143]. The larger fraction of debris contained within the sliding contact at any given time during testing at 250°C increases the statistical likelihood of particle agglomeration prior to ejection from the sliding contact; this may be a factor which contributes to the deeper abrasion marks and increased three-body sliding abrasion observed at 250°C .

6.4. CONCLUSIONS

As received HIPed Stellite 6 (Co-27.08%Cr-5.01%W-1.47%C-0.87%Ni-0.73%Fe-0.07% Other in wt%) is comprised of ~ 13.3 vol % of equiaxed Cr-based M_7C_3 precipitates ($\sim 1 - 4 \mu\text{m}$ in size) which are surrounded by a Co-based (fcc) solid solution matrix (~ 86.3 vol %) and a very small fraction (~ 0.4 vol %) of a Co-based ϵ -phase (hcp).

The tribologically affected material beneath the sliding surface is subject to a deformation gradient where the highest strains are generated at the contacting surface. In the early stages of plastic deformation (furthest from the contacting surface), strain is principally accommodated by the complete deformation induced martensitic transformation of the γ -phase to ϵ -martensite. This ϵ -martensite phase accommodates further strain via twinning and basal and prismatic dislocation slip as the sample surface is approached. In the highest strained regions directly adjacent to the contacting surface, the ϵ -martensite subsurface microstructure is nanocrystalline and microstructural refinement and strain accommodation are principally driven by dislocation slip. Stellite 6 is highly resistant to plastic strain

localisation phenomena due to an ability to sustain a sufficient strain hardening rate (continued defect storage at high strains) which prevents the accumulation of large strains in localised regions.

It is speculated that the synergistic effect of the chemical manipulation of the near surface due to passivating behaviour and mechanical stimulation by sliding contact results in the removal of nanoscale particles from the contacting surface which may also cause further nanoscale degradation via three-body abrasion. The detachment of nanoscale particulates cannot be attributed to a singular phenomenon; moreover the unique subsurface deformation characteristics exhibited by Stellite 6 suppress material removal to the nanoscale where chemical oxidative reactions and other tribochemical interactions are capable of greatly influencing material detachment during sliding. A synergistic temperature dependent increase in corrosion rate and stacking fault energy principally account for the increased wear rates observed at 250 °C, however the rate of corrosion is believed to be the dominant factor influencing wear. These factors effect degradation through the modification of: mechanical deformation characteristics, the extent of corrosion enhance wear and/or wear enhanced corrosion, the amount of nanoscale mechanical mixing, the frictional state of the contact, the amount of material detachment and the degree of three-body abrasion. The amalgamation of these various factors is believed to result in the $\sim 16 - 39$ times increase in material removal when the test temperature is increased from 20 to 250 °C. This further highlights the importance of the specific test environment when assessing the suitability of materials for specific applications.

TRIBOLOGICAL ASSESSMENT OF SELF-MATED HIPED TRISTELLE 5183 SUBJECTED TO SLIDING IN LITHIATED WATER

7.1. INTRODUCTION

The current chapter aims to provide a detailed tribological assessment of HIPed Tristelle 5183 during sliding in lithiated water at 20 and 250 °C. To date, the exceptional wear and corrosion resistance exhibited by Stellite 6 cannot be readily replicated in Fe-based alloy systems. This is generally acknowledged within the literature [13,14], however a mechanistic understanding of this disparity in performance between Fe and Co based hardfacings has not yet been comprehensively evaluated. Tristelle 5183 [6–9] is one of a handful of alloys developed in an initial response to minimise the use of cobalt in PWR systems and can therefore, be regarded as one of the baseline alloys from which more recent Fe-based hardfacings have evolved. The design rationale of Tristelle 5183 is essentially simple yet robust. It was recognised that chromium-nickel-silicon austenitic stainless steels are especially suited for nuclear applications due to their corrosion resistance and that alloying could be performed to optimise the tribological and engineering properties whilst retaining a sufficient degree of corrosion resistance [6]. The tribological performance of Tristelle 5183 is principally manipulated via alloying additions which promote the precipitation of secondary hard carbide phases, namely, M_7C_3 and NbC.

In response to the industrial pressures demanding an Fe-based replacement for Stellite 6, a large proportion of the research interest in this area has been

focused on the empirical development of next generation Fe-based hardfacings. Unfortunately, as a result, the mechanisms dictating the tribological degradation of Fe-based alloy systems are still not well understood. Therefore, the design rationale behind next generation Fe-based hardfacings is arguably lacking in scientific robustness. In light of the above, the present study focuses on developing a comprehensive understanding of the deformation and degradation mechanisms of the baseline hardfacing alloy designated Tristelle 5183. In the authors opinion, this is a necessary step to enable the more informed design of Fe-based hardfacing intended for nuclear applications. The subsurface deformation mechanisms have received particular attention in this chapter as wear is an evolutionary process which is often critically dependant on the load specific deformation mechanisms which lead to and permit the operation of specific wear mechanisms.

7.2. RESULTS

The chemical analysis, phase makeup and microstructural characterisation of HIPed Tristelle 5183 are reported in Chapters 3 and 5. This chapter specifically focuses on sliding contact tribological behaviour of Tristelle 5183 within an autoclave environment.

7.2.1. Autoclave sliding contact test results - mass and volume loss measurements

The combined pin and disk mass and volume losses for Tristelle 5183 after 5 h sliding contact tests at 20 and 250 °C within an autoclave environment are shown in Fig. 7.1. The volume loss measurements were calculated from the mass loss values using a measured density of $7505 \pm 5 \text{ kgm}^3$. The average volume loss values equate to an average total specific wear rate of $3.42 \times 10^{-6} \text{ mm}^3 \text{m}^{-1} \text{N}^{-1}$ and $5.25 \times 10^{-5} \text{ mm}^3 \text{m}^{-1} \text{N}^{-1}$ for testing at 20 °C and 250 °C respectively. The combined pin and disk volume and mass loss increased by a small factor (between ~ 1.1 and ~ 2.1) when the temperature was raised from 20 °C to 250 °C. Table 7.1 shows a breakdown of the individual pin and disk mass losses following testing at 20 and

250 °C. At 250 °C, there is a notable disparity between the pin and disk mass loss, and the disk wears significantly more than the pin (Table 7.1). This is not the case following testing at 20 °C (Table 7.1) and suggests there is a significant difference in wear mechanism between the two different test temperatures. It could be argued that the influence of corrosion on the regions of the sample surface not exposed to mechanical stimulation will also contribute to the mass change that is measured during testing. However, measurements made on corrosion samples at 250 °C in the absence of sliding contact showed that the contribution of corrosion alone was insignificant over the 5 h testing period used in the present experiments.

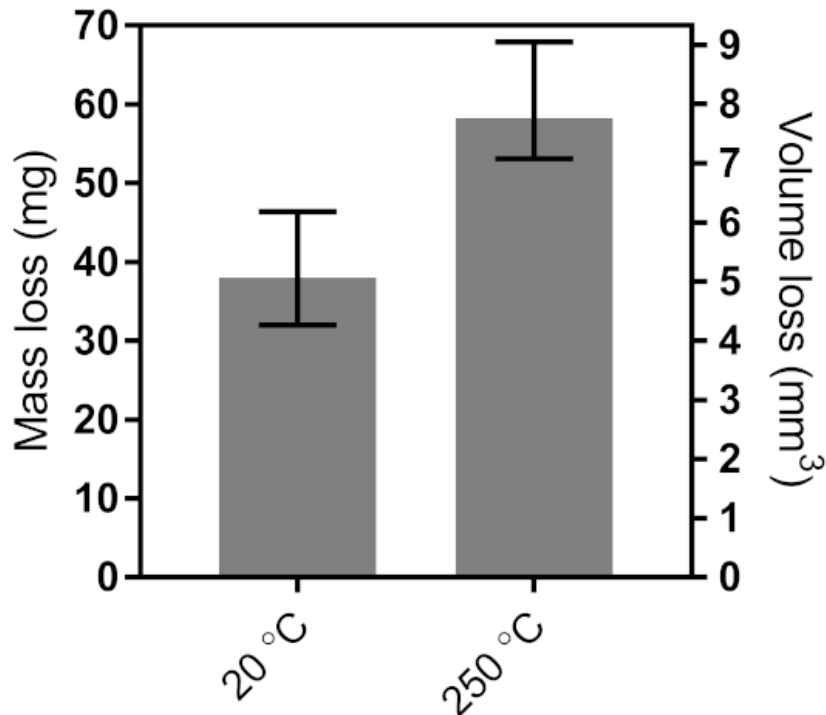


Figure 7.1: Graph showing the effect of autoclave test temperature on the mass and volume loss of self-mated Tristelle 5183 following 5 h sliding contact testing with a 4 kg dead load. The bars represent mean values and the error bars represent the minimum and maximum values of combined pin and disk wear ($n_{20}=3$, $n_{250}=6$).

Table 7.1: The effect of test temperature on the individual components of pin and disk mass loss of Tristelle 5183 following 5 h autoclave sliding contact testing with a dead load of 4 kg. The errors have been reported as the standard error of the mean ($n_{20}=3$, $n_{250}=6$).

Test temperature ($^{\circ}\text{C}$)	Pin mass loss (mg)	Disk mass loss (mg)	Total mass loss (mg)
20	15.1 ± 1.4	22.9 ± 3.8	38.0 ± 4.3
250	13.7 ± 1.5	44.5 ± 1.6	58.2 ± 2.6

7.2.2. Sub-surface microhardness profiles

Fig. 7.2 shows Knoop hardness profiles from perpendicular cross sections of wear scars following autoclave testing at both 20 and 250 $^{\circ}\text{C}$. In both instances, a similar degree of work hardening has been achieved in response to sliding contact.

7.2.3. Microstructural characterisation of the contacting surfaces - surface topography

Fig. 7.3 shows low magnification optical micrographs of Tristelle 5183 disks (Fig. 7.3 (a) and (b)) and pins (Fig. 7.3 (c) and (d)) after sliding contact tests at 20 (Fig. 7.3 (a) and (c)) and 250 $^{\circ}\text{C}$ (Fig. 7.3 (b) and (d)). The disk wear tracks presented in Fig. 7.3 measure ~ 6.9 mm and ~ 6.5 mm in width following testing at 20 and 250 $^{\circ}\text{C}$ respectively. These images confirm the trends observed in the mass and volume loss measurements presented in Fig. 7.1, and the test temperature (specifically when comparing testing between 20 and 250 $^{\circ}\text{C}$) clearly has little effect on the wear track width. However, there is a noticeable discolouration of the alloy surface following exposure at 250 $^{\circ}\text{C}$, suggesting that a thin corrosion product formed more readily at this temperature than at 20 $^{\circ}\text{C}$. Additionally, at 250 $^{\circ}\text{C}$, dark contrast regions which are elongated in the direction of sliding are observed throughout the wear tracks and these features are consistent with increased corrosion/oxidation (Fig. 7.3 (b) and (d)). The worn surfaces of the Tristelle 5183 samples (Fig. 7.3) exhibit features characteristic of adhesive wear and can principally be characterised by scuffing; however, the extent of scuffing is more extensive at room temperature when compared to that observed at 250 $^{\circ}\text{C}$. As a result, the wear track has a smoother topography following testing at 250

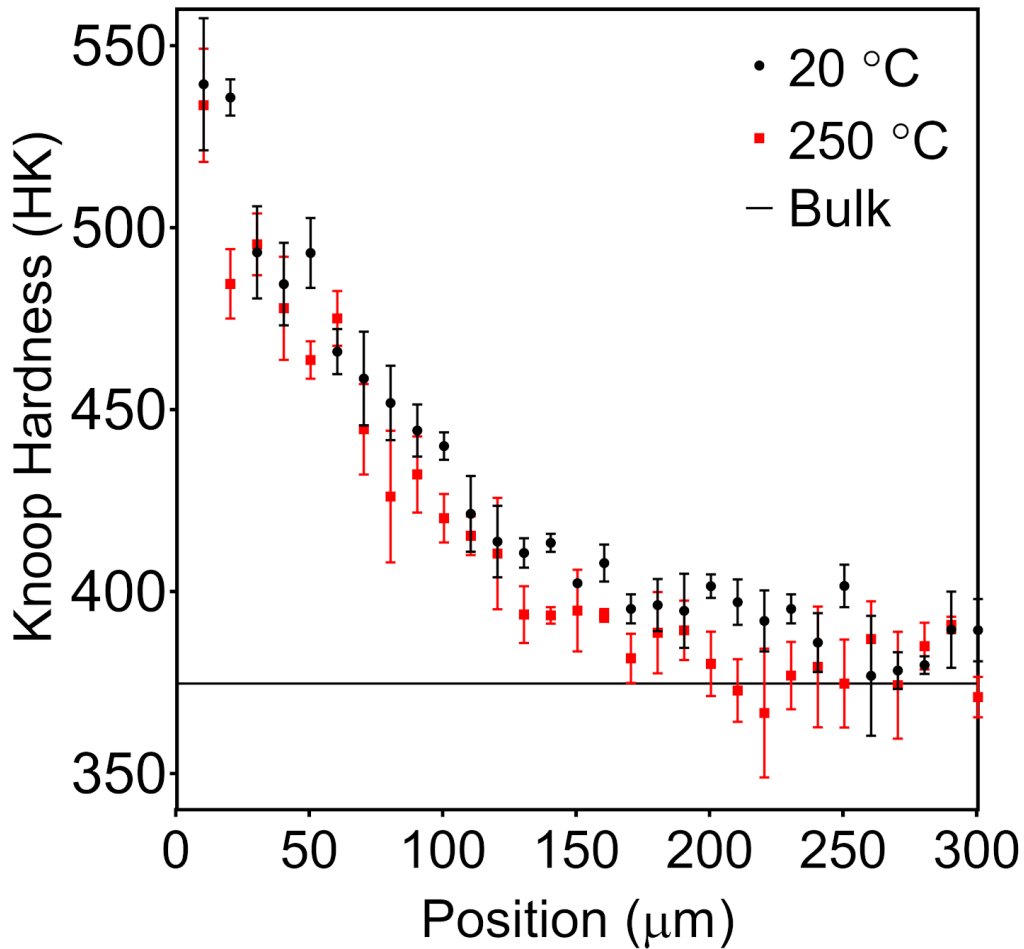


Figure 7.2: Hardness microhardness (10 g load) profiles taken from perpendicular cross sections of wear tracks following autoclave sliding contact at both 20 and 250 °C. The errors have been reported as the standard error of the mean ($n = 3$).

°C compared to 20 °C. Calculated average maximum wear track depths were estimated at ~ 10.6 and $21.8 \mu\text{m}$ following testing at 20 and 250 °C respectively. These values have been calculated from the disk mass loss measurements (Table 7.1), the measured density, the measured average final wear track width (Fig. 7.3), the radius of the wear track, and the assumption that the wear track transverse cross section conforms to the geometry of a segment of a circle.

The surface features revealed by SEM examination show significant differences between testing at 20 and 250 °C. Fig. 7.4 shows plan view SE (Fig. 7.4 (a)) and BSE (Fig. 7.4 (b) and (c)) micrographs from central regions within a wear track following

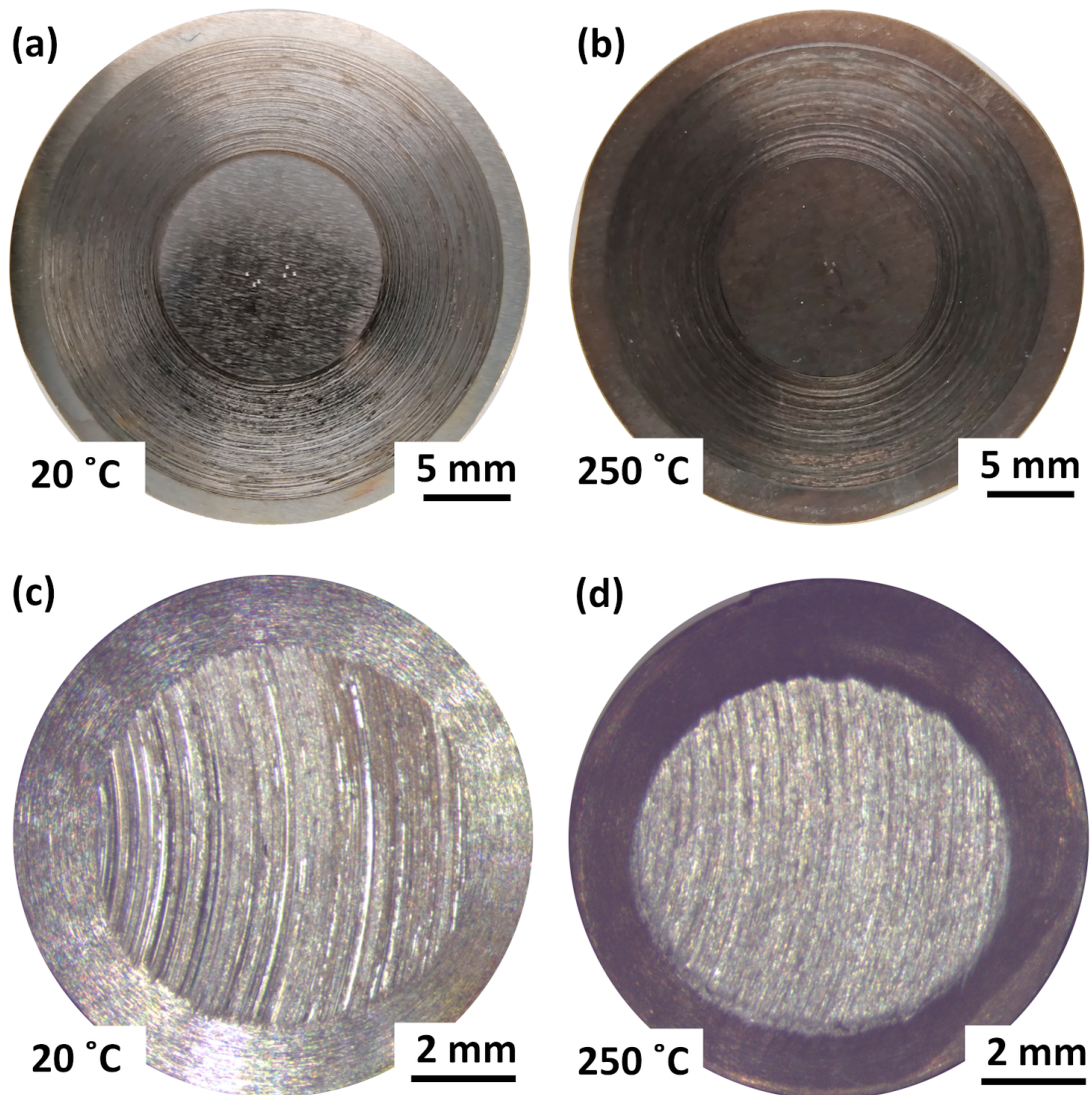


Figure 7.3: Stereoscope optical micrographs of Tristelle 5183 disk ((a) and (b)) and pin ((c) and (d)) tribologically affected surfaces following sliding contact autoclave tests at 20 °C ((a) and (c)) and 250 °C ((b) and (d)).

testing at 20 °C (sliding direction horizontal). The worn surface is characteristic of plasticity dominated wear and exhibits highly deformed slivers/platelets of material which are metallic in nature. Extruded slivers which have incurred gross plastic deformation are extensively observed within the wear track and are clearly elongated in the direction of shear (horizontal). In some instances, there is clearly some form of discontinuity between the extruded slivers and underlying material in the form of ductile shear crack seemingly generated by extrusion. This makes the extruded slivers appear partially delaminated in appearance. However, other forms of surface defect and crack generation are apparent within the contacting

surface. The bright and dark contrast precipitates visible in the BSE micrographs (Fig. 7.4 (b) and (c)) are the NbC and Cr-based M_7C_3 carbide phases respectively; these have previously been identified in the as-received material (Chapter 5).

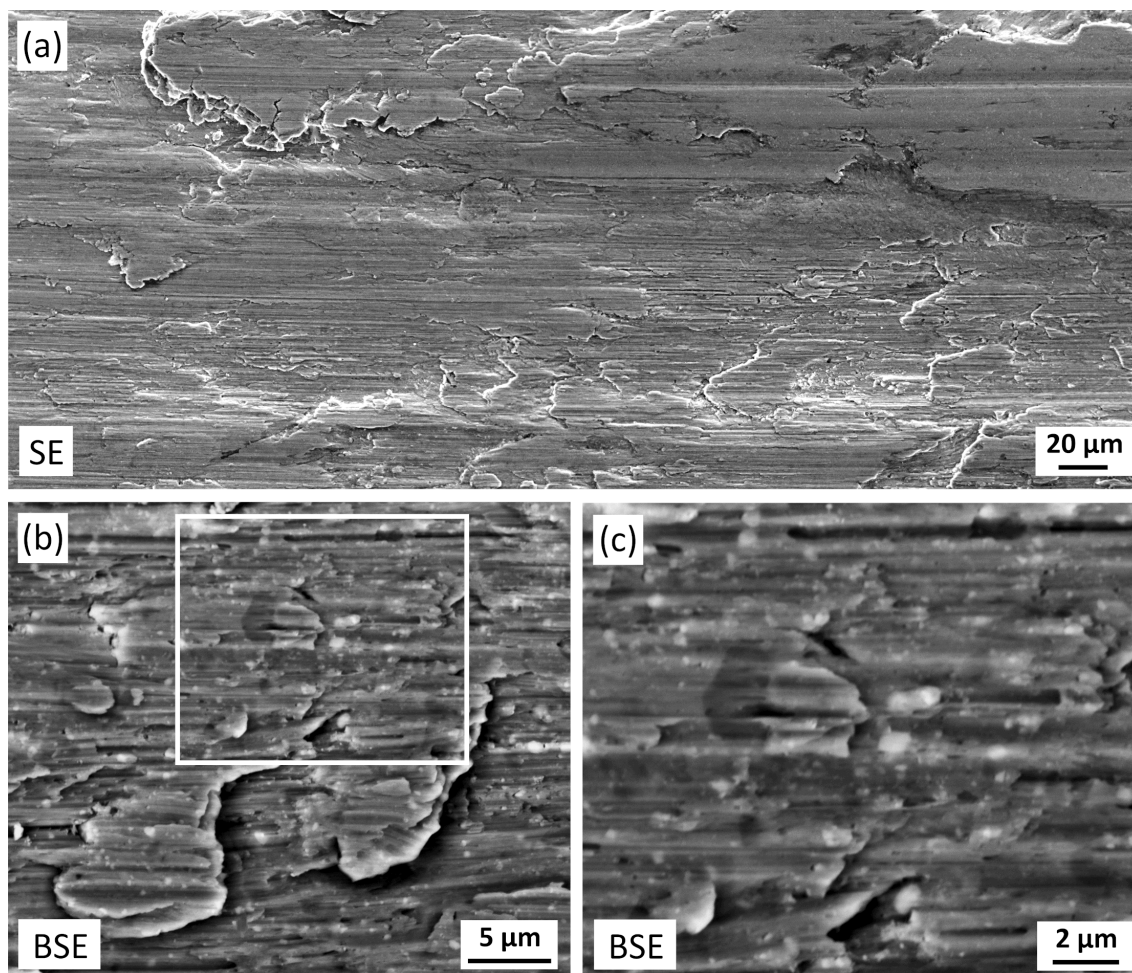


Figure 7.4: SE (a) and BSE (b and c) SEM micrographs showing the microstructure of the tribologically affected surface of Tristelle 5183 disk samples after sliding contact tests in an autoclave environment at 20 °C for 5 hours. (c) is a higher magnification image of the region marked with the white square in (b). The sliding direction is horizontal to the figure in all cases.

Fig. 7.5 (a) displays a plan view BSE micrograph, the entire width of a wear track, from a disk sample (sliding direction horizontal) following testing at 250 °C, and grinding marks are clearly visible at both the top and bottom of this image. Fig. 7.5 (b) and (c) show a matched pair of plan view BSE and SE images of the wear track also following testing at 250 °C (sliding direction vertical). The worn surface is complex, highly variable in appearance and notably different to that

which formed at 20 °C (Fig. 7.4). One dominant feature is the accumulation of material on the surface revealed as dark contrast regions in the BSE images, Fig. 7.5 (a) and (b), and as agglomerates of compressed fine scale material in the SE image, Fig. 7.5 (c). The EDX maps, Fig. 7.5 (d) and (e), indicate that these regions are most likely mixed accumulations of predominantly oxidised material and debris which form compacted beds. These compacted beds are extensively observed on both a macro- and micro-scale throughout the wear track (Fig. 7.5 (a) and (b)) and become smeared in the direction of sliding, seen as dark grey contrast striations in Fig. 7.5 (a) and (b). The region to the right of the wear track observed in Fig. 7.5 (b) and (c) exhibits the characteristics of plastically dominated wear and slivers of plastically extruded metallic material are clearly visible. These slivers are clearly elongated in the direction of sliding (vertical) and appear to exhibit some form of discontinuity with the underlying material; principally in the form of ductile shear cracks although other defects are observed. The EDX maps, Fig. 7.5 (d) and (e), reveal that the plasticity dominated wear region is principally metallic in nature and give a comparably low oxygen signal from EDX analysis. Vertical streaks of Nb-rich material consistent with the NbC phase are observed in Fig. 7.5 (f); these features almost certainly depict the break up/fracture of the large scale (up to $\sim 20 \mu\text{m}$ sized) NbC particles previously identified within the as-received material (Chapter 5). The Nb (Fig. 7.5 (f)) and Cr (Fig. 7.5 (g)) EDX maps show very fine particulates which are entirely consistent with the NbC and M_7C_3 precipitates identified in the as-received HIPed material.

Fig. 7.6 shows higher magnification SEM images after testing at 250 °C. The BSE image, Fig. 7.6(a), reveals bright and dark contrast precipitates at the surface which are the NbC and Cr-based M_7C_3 phases respectively. The regions of darkest contrast in the BSE image, Fig. 7.6 (a), probably show micro-scale accumulations of oxidised material and debris which form compacted beds. These compacted beds conform to the topography of voids/depressions caused by either, (i) scuffing events, (ii) carbide pullout or (iii) material removal. The SE image, Fig. 7.6 (b), shows faceted sub-micron crystals decorating the surface which are most probably individual nanoscale oxide crystals.

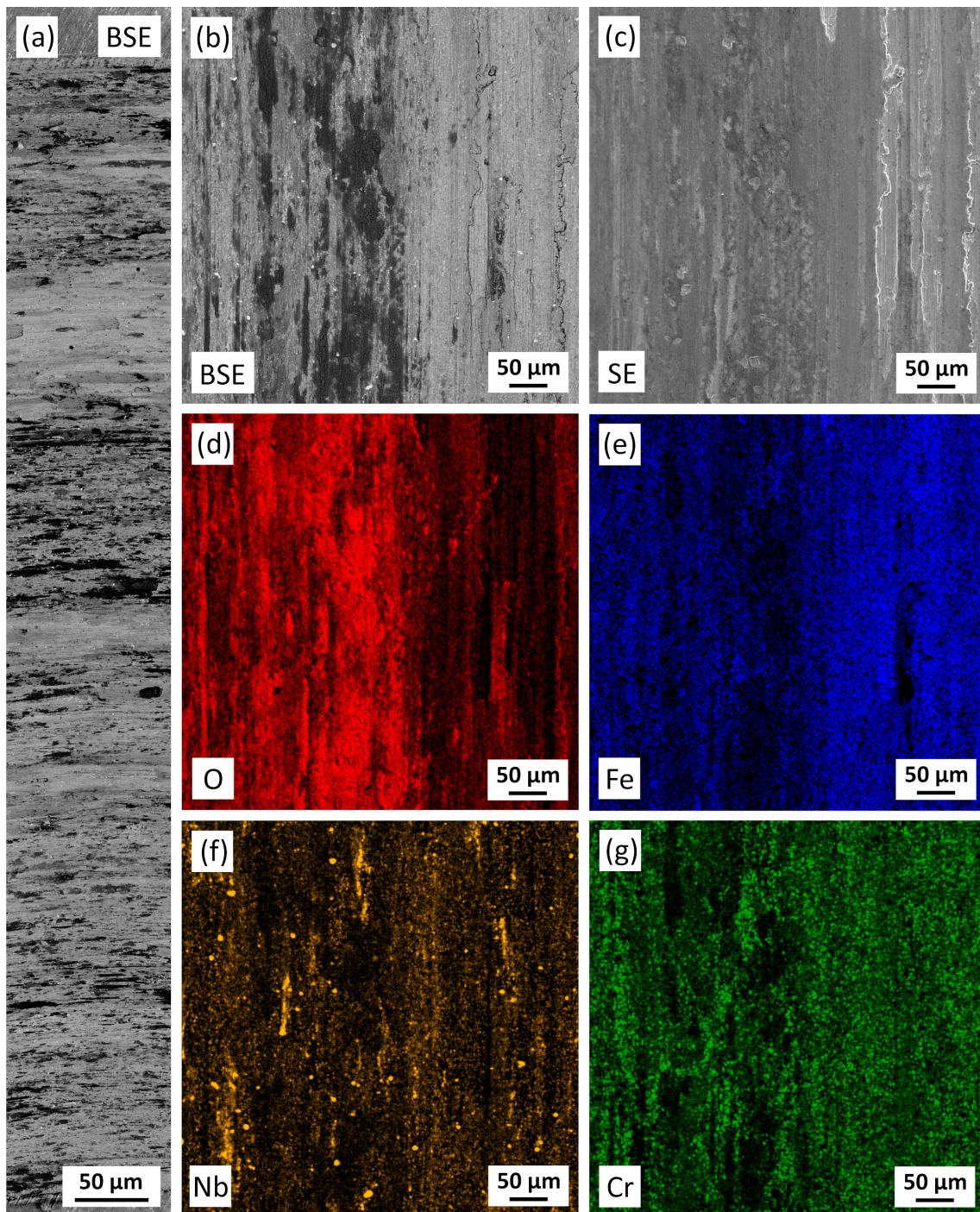


Figure 7.5: BSE (a and b) and SE (c) SEM micrographs showing the microstructure of the tribologically affected surface of Tristelle 5183 disk samples after sliding contact tests in an autoclave environment at 250 °C for 5 hours. (a) covers the entire width of the wear track and the sliding direction is horizontal. The sliding direction is vertical in (b) and (c). (d), (e), (f) and (g) show EDX maps of the same region depicted in (b and c) and correspond to the maps for O, Fe, Nb and Cr respectively. The sliding direction is horizontal in (a) and vertical in (b - g).

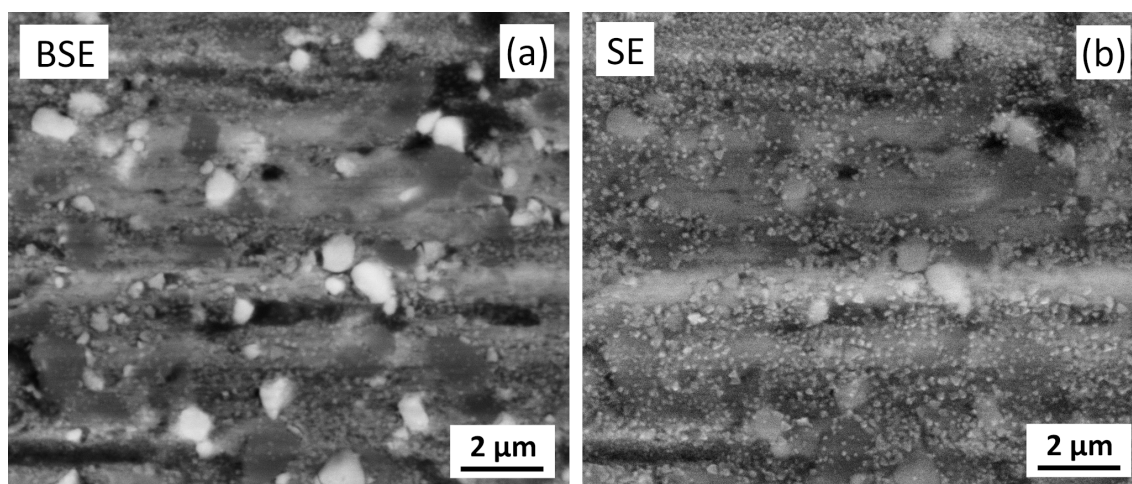


Figure 7.6: High magnification BSE (a) and SE (b) SEM micrographs showing the microstructure of the tribologically affected surface of Tristelle 5183 disk samples after sliding contact tests in an autoclave environment at 250 °C for 5 hours. The sliding direction is horizontal to the figure in all cases.

7.2.4. X-ray diffraction analysis of sliding contact test samples

The X-ray diffractograms shown in Fig. 7.7 were obtained from the as-received HIPed material (polished surface) and from regions within the wear tracks following testing at 25 and 250 °C. As expected, all the phases observed in the as-received material are still present following autoclave testing at both temperatures. However, autoclave testing has clearly had a profound effect on the peak shapes of all the phases relative to the polished surface of Tristelle 5183. This change in peak shape is a result of crystallographic faulting and crystallite size and strain broadening effects induced by autoclave sliding contact. Reflections that are consistent with bcc/bct α/α' -Fe (e.g. at $\sim 44.8^\circ$) are also observed in the XRD pattern following testing at 20 °C and are due to deformation induced martensitic (DIM) transformation. This martensitic transformation is not detected following testing at 250 °C, and it is suggested that martensitic transformation is suppressed under these testing conditions. Reflections (e.g. at 35.5°) consistent with a spinel iron oxide (isostructural to magnetite) are also observed in the diffractogram obtained from the wear track of Tristelle 5183 tested at 250 °C. This iron oxide is presumably consistent with the crystalline oxide-rich microstructural features seen on the contacting surface of Tristelle 5183 after testing at 250 °C (Fig. 7.6 (b)).

The γ -Fe reflections are particularly sensitive to autoclave testing, and profound differences concerning the peak broadening, maximum peak intensities, peak shift, and peak asymmetry of the γ -Fe reflections are observed between the polished surface, autoclave testing at 20 °C and autoclave testing at 250 °C. Firstly, autoclave sliding testing at both temperatures clearly causes a broadening of the γ -Fe reflections. However, the broadening of the γ -Fe reflections is greater following testing at 20 °C and this broadening is particularly noticeable in the {200} reflection. Secondly, there is a notable difference in the peak height ratios of the {111} : {200} γ -Fe reflections in the diffractograms following autoclave testing compared to the polished sample, and this disparity is larger following testing at the lower temperature. Finally, there is a significant shift of the {200} reflection towards lower 2θ values following autoclave testing relative to the polished HIPed sample, and this shift is larger following testing 20 °C compared to 250 °C. These phenomena are all believed to be due to a number of factors including, crystallographic flaws (stacking faults), crystallite size and microstrain broadening and a possible contribution from a sliding induced preferred orientation of the {111} reflections.

7.2.5. Sub-surface microstructural characterisation - SEM

BSE-SEM micrographs taken from within the wear track parallel to the sliding direction are shown following autoclave testing at 20 °C (Fig. 7.8 (a), (c) and (f)) and 250 °C (Fig. 7.8 (b), (e) and (g)). At both test temperatures, the matrix microstructure below the surface has undergone considerable microstructural refinement due to severe plastic deformation and reveals a clear deformation gradient. The matrix deformation microstructure is principally composed of elongated structures/crystallites of varying contrast which become aligned parallel to the sliding direction in the regions closest to the contacting surface and clearly defined matrix grain boundaries are no longer easily distinguishable. This matrix has clearly incurred a highly localised deformation and the microstructure appears analogous those typically observed during shear banding. Despite the similarities in the total material removal after testing at 20 and 250 °C (Fig. 7.1), the cross-sectional SEM

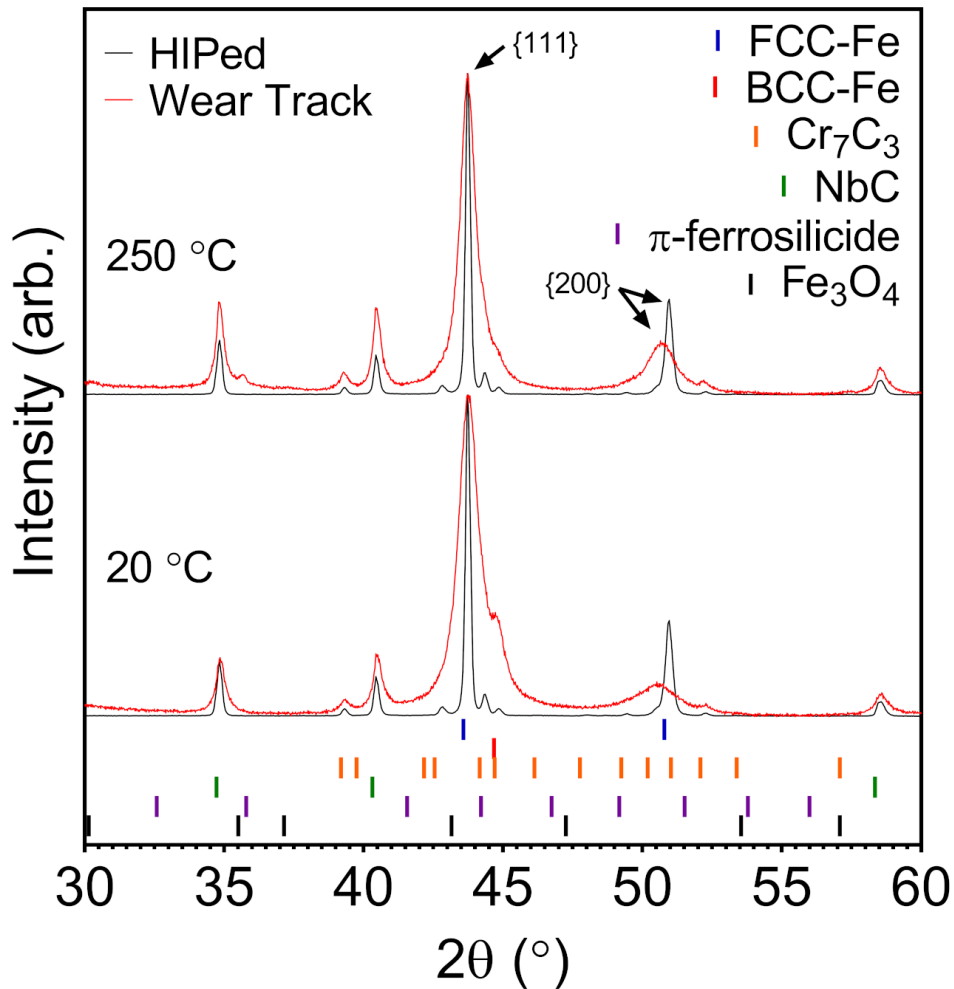


Figure 7.7: XRD patterns of Tristelle 5183 in the as-received HIPed form and from within the wear track (following testing at 20 and 250 °C). Patterns normalised to the reflection of maximum intensity.

analysis shows distinctly different subsurface features in the regions up to $\sim 4 \mu\text{m}$ from the contacting surface.

Fig. 7.8 (a) and (f) show that during testing at 20 °C extruded slivers/layers of grossly deformed material form at the contacting interface which are principally composed of heavily mixed matrix (grey contrast) and whole or fractured NbC (bright white contrast) and M_7C_3 (dark contrast) carbides. There is some evidence that NbC particles tend to undergo fracture whereas M_7C_3 tend to exhibit wear-induced flat spots. These observations suggest that the M_7C_3 carbide is the more tribologically effective secondary hard phase. The generation of extruded features at the contacting surface is entirely consistent with plasticity dominated wear and

the surface regions identified by plan view SEM (Fig. 7.4). Fig. 7.8 (f) shows a region of discontinuity in the form of a ductile shear crack between two extruded slivers which, in this instance, are both approximately 1 μm in thickness. This ductile shear crack is seemingly formed by extrusion and makes the uppermost sliver appear partially delaminated.

Following testing at 250 $^{\circ}\text{C}$, the highly sheared/extruded material at the contacting surface (Fig. 7.8 (b), (d) and (g)) is highly variable in nature and is typically comprised of mixed metal/carbide/oxide and/or oxide based tribofilms. However, surface features characteristic of plasticity dominated wear, for example extruded slivers of predominantly metallic material, are still observed at the contacting interface. The stochastic nature of wear and extensive mixing which occurs at the contacting interface means that near surface layer is highly inhomogeneous at 250 $^{\circ}\text{C}$. The presence of a discontinuous oxygen-rich tribofilm is revealed in the insert in Fig. 7.8 (b) as a thin dark grey contrast layer on the contacting surface which correspond to regions high oxygen signal in the EDX map, Fig. 7.8 (d). A thin oxygen-rich tribofilm is also observed along the right hand side of the contacting surface in Fig. 7.8 (g). Depressions and discontinuities on the worn surface seemingly enable the accumulation, agglomeration, and compaction of oxidised and metallic material. More specifically, Fig. 7.8 (g) shows the accumulation of mixed metal plus oxidised material in a depression below the contacting surface; this region is predominantly comprised of dark contrast (low mean atomic number) oxidised material (identified as oxygen-rich by EDX).

Fig. 7.9 (a) and (b) show cross-sectional BSE images of plate/sliver like wear debris retrieved following autoclave sliding contact testing at 20 $^{\circ}\text{C}$. This debris is consistent with the extruded slivers observed at the contacting surface in Fig. 7.4 and Fig. 7.8 (a and f) and suggests that debris generation principally arises from the detachment of the extruded slivers. Likewise, the matrix deformation microstructure within this debris is principally composed of elongated structures/crystallites of varying contrast which are generally aligned parallel to the direction shear (along the length of the debris). In some regions within the debris, fine networks of cracks are observed. These cracks are clearly different to the larger ductile

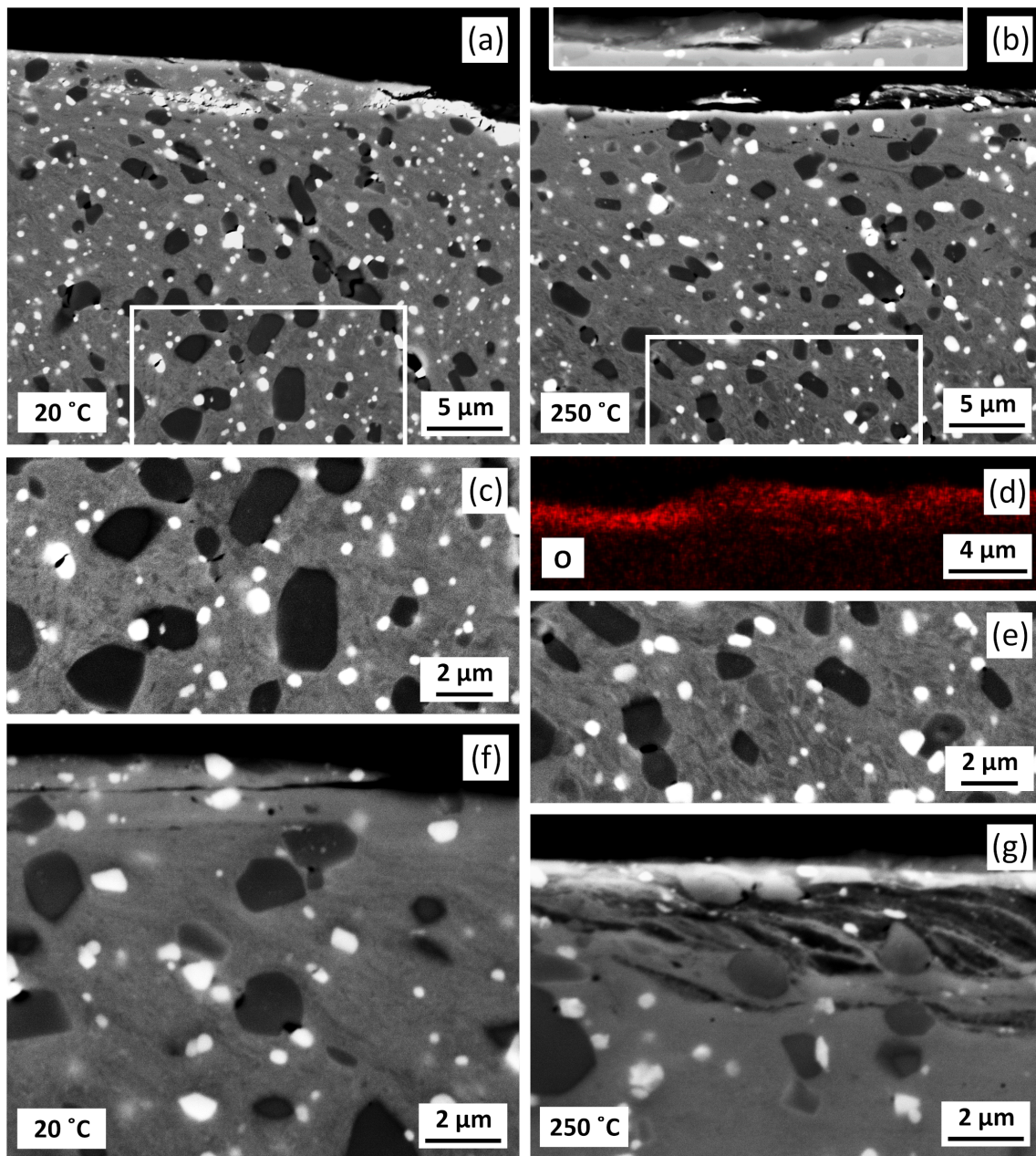


Figure 7.8: Cross-sectional BSE-SEM channelling contrast micrographs of Tristelle 5183 taken from within the wear track (parallel to the sliding direction) after testing at 20 °C (a, c and f) and 250 °C (b, e and g). The insert in (b) shows the contacting surface at a different brightness and contrast revealing the presence of a tribofilm. (d) shows an oxygen EDX map of the surface region depicted in (b). (c) and (e) show higher magnification images of the regions marked with the white square in (a) and (b) respectively. The sliding direction is horizontal to the figure in all cases.

shear cracks observed in Fig. 7.8 (f), and are possibly fatigue cracks, which may be associated with the final detachment of the extruded slivers.

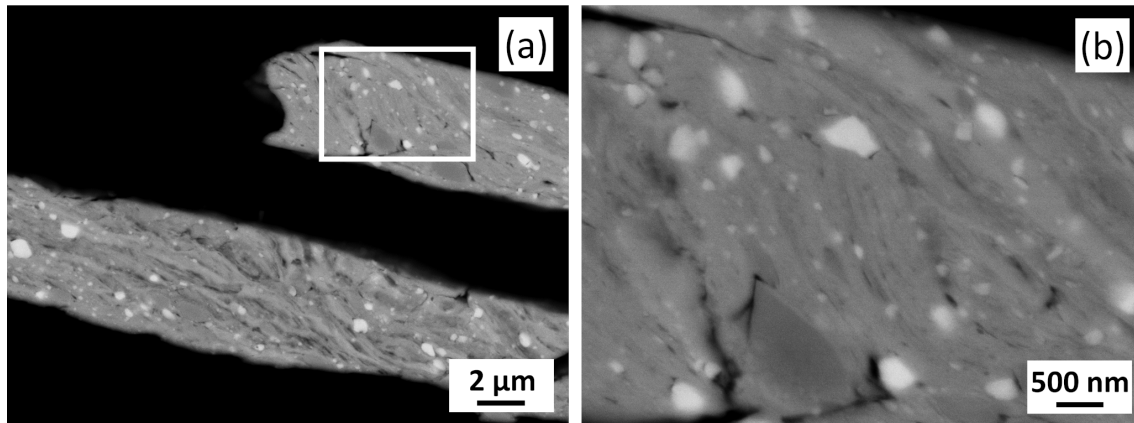


Figure 7.9: Cross-sectional BSE-SEM channelling contrast micrographs of Tristelle 5183 plate-like wear debris retrieved after testing at 20 °C. (b) is a higher magnification image of the region marked with the white square in (a).

7.2.6. Sub-surface microstructural characterisation following 20 °C testing - TEM

The BF-STEM micrographs (all taken with the same sample tilt) presented in Fig. 7.10 reveal the microstructural detail of the tribologically affected material at a distance of 60 μm beneath the contacting surface following testing at 20 °C. This deformation microstructure is complex and composed of a large number of different features, more specifically, lath-like structures, dark contrast needle structures forming at lath intersections, planar dislocation arrangements, stacking faults, dislocation lines and dislocation tangles. The intersections of planar deformation structures form a 70.5 ° angle with one another which is the angle between two $\{111\}$ crystallographic planes. Clearly, the secondary hard carbide phases play a role in the accumulation and generation of defect structures as high densities of defects are generally observed surrounding carbides. At this depth below the surface, lath and planar-type features appear dominant. The sliding direction is marked by the red arrows and a high density of planar defects is often observed in this direction.

Fig. 7.10 (c) shows the initial growth and development of a very small dark contrast lath-like feature which appears to grow in the plane of an existing planar defect structure. This dark contrast lath has seemingly grown by the coalescence

of individual segments of dark contrast within a region of high defect density. Additionally, these embryos appear to form at defect intersections which are finely spaced adjacent to one another. This growth mechanism may also explain the more developed dark contrast lath like structures observed in Fig. 7.10 (a, b and d) which seemingly propagate from regions of high defect density namely lath intersections.

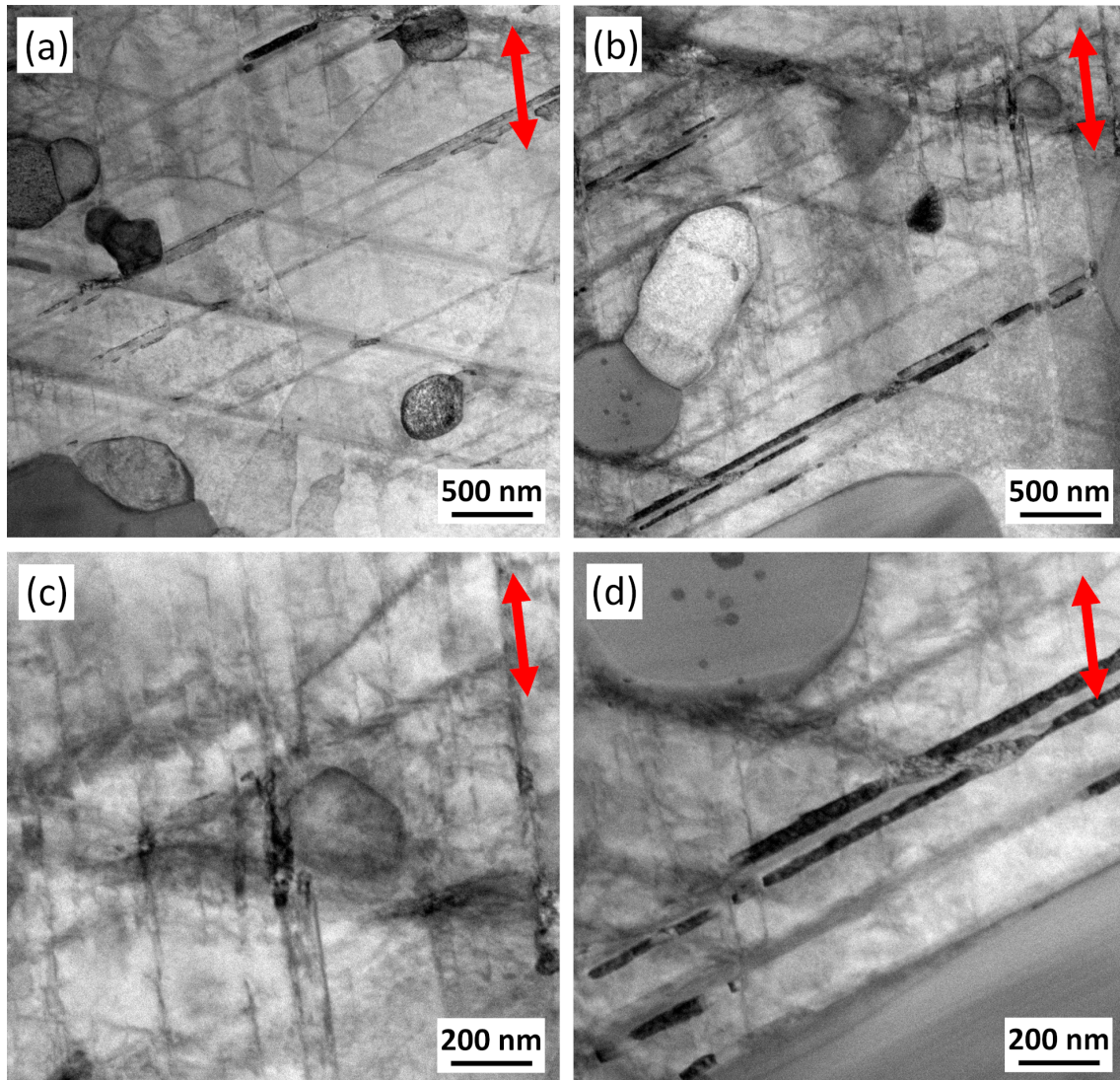


Figure 7.10: Representative BF-STEM micrographs depicting the tribologically induced deformation structures in a FIB lamellae of Tristelle 5183 taken from $60 \mu\text{m}$ beneath the contacting surface (parallel to the sliding direction) following autoclave sliding testing at 20°C . (c) shows the microstructural detail of the region marked with the white box in (b). The sliding direction is indicated by the red arrows.

Fig. 7.11(a), from the same region as Fig. 7.10, shows a BF-TEM micrograph of

a region rich in lath-like deformation structures aligned parallel to the direction of sliding Fig. 7.11 (b) and (c) show the same SADP taken from the circled region in Fig. 7.11 (a), and can be indexed to γ -austenite, ϵ -martensite (heavily flawed). This SADP also exhibits streaking which is consistent with stacking faults on the γ -Fe $\{111\}$ planes. Fig. 7.11 (d) is a DF-TEM micrograph taken with the ϵ -martensite diffraction spot marked with the blue circle in Fig. 7.11 (b). This confirms that a large fraction of the lath like structures are ϵ -martensite. Fig. 7.11 (c) shows that the ϵ -martensite laths exhibit an orientation relationship defined by $\{111\}_\gamma \parallel \{0001\}_\epsilon, \langle 10\bar{1} \rangle_\gamma \parallel \langle 11\bar{2}0 \rangle_\epsilon$ with the parent γ -Fe phase.

Fig. 7.12 (a) is a BF-TEM micrograph depicting the microstructural detail of several intersecting laths and two dark contrast needle-like structures which form at the lath intersections. In accord with Figs. 7.10 and 7.11, a large fraction of the lath-like structures observed in Fig. 7.12 (a) are generated parallel to the sliding direction which has been indicated by the red arrow. Fig. 7.12 (b) and (c) show the same SADP taken from the circled region in Fig. 7.12 (a), and can be indexed to γ -austenite, ϵ -martensite (heavily flawed) and α' -martensite whilst streaking consistent with stacking faults on the γ -Fe $\{111\}$ planes is also observed. The DF-TEM images, Fig. 7.12 (d) and (e), have been taken with the ϵ -martensite diffraction spots denoted (d) (orange circle) and (e) (blue circle) in Fig. 7.12 (b) respectively and confirm that, in this instance, the intersecting laths are ϵ -martensite. These ϵ -martensite laths intersect with an angle of 70.5° which is the angle between two $\{111\}$ crystallographic planes. The DF-TEM micrograph, Fig. 7.12 (f), has been taken with the isolated α' -martensite diffraction spot marked as (f) (green circle) in Fig. 7.12 (b), and shows that the needle like deformation structures which form at ϵ -martensite intersections are α' -martensite. Fig. 7.12 (c) shows that the α' -martensite phase exhibits the Nishiyama-Wasserman orientation relationship $\{111\}_\gamma \parallel \{110\}_{\alpha'}, \langle 112 \rangle_\gamma \parallel \langle 110 \rangle_{\alpha'}$ with the γ phase.

The HAADF-STEM micrographs presented in Fig. 7.13 (a and b) show tribologically affected material up to $\sim 5 \mu\text{m}$ below the contacting surface after testing at 20°C . These images were obtained from cross-sectional FIB samples taken parallel to the direction of sliding. EDX maps from the same region shown in Fig. 7.13

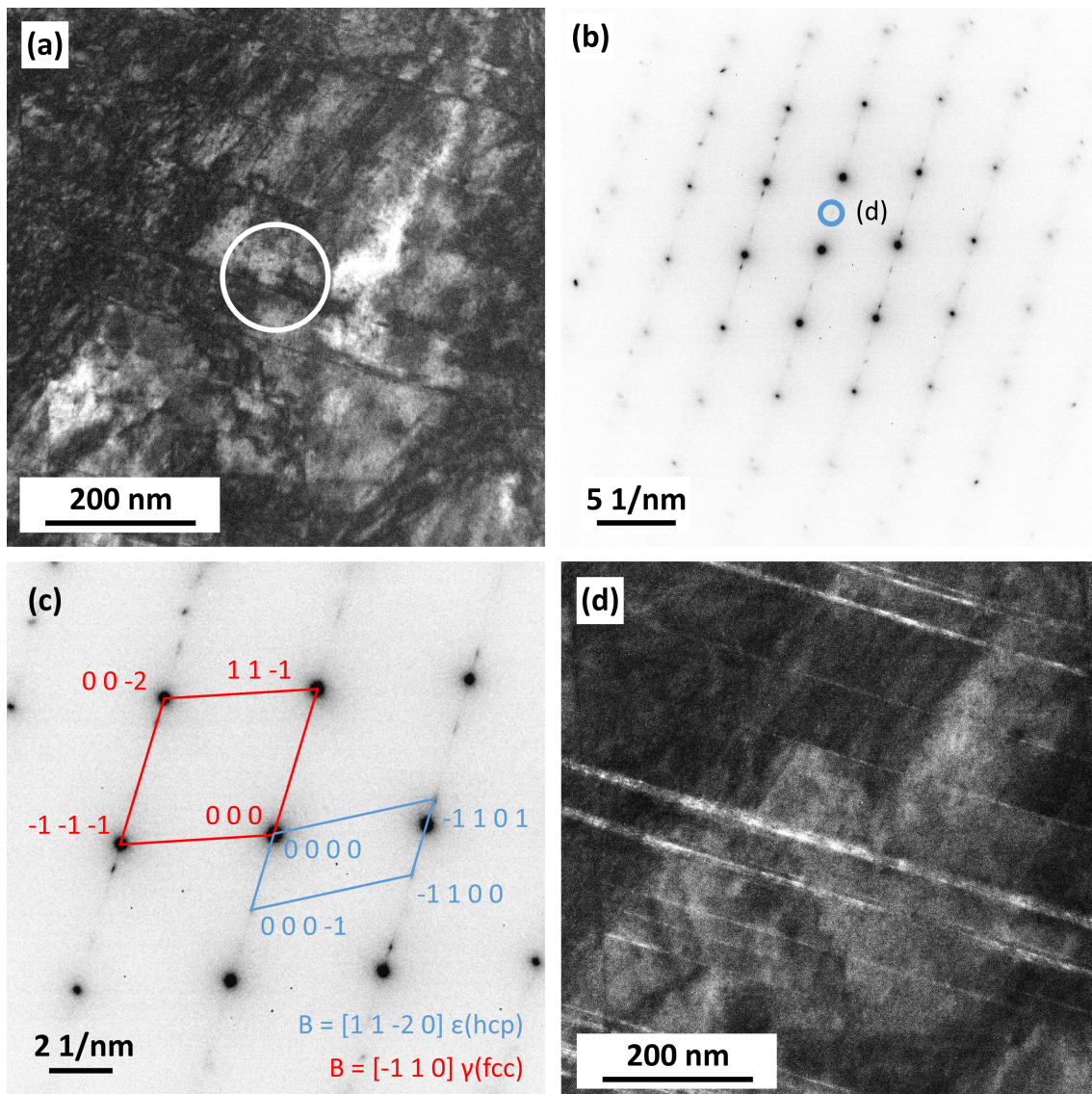


Figure 7.11: TEM analysis illustrating the $\gamma \rightarrow \epsilon$ deformation induced martensitic transformation in Tristelle 5183. (a) shows a representative BF-TEM micrograph of Tristelle 5183 taken from $60 \mu\text{m}$ beneath the contacting surface (parallel to the sliding direction) following autoclave sliding testing at 20°C . (b and c) show the same select area diffraction pattern taken from the region marked with the white circle in (a). (c) shows that this SADP indexes to both fcc γ -Fe (red) and hcp ϵ -Fe (blue). (d) shows a DF-TEM micrograph of the same region depicted in (a), taken with the ϵ -Fe diffraction spot marked with the blue circle in (b).

(a) are presented in Fig. 7.13 (c-h). Overall, the microstructures exhibit a highly localised mechanically refined nanocrystalline matrix with embedded bright and dark contrast precipitates which are M_7C_3 and NbC carbides respectively, as identified by the EDX maps (Fig. 7.13 (d) and (e)). The subsurface microstructure is

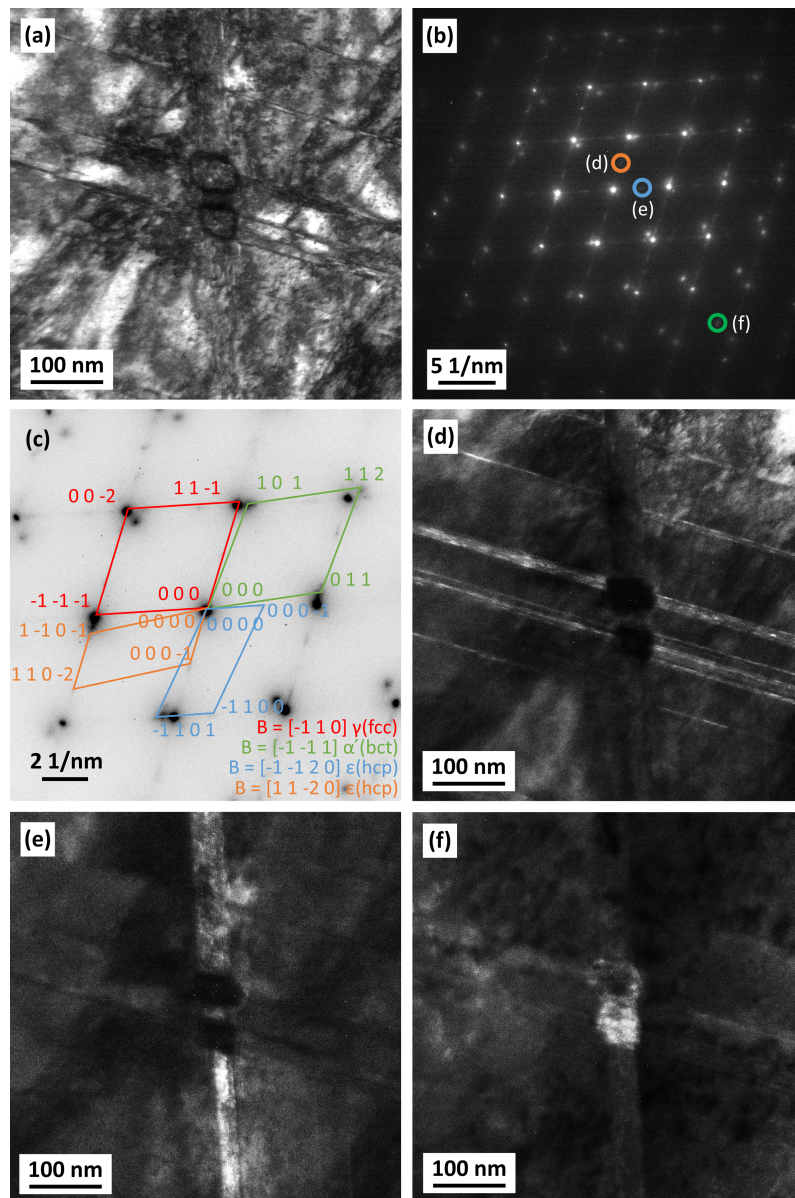


Figure 7.12: TEM analysis illustrating the $\gamma \rightarrow \epsilon \rightarrow \alpha'$ deformation induced martensitic transformation in Tristelle 5183. (a) shows a representative BF-TEM micrograph of Tristelle 5183 taken from 60 μm beneath the contacting surface (parallel to the sliding direction) following autoclave sliding testing at 20 $^{\circ}\text{C}$. (b and c) show the same select area diffraction pattern taken from the region marked with the white circle in (a). (c) shows that this SADP indexes to fcc γ -Fe (red), bct α' -Fe (green) and hcp ϵ -Fe (blue and orange). (d), (e) and (f) show DF-TEM micrographs of the same region depicted in (a). (d) was taken with the ϵ -Fe diffraction spot marked with the orange circle in (b). (e) was taken with ϵ -Fe diffraction spot marked with the blue circle in (b). (f) was taken with α' -Fe diffraction spot marked with the green circle in (b). The sliding direction is indicated the by red arrow.

composed of (i) several layers of overlapping extruded slivers/striations which contain whole and fractured carbides to a depth of $\lesssim 3 \mu\text{m}$ from the surface and (ii) a region of highly deformed material at a depth $\gtrsim 3 \mu\text{m}$ from the surface. In this instance, the extruded slivers are highly coherent with one another and are best revealed in the EDX maps. However, the uppermost two slivers are clearly identifiable by small ductile shear cracks which form between their interfaces. The fragmented nature of the carbides within the extruded slivers is revealed in the Cr (Fig. 7.13 (d)) and Nb (Fig. 7.13 (e)) EDX maps, and it is also clear that the NbC carbide is more susceptible to fragmentation during sliding. Additionally, Fig. 7.13 shows that a large fraction of the carbide fragments are isolated and surrounded by matrix material. This is presumably due to the high degree of mechanical mixing that occurs during sliding. The highly deformed matrix material is nanocrystalline and is comprised of high aspect ratio crystallites which have become aligned parallel to the direction of shear. In addition to carbides, the EDX maps also reveal deformed ferrosilicide grains which are rich in Cr and Si and depleted in Ni and Fe relative to the matrix.

Fig. 7.14 (a) and (b) show BF-STEM micrographs depicting the microstructural detail of the highly localised tribologically induced deformation microstructure below the contacting surface. These micrographs clearly depict high aspect ratio crystallites which are generally aligned with the direction of shear. The individual crystallites often exhibit high angle boundaries with their neighbours which is revealed by stark differences in contrast between adjacent crystallites. Large contrast variations are also observed within individual crystallites which arise from fluctuations in internal defect density.

7.2.7. Sub-surface microstructural characterisation following 250

^oC testing - TEM

Fig. 7.15 (a) shows a HAADF-STEM micrograph taken parallel to the sliding direction which shows the tribologically affected microstructure within the top $\sim 5 \mu\text{m}$ beneath the contacting surface. The highly localised matrix deformation structure surrounds bright and dark contrast precipitates which are the M_7C_3 and

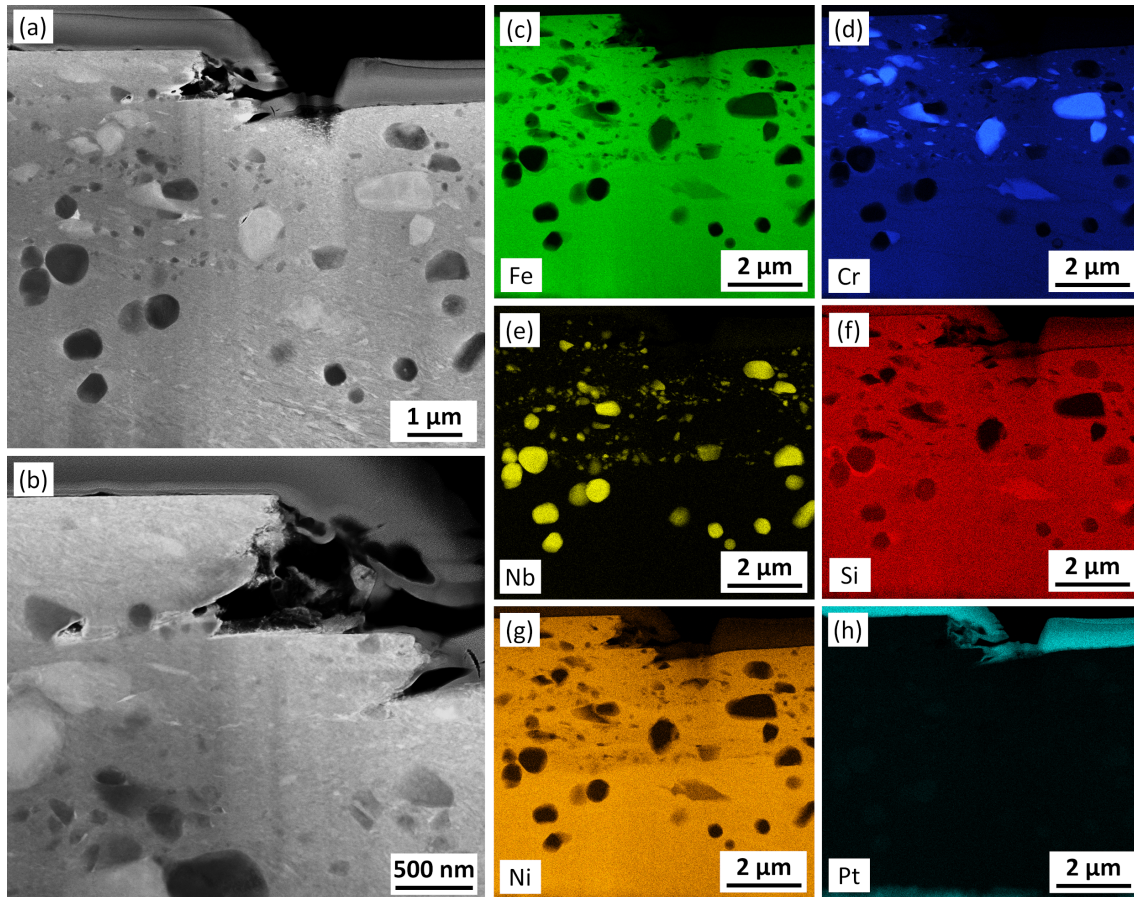


Figure 7.13: (a) and (b) show representative HAADF-STEM micrographs taken parallel to the sliding direction showing the deformation structures directly beneath the contacting surface following sliding contact at 20 °C. (c), (d), (e), (f), (g) and (h) show EDX maps of the same region depicted in (a) and correspond to the maps for Fe, Cr, Nb, Si, Ni and Pt respectively. The sliding direction is horizontal to the figure in all cases.

NbC carbides respectively. The HAADF-STEM micrograph (Fig. 7.15(b)) shows the boxed area in (a) at higher magnification where a partially detached and fractured sliver of plastically extruded material is clearly visible. This sliver appears to be separated from the bulk by a layer of faceted crystals which are presumably oxide crystals. The BF-TEM micrograph, Fig. 7.15 (c), clearly shows that the subsurface nanocrystalline matrix is principally composed of high aspect ratio crystallites which have become aligned parallel to the direction of shear. There is often a large difference in contrast between adjacent crystallites, which shows that neighbouring crystallites often exhibit high angle boundaries. Individual crystallites also exhibit large variations in internal contrast which is clearly a result of regions of high and

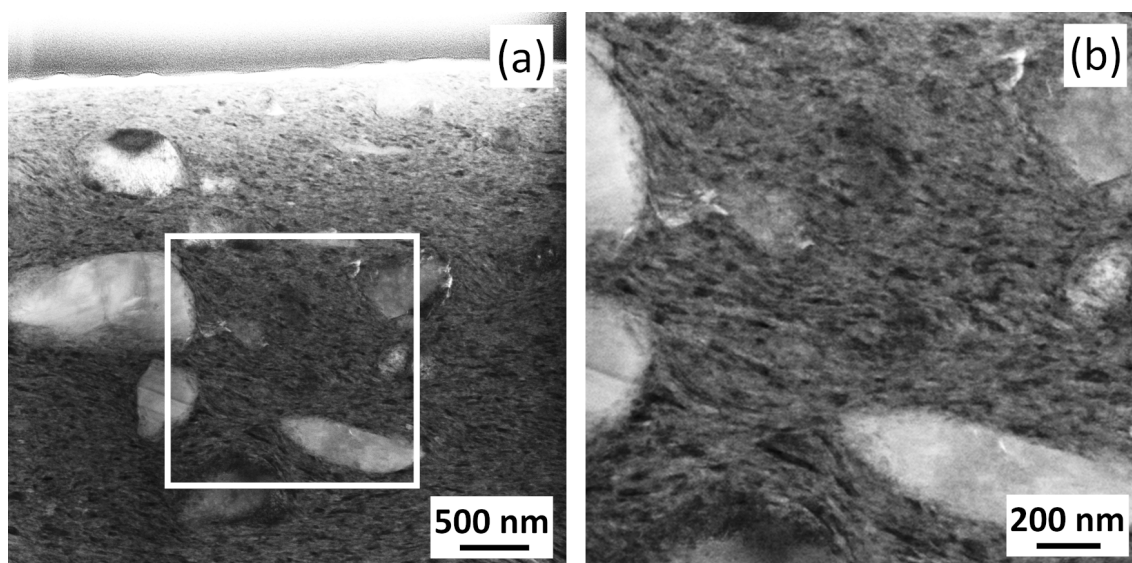


Figure 7.14: (a) and (b) show representative BF-STEM micrographs taken parallel to the sliding direction showing the deformation structures directly beneath the contacting surface following sliding contact at 20 °C. (b) shows the microstructural detail of the region marked with the white box in (a). The sliding direction is horizontal to the figure in all cases.

low defect density. Fig. 7.15 (c) shows some evidence of globular structures which are generally larger than the high aspect ratio crystallites; these structures appear to be composed of multiple different crystallites which possess a similar defect density and crystallographic orientation. The SADP in Fig. 7.15 (d) was taken from the circled region in Fig. 7.15 (c) and indexes to γ -Fe (fcc). Deformation induced α' -martensite or ϵ -martensite cannot be detected following testing at 250 °C which is entirely consistent with XRD (Fig. 7.7). This SADP exhibits a diffuse texture of the S1 type where the strongest component is $\{111\}[110]$, typically tilted up to 10 ° from the sliding direction.

After testing at 250 °C, a layer of faceted particles can be observed at the surface, as can be seen in Fig. 7.16. The HAADF-STEM micrograph and corresponding EDX maps reveal a duplex-type oxygen rich layer \sim 150 nm thick which is composed of the following: (i) a thin \sim 20 nm thick Ni- and Cr-rich layer at the matrix interface and (ii) an outer layer of faceted crystals that are principally composed of Fe and Ni. A Pt map is included to show where a protective layer was deposited on the sample as part of the FIB sample preparation process. All the faceted crystals contain Fe and Ni but regions within this corrosion layer also contain Cr. SADPs

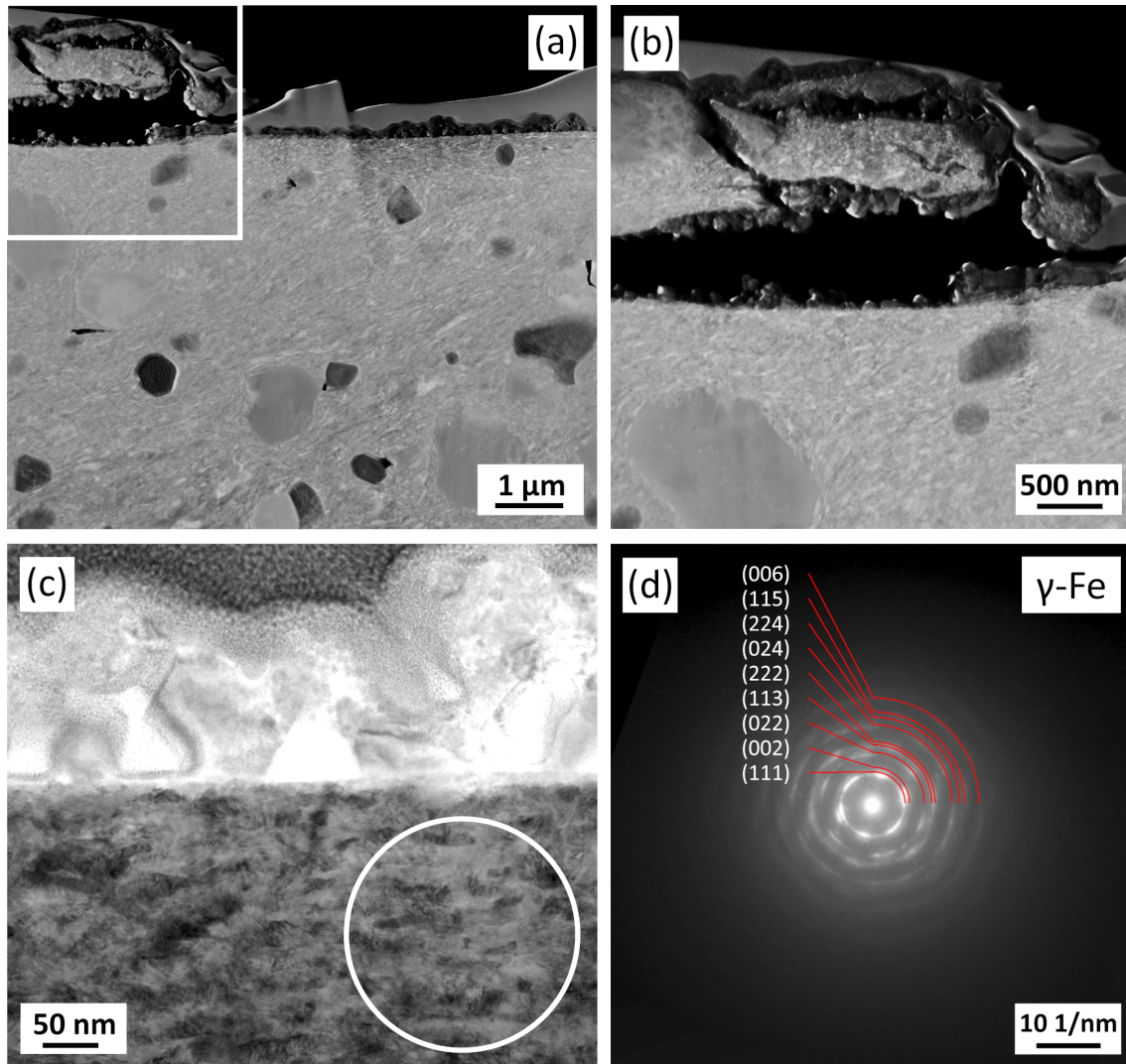


Figure 7.15: Representative HAADF-STEM (a and b) and BF-TEM (c) micrographs taken parallel to the sliding direction showing the deformation structures directly beneath the contacting surface following autoclave sliding contact at 250 °C. (b) shows the microstructural detail of the region marked with the white box in (a). (d) shows a SAEDP from the circled region in (c) and indexes to γ -Fe (fcc). The sliding direction is horizontal to the figure in all cases.

identified the faceted crystal layer as a spinel iron oxide isostructural to magnetite. A duplex type oxide such as this is commonly observed on austenitic stainless steel post exposure to PWR conditions [35–37,307]. Fig. 7.16 (d) shows that the uppermost 200 nm beneath the contacting surface is slightly Cr depleted relative to the rest of the matrix. Very fine striations which differ in their Fe, Ni, Cr and Si content relative to the surrounding matrix are also observed within the uppermost 200 nm. These striations may possibly relate to the interfaces between very fine

plastically extruded slivers.

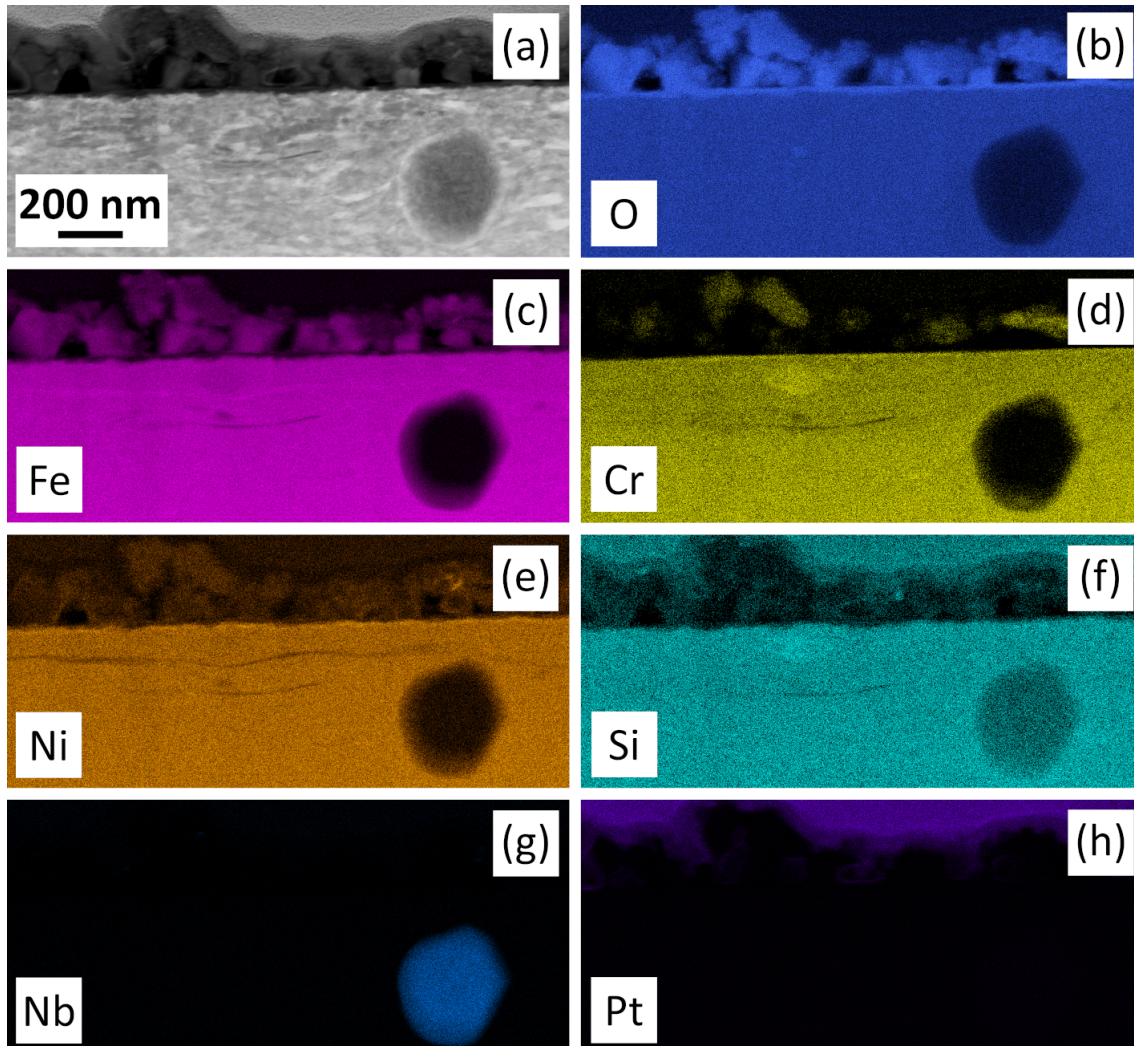


Figure 7.16: (a) HAADF-STEM micrograph of Tristelle 5183 taken parallel to the direction of shear following exposure to sliding contact at 250 °C showing the microstructural detail of a duplex-type corrosion product on the contacting surface. (b), (c), (d), (e), (f), (g) and (h) show EDX maps of the same region depicted in (a) and correspond to maps for O, Fe, Cr, Ni, Si, Nb and Pt respectively. The sliding direction is horizontal to the figure in all cases.

7.3. DISCUSSION

Experimental evidence presented in the previous section has shown that the mechanisms dictating the degradation of Tristelle 5183 subjected to sliding contact in lithiated water are sensitive to test temperature. Despite these clear mechanistic differences, the material loss during testing only increases by a factor between \sim

1.1 and ~ 2.1 times when the test temperature is increased from 20 °C to 250 °C (Fig. 7.1). In light of this, the following section aims to elaborate on the various factors which influence the clear temperature dependent wear and deformation mechanisms observed in Section 7.2.

The HIPed microstructure of Tristelle 5183 is comprised of two types of equiaxed carbide precipitate namely, ~ 14.0 vol% M_7C_3 ($\sim 1 - 5 \mu\text{m}$ in size) (Vickers hardness: 13-22 GPa [47,308]) and ~ 9.6 vol% NbC (typically $< 2 \mu\text{m}$ in size) (Vickers hardness: 19-24 GPa [47,308,309]). These are surrounded by an Fe-based predominantly austenitic (fcc γ -Fe) solid solution matrix (composition reported in Table 5.2) although, trace amounts of bcc α -Fe and a π -ferrosilicide phase have also been identified (Chapter 5). Irrespective of test temperature, the subsurface of the alloy following testing (Fig. 7.8) has clearly accommodated large strains and shows an evolution in deformation microstructure which depends on the depth below the contacting surface. This tribologically affected material (TAM) can otherwise be described as a continuum of deformation which results from the strain gradient induced by the loaded sliding contact. However, for the purpose of detailing the microstructural evolution beneath the contacting surface, it is convenient to sub-divide the TAM into three layers as schematically illustrated in Fig. 7.17. Layer 1 is the TAM furthest from the contacting surface where the modes of deformation are principally homogeneous and sensitive to test temperature (which alters the SFE). In layer 2, strain is principally accommodated by grain boundary mediated deformation mechanisms and crystallographic slip; localised deformation structures completely consume the microstructure and an ultrafine grain/nanocrystalline lamellar microstructure is generated. Finally layer 3 is a region closest to the sample surface, where plastic ratcheting, mechanical mixing, tribochemical reactions, oxidation, and oxide containing tribofilm development may take place depending on the test conditions. Throughout the TAM, it is also noted that the complex evolution in deformation microstructure is likely to be influenced by sliding induced thermal gradients and adiabatic heating effects in response to deformation.

During uniaxial tensile testing, the tensile strain to failure for HIPed Tristelle

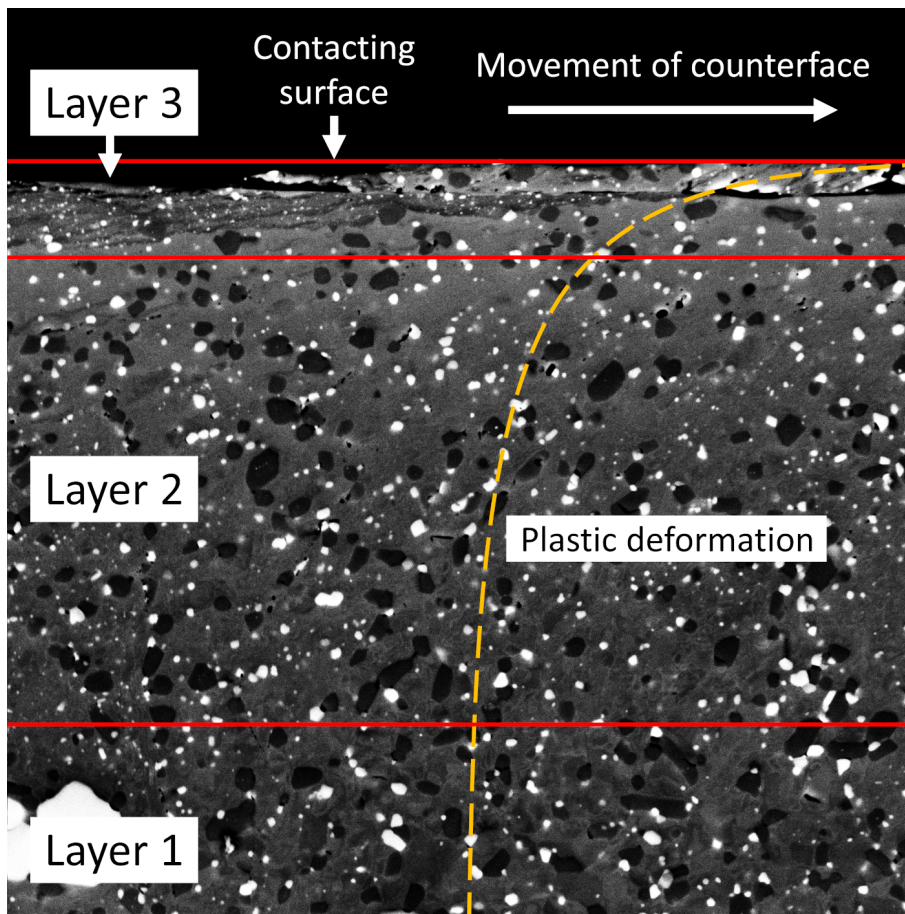


Figure 7.17: Schematic illustrating the different layers within the TAM used to describe the continuum of plastic deformation within the subsurface. The dashed line is an idealised representation of the extent of plastic flow within the subsurface (not to scale).

5183 is reportedly $< 2\%$ [7]. However, by inspection of Figs. 7.4, 7.5 and 7.8, it is clear that the subsurface shear strains following sliding at both test temperatures are much greater than this failure strain. The accommodation of such large plastic strains within the TAM can be explained by the plastic ratcheting phenomenon [310,311] in which large unidirectional plastic strains are incrementally accumulated during cyclic loading. The ratcheting phenomenon occurs when the so-called 'plastic shakedown limit' or the 'ratcheting threshold' is exceeded [310,311]; this can otherwise be described as the point when the intensity of loading surpasses the yield criterion of the material even in the presence of protective residual stresses and strain hardening. This seemingly ductile response from Tristelle 5183 during sliding induced plastic ratcheting is a consequence of the high hydrostatic component of stress imposed by the sliding contact [310,312,313].

It should be noted that the concept of plastic ratcheting is also applicable to the pin during sliding, as it is unlikely that a given asperity remains in a constant state of loading per disk revolution, so the contacting asperities of the pin are also subjected to cyclic loading.

7.3.1. Layer 1 - homogeneous modes of deformation

The term “homogeneous modes of deformation” encompasses a wide range of deformation mechanisms which occur prior to strain localisation, and is used as these deformation mechanisms conventionally result in a more macroscopically uniform accommodation of strain relative to the deformation mechanisms associated with the layers closer to the contacting surface.

7.3.1.1. Deformation structures and microstructural evolution at 20 °C - 60 μm beneath the contacting surface

A site-specific TEM study was performed 60 μm beneath the contacting surface of a sample tested at 20 °C. The deformation mechanisms and subsequent work hardening behaviours of austenitic stainless steels are known to be fundamentally dependent upon their stacking fault energy (SFE) which, in turn, is influenced by both temperature and composition [175–177, 179–182, 314]. Therefore, this site-specific study should help gain insight into the homogeneous modes of plastic deformation that become active within layer 1 in response to sliding contact.

To summarise Section 7.2.6, layer 1 (Figs. 7.10 to 7.12) (specifically at a distance of 60 μm from the contacting surface following testing at 20 °C) exhibits many deformation structures including, ϵ -martensite laths, α' -martensite, twins, planar defect intersections and planar dislocation arrangements (generated by planar slip) as well as stacking faults, dislocation lines and dislocation tangles. However, it would appear that the SFE of the γ -phase is sufficiently low that planar defects, for example martensite laths and planar dislocation arrangements, are the most frequently observed deformation features within this region of layer 1 (Figs. 7.10 to 7.12). All deformed grains exhibit two or more activated slip systems, multiple variants of planar defect structures and extensive interactions between

the volumetric planar defects (Fig. 7.10). In accord with the above, similar deformation structures have also been observed during the ambient temperature deformation of stainless-steel alloys with compositions that are analogous to the matrix composition of Tristelle 5183 (Table 5.2) [186, 197, 286, 315–320].

The deformation structures within the γ -Fe phase are principally associated with the $\{111\}$ planes, which is typical of materials with low SFE values and, as expected, the planar defects intersect with an angle of $\sim 70.5^\circ$ which is the angle between two $\{111\}$ crystallographic planes (Fig. 7.12). Such intersections subdivide the matrix into both sub-micron and nanoscale rhombic, trigonal and quadrilateral blocks (Fig. 7.10). In light of the above, it is postulated that the matrix microstructural refinement in layer 1 at a distance $60\ \mu\text{m}$ from the contacting surface (Figs. 7.10 to 7.12) principally involves: (i) the formation of volumetric planar defects/deformation bands namely ϵ -martensite laths, twins and planar dislocation arrangements; and (ii) the intersection of multidirectional planar defects leading to grain subdivision and α' -martensitic transformation. The shear direction (or direction of sliding) is parallel with one of the directions about which the planar volumetric defect boundaries form (Figs. 7.10 to 7.12). This suggests that one of the fcc slip systems was possibly rotated towards, and subsequently activated along, the direction of shear. The highest density of volumetric defects is generally observed in this direction which often generates elongated blocks aligned with the direction of shear (Figs. 7.10 to 7.12).

Secondary hard precipitates play a significant role in the generation and accumulation of defects within the matrix (Fig. 7.10), and deformation zones are induced around the precipitates. The mismatch in the mechanical properties between the matrix and secondary hard phase precipitates [47, 163, 308, 309, 321, 322] means that complex multiaxial stress states are generated in the matrix and a stress gradient originating from the interphase interface during sliding is produced. This will assist with the activation of both faulting on all available $\{111\}$ planes and slip systems and promote further work hardening. It is also suggested that dislocation cross slip is activated in these highly deformed regions which permits the increased formation of dislocation tangles and possibly even incipient dislo-

cation walls (Fig. 7.10 (c)). Within this deformation zone, the rate of dislocation and defect accumulation increases which promotes rapid effective microstructural refinement [284,323] (Fig. 7.10).

Figs. 7.11 and 7.12 have shown that the γ (fcc) $\rightarrow \epsilon$ (hcp) (Fig. 7.11) and γ (fcc) $\rightarrow \epsilon$ (hcp) $\rightarrow \alpha'$ (bct) (Fig. 7.12) deformation induced martensite (DIM) transformation pathways dominate the formation of the ϵ (hcp) and α' (bct) phases during testing at 20 °C (60 μm below the contacting surface). However, the nucleation of DIM (ϵ (hcp) and α' (bct)) is known to occur via a variety of different mechanisms in austenitic stainless steels [112,179,181,183,184,186,188–190,196]; for example, γ (fcc) $\rightarrow \epsilon$ (hcp), γ (fcc) $\rightarrow \epsilon$ (hcp) $\rightarrow \alpha'$ (bct), γ (fcc) \rightarrow deformation twinning $\rightarrow \alpha'$ (bct) and γ (fcc) $\rightarrow \alpha'$ (bct). These martensitic phases can nucleate at a number of different sites of crystallographic variability/discontinuity where the interaction energy favours martensitic transformation; for example, overlapping stacking faults, planar defect intersections (twin/transformation intersections), isolated planar defects, grain boundary - planar defect intersections and dislocation interactions etc.. The nature and occurrence of the deformation induced martensitic transformations in austenitic stainless steel is also susceptible to both the type of loading and strain rate [199,316,324]. Whilst all the above may be relevant to Tristelle 5183, the dominant DIM transformation mechanisms shown in Figs. 7.10 to 7.12 are most probably a result of the specific matrix composition (Table 5.2), the loading conditions imposed (60 μm below the contacting surface), and the temperatures induced during sliding.

The ϵ -martensite laths observed via TEM are heavily flawed, and the ϵ -martensite diffraction spots (Figs. 7.11 and 7.12) are directly related to elongated regions of high intensity within diffraction streaks formed due to stacking faults on the γ -Fe $\{111\}$ slip planes. Therefore, it is suggested that during deformation, stacking faults are preferentially generated adjacent to existing stacking faults on every second $\{111\}$ slip plane. This bundling of stacking faults generates plate-like volumetric defects which match the crystallography of heavily flawed hcp ϵ -martensite with an orientation relationship to the parent γ -phase defined by $\{111\}_\gamma \parallel \{0001\}_\epsilon, \langle 10\bar{1} \rangle_\gamma \parallel \langle 11\bar{2}0 \rangle_\epsilon$ which is otherwise known as the Shorji-

Nishiyama orientation relationship [179, 188, 189] (Figs. 7.11 and 7.12). This is in line with several other studies [179, 189, 190] which suggest that the $\gamma \rightarrow \epsilon$ transformation occurs via an irregular overlapping process. More specifically, stacking faults form irregularly at first on the $\{111\}_\gamma$ slip planes after which further stacking faults are preferentially induced on nearby $\{111\}_\gamma$ planes as this is more energetically favourable with regards to the minimisation of the bulk free energy and the total energy of the stacking faults. The formation of ϵ -martensite via overlapping stacking faults has also been reported by several other authors and accounts for the heavily flawed nature of the ϵ -martensite platelets (Figs. 7.11 and 7.12) [179, 189, 190].

At a distance of $\sim 60 \mu\text{m}$ beneath the contacting surface, TEM (Fig. 7.12) has shown that α' -martensite principally nucleates at the intersection between two ϵ -martensite laths and in this instance exhibits the Nishiyama-Wasserman orientation relationship ($\{111\}_\gamma \parallel \{110\}_{\alpha'}, \langle 112 \rangle_\gamma \parallel \langle 110 \rangle_{\alpha'}$) with the γ -phase (Fig. 7.12 (c)). At this distance beneath the contacting surface, a notable fraction of α' -martensite is retained within the intersections of ϵ -martensite laths (Fig. 7.12) and the dark contrast features observed at the lath intersection in Fig. 7.10 are also most probably α' -martensite and not just simply regions of high crystallographic discontinuity. The irregular contrast variation observed at the intersections of ϵ -martensite laths shown in Fig. 7.12 (d) demonstrates that, in this particular instance, the α' -martensite exhibits spatial inhomogeneities and can be regarded as irregular α' -martensite embryos [325]. This is possibly the result of an irregular compliance of the necessary fault-displacements required for α' -martensite transformation within the intersection of these relatively large, heavily faulted, ϵ -martensite laths. Fig. 7.10 shows that the dark contrast features (presumably α' -martensite), which often initially form at ϵ -martensite lath intersections, seemingly propagate out forming laths of dark contrast along existing planar defects which reside on γ -Fe $\{111\}$ planes. Closer inspection (Fig. 7.10 (c and d)) shows that these laths are in fact composed of separate segments of embryos of what is presumably α' -martensite closely stacked together. It is therefore postulated that the growth of the α' -martensite phase into laths occurs via the coalescence of closely spaced

embryos of α' -martensite at defect intersections along an ϵ -martensite lath. The coalescence of these closely spaced embryos seemingly generates continuous laths of what is most probably α' -martensite. This nucleation and irregular grown mechanism is entirely consistent with previous observations on the growth of α' -martensite in austenitic stainless steel [199,316,325]. In this region, out of plane growth of the α' -martensite phase is not observed and this phase is generally confined within intersection volumes or existing planar defects which reside on the γ -Fe {111} planes. Additionally, the growth of blocky α' -martensite at this depth beneath the contacting surface is unlikely given the limited number of planar defect intersection observed [199].

7.3.1.2. Deformation structures and microstructural evolution at 20 °C - change of deformation mechanisms with depth

The deformation mechanisms are expected to change/evolve as the depth beneath the contacting surface decrease. During the cyclic loading imposed during sliding, it is hypothesised that at a given distance below the contacting surface a critical threshold peak stress is reached which corresponds to a critical cross slip activity promoted by a specific long range internal stress state [326–328]. In terms of deformation evolution as the sample surface is approached, it is suggested that an increased fraction of planar defects generates the specific long range internal stress state required for cross slip [326–328]. The specific long range internal stress state generated through the rapid accumulation of dislocations reduces the width of stacking faults and permits the cross slip of dislocations whilst reducing the interaction of partial dislocations that is otherwise required for transformation and twinning [329]. This shift in deformation mechanisms will also be influenced by the thermal gradients and possible adiabatic heating effects generated during sliding. This critical state of cross slip activity increases slip irreversibility and subsequently favours progressive deformation during sliding. The above hypothesis is analogous to the microstructural evolution observed during the plastic ratcheting of austenitic stainless steels with compositions which are comparable to the matrix composition of Tristelle 5183 [326, 327, 330–334].

Microstructurally, it is suggested that the critical activation of cross slip permits the formation of heterogeneous dislocation structures whereby the dislocation configuration evolves from low density dislocation configurations (Fig. 7.10) such as dislocation lines, planar dislocation arrangements and very light dislocation tangles to higher density dislocation arrangements such as heavy dislocation tangles, walls, veins and subsequently dislocation cells (dislocation trapping by polarised dislocation patterns) as the sample surface is approached. The increased activation of cross slip and the increased fraction of heterogeneous dislocation structures provides an explanation for the microstructures observed at $\sim 25 \mu\text{m}$ below the contacting surface which is arguably more cellular in nature (Fig. 7.8(d and e)). This evolution in dislocation structures results in a further increase of work hardening as the sample surface is approached (Fig. 7.2).

To summarise, it is suggested that various modes of plastic deformation operate synergistically within this layer and the microstructure evolves as the sample surface is approached such that the fine networks of volumetric planar defects, intersecting planar defects, dislocation interactions, heterogeneous dislocation structures and dislocation cells comprehensively restrain the microstructure from further plastic deformation via the homogeneous modes of deformation. This microstructural evolution permits the incremental accommodation of large strains during the cyclic loading imposed by sliding. However, the generation, accumulation and interaction of these defect structures is known to be a precursor to shear localisation [302,335–337].

7.3.1.3. The influence of test temperature on the homogeneous modes of deformation in layer 1

The temperature dependence of SFE, and thus deformation modes, exhibited by austenitic stainless steels including Tistelle 5183 influences the mechanisms of microstructural refinement. The generation of dislocation cells requires dislocation cross slip. Cross slip in fcc materials occurs via the pinching of partial dislocations on the original slip plane followed by extrusion on the cross-slip plane [187,286]. The SFE of the γ -phase influences the separation between partial dislocations.

Therefore, if the SFE is high the separation between partials is small which favours dislocation pinching and therefore, cross slip, heterogenous dislocation structures and dislocation cell formation. In contrast, when the γ -phase has a low SFE, the separation between partial dislocations is large so dislocation cross slip and dislocation cell formation is inhibited. With respect to dislocation motion, the suppression of cross slip causes dislocations to arrange themselves in planar arrays on the primary $\{111\}$ slip planes. Deformation twinning and martensitic transformation compete with dislocation slip, and the critical resolved shear stress for these deformation mechanisms decreases with the SFE of the γ -phase. Both deformation twinning and martensitic transformation mechanistically result from Shockley partial dislocation movement and stacking fault generation [182, 189, 190, 338, 339]. As the SFE is decreased, twinning followed by martensitic transformation become the favoured modes of deformation especially at low temperatures and/or high strain rates [112, 176, 177, 179–182, 189, 292, 338, 340, 341].

Valuable information about the modes of deformation in layer 1 can be ascertained by XRD (Fig. 7.7). Wear is an evolutionary process and, under steady state sliding conditions, the near surface region probed via XRD has a deformation history which at one point during sliding evolved from microstructures and phases present within layer 1. Following testing at 250 °C DIM was not observed in the XRD (Fig. 7.7) patterns which suggests that martensitic transformation did not take place throughout the entirety of the TAM including within layer 1. This point is made based on the logic that DIM cannot take place throughout the deformation evolution of Tristelle 5183 if DIM is not observed in the most highly strained (evolved) regions of the TAM probed by XRD. It is postulated that the increase in test temperature to 250 °C sufficiently increases the SFE of the γ -phase such that DIM transformation is inhibited. This hypothesis concurs with previous studies [28, 29, 202, 314, 341] which show that DIM in austenitic stainless steels and austenitic hardfacings ceases beyond the characteristic temperature (M_d). More specifically, the M_d temperature represents the limit for deformation induced transformation, and no deformation induced martensite can form above this temperature. It is further suggested that the temperature dependent increase

in SFE may be enough to permit extensive dislocation cross slip from the onset of deformation during testing at 250 °C. Similar findings have been reported in the work of Kim and Kim [28] who observed only heterogeneous dislocation structures permitted by cross slip in the austenitic hardfacing Norem 02 following in air sliding wear testing at temperatures in excess of 190 °C. The hypothesis that dislocation cross slip occurs extensively throughout layer 1 concurs with the microstructural observations and Fig. 7.8 (e), $\sim 25 \mu\text{m}$ from the contacting surface, depicts a highly heterogeneous seemingly cellular matrix microstructure with no evidence of any notable/resolvable lath type microstructures.

7.3.2. Layer 2 - strain localisation and inhomogeneous modes of deformation

TEM of the near surface shows a highly localised deformation microstructure composed of ultrafine/nanoscale high aspect ratio (elongated) crystallites generally aligned parallel to the direction of shear with high angle boundaries at both test temperatures (Figs. 7.13 to 7.15). This general alignment of the lamellar crystallites parallel to the sliding direction confirms that the maximum shear stress lies parallel to the sliding direction and that the loading conditions can be described as simple shear (torsion) and compression [302]. The subsurface microstructures in this region appear vulnerable to shear (strain) localisation at both test temperatures and are characteristic of the microstructures generated during shear banding [302,335–337]. The resolvable matrix microstructural features observed via SEM (Fig. 7.8) suggest that layer 2 penetrates to depths of the order of a few/several tens of microns beneath the contacting surface. It is suggested that as the surface is approached, the homogeneous modes of deformation observed in layer 1 become inhibited, the subsurface becomes unstable, and localised shear phenomena completely engulf the near surface microstructure within layer 2 (Figs. 7.13 to 7.15). These microstructures are consistent with the formation of shear bands and the accommodation of large strains principally by grain boundary mediated deformation mechanisms (e.g. grain boundary sliding/migration, grain rotation and grain boundary diffusion) and crystallographic slip [302,335–337].

This ability to sustain high levels of deformation within layer 2 is clearly a result of the specific loading conditions of simple shear (torsion) and compression where a high hydrostatic component of stress is generated. Furthermore, the deformation mechanisms and microstructural evolution within layer 2 may be influenced by adiabatic heating during the localisation phenomena and the flash temperatures and thermal gradients induced by sliding.

It is suggested [335–337] that high accumulations of defects, for example transformation/twin networks and dislocation structures including heterogeneous dislocation cells, provide the pre-requisite for a sudden release of deformation energy that is generally considered to be the driving force for shear localisation and the generation of a shear banded type microstructure. Shear banding is believed to occur when the homogeneous deformation modes cannot accommodate any further deformation via defect generation or motion. A new deformation mode, in the form of localisation, then occurs which breaks up the microstructure previously constrained by defects. Deformation mechanisms (for example transformation and twinning) are restricted and grain boundary mediated deformation mechanisms and crystallographic slip during localisation (shear banding) become the principal modes of plastic deformation. Prior to or during the initial stages of localisation, elongated microstructural features are generated in the direction of shear probably by: (i) heterogeneous dislocation structures (specifically dislocation cells) which become elongated due to plastic deformation, or (ii) lath like microstructures generated via primary/secondary deformation twinning (particularly during testing at 20 °C). With specific reference to dislocation cells, the lateral dislocation walls which are aligned parallel with the direction of shear are thinned due to dislocation annihilation and new boundaries may be formed [337].

It is hypothesised that the localised matrix microstructural evolution/refinement observed in layer 2 (Figs. 7.13 to 7.15) is in part influenced by an avalanche of dislocations which assists with the localised flow of material by crystallographic slip. This is based on the observation that the localised microstructure is largely composed of elongated crystallites which exhibit large internal misorientations generally along their length (Figs. 7.14 and 7.15). These large misorientations

are most probably the product of domains of high and low defect (dislocation) density resulting in large contrast variations within a given elongated crystallite (Figs. 7.14 and 7.15). During sliding, dislocation accumulations, such as dislocation tangles or pile ups may form along the length (often at the ends) of elongated crystallites. Dislocations continue to accumulate within these elongated crystallites and separate domains that are composed of high and low dislocation/defect densities are formed. These domains of dense dislocations become thicker and thicker until the elongated microstructural features collapse, breakdown or split and new boundaries are formed [302, 337]. This process, which is often termed the avalanche of dislocations, is dominated by (internal) crystallographic slip and observed throughout the entirety of the localised deformation layer (Figs. 7.13 to 7.15). This confirms that crystallographic slip and the avalanche of dislocations is an important deformation mode which assists with strain accommodation within layer 2 of the TAM. This breakdown of elongated crystallites appears to heavily influence the microstructural evolution/refinement within layer 2.

It is postulated that strain accommodation within the nanocrystalline localised microstructure is heavily influenced by grain boundary mediated deformation mechanisms which differ from the traditional deformation modes observed in layer 1 (and other coarse grained materials). Once a nanocrystalline structure is generated in layer 2 (Figs. 7.13 to 7.15), large strains are believed to be principally accommodated by grain boundary mediated deformation modes including grain boundary sliding and rotation. This hypothesis is proposed based on two observations: (i) the width of elongated crystallites is subject to very slow/little microstructural refinement during shear deformation (as the contacting surface is approached); and (ii) the most notable microstructural variation/evolution occurs via the breakdown of elongated crystallites which is reliant on internal dislocation slip (Figs. 7.13 to 7.15). If the large strains accommodated within layer 2 are completely accounted for by internal dislocation slip, one would expect both a potent breakdown and narrowing in the width of the elongated crystallites within layer 2. However, this is not the case and indicates that grain boundary mediated deformation mechanisms are the principal mode through which enormous strains

are accommodated within layer 2.

Within the strain localised layer, globular nanoscale regions are seemingly generated which possess both a roughly uniform crystalline orientation and defect density and thus, appear to have similar contrast in Figs. 7.14 and 7.15. The dimensions of these regions are seemingly larger than the parent microstructural features (elongated crystallites) and appear to be composed of multiple different crystallites. This observation further strengthens the theory that grain boundary mediated deformation mechanisms (namely grain boundary slip and rotation) are the principal mode of strain within the localised layer. This hypothesis is consistent with both the microstructures and deformation mechanisms previously reported during severe plastic deformation involving nanocrystalline principally austenitic microstructures [284, 286, 335–337]. Grain boundary mediated deformation within shear banded microstructures has also been reported [335], and it is believed to play a significant role in the accommodation of shear through both the rotation of individual crystallites and clusters of crystallites.

Although not the dominant mode of strain accommodation, notable strains may still be accommodated via crystallographic slip within layer 2 because the small dislocation path length associated with the ultrafine/nanocrystalline microstructure means that dislocations can be readily and easily incorporated within the high angle crystallite boundaries (Figs. 7.14 and 7.15). Additionally, the probability of dislocation interaction events within a given crystallite is reasonably low due to the small dislocation path length. Therefore, the development of the internal dislocation accumulations (and low angle boundaries) that are required for microstructural evolution and refinement requires large strains [302] (Figs. 7.13 to 7.15). It is also suggested that dynamic recovery in the initial stages of localisation may aid with the formation of low-angle boundaries. It is postulated that a large fraction of dislocations are simply consumed within the crystallite boundaries which means that the rate of microstructural evolution and strain hardening is low relative to the strains which are accommodated via crystallographic slip within layer 2 (Figs. 7.13 to 7.15). However, this mode of deformation may be important as grain boundary sliding, grain rotations, and lattice dislocation slip de-

formation modes have been reported to strongly influence one another [342–344].

Other mechanisms may also be important in the evolution of the microstructure generated within layer 2, particularly during the early stages of localisation. By way of example, given that γ -Fe (fcc) has 24 available twin systems operative on the $\{111\}$ planes, a deformation induced rotation inside or outside the localised layer may easily permit the activation of twin systems (especially at lower temperature) which become orientated towards the direction of shear. In this instance, twins will rapidly multiply and a state of saturation will be reached which generates a microstructure of fine laths [337]. This microstructure will subsequently further evolve due to grain boundary mediated deformation and crystallographic slip and the avalanche of dislocation. More generally however, deformation induced rotations may permit the activation of deformation twin and slip systems (also on the $\{111\}$ plane) which will readily generate elongated microstructures aligned with the direction of shear. Sliding induced rotations which permit the preferred alignment of the $\{111\}$ planes parallel to the sliding direction may be a factor that contributes to the preferred alignment of the $\{111\}$ planes parallel to the sliding direction observed in the XRD patterns (Fig. 7.7). This preferred alignment is one factor which causes an increase in the relative peak height of the $\{111\}_{\gamma}$ reflection following autoclave testing compared to as received Tristelle 5183.

The microstructures within layer 2 (Figs. 7.13 to 7.15) retain a lineage with the original deformation microstructure prior to shear localisation whereby, the breakdown of high aspect ratio (elongated) microstructural features provides compelling evidence that they directly evolved from elongated lath or cellular type microstructures. Therefore, dynamic recovery followed by continuous dynamic recrystallisation resulting in microstructural refinement are believed to be the principal mechanisms controlling the microstructural development within the localised regions beneath the contacting surface [267,335,337,345]. This microstructural evolution mechanism is supported by the diffuse texture within the localised region which conforms to the S1 type where the strongest component at the near surface is $\{111\}[110]$, typically tilted up to 10° from the sliding direction (Fig. 7.15). Dynamic recrystallisation is not believed to be operative as

there appears to be no nucleation/growth period and the localised regions are not composed of defect-free equiaxed grains typically observed in dynamically recrystallised materials (Figs. 7.13 to 7.15) [345]. Additionally, within the strain localised region, a large fraction of boundaries appear ill-defined - which is a significant deviation from nucleation/growth type of recrystallised grains. No recrystallisation texture was observed (Fig. 7.15) which further supports the idea that the microstructure evolves via continuous dynamic recrystallization as opposed to classical dynamic recrystallization. The high degree of random orientation does however support the argument that recrystallization has taken place in the form of continuous dynamic recrystallization. It is also noted that as the sample surface is approached, the nanoscale crystallites within the strain localised region tend to become increasingly more equiaxed (Figs. 7.13 to 7.15).

TEM (Figs. 7.13 to 7.15) shows that carbides have a profound effect on the localisation phenomena whereby hard carbide phases clearly act as impenetrable barriers to localisation (shear banding) and disrupt the localised deformation pattern of elongated matrix crystallites in the immediate vicinity of the carbides. The mismatch in the mechanical properties between the carbide and matrix phases means complex multiaxial stresses are induced in the matrix during sliding; this distorts the localised direction of plastic flow (the direction of shear) which would otherwise be aligned parallel to the sliding direction. This explains the wavy appearance of the localised matrix crystallite deformation pattern within layer 2 (Figs. 7.13 to 7.15) which directly relates to the presence of carbides. Considering the above, it is hypothesised that the presence of carbides will increase the critical strains for localisation and to some minor extent homogenise and distribute shear (Figs. 7.13 to 7.15).

7.3.3. Layer 3 - The tribological interaction layer

Layer 3 (Fig. 7.17) is highly variable, very sensitive to test temperature and encompasses many tribological phenomena including (but not limited to) the plastic ratcheting of extruded slivers, fracture, mechanical mixing, tribochemical reactions and oxidation. However, layer 3 can more generally be defined as layer directly

adjacent to the interface within which material removal (debris generation) and both physical and chemical interactions with the environment and counterface occur. The details of the interacting tribological phenomena which are observed at the contacting surfaces during autoclave sliding contact testing will be discussed in the following sections.

7.3.3.1. Degradation via plasticity dominated wear

Following testing at 20 °C (Figs. 7.4, 7.8 and 7.13) (and to a lesser extent 250 °C (Fig. 7.5)), highly deformed striations/slivers of mechanically mixed material, which are principally metallic in nature, have been identified at the contacting surface (Fig. 7.4). These tribological layers are characteristic of plasticity dominated wear [11,73,79,303,304,346,347] which is almost certainly one of the principal mechanisms governing the degradation of Tristelle 5183, particularly during testing at 20 °C. It should also be noted that metallic plate/flake-like wear debris, which is entirely consistent with plasticity dominated wear, was observed and recovered following testing at 20 °C (Fig. 7.9) [11]. Whilst the material contained within the tribological layers following testing at 250 °C is highly variable in nature, and typically influenced to some extent by oxidation/corrosion (Figs. 7.5, 7.8, 7.15 and 7.16), plasticity dominated wear has not been completely suppressed (Fig. 7.5), so the degradation mechanisms discussed in the present section are still applicable. However, this specific section on plasticity dominated wear is particularly relevant to autoclave testing at 20 °C.

A number of theories have been proposed in the literature which attempt to identify the mechanisms of degradation leading to the generation of plate/flake-like debris during plasticity dominated wear [311,312,348–351]. Nevertheless, two notable mechanisms of plasticity dominated wear have been identified in the literature which provide some insight into the generation of the thin plate type wear features and debris observed in the present study. Firstly, the extrusion of thin slivers via plastic ratcheting which subsequently break off [310–312]. Fracture does not play an intrinsic role in this wear mechanism and fracture is only relevant to the detachment of the extruded slivers. Secondly, crack nucleation and

propagation via the fracture of a thin surface layer resulting in detachment (often termed 'delamination' wear) [351,352]. The latter of these two mechanisms can be related to surface failure via low cycle fatigue [353,354]. However, both of these wear mechanisms can be linked to the plastic ratcheting phenomenon. Therefore degradation can be more generally described as 'wear by plastic ratchetting' [310] as, irrespective of the failure mode, large subsurface strains have been accommodated via plastic ratcheting which provides the necessary criterion/condition for near surface failure. In light of the this, two competing failure modes have been identified [310,355], specially: (i) material detachment when the accumulated strain reaches a critical value (this is analogous to the strain to failure observed in monotonic tests and is termed ratchetting failure) and, (ii) failure by low cycle fatigue.

During the sliding conditions investigated in this study (Figs. 7.3 to 7.6, 7.8, 7.9 and 7.13 to 7.15), plastic ratcheting and extrusion leading to fracture seems to be the most dominant mode of plasticity dominated wear. The accumulation of strain via ratcheting generates a tribological layer within which the deformation structures are inherently more heterogeneous relative to the rest of the TAM and often composed of numerous discernible layers (Figs. 7.8 and 7.13). The thickness of this tribological layer is highly variable and typically of the order of 0 - 10 μm following testing at 20 and 250 $^{\circ}\text{C}$ (Figs. 7.8, 7.13 and 7.15). It is clear that a large fraction of the so-called subsurface cracks are in fact generated via extrusion; this is made evident by the observation of extruded plate-like features, gross plastic deformation, and the presence of cracking in heavily plastically deformed material (Figs. 7.4, 7.5, 7.8, 7.13 and 7.15). It is postulated that these so-called subsurface cracks (Figs. 7.4, 7.5, 7.8, 7.13 and 7.15) grow each loading cycle and can be regarded as ductile shear cracks which are governed by plastic strain [312] and not by elastic stress intensity conventionally used in linear elastic fracture mechanics [356,357]. Based on these observations, it seems probable that ratcheting failure is the dominant mode of failure resulting in material detachment.

Whilst the plastic ratcheting phenomenon provides one with a dominant mechanism of material detachment, some additional consideration needs to be made

concerning material transfer, mechanical mixing, and 'third body' effects within an autoclave environment. Mechanical mixing permitted by the plastic ratcheting phenomenon also appears to be prevalent throughout the tribological layer and the evidence for this has been provided by three notable observations. Firstly, isolated fragments of both NbC and M_7C_3 exist in the tribological layer (Figs. 7.8 and 7.13) which can only have formed via fragmentation followed by mechanical mixing with the matrix. Secondly, the matrix composition in the tribological layer is inhomogeneous and deviates from that of the bulk following testing at 20 °C (Fig. 7.13). In this self-mated sliding situation, the chemical modification of the tribological layer is most probably a result of chemical interaction (possibly oxidation) and mechanical mixing within the autoclave environment [304]. Finally, the extensive strains accommodated within the tribological layer can only have been achieved in conjunction with mechanical mixing where the principal deformation modes are grain boundary mediated as well as a contribution from crystallographic slip.

The transfer phenomenon [304] is inherently difficult to investigate and confirm within self-mated sliding systems. However, it seems unlikely that a detached plate-like feature is instantaneously ejected from between the contact without further interaction with the contacting surfaces. Therefore, it is hypothesised that an element of material may be transferred, reattached to either of the contacting surfaces, and further deformed prior to debris ejection from within the wear track. During steady state wear, it is suggested that the following transfer phenomena may occur: (i) the repeated transfer of previously transferred material, (ii) the integration and transfer of previously undetached material, or (iii) the formation of new transfer elements. During steady state sliding, the repeated adhesion, deformation, and transfer of material at the interface may lead to the generation of a plate-like wear particle [11, 73]. This plate-like wear particle (third body) is either, ejected from the contacting surfaces (Fig. 7.9) or re-integrated within the contacting surface. Regardless, based on the observations made in the present work, it seems probable that the generation of a tribological layer is necessary for material detachment during steady state wear.

The in-depth analysis of the deformation evolution within the TAM has shown

that strain localisation driven by concurrent operation of grain boundary mediated deformation mechanisms and crystallographic slip is fundamentally important in the accommodation of extensive strain during plastic ratchetting. Additionally, the loading conditions imposed during sliding (simple shear and compression) generate a high hydrostatic component of stress which permits the somewhat ductile response of an alloy that would otherwise be considered brittle. It is therefore postulated that localisation principally driven by grain boundary mediated deformation and crystallographic slip (Section 7.3.2) within the TAM is intrinsically linked to the plasticity-dominated wear phenomenon which is crucial to the degradation of the sliding contact investigated in the present study. In other words, regardless of the mode of surface failure discussed above, localisation is considered to be essential for plasticity-dominated wear to be operative. The TAM succumbs to localisation and extensive grain boundary mediated deformation and crystallographic slip at depths up to approximately several tens of micron beneath the contacting surface. Therefore, under the present sliding conditions, Tristelle 5183 is incapable of suppressing the detachment of microscale debris via plasticity dominated wear.

The presence of tribological layers greatly influences the contact state of the frictional surfaces and acts to partially suppress the extent of subsurface deformation by accommodating large shear strains [11]. Under the contacting conditions employed in this work, the presence of a stable metallic tribological layer seemingly suppresses the onset of deep penetrating gross plastic deformation and transfer. Unfortunately, the tribological layer is clearly readily removed and subsequently replenished by either the underlying zones or the counterface once a steady state sliding wear regime is established.

7.3.3.2. Degradation during sliding contact at 250 °C

In contact mechanics, the influence of both chemical and mechanical degradation at the contacting surface cannot be considered independently [11, 54]. Additionally, the deformation induced microstructure at the contacting surface inevitably influences chemical degradation and likewise, the extent of chemical degradation

influences the deformation microstructure [74,75]. However, it is convenient for the purposes of discussion to first reflect on the temperature dependent chemical degradation of Tristelle 5183 prior to elaboration on its relationship with the applied mechanical stimuli. Nevertheless, it should be noted that this study is concerned with the chemical degradation of a deformed microstructure and not the as received HIPed microstructure of Tristelle 5183.

TEM (Fig. 7.13) and XRD (Fig. 7.7) of the TAM shows no evidence of any breakdown in passivity post autoclave exposure at 20 °C. This is consistent with the literature, and in water and aqueous solutions at ambient temperature, a passive film (\sim 1-3 nm thick) composed of chromia (Cr_2O_3) or hydrated chromium-oxyhydroxide is known to develop on austenitic stainless steels with similar compositions to the austenitic matrix of Tristelle 5183 [32, 35]. In contrast, in lithiated water at elevated temperature (250 °C), a breakdown in passivity was observed, and Tristelle 5183 developed a duplex spinel type corrosion film (Fig. 7.16). This duplex corrosion film is composed of: (i) an outer layer of non-stoichiometric $\text{Ni}_x\text{Fe}_{3-x}\text{O}_4$ octahedral crystals (Fig. 7.6 (b) and Fig. 7.16) which form via the precipitation of metal ions released from the contacting surface and (ii) a Cr and Ni enriched inner layer which is most probably $\text{Ni}_x\text{Cr}_y\text{Fe}_{3-(x+y)}\text{O}_4$ [35–37, 358–360]. Cr-rich particles in the outer-most layer (Fig. 7.16) have not previously been reported in the literature and are possibly foreign debris/oxide generated via wear which is incorporated within the corrosion film. In addition to the above, the rate of oxidation is reportedly much more rapid under sliding conditions relative to static oxidation for numerous related alloy systems [11, 361]. It has previously been suggested that the increased rates of oxidation observed during sliding may result from the increased diffusion rates of ions through a growing oxide layer that contains a high density of defects as a result of mechanical perturbation [11].

The breakdown in passivity observed at 250 °C (Figs. 7.7 and 7.16), and the sliding conditions imposed during testing generate a frictional contact where complex oxidative and plasticity-type wear mechanisms are operative (Fig. 7.5). This is highlighted by the variability in the tribological features observed at the contacting surface, namely: (i) plasticity-type metallic tribological layers (Figs. 7.5

and 7.15); and (ii) mixed metal plus oxide tribological layers, and beds of varying degrees of mixing (Figs. 7.5, 7.8 and 7.15). The introduction of a significant corrosive/oxidative component of wear further complicates the interpretation of degradation and, as with the plasticity-type wear phenomenon, it is probable that there is no single dominant wear mechanism for the sliding contact during testing at 250 °C. It is believed that several degradation mechanisms are important and that these mechanisms may operate competitively, synergistically, or sequentially. For the purposes of the following discussion, degradation at 250 °C is summarised in the simplified flow chart, Fig. 7.18, where the mechanisms through which material detachment may occur are shown in red. Naturally, the removal of material from the contacting surface potentially generates new contacting asperities, so the flow chart (Fig. 7.18) is cyclic in nature.

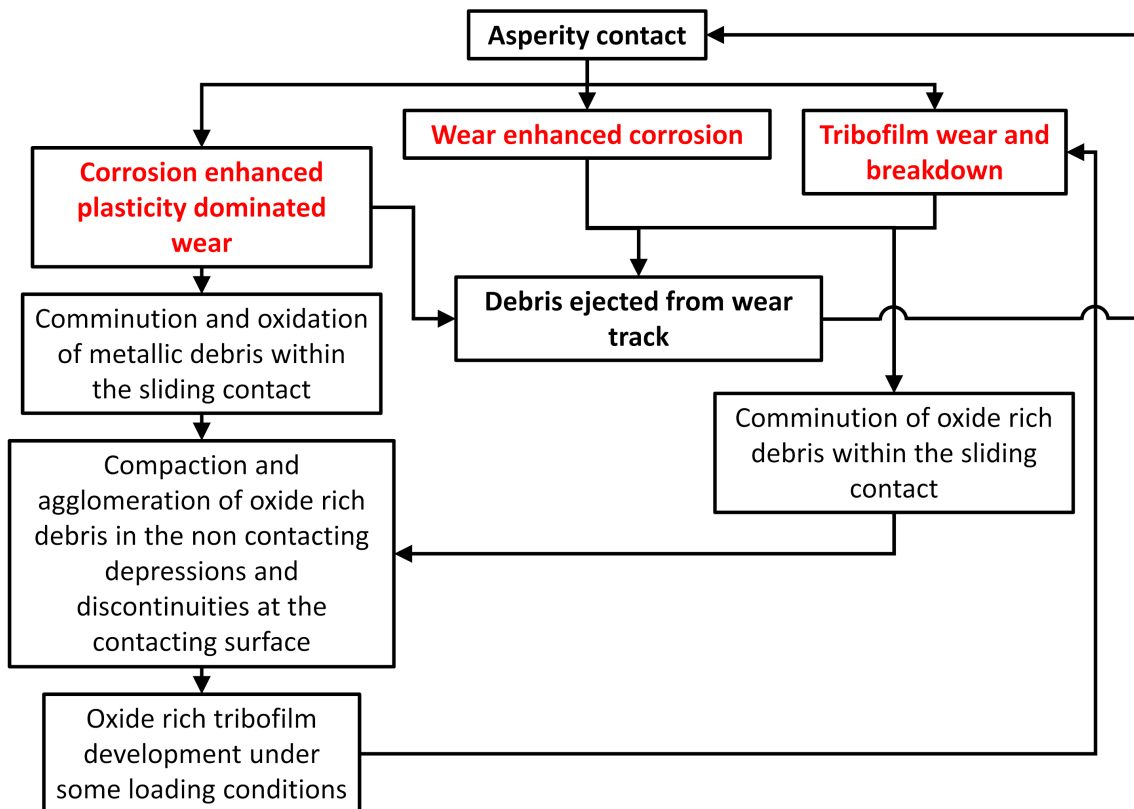


Figure 7.18: Simplified flow diagram showing the key phenomena and modes of degradation which occur during autoclave sliding contact at 250 °C.

7.3.3.3. Degradation during sliding contact at 250 °C -

Plasticity-type wear

Experimental observations (Figs. 7.5 and 7.15) show that thin striations/plate-like features of mainly metallic material may be generated at the contacting surface presumably by plastic ratcheting. Hence it is believed that the plasticity-type wear mechanisms discussed in the previous section (Section 7.3.3.1) are still operative during sliding contact testing at 250 °C and thus, plasticity-type wear is one of the mechanisms through which material may become detached and possibly ejected from the sliding contact (Fig. 7.18). Plasticity-type wear is generally observed in the wear track regions largely free from significant amounts of oxidised material or oxide containing tribofilms (Fig. 7.5). In these instances, any oxide-containing surface features have most probably been broken down and removed which permits the intimate contact of metallic surfaces. However, Figs. 7.5 and 7.15 suggest that the rate of material removal due to plasticity-type wear may be influenced by the presence of a corrosion product. Firstly, the presence of a corrosion product may interfere with the plastic extrusion of metallic striations by providing a barrier between otherwise contacting metallic surfaces (Figs. 7.15 and 7.16), this may promote the growth of ductile shear cracks and ultimately engender failure. Secondly, corrosion will affect the surface chemistry (Fig. 7.16) and possibly generate defects/discontinuities in the material undergoing plastic extrusion which may influence material detachment. Thirdly, the presence of a corrosion product may interfere with the transfer of metallic material which may accelerate particle detachment. However, it should be noted that the corrosion product observed in Fig. 7.16 may be influenced by the time spent in lithiated water during the autoclave cool down period following testing at 250 °C. Whilst additional growth of the passive film and/or metal dissolution is theoretically possible during this period, it is likely that the extent of chemical degradation would be small as the reaction kinetics must decrease as the temperature falls.

7.3.3.4. Degradation during sliding contact at 250 °C - The generation of oxide-containing debris

Several mechanisms have been identified for the generation of fine oxide-containing debris during sliding contact at 250 °C (Fig. 7.18). Firstly, the removal/spalling of the oxide rich tribofilm observed at the contacting surface [362]. Secondly, the removal of a corrosion film or transient oxide by mechanical stimulation [363] otherwise known as ‘wear enhanced/accelerated corrosion’ [54,57,62,74,75] or ‘oxidation scrape reoxidation’ [11]. Finally, the oxidation and comminution of metallic debris within the sliding contact. With respect to the first two mechanisms, the oxide rich debris which is removed directly from the surface may also undergo further fragmentation between the contacting surfaces during sliding (Fig. 7.18). It is also possible that the wear enhanced corrosion phenomenon may be important when the corrosion film thickness is insufficient to support tribofilm generation. By way of example, the thin (~ 200 nm) duplex corrosion product which contains faceted crystals shown in Fig. 7.16 appears to have the potential to be easily removed by mechanical sliding. When metallic debris is generated via (corrosion enhanced) plasticity-type wear, it is probable that this debris is further deformed and comminuted between the contacting surfaces instead of being completely removed from the contact zone. During comminution, the surfaces of these debris particles could oxidise/corrode [362–364] which is further assisted by the increased surface area generated by the breakup and fragmentation of debris. The corrosion of this debris will also be aided by the heat induced by deformation and the increased debris surface energy and defect density [362]. If one considers the heat of oxidation released, and the potentially fine morphology of metallic particles, it is possible that a metallic particle may be oxidised very rapidly within the sliding contact under certain conditions depending on the localised temperature, environment and particle size [36,362].

7.3.3.5. Degradation during sliding contact at 250 °C - Oxide accumulations and the development of oxide-containing tribofilms

The mechanisms identified above have the potential to generate a sufficient quantity of oxide-rich third-body particles for oxide-containing tribofilms (or a so called 'glaze') to develop on the contacting surface via a tribo-sintering process which will be discussed in the following sections [362, 364, 365]. It is postulated that the formation of the oxide-containing tribofilms observed at the contacting surface (Figs. 7.5 and 7.8) involve several phenomena which occur simultaneously, i.e. the generation, agglomeration, and compaction of oxidised debris [362–365]. Fine, wear-induced oxide-containing particles adhere to the contacting surface and agglomerate in the non-contacting depressions and discontinuities within the sliding interface (Figs. 7.5 and 7.8). These agglomerated clusters of particles grow and become increasingly compacted, fractured, and rearranged during sliding which increases their packing density [362, 363]. During this time, any metallic components within the particles may also oxidise/corrode further. It is hypothesised that these mechanisms also permit the formation and growth of the mixed metal plus oxidised beds observed on the contacting surface following testing at 250 °C (Figs. 7.5 and 7.8). It is possible that these oxide-containing beds potentially act as sources for the generation of oxide-containing tribofilms (Fig. 7.5).

The extensive plastic flow of the oxide-containing tribofilms is believed to be controlled by two factors: (i) The high hydrostatic stresses generated during sliding permit the extensive plastic deformation of the otherwise brittle oxide-containing agglomerates [313, 366]. (ii) Auerbach's effect for brittle solids whereby the critical load for cone crack production (unstable crack growth) increases with decreasing nondeformable indenter diameter [366, 367]. Whilst it has been suggested that brittle cracks develop during even small indenter (asperity) contacts [366, 367], these cracks remain stable and are unable to propagate leading to catastrophic failure with increasing load prior to the generation of sufficiently large hydrostatic pressures which enables plastic flow. It has been further suggested that plastic flow

may also promote the healing of cracks [366]. Auerbach's effect is applicable to the present sliding contact, and it is hypothesised that oxide-containing tribofims may develop and become active when the contact areas between oxide based asperities are sufficiently small for large hydrostatic stresses to develop; this prevents catastrophic crack propagation and enables plastic flow [366]. It is postulated that these two factors govern the depth beneath the contacting surface to which plastic flow of the oxide-containing material can occur and therefore also the depth of the tribofilm (up to $\sim 1 \mu\text{m}$ (Fig. 7.8)).

7.3.3.6. Degradation during sliding contact at 250 °C -

Oxide-containing tribofilm failure and degradation

Based on the conditions influencing the ductile behaviour of the oxide-containing tribofilms, it seems likely that once formed, the oxide-containing tribofilms may easily become unstable and break up. Experimental observations suggest that the oxide-containing layers ultimately fail and break down via crack initiation and propagation (Fig. 7.8 (b)). Additionally, tribofilm failure has been observed to generally be related to the interface between the tribofilm and the substrate (Fig. 7.8 (b)). The surfaces generated in the presence of an oxide-containing tribofilms have a more burnished appearance relative to the rougher surface regions generated via (corrosion enhanced) plasticity-type wear (Figs. 7.3 and 7.5). Once formed, it seems probable that with continued sliding, the oxide-containing tribofilms increasingly become more burnished and the area of the contacting asperity junctions increases. This reduces the hydrostatic component of stress generated during sliding which may permit the brittle failure of the oxide-containing tribofilms (Auerbach's effect). Given that the oxide films can be plastically deformed under the present loading conditions, it may also be possible that these tribofilms fail via plastic ratcheting. It is also suggested that as the oxide-containing tribofilms are drawn out across the contacting surface, their failure may be assisted by their depletion in oxide rich material (Fig. 7.5). It is therefore suggested that there exists a critical tribofilm thickness range over which the oxide-containing tribofilms may be stable. The breakdown of an oxide-containing tribofilm may permit the intimate contact of

predominantly metallic surfaces and thus permit (corrosion enhanced) plasticity-type wear (Fig. 7.18).

7.3.3.7. Degradation during sliding contact at 250 °C - The impact of oxidation and oxide-containing tribofilms on wear

The formation of oxide-containing tribofilms in the present study are believed to influence wear in several ways. Firstly, oxide-containing tribofilms are believed to suppress plasticity-type wear by way of reducing both the number of metal to metal contacting asperities and shear strength at the interface [11]. Secondly, the reintegration of oxidised third bodies into the surfaces reduces the extent of material removal (Fig. 7.18). Finally, if an oxide-containing tribolayer becomes unstable and is broken-down, the release of hard oxide-containing particles may abrade the contacting surfaces. It is also noted that debris particles released by wear enhanced corrosion and (corrosion enhanced) plasticity-type wear may also have a third-body abrasive effect on the contacting surfaces prior to being ejected from the tribological contact or reintegrated within the contacting surfaces.

The large disparity between pin and disk wear observed following testing at 250 °C (Table 7.1) may possibly be explained in terms of the difference in contact conditions between the pin and the disk and its influence on oxidation/corrosion. More specifically, the pin remains in permanent sliding contact with the disk, whereas a given point on the disk is only in contact with the pin once per revolution (approximately every 0.3 s). It is postulated that this difference in contacting condition has a profound effect on the corrosive environment exposed to the wearing surfaces. The intermittent sliding contact the disk is subjected to means the disk is readily exposed directly to the corrosive medium and has a period without mechanical stimulation where a corrosion film may easily develop on the contacting surface. In contrast, as the pin remains in perpetual contact with the disk, the pins contacting surface may be partially shielded from direct contact with the chemical medium. The corrosion film has previously been shown to be readily removed therefore these differences in contact conditions means the pin and disk are subjected to different rates of corrosion and thus wear.

In summary, three modes of material detachment have been identified which may result in the ejection of debris from the contacting surfaces: (i) removal of material via (corrosion enhanced) plasticity-type wear, (ii) mechanical removal of a corrosion product (wear enhanced corrosion), and (iii) breakdown of oxide-containing tribofilms (Fig. 7.18). The above discussion (Sections 7.3.3.2 to 7.3.3.6) accounts for the experimental observations of the contacting surface which can be described by the following two limiting cases (Fig. 7.5): (i) regions within the wear track dominated principally by oxidative wear. (ii) regions within the wear track predominantly governed by (corrosion enhanced) plasticity-type wear. It is clear that the rate of oxidation/corrosion is insufficient for oxide-containing tribofilms to cover the entire contacting surfaces therefore (corrosion enhanced) plasticity-type wear and oxidative wear mechanisms operate simultaneously and strongly interact with one another. Obviously, the nature of wear is such that transition regions between these two limiting cases exist within the worn surface. Additionally, the fluctuant/stochastic nature of wear is highlighted by the variability in the topological scales over which the mechanisms and surface features described above are observed throughout the wear track (Fig. 7.5).

7.3.4. Evaluating the TAM via X-ray diffraction

7.3.4.1. *The influence of sliding conditions on deformation induced martensitic transformation*

XRD from the contacting surface following autoclave sliding contact testing at 20 °C (Fig. 7.7) shows that only a small fraction of the γ -Fe matrix undergoes the deformation induced martensitic transformation to α' -martensite. Nevertheless, this transformation appears to be saturated (under these sliding conditions), and no evidence of the intermediary ϵ -martensite phase is observed within the uppermost regions of the TAM contributing to the diffracted signal in XRD. However, the ϵ -martensite phase is observed via TEM 60 μm beneath the contacting surface (Figs. 7.10 to 7.12) and, at this depth, the γ (fcc) \rightarrow ϵ (hcp) \rightarrow α' (bct) transformation pathway has been identified as the principle mode through which α' -martensite is

generated during sliding. The ϵ -martensite observed 60 μm beneath the contacting surface must therefore further evolve and transform as the contacting surface is approached in order to remain consistent with the absence of ϵ -martensite in XRD (Fig. 7.7). It is possible that as the surface is approached, further transformation to ϵ -martensite is suppressed and α' -martensite may be generated via alternative pathways which may consume the remaining ϵ -martensite (Section 7.3.1.1). Regardless, under these sliding conditions the total fraction of α' -martensite is seemingly restricted even though the TAM contributing to the diffracted signal in XRD ($\sim 8 \mu\text{m}$ beneath the contacting surface) has been exposed to extensively high strains (Figs. 7.8, 7.13 and 7.14) at testing temperatures below the M_d temperature of Tristelle 5183. Section 7.3.1.2 has shown that other deformation modes are seemingly more energetically favourable as the sample surface is approached and DIM is seemingly terminated and saturated in a premature state under these specific sliding conditions.

In light of the above, XRD was employed to investigate how specific sliding conditions influence the extent of deformation induced transformation to α' -martensite. This was evaluated by comparing the extent of α' -martensite generated during self-mated autoclave sliding wear testing at 20 $^{\circ}\text{C}$ with that of a simple grinding experiment where HIPed Tristelle 5183 was deformed by water lubricated, low load abrasive sliding at room temperature ($\sim 20 \text{ }^{\circ}\text{C}$) (Fig. 7.19). More specifically, the abrasive medium used in the grinding experiment was a resin bonded diamond grinding disk (P120). In both sliding experiments the loading conditions are comparable, although different in magnitude, and can be described as simple shear and compression. However, the contact pressures, sliding speeds, frictional state of the contact and the wearing mechanisms are fundamentally different between these two experiments. As such, the TAM following these two sliding experiments is subjected to notably different strains, strain rates, and strain and thermal gradients. This ensures that there are two fundamentally different sliding induced deformation profiles which can easily be compared via XRD. Following the grinding experiment, it is clear that a significantly large fraction of the irradiated TAM contributing to the diffracted signal is transformed

to α' -martensite (Fig. 7.19). This shows that under certain sliding conditions, Tristelle 5183 can undergo an extensive and potent martensitic transformation to α' -martensite. In contrast, very little α' -martensite was observed following the autoclave sliding experiments at 20 °C even though both experiments were conducted within environments where the global temperatures are comparable.

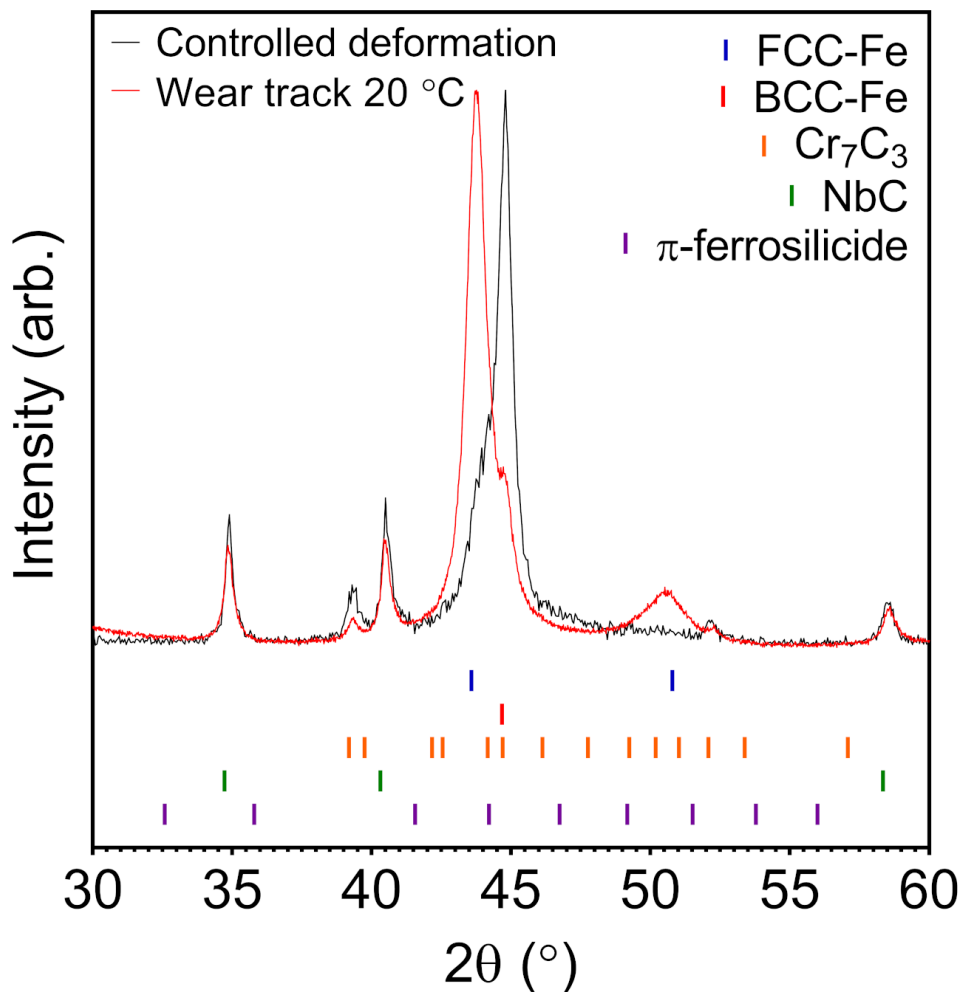


Figure 7.19: XRD patterns of Tristelle 5183 from within the wear track following testing at 20 °C and from within the wear track of a controlled grinding experiment conducted at room temperature. Patterns normalised to the reflection of maximum intensity.

One may argue that this disparity in the fraction of α' -martensite generated in these two sliding experiments may be influenced by the specific loads and strain rates associated with each of the given sliding situations. The deformation induced transformation to α' -martensite is known to be very sensitive to

varying combinations of strain and strain rate [199,324] and deformation at high strain rates increases the number of intersections which are known to permit the growth and coalescence of α' -martensite. However, at both large strains and strain rates, adiabatic heating effects can greatly restrict the nucleation of α' -Fe (bct) and act to increase the stability of γ -Fe (fcc) and reduce the driving force for transformation [199,324]. As such, adiabatic heating limits both the probability of forming α' -martensite embryos and growth of α' -martensite via coalescence such that α' -martensite is principally confined to the immediate intersection volumes of deformation structures. Therefore, at high strains, the rate of α' -martensite formation is considerably slower at high strain rates and larger fractions of α' -martensite can be generated at lower strain rates [199,324]. It is possible that differences in strain rate and the subsequent adiabatic heating effects between the two sliding experiment may be a factor contributing to the disparity in the fraction of α' -martensite generated during sliding.

Another factor which may have a profound influence on the fraction of martensite generated during sliding is the interaction between the overlapping strain and thermal profiles induced within the subsurface. For the purpose of aiding the discussion, Fig. 7.20 depicts a schematic representation of the thermal and strain profiles generated in response to sliding as a function of depth beneath the contacting surface for two hypothetical sliding situations. In this instance, the thermal profiles show the subsurface temperature variation at the point of contact and therefore, encompass the effects of both flash temperatures and steady state heating. Autoclave sliding contact testing at 250 °C has shown that the M_d temperature of Tristelle 5183 lies below 250 °C and it seems entirely reasonable to suggest that such temperatures may be ascertained within the thermal profile induced during autoclave sliding testing at 20 °C. It is possible that the combination of frictional heating and the heat of deformation raise the subsurface temperature above the M_d temperature of Tristelle 5183 thus creating a near-surface region where martensitic transformation is inhibited (Fig. 7.20). This region can be defined by a depth beneath the contacting surface which has been termed the critical transformation depth (D_c) and the strain which is generated at this depth is termed the

maximum strain for transformation (ϵ_{max}) (Fig. 7.20). This strain is the maximum strain which can yield transformation and any further accumulation of strain as the sample surface is approached does not yield martensitic transformation. The thermal and strain profiles induced by sliding are unquestionably different during the two sliding experiments and critically dependent on many factors: for example, contact pressures, sliding speeds, the frictional state of the contact and the wearing mechanisms. As shown in Fig. 7.20, the maximum strain for transformation (ϵ_{max}) is dependant on the overlapping nature of the thermal and strain profiles and variations in these profiles can result in large fluctuations in the fraction of α' -martensite generated during sliding. It is also possible that localised temperature increases within the subsurface may alter the pathways of transformation and the probability of martensite nucleation and growth. This seems entirely possible as the SFE increases with increasing temperature.

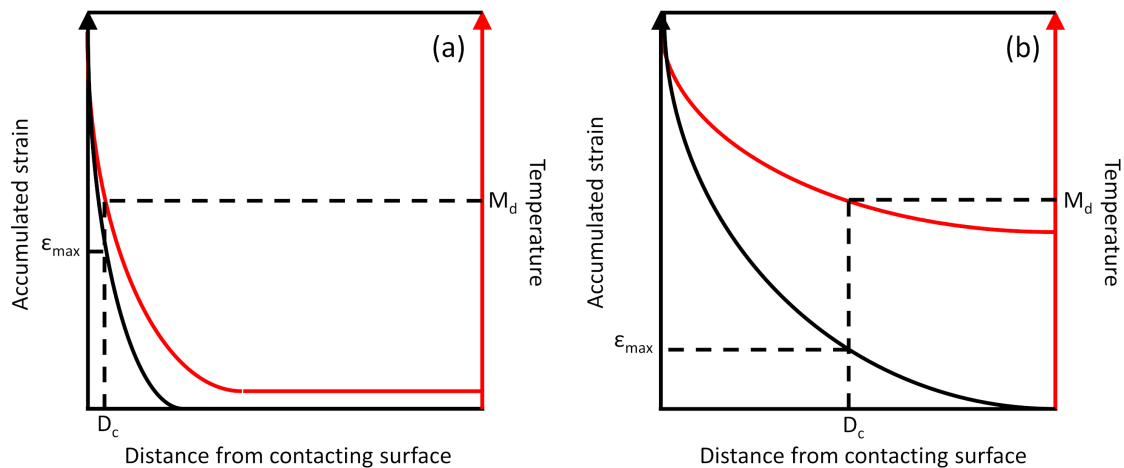


Figure 7.20: Schematic showing the accumulated strain (black) and thermal (red) profiles against the depth beneath the contacting surface for two hypothetical sliding situations following steady state wear. The thermal profile represents the temperature gradient at the point of sliding contact and encompasses a flash heating component in addition to a steady state temperature. The M_d temperature represents the limit for deformation induced martensitic transformation, and no deformation induced martensite can form above this temperature. D_c and ϵ_{max} correspond to the critical transformation depth and the max strain for transformation respectively.

The number of easily faulted (111) planes which may be activated during sliding is another factor which may influence the deformation induced transformation to α' -martensite. The number of easily faulted (111) planes influences the

probability of intersection between ϵ -martensite laths (and/or twins) which, has been shown to be a key mechanism through which α' -martensitic is generated (Fig. 7.12). However, it is unclear how this factor could account for the differences in martensitic transformation observed between the sliding experiments shown in Fig. 7.19 given that both loading conditions can be described as simple shear and compression and larger subsurface strains are most probably generated during wear by plastic ratcheting.

Adiabatic heating effects during deformation have been identified as one possible mode through which the generation of DIM may be constrained. However, adiabatic heating effects during dynamic loading in the most highly deformed regions of the TAM may also influence the stability of existing martensitic structures. For example, the α' (bct) \rightarrow γ (fcc) transformation has been reported by several authors during the severe plastic deformation of austenitic steels at high strain rates [368–373]. The driving force for reverse martensitic transformations is reportedly provided by: (i) adiabatic heating effects which stabilise the γ -Fe phase [368–370], (ii) the Gibbs free energy of ultrafine/nanoscale martensite structures [368–370], and (ii) the extremely high shear stresses induced during sliding [368–370]. In these studies the forward (γ (fcc) \rightarrow α' (bct)) and reverse (α' (bct) \rightarrow γ (fcc)) transformations are principally driven by twinning and very little ϵ -martensite is observed [368–373]. Diffraction studies have shown that α' -martensite is never extensively observed within the TAM following autoclave sliding at 20 °C, therefore it seems highly unlikely that reverse martensitic transformation is responsible for the disparity in the fraction of α' -martensite generated between the two different sliding experiments (Fig. 7.19). Based on this same observation, the thermal reversion of martensite due to a sliding induced temperature increase also seems unlikely to be a dominant factor accounting for the disparity in the α' -martensite. Additionally, the thermal reversion of α' -martensite would require a minimum temperature increase of the order of ~ 500 °C [374].

In summary, it is recognized that the martensitic transformations observed during sliding are inherently complicated and more work is clearly needed to better understand the mechanisms and factors which influence martensitic trans-

formation during sliding. However, the transformation characteristic observed within the TAM in the present study are seemingly heavily dependent on thermal effects induced by sliding.

7.3.4.2. Crystallographic faulting and crystallite size and strain broadening

The stacking fault probability within the irradiated volume of the TAM contributing to the diffracted signal was evaluated by XRD following testing at 20 and 250 °C. Even though the X-ray intensity contributing to the diffracted signal decreases exponentially with increasing depth into the sample [234], the average X-ray penetration depth contributing 99% of the diffracted intensity was on average $\sim 8 \mu\text{m}$ over the range of 2θ values used in the stacking fault probability calculations. In fcc metals and alloys, deformation faulting on the (111) planes (planar defects) in the form of stacking faults and twin faults have a profound influence on X-ray diffraction patterns [375–379]. The maximum intensities, broadening, shift and asymmetry of the γ -phase reflections are critically dependent on the presence, ordering and density of stacking faults on the (111) planes. The distance between the maxima of the {111} and {200} reflections decreases with increasing stacking fault concentration [376–378]. Additionally, the stacking fault concentration modifies peak profiles in different ways depending on the line indices [377]. With respect to the {111} reflection, an increase in the deformation stacking fault concentration causes an asymmetric broadening towards higher diffraction angles, but the peak position remains nearly in the Bragg position [377, 378] (Fig. 7.7). On the contrary, the {200} peak is shifted towards lower diffraction angles whilst remaining symmetrical [377, 378] when the deformation stacking fault concentration increases (Fig. 7.7). By way of rough approximation, the stacking probability, α , can be approximated at the two different temperatures by comparing the relative peak shifts of the {111} and {200} reflections with a standard sample (the undeformed HIPed microstructure) in accordance with equation Eq. (7.1) [379].

$$\Delta (2\theta_{200} - 2\theta_{111})^o = \frac{-90\sqrt{3}\alpha}{\pi^2} \left(\frac{\tan(\theta_{200})}{2} - \frac{\tan(\theta_{111})}{4} \right) \quad (7.1)$$

This gives notably different stacking fault probabilities of 0.036 and 0.025 for testing at 20 and 250 °C respectively. This highlights the extent to which the SFE is increased with increasing test temperature in this alloy system. The influence of planar defects on peak broadening is reportedly non-monotonically dependent on planar defect concentration except for the $H00\{200\}$ reflections which monotonically broaden [377,380]. This notable broadening of specifically the $\{200\}$ reflection with increasing planar defects is one significant factor which contributes to the variation in peak height ratio between the $\{111\}$ and $\{200\}$ reflections with respect to increasing test temperature (Fig. 7.7). Inspection of diffractograms following testing at 20 and 250 °C suggests that there is a reduction in the generation of deformation induced planar defects with increasing test temperature due to the increase in SFE (Fig. 7.7).

Fig. 7.7 shows that the influence of crystallite size and strain broadening on the γ -Fe peak profiles may also significantly change dependant on the autoclave test temperature. Rather than attempting to deconvolute the complex phenomena contributing to peak broadening, for the purposes of this simple comparison, the full width half maximum (FWHM) of largely isolated γ -Fe reflections were directly compared in order to quantitatively assess the apparent differences in crystallite size and strain broadening between the two different test conditions. The FWHM of the $\{200\}$ reflection following testing at 20 and 250 °C was 1.45 and 1.11 ° 2θ respectively. Likewise, the FWHM of the $\{311\}$ reflection following testing at 20 and 250 °C was 1.70 and 1.46 ° 2θ respectively. This suggests that the peak broadening contributions resulting from the crystallite size and strain effects are more dominant following testing at 20 °C relative to 250 °C. This is almost certainly influenced by the different deformation mechanisms operative at 20 and 250 °C (Sections 7.3.1 and 7.3.2). An additional factor which may also influence this difference is the presence of an oxide-containing tribofilm during testing at 250 °C (Fig. 7.8). This tribofilm is believed to suppress plasticity-type wear by reducing both the number of metal to metal contacting asperities and shear strength at the interface. This possibly reduces the subsurface strains and extent of crystallite refinement during autoclave sliding.

7.4. CONCLUSIONS

The tribologically affected material (TAM) can be described as a continuum of deformation which results from the strain gradient induced by the loaded sliding contact. The initial mechanisms of plastic deformation within the TAM (furthest from the sliding contact) are sensitive to fluctuations in stacking fault energy (SFE) and thus the test temperature. Following testing at 20 °C (lower SFE), the initial mechanisms of plastic deformation include: deformation induced martensitic transformation to ϵ -martensite and α' -martensite principally via the $\gamma \rightarrow \epsilon$ and $\gamma \rightarrow \epsilon \rightarrow \alpha'$ transformation pathways, twinning, the generation of planar dislocation arrangements (generated by planar slip) and the generation of dislocation tangles. However, following testing at 250 °C (higher SFE), the initial deformation microstructure is characteristic of a higher degree of cross slip activity and is thus dominated by heterogenous dislocation structures. Additionally, deformation induced martensitic (DIM) transformation and twinning (planar volumetric defect structures) are not observed at this test temperature. At both test temperatures, the deformation and transformation characteristics observed within the TAM are also influenced by sliding induced thermal effects.

Within the higher strained regions of the TAM (closer to the contacting surface) at both testing temperatures, the initial modes of plastic deformation become inhibited, the subsurface becomes unstable, and localised shear phenomena driven by grain boundary mediated deformation mechanisms and crystallographic slip completely engulf the near surface microstructure. A nanocrystalline microstructure is generated during shear localisation and enormous stains are accommodated by the concurrent operation of grain boundary mediated deformation mechanisms and crystallographic slip. Microstructural evolution/refinement within this region is notably influenced by dynamic recovery and continuous dynamic recrystallisation. High levels of strain prior to failure are permitted due to the specific loading conditions of simple shear (torsion) and compression where a high hydrostatic component of stress is generated.

The mechanisms of material removal in response to sliding in lithiated water are highly variable and sensitive to test temperature. Following testing at 20 °C,

degradation is principally governed by plasticity dominated wear. The extrusion of metallic slivers via plastic ratcheting generates ductile shear cracks governed by plastic strain, and the failure of these slivers generates plate/flake-like wear debris. At 250 °C, Tristelle 5183 incurs a breakdown in passive behaviour, a duplex-type corrosion product is generated, and complex oxidative and plasticity-type wear mechanisms are synergistically operative. Oxide accumulations/agglomerates permit the formation of oxide-based tribofilms during sliding which reduce both the number of metal to metal contacting asperities and shear strength at the sliding interface. Three mechanisms of degradation have been identified during sliding at 250 °, namely: (i) removal of material via (corrosion enhanced) plasticity-type wear, (ii) mechanical removal of a corrosion product (wear enhanced corrosion), and (iii) breakdown of oxide-containing tribofilms.

A COMPARATIVE ASSESSMENT OF THE TRIBOLOGICAL PERFORMANCE OF TRISTELLE 5183 AND STELLITE 6

8.1. INTRODUCTION

In this chapter, the tribological performance of Tristelle 5183 and Stellite 6 are compared following exposure to autoclave sliding contact tests in lithiated water at temperatures between 20 and 250 °C. In the previous chapters, investigations into the fundamental degradation mechanisms of Stellite 6 (Co-based) and Tristelle 5183 (Fe-based) are reported. However, this short chapter aims to identify the mechanistic differences which give rise to the disparities in tribological behaviour between them. Identifying these mechanistic differences and alloy characteristics is key to understanding why Co-based hardfacing alloys inherently exhibit excellent tribological performance. More importantly, however, the alloy design of improved Fe-based hardfacings for PWR primary system applications can be rationalised and centred on improving these characteristics.

8.2. AN OVERVIEW OF DEGRADATION MECHANISMS IN RESPONSE TO AUTOCLAVE SLIDING CONTACT

8.2.1. Stellite 6

Under the present autoclave sliding contact testing conditions at both 20 and 250 °C, Stellite 6 generally resists gross plastic instabilities and strain localisation phenomena that lead to plasticity dominated wear by plastic ratcheting. The mechanisms of strain accommodation within the sliding induced deformation gradient

of the tribologically affected material (TAM) remain largely microstructurally homogenous and any evidence of localised deformation microstructures is restricted to within the top 2 μm beneath the contacting surface (Figs. 6.10 and 6.11). Many deformation mechanisms have been identified within the TAM (Table 6.3) and these remain operative irrespective of test temperature between 20 and 250 $^{\circ}\text{C}$ (Section 6.3.1). However, the depths to which different deformation mechanisms penetrate beneath the contacting surface are observed to be temperature dependent (Figs. 6.8 to 6.11). In the early stages of deformation, strain is principally accommodated by $\gamma \rightarrow \epsilon$ deformation induced martensitic (DIM) transformation and the subsurface is completely transformed to ϵ -martensite as the contacting surface is approached (Figs. 6.9 and 6.11). This ϵ -martensite subsequently accommodates further strain, and it is suggested that a number of deformation modes (for example twinning and basal and prismatic dislocation slip) may be operative (Section 6.3.1). In the regions closest to the contacting surface, the microstructure is nanocrystalline and it is suggested that microstructural refinement and strain accommodation are principally driven by dislocation slip (Section 6.3.1). Nevertheless, the specific plastic deformation characteristics exhibited by Stellite 6 in response to the present sliding conditions mean that wear is confined to the removal of material on the nanoscale where chemical interactions with the autoclave environment affect material removal.

Stellite 6 exhibits passivating behaviour during testing at both 20 and 250 $^{\circ}\text{C}$ (Fig. 6.12), and it is believed that the synergistic effects of chemical degradation in conjunction with mechanical stimulation by sliding contact result in the removal of nanoscale particles from the contacting surface via tribocorrosion. However, the overall removal of material has proven to be sensitive to test conditions and increases by $\sim 16 - 39$ times when the test temperature is raised from 20 to 250 $^{\circ}\text{C}$ (Fig. 6.4). A synergistic temperature dependent increase in corrosion rate and SFE are believed to be the principal factors influencing this temperature dependent increase in wear by tribocorrosion, although the rate of corrosion is believed to be the dominant factor. These temperature dependent factors modify the mechanical deformation characteristics of the alloy, the extent of corrosion enhance wear

and/or wear enhanced corrosion, the amount of nanoscale mechanical mixing, the frictional state of the contact, the amount of material detachment and the degree of three-body abrasion. In summary, although there are clear differences in the rate of material removal following testing at 20 and 250 °C, the general mechanisms governing deformation and degradation remain the same irrespective of test temperature.

8.2.2. Tristelle 5183

In contrast to Stellite 6, under the present test conditions, Tristelle 5183 exhibits extensive subsurface plastic instability and strain localisation at both 20 and 250 °C. This permits the accommodation of gross plastic strains and renders Tristelle 5183 susceptible to wear by plastic ratchetting. The mechanisms of plastic strain accommodation furthest from the contacting surface are dependent on SFE and thus test temperature between 20 and 250 °C (Section 7.3.1). At 20 °C (lower SFE), strain is initially accommodated by mechanisms including: deformation induced martensitic transformation to ϵ -martensite and α' -martensite principally via the $\gamma \rightarrow \epsilon$ and $\gamma \rightarrow \epsilon \rightarrow \alpha'$ transformation pathways, twinning, the generation of planar dislocation arrangements (generated by planar slip) and the generation of dislocation tangles. At 250 °C (higher SFE), the deformation microstructures are characteristic of a higher degree of cross slip activity, dominated by heterogeneous dislocation structures, and deformation induced martensitic transformation and twinning are absent. With increasing strain (closer to the contacting surface), the initial (homogenous) modes of plastic deformation readily become saturated at both test temperatures and a new deformation mode in the form of strain localisation consumes the near surface and generates a nanocrystalline microstructure (Section 7.3.2). Within this localised nanocrystalline microstructure, extremely high strains can be accommodated by grain boundary mediated deformation mechanisms and crystallographic slip. Microstructural evolution/refinement within this strain localised region is notably influenced by dynamic recovery and continuous dynamic recrystallization, and the high hydrostatic component of stress generated during loaded sliding contact permits the accommodation of high levels of strain

prior to failure.

Under the present autoclave sliding contact testing conditions, the modes of tribological degradation for Tristelle 5183 are sensitive to test temperature between 20 and 250 °C. At 20 °C, degradation is governed by plasticity dominated (adhesive) wear - more specifically, wear by plastic ratcheting generates extruded metallic slivers and ductile shear cracks governed by plastic strain; the subsequent failure of these metallic slivers generates plate/flake like wear debris (Section 7.3.3.1). In contrast, Tristelle 5183 incurs a breakdown in passive behaviour as the test temperature is increased from 20 to 250 °C. This is accompanied by a shift in wear mechanisms from plasticity dominated wear during testing at 20 °C, to a wear regime where (corrosion enhanced) plasticity-type wear and oxidative wear mechanisms operate simultaneously/synergistically during testing at 250 °C (Section 7.3.3.2). Oxide accumulations/agglomerates permit the formation of oxide-based tribofilms which reduce both the number of metal to metal contacting asperities and the shear strength at the sliding interface. The modes of material removal at 250 °C can be subdivided into three categories: (i) the removal of material via plasticity-type wear; (ii) the mechanical removal of a corrosion product (wear enhanced corrosion); and (iii) the breakdown of oxide-containing tribofilms.

8.3. RESULTS - AUTOCLAVE SLIDING CONTACT TESTS AT TEMPERATURES BETWEEN 20 AND 250 °C

The combined pin and disk volume loss for Stellite 6 and Tristelle 5183 after 5 h, 4 kg dead load sliding contact tests at 20 and 250 °C within a lithiated water environment are shown in Fig. 8.1. These results have previously been reported in Chapter 6 and Chapter 7 for Stellite 6 and Tristelle 5183 respectively. All the volume loss measurements presented in this chapter were derived from mass loss values and converted to volume loss using a measured density of 8370 ± 1 kg/m³ and 7505 ± 5 kg/m³ for Stellite 6 and Tristelle 5183 respectively. By way of comparison, following testing at 20 °C, the combined pin and disk volume loss of Tristelle 5183 was between ~ 19.8 and ~ 47.0 times greater than that of Stellite 6.

However, at 250 °C, the difference in behaviour decreased significantly and the volume loss of Tristelle 5183 was only about 1.4 - 2.5 times greater than that of Stellite 6.

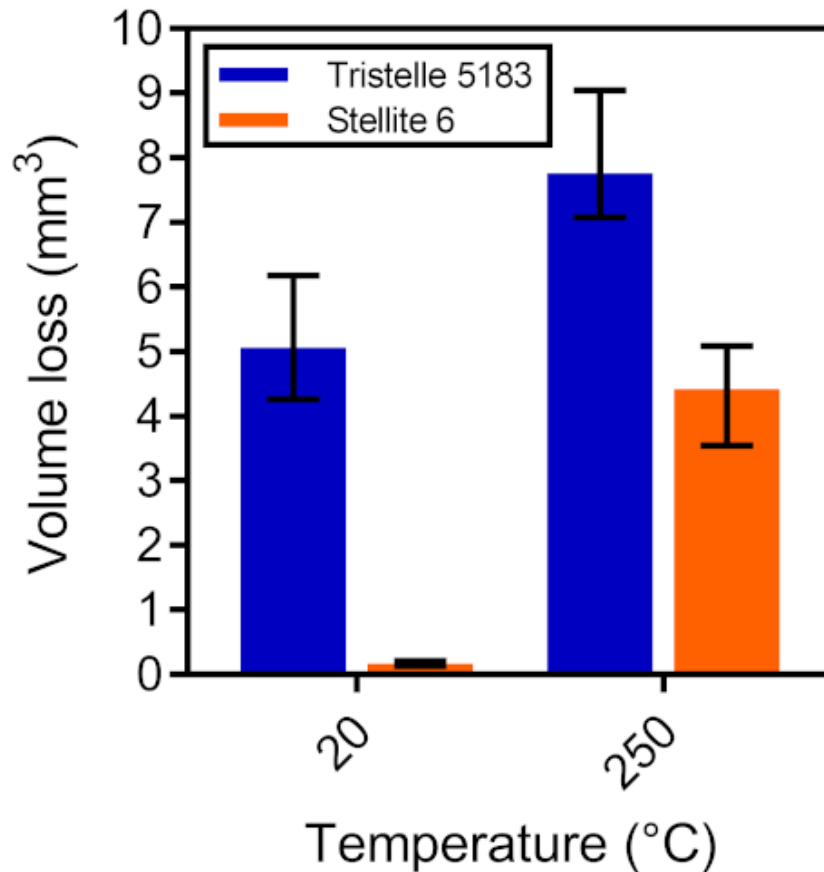


Figure 8.1: Graph showing the effect of autoclave test temperature on the volume loss of self-mated Tristelle 5183 and Stellite 6 following 5 h sliding contact testing with a 4 kg dead load. The bars represent mean values and the error bars represent the minimum and maximum values of combined pin and disk wear.

In order to further investigate the temperature dependent nature of material removal and better understand the synergistic interactions between chemical and mechanical degradation, autoclave sliding wear tests were conducted at intermediate temperatures between 20 and 250 °C. In the case of Stellite 6 (Fig. 8.2), the amount of material removal in response to autoclave sliding contact monotonically increases with respect to increasing test temperature. A notable change in the amount of material removal is observed at and above temperatures of 150 °C. The

total combined pin and disk volume loss at 250 °C is between ~ 9.3 and 19.4 times that observed at 150 °C and between ~ 2.4 and 3.8 times that observed at 200 °C. The individual components of pin and disk wear following a given test are often notably different however, based on these tests, no meaningful overall statistical observations can be made with respect to the difference between pin and disk wear and its dependence on test temperature.

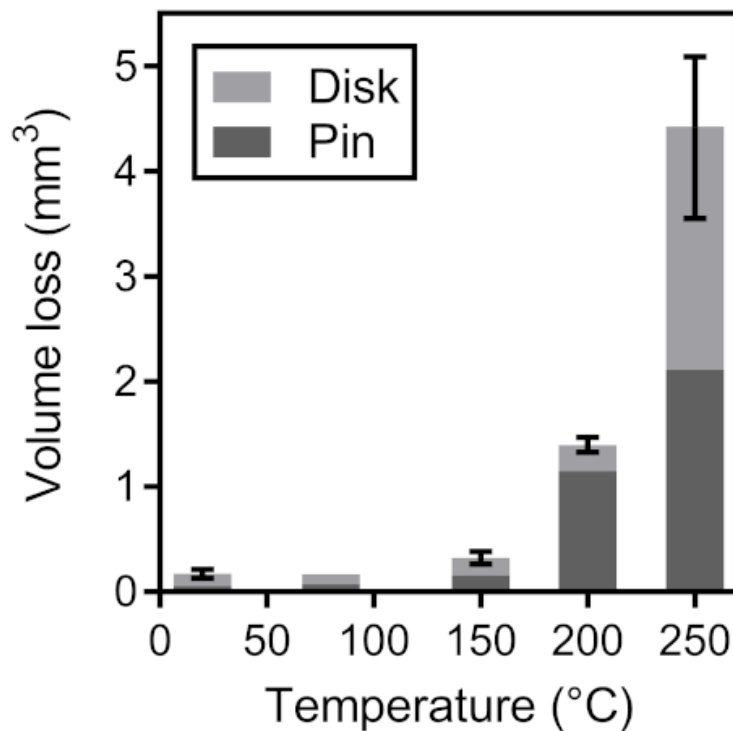


Figure 8.2: Graph showing the effect of autoclave test temperature on the volume loss of self-mated Stellite 6 following 5 h sliding contact testing with a 4 kg dead load. The bars are composed of two separate components relating to the mean values of pin (dark grey) and disk (light grey) volume loss. The error bars represent the minimum and maximum values of combined pin and disk wear.

With respect to Tristelle 5183 (Fig. 8.3), the amount of material removed in response to autoclave sliding contact is heavily influenced by the test temperature. Raising the temperature from 20 to 150 °C causes an increase in combined pin and disk volume loss by a factor of between ~ 3.0 and 5.4. However, increasing the test temperature above 150 °C causes a notable reduction in the combined pin

and disk wear; whereby, at 200 °C the combined pin and disk volume loss is only between ~ 1.7 and 2.9 times greater than that observed at 20 °C. It is also noted that at 250 °C, the disk wears significantly more than the pin.

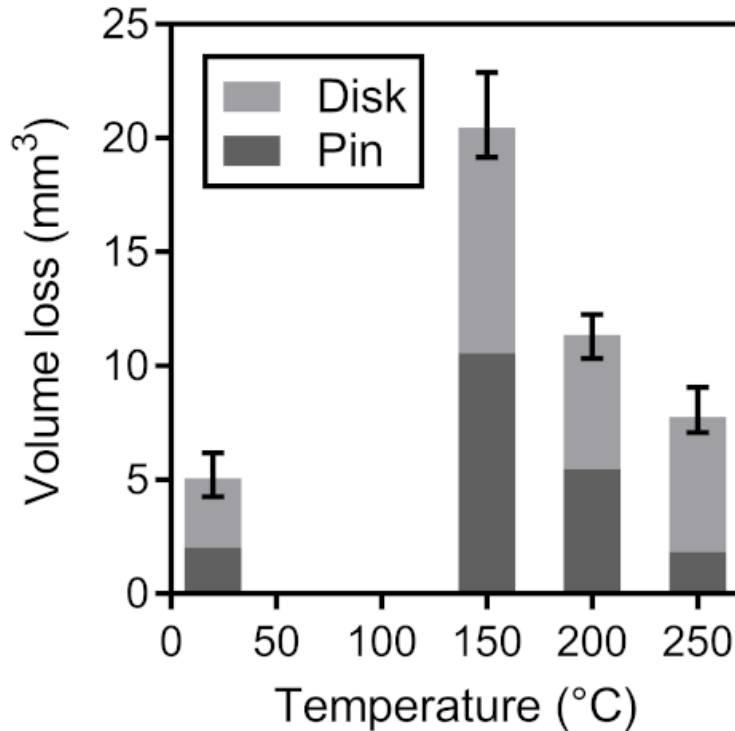


Figure 8.3: Graph showing the effect of autoclave test temperature on the volume loss of self-mated Tristelle 5183 following 5 h sliding contact testing with a 4 kg dead load. The bars are composed of two separate components relating to the mean values of pin (dark grey) and disk (light grey) volume loss. The error bars represent the minimum and maximum values of combined pin and disk wear.

Fig. 8.4 shows plan view BSE (Fig. 8.4 (a) and (c)) and SE (Fig. 8.4 (b) and (d)) micrographs (sliding direction horizontal) from central regions within wear tracks following testing at 150 °C (Fig. 8.4 (a) and (b)) and 200 °C (Fig. 8.4 (c) and (d)). The surface features revealed by SEM examination show some significant differences between testing at 150 and 200 °C. Nevertheless, the worn surfaces in all cases show surface features characteristic of plasticity dominated wear (Section 7.3.3.1) and exhibit highly deformed metallic slivers/plate-like features. These slivers are extruded in the sliding direction and have clearly incurred gross plastic deformation. However, the abundance of these sliver/plate-like features

is greater following testing at 150 °C compared to 200 °C. At 200 °C the BSE micrograph, Fig. 8.4 (c), reveals dark grey contrast regions which appear smeared in the sliding direction. These surface features are rarely observed following testing at 150 °C and are consistent with the smeared oxide containing accumulations observed following testing at 250 °C (Fig. 7.5).

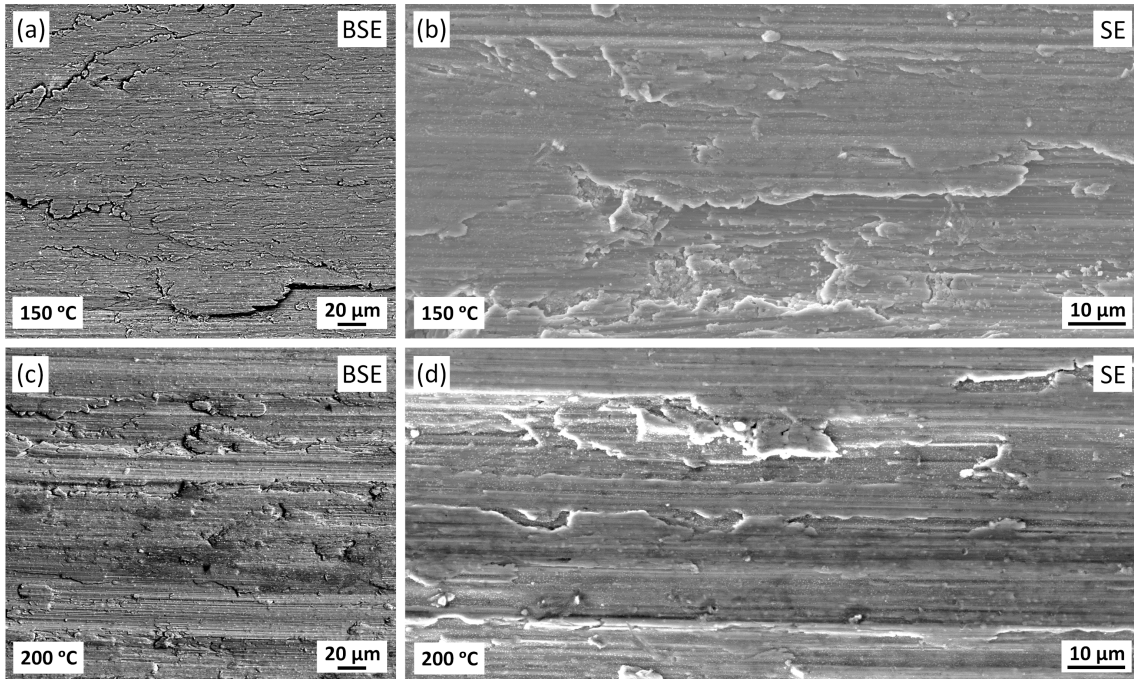


Figure 8.4: BSE (a and c) and SE (b and d) SEM micrographs showing the microstructure of the tribologically affected surface of Tristelle 5183 disk samples after sliding contact tests in an autoclave environment at 150 °C (a and b) and 200 °C (c and d) for 5 h. The sliding direction is horizontal to the figure in all cases.

Fig. 8.5 (a) and (b) show plan view SE micrographs (sliding direction horizontal) from central regions within a wear track following testing at 150 °C (Fig. 8.5 (a)) and 200 °C (Fig. 8.5 (b)). At both temperatures, the surfaces are decorated with faceted submicron crystals which are a spinel iron oxide isostructural to magnetite (Sections 7.2.4 and 7.2.7). The general size and abundance of these faceted oxide crystals is greater following testing at 200 °C compared to 150 °C. It is clear that there is a breakdown in the passive behaviour of Tristelle 5183 at both 150 and 200 °C, however the rate of oxidation is larger at 200 °C which permits the formation of the smeared oxide-rich surface features identified in Fig. 8.4 (c).

In the case of Tristelle 5183, understanding the degradation characteristics at

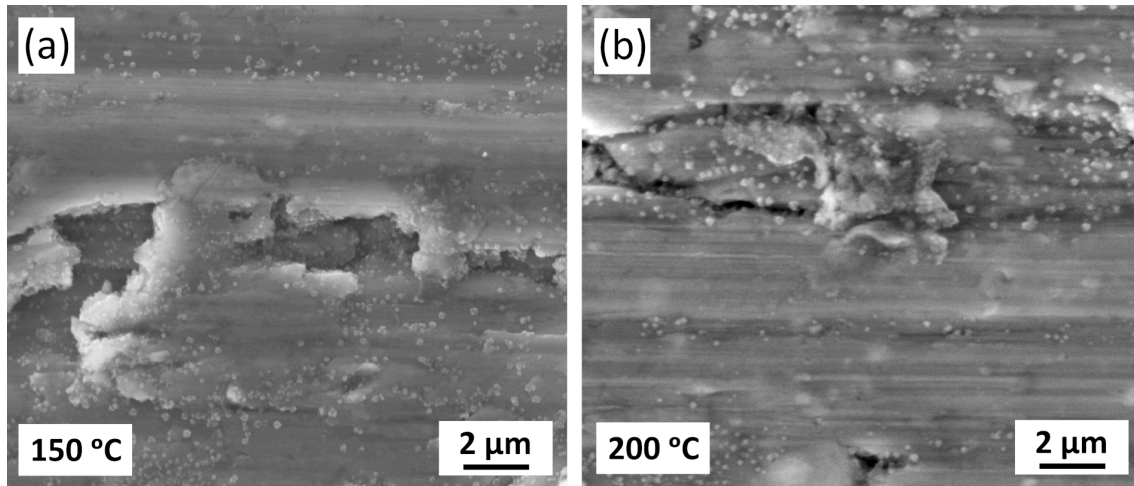


Figure 8.5: High magnification SE-SEM micrographs showing the microstructure of the tribologically affected surface of Tristelle 5183 disk samples after sliding contact tests in an autoclave environment at 150 °C (a) and 200 °C (b) for 5 hours. The sliding direction is horizontal to the figure in all cases.

temperatures between 20 and 250 °C has provided significant insight into the relative tribological impact of oxidative and plasticity-type wear. More specifically, a significant oxidative/corrosive component of wear is observed when testing at temperatures higher than 150 °C in response to an observed breakdown in passive behaviour of Tristelle 5183 (Fig. 8.5). The observation of surface features consistent with oxidative wear increases with increasing temperature up to 250 °C (Figs. 7.5, 8.4 and 8.5), and this coincides with a significant reduction in the amount of material removal (Fig. 8.3). This shows that between 20 and 250 °C the breakdown in passive behaviour and the subsequent generation of oxide containing surface features acts to reduce wear under the current sliding conditions.

8.4. DISCUSSION - THE MECHANISTIC DIFFERENCES IN TRIBOLOGICAL PERFORMANCE

8.4.1. Deformation characteristics in response to sliding contact

Wear is considered to be an evolutionary process, and the comparison of Stellite 6 and Tristelle 5183 in the present study has shown that the subsurface modes of deformation critically influence wear mechanism activation and tribological

performance. It is hypothesised that the inherent differences in deformation characteristics between Tristelle 5183 and Stellite 6 in response to sliding contact is one reason why Stellite 6 is the tribologically superior alloy following autoclave testing in the present study (Fig. 8.1). In the case of Tristelle 5183, it is suggested that plastic strain localisation principally driven by grain boundary mediated deformation mechanisms, crystallographic slip, dynamic recovery and a microstructure composed of incredibly fine deformation induced lamellae crystallites is critical to the accommodation of the extensively large localised strains required for the activation of plasticity dominated wear by plastic ratcheting. In contrast, the specific subsurface deformation characteristics of Stellite 6 inhibit extensive plastic strain localisation phenomena and the severe removal of material by plasticity dominated wear mechanisms. As such, the tribological degradation of Stellite 6 is generally confined to the removal of nanoscale particulates which is driven by the synergistic effects of chemical degradation within a corrosive environment and the application of a mechanical stimulus.

In light of the above, it is hypothesized that a high resistance to plastic strain localisation in response to sliding contact is a highly desirable alloy characteristic which acts to reduce degradation via plasticity dominated (adhesive) wear. It is recognised that localised plastic deformation occurs when the microstructures associated with homogeneous deformation can no longer sustain work hardening with increasing strain. Thus one of the principal causes of localised plastic deformation is the inability to sustain a sufficient strain hardening rate to prevent the accumulation of large strains in local regions. Strain hardening rate is controlled by two components, specifically: (i) dislocation storage (work hardening), and (ii) dynamic recovery (softening) which is related to the annihilation of dislocations. Sustaining and prolonging a high rate of work hardening at high strains by increasing the hardening component and reducing the softening component will delay the onset of localised deformation and increase the strains which can be accommodated via homogeneous deformation. It is hypothesised that this will increase the contact pressures required to initiate plasticity dominated wear and aggressive material removal, because plastic strain localisation has been shown

to be fundamentally linked to plasticity dominated wear by plastic ratchetting (Section 7.3.3.1). This concurs with recent observations of the plastic ratchetting phenomenon of self-mated HIPed Stellite 6 during in-air sliding contact at contact pressures greater than those investigated in the present study [381].

A low stacking fault energy which remains sufficiently low with increasing temperature up to 250 °C is one particularly advantageous alloy characteristic which favourably influences the rate of strain hardening in several ways. Firstly, a low SFE makes it easy for a full dislocation to dissociate into partials, which hinders the whole dislocation's ability to circumvent barriers/obstacles via cross slip or climb. This inhibits dynamic recovery via cross slip and climb, favours dislocation storage, and thus enhances the rate of strain hardening. Secondly, a low SFE favours strain accommodation via twinning and transformation (volumetric planar defects), both of which are critically dependant on the generation stacking faults. The formation of such planar volumetric defects are particularly effective structures in the storage and blocking of dislocations/defects which enhances the rate of strain hardening. Finally, the generation of stacking faults favourably influences the rate of strain hardening by interacting with slipping dislocations. In summary, lowering the SFE hinders the cross slip of dislocations for as long as possible during deformation evolution, and increases the volume fraction of volumetric planar defects which are particularly effective at storing dislocations during the subsequent stages of deformation evolution.

The low-energy (high angle) twin and transformation boundaries are believed to be highly effective at storing dislocations, hindering dislocation annihilation and suppressing dynamic recovery for several reasons. The lamella-like nature of a volumetric planar defect means the length scales of the two directions parallel to the planar defect boundaries are significantly larger than the ultrafine/nanoscale lengths associated with the direction perpendicular to the planar defect boundaries. Thus, dislocations may readily accumulate along the length of these lamellae-like microstructural features forming tangles and subdividing lamellae (Fig. 6.10) [382]. Twin boundaries also reportedly act as the locations where high densities of dislocations can move and accumulate from low levels [382]. The intersection

of volumetric planar defect structures will also favour the strain hardening rate as it essentially inhibits slip on all the available slip systems [383]. Additionally, the accumulation of large volumes of defects within planar volumetric defects cause the boundaries to become increasingly more stepped and bent (Fig. 6.10), and the resulting strain fields may generate dragging forces which act on moving dislocations. With increased deformation the planar volumetric defect boundaries lose coherency and become sources of dislocations.

In contrast, conventional grain boundaries (generated via deformation) are comparably less effective at enhancing the rate of strain hardening and delaying localisation. The short dislocation path lengths associated with equiaxed ultra-fine grain and nanograin deformation structures means dislocations cannot be easily trapped and are readily re-incorporated into grain boundaries. More specifically, dislocations generated by multiplication often simply escape to dislocation sinks prior to interacting with other dislocations and therefore the rate of defect accumulation is slow. It is postulated that a pronounced rate of work hardening cannot be sustained because the storage of dislocations at high angle conventional grain boundaries is reduced by the reorganisation and annihilation of dislocations inside the grain boundaries. Additionally, it is hypothesised that if the deformation induced effective grain size is smaller than the distance a dislocation glides before creating another dislocation via multiplication, the multiplication process may be terminated [382,384].

In light of the above, the profuse development of planar defect structures (for example stacking faults, twins and martensite laths) are believed to enhance the rate of strain hardening, impede the cross slip of dislocations, suppress the onset of dynamic recovery, hinder the annihilation of dislocations, and delay the onset of plastic strain localisation. In the case of Stellite 6, the SFE seemingly remains sufficiently low during sliding contact testing at both 20 and 250 °C for the potent development of planar defect structures. In contrast, despite the fact that Tristelle 5183 has a SFE which permits the generation of planar defects under certain sliding contact conditions at 20 °C (Section 7.3.1.1), the ability to generate such defects seems highly susceptible to thermal effects during sliding contact

(Sections 7.3.1.3 and 7.3.4.1). Additionally, planar defect structures within the matrix were not observed in the present study following testing at 250 °C. During testing at 20 °C, the generation of martensite laths, γ -Fe twins and stacking faults are easily terminated during deformation evolution. Cross slip becomes highly active early on during plastic deformation and extensive plastic strain localisation engulfs the near surface which permits gross plastic deformation and degradation via plasticity dominated (adhesive type) wear. Upon comparing Tristelle 5183 to Stellite 6 under the present sliding conditions, it is postulated that Tristelle 5183 has a lower ability to generate planar defects throughout deformation evolution and, in contrast to the case of Stellite 6, its SFE is easily increased into regimes where other modes of strain accommodation prevail - most probably due to a sensitivity to fluctuations in temperature (Sections 7.3.1.3 and 7.3.4.1). This means that the strain hardening ability of Tristelle 5183 diminishes more rapidly with increased strain compared to Stellite 6 and thus Tristelle 5183 is more susceptible to plastic strain localisation and wear by plastic ratchetting. Noting that DIM is critically dependent on the generation of stacking faults (Sections 6.3.1 and 7.3.1.1), the above hypothesis is reflected in the M_d temperatures of the two alloys. Stellite is capable of DIM up to temperatures of ~ 700 °C [29] whereas this study has shown that the M_d temperature of Tristelle is < 250 °C. The above hypothesis agrees with several other studies on the influence of SFE in wear [151,202].

Other factors also need to be considered in the activation of dislocation cross slip - more specifically, the cross-slip frequency is not only dependent upon SFE but also the dislocation-solute field interactions [383,385,386]. Interstitial atoms (specifically C and N) within the matrix solid solution have been shown to have a strong positive contribution to the constriction energy required for the pinching of two partial dislocations and cross slip activation [383,385,386]. In other words, the presence of interstitial elements hinders dislocation cross slip which therefore delays the generation of the dislocation structures associated with cross-slip and shifts them to higher levels of macroscopic stress. An increased fraction of interstitial elements within the matrix solid solution could therefore increase the tendency to form planar deformation structures as dislocation-solute field interactions could

severely restrict dislocation cross-slip.

8.4.2. Chemical degradation during sliding contact

In addition to the deformation response to sliding contact, chemical degradation within a PWR environment also critically influences wear mechanism activation and tribological performance. It has been demonstrated that there is a synergistic relationship between wear, deformation, and corrosion in both the alloys investigated in the present work (Sections 6.3.4 and 7.3.3). However, the temperature dependent chemical response of Tristelle 5183 and Stellite 6 are notably different; Tristelle 5183 exhibits a breakdown in passivity whereas Stellite 6 remains truly passive when the test temperature is increased to 250 °C.

In the case of Tristelle 5183, it is suggested that the oxide based tribofilms which form due to a breakdown in passive behaviour during testing at 250 °C may act to reduce the shear strength associated with the interface, reduce the number of metal to metal contacting asperities, and influence wear by the reintegration and release of oxide containing third bodies (Section 7.3.3.2). The development of these tribofilms is critically dependent on the formation of a duplex spinel type corrosion product (M_3O_4). However, the influence of this corrosive component of wear is inherently difficult to evaluate because, in the present sliding contact, oxidative wear operates in conjunction/synergistically with plasticity type wear which is also sensitive to both the test temperature and autoclave environment (Section 7.3.3.2). Testing at a variety of temperatures between 20 and 250 °C (Figs. 8.3 to 8.5) has, however, shed some light on how the breakdown passive behaviour influences the tribological performance of Tristelle 5183. The significant reduction in wear following testing at temperatures in excess of 150 °C (Fig. 8.3) is accompanied by a notable increase in the fraction of corrosion products (facet oxide crystals (Fig. 8.5)), oxide-containing agglomerates (Fig. 8.4 (c)) and oxide-containing tribofilms observed within the sliding contact. As the test temperature is raised above 150 °C the increased rate of corrosion permits the widespread development of lubricating tribofilms throughout the contacting surface. It is therefore postulated that the generation of load bearing oxide-containing tribofilms in response to the break-

down in passive behaviour favourably influences the tribological performance of Tristelle 5183 in the current autoclave sliding contact tests. This therefore implies that the principal factor which degrades the tribological performance of Tristelle 5183 with increasing test temperature is the temperature dependent shift in deformation characteristics (Section 7.3). However, it must be emphasised that chemical and mechanical degradation are synergistically coupled and directly influence one another.

As discussed in Section 7.3.3.5, the stability and development of oxide-based tribofilms is notoriously sensitive to the sliding conditions and the rate of oxidation/corrosion. Given the complexities and variability of the sliding conditions that real world hardfaced engineering components are exposed to within PWRs, the use of Fe-based alloys relying on corrosion and oxide containing tribofilm development for wear resistance may not always be effective. Corrosion may also negatively affect component functionality for example by: (i) stress corrosion cracking, and (ii) permitting leakage in components (for example, valve seats) which require intimate contact over large surface areas. Regardless of this, even though corrosion may favourably influence the tribological performance of Tristelle 5183 in the present tests, elevated corrosion product release rates are generally not acceptable and should be minimised within PWR systems. The release of a corrosion product into coolant systems and process streams can have many consequences that are less direct than the immediate attack and degradation of hardfacings. For example [36]: (i) the deposition of corrosion products onto heat transfer surfaces can act as thermal barriers; (ii) porous deposits of corrosion products may lead to accelerated localised corrosion; and (iii) by accelerating and enhancing crud deposition. Such factors can compromise the lifetimes of components and increase radiation fields which can hamper reactor operation and maintenance. In summary, a high degree of corrosion resistance is generally considered to be a desirable alloy characteristic for the hardfacings and other materials in contact with the primary coolant, however, an assessment of the relative advantages and disadvantages of corrosion and tribofilm development in relation to Fe-based hardfacing alloys used in the primary cooling system is beyond the

scope of this work.

In contrast, Stellite 6 remains passive and highly corrosion resistant irrespective of the test temperature between 20 and 250 °C. Additionally, the roles of mechanical and chemical degradation in relation to the wear of Stellite 6 are both temperature dependent and inherently coupled to one another (Section 6.3.4) even though the rate of passive film development is considered to be the dominant factor influencing the temperature dependent nature of wear (Fig. 8.2). The detailed characterisation of the contacting and sub surfaces presented in Chapter 6 has shown that variation in both the chemical and mechanical degradation of Stellite 6 with respect to increasing test temperature negatively impinge on tribological performance.

Unsurprisingly, the impact of oxidation on tribological performance is highly variable depending on the alloy system and thus tribological comparison between Stellite 6 and Tristelle 5183 based on their chemical response to an autoclave environment is inherently difficult. To summarise, the tribological influence of oxidation/corrosion is clearly dependent on many factors, for example: (i) the species of oxide generated, (ii) the rate of oxidation, and (iii) the specific plant (or autoclave) operating conditions (temperature and chemistry of the coolant water). However, from a purely tribological point of view, the combination of both passive behaviour and resistance to plastic instabilities during sliding contact means Stellite 6 consistently outperforms Tristelle 5183 in the current sliding contact conditions at any temperature between 20 and 250 °C.

8.4.3. The influence of frictional heating

It is well known that frictional heating and flash temperatures generated during sliding can have a profound effect on wear [387, 388]; this needs to be considered when comparing the tribological performance of Stellite 6 and Tristelle 5183. Frictional heating may manipulate the near surface deformation mechanisms; it may cause both accelerated oxidation and/or tribocorrosion; or it may induce tensile stresses due to a mismatch in thermal expansion [11]. Fig. 8.6 shows the effect of temperature on the thermal conductivity (k) and thermal diffusivity (α) of Stellite

6, Nitronic 60, and 316L stainless steel [389,390]. Unfortunately, there currently exist no published data on the thermal conductivity and thermal diffusivity of Tristelle 5183, thus Nitronic 60 and 316L have been plotted in Fig. 8.6 as these alloys have compositions comparable to the matrix composition of Tristelle 5183. However, it is recognised that the secondary hard phase precipitates in Tristelle 5183 will influence the alloys thermal properties relative to Nitronic 60 and 316L. Fig. 8.6 shows that the reported thermal conductivities and thermal diffusivities are similar between Stellite 6, Nitronic 60, and 316L. Therefore, differences in these thermal properties is not believed to be a dominant factor which influences the notable disparity in the tribological performance of Stellite 6 and Tristelle 5183 observed in the present work. It is also recognised that variation in the coefficient of friction resulting in different degrees of frictional heating between the two different alloy systems may still be an important factor which requires further investigation. This is particularly important as the deformation mechanisms of Tristelle 5183 have been shown to be sensitive to temperature.

8.5. DISCUSSION - THE SUITABILITY OF TRISTELLE 5183 IN PWR PRIMARY CIRCUIT OPERATING CONDITIONS (250 °C)

One may argue that under the present sliding conditions at 250 °C, the small 1.4 - 2.5 times increase in wear observed by Tristelle 5183 compared to Stellite 6 significantly outweighs the consequences of Co release into the primary circuit. This is most probably the case, and the deployment of Tristelle 5183 is suitable for components exposed to comparatively low contact pressure sliding conditions analogous to those investigated in the present study. However it is noted that the performance of Tristelle 5183 at 250 °C is critically dependent on a breakdown in passive behaviour and the development of oxide-rich tribofilms. Microstructural characterisation of the TAM (Chapter 7) has shown that Tristelle 5183 is highly susceptible to plastic instabilities and plastic strain localisation due to a deformation response that is unable to maintain a sufficient rate of strain hardening

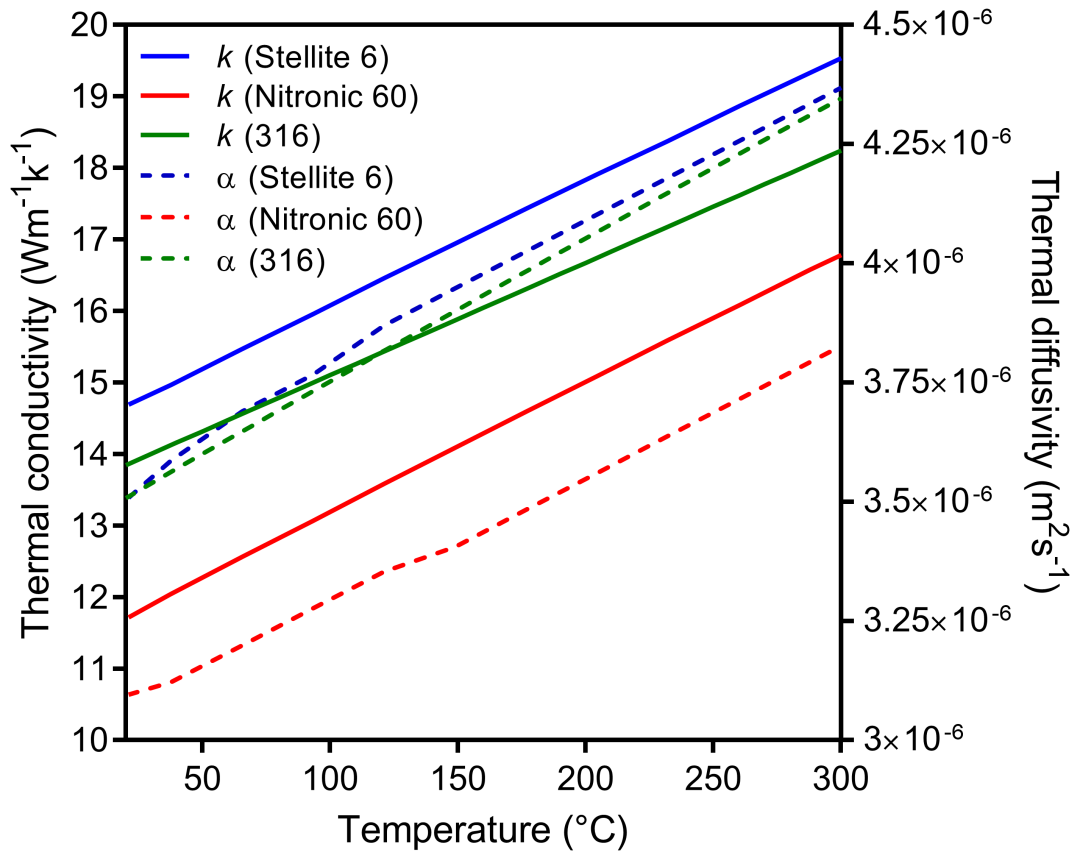


Figure 8.6: The effect of temperature on the thermal conductivity (k) and thermal diffusivity (α) of Stellite 6, Nitronic 60 and 316L stainless steel [389,390].

at high strains. This renders Tristelle 5183 suitable only for low contact pressure applications. It is postulated that with increased contact pressures, the highly localised deformation response exhibited by Tristelle 5183 will lead to catastrophic component failure by galling or severe plasticity dominated (adhesive type) wear at much lower loads compared to Stellite 6. To summarise, based on the deformation characteristics exhibited by Tristelle 5183 in response to the comparatively low contact pressure sliding tests conducted in the present study, it seems unlikely that a conventional austenitic Fe-based hardfacing alloy system will ever be able to rival the tribological superiority of Co-based hardfacings.

8.6. CONCLUSIONS

Based on the present observations, it seems unrealistic to suggest that conventional Fe-based austenitic hardfacings, composed of hard phase particles surrounded by a matrix, may ever be developed that are capable of rivalling/outperforming the deformation, corrosion resistant and wear characteristics of Stellite 6. However, this does not mean the tribological performance of conventional austenitic Fe-based hardfacings cannot be drastically improved, nor does it mean that innovative/novel Fe-based alloys systems may not be developed in the future.

It has been shown that the tribological performance of Tristelle 5183 is significantly hampered by the deformation characteristics of the austenitic matrix phase; more specifically an inability to suppress the onset of plastic strain localisation relative to Stellite 6. An enhanced rate of work hardening at high strains, and thus an ability to store dislocations and prevent softening via dislocation annihilation have been identified as highly desirable deformation characteristics which are essential for excellent tribological performance. In terms of the deformation microstructural evolution of the matrix, this is achieved by hindering dislocation cross slip and encouraging the profuse development of volumetric planar defects irrespective of testing temperature. In accord with the above, alloying to reduce the SFE and increase the dislocation-interstitial solute field interactions of the matrix are two pathways thorough which the deformation response of hardfacings may be enhanced.

From a purely tribological point of view, the breakdown in passive behaviour exhibited by Tristelle 5183 acts to reduce wear under the current sliding contact tests due to the development of oxide-based tribofilms. Whilst the relative assessment of the pros and cons of such corrosive behaviour within PWR systems is beyond the scope of this work, it is clear that hardfacings must exhibit a sufficient degree of corrosion resistance in order to maintain component functionality. It has been demonstrated by this work that the principal factor degrading the tribological performance of Tristelle 5183 is a temperature shift in deformation characteristics. This work has also shown that Stellite 6 remains truly passive between 20 and 250 °C, and an increased rate of oxidation with respect to increasing test temperature

acts to degrade tribological performance in the current sliding contact tests.

This work has provided a detailed explanation of the tribological behavioural differences between Tristelle 5183 and Stellite 6 so that future research can attempt to improve on the characteristics of future Fe-based alloys designed to be used in the primary systems of PWRs. Based on this detailed assessment, alloy design to reduce the SFE and increase the dislocation-interstitial solute field interactions of the matrix are two alloy characteristics which should be targeted in the development of future Fe-based hardfacings.

CONCLUSIONS AND FUTURE RESEARCH

The main aims of this research were to: (i) characterise the Fe-based hardfacing alloy Tristelle 5183 in its inert gas atomised and powder hot isostatically pressed (HIPed) forms; and (ii) develop a mechanistic understanding of the tribological performance of both Tristelle 5183 and Stellite 6 during sliding within a simulated primary cooling system pressurised water reactor (PWR) environment. This was undertaken to establish a framework for the development of improved Fe-based hardfacing alloys in order to further decrease the present use of Co-based StelliteTM hardfacing alloys within the primary cooling system of PWRs.

9.1. CONCLUSIONS

9.1.1. Microstructural characterisation of Tristelle 5183

In nitrogen gas atomised Tristelle 5183, phase selection and microstructural development are significantly influenced by powder size and thus cooling rate. Depending on powder particle size cooling rates are estimated to be in the range 10^2 to 10^4 K/s. Powder particles $\gtrsim 53 \mu\text{m}$ are principally composed of γ -Fe dendrites with smaller quantities of α -Fe, an interdendritic silicide phase and Nb-based MX-type precipitates. Powder particles $\lesssim 53 \mu\text{m}$ also contain Nb-based MX-type precipitates and have increasing quantities of either α -Fe or a cellular silicide phase with decreasing amounts of γ -Fe. The increasing quantities of α -Fe and silicide in the smaller powder particles is consistent with increased undercooling prior to nucleation permitting metastable phase formation. Powder particles contain coarse ($> 10 \mu\text{m}$) crystals which pre-exist in the melt prior to atomisation, whereas faceted micron-sized MX precipitates are the primary solidification phase. Nanoscale Nb-based MX precipitates also form interdendritically in large powder particles or in the cell boundaries of the silicide phase in small powder particles

in the later stages of solidification. Rapid solidification significantly alters the solidification pathway of Tristelle 5183 and the formation of M_7C_3 is completely suppressed compared to a conventional mould cast sample which forms NbC, γ -Fe, M_7C_3 , α -Fe and silicide phase in the as-cast condition.

HIP consolidated (HIPed) Tristelle 5183 is principally composed of a γ -Fe solid solution matrix (\sim Fe-16Cr-13Ni-6Si (wt%)) which surrounds \sim 14 vol % M_7C_3 ($\sim(0.82Cr0.18Fe)_7C_3$) and \sim 9.6 vol% Nb-based MX secondary hard phase precipitates. Smaller fractions of ferrite (\sim 1.0 vol%) and a π -ferrosilicide phase (\sim 0.3 vol%) are also present within the HIPed alloy. Oxide inclusions (\sim 0.1 – 0.3 μ m in size) indicate the prior particle boundaries within the microstructure and these inclusions probably form during HIPing due to the breakdown and coalescence of the nanoscale oxide films which are present on the gas atomised powder. The microstructure has not been completely recrystallised during HIPing therefore, the γ -Fe grain size varies in size; some regions within the microstructure retain a strong morphological and crystallographic relationship with the inert gas atomised powder. Recrystallisation is apparently controlled by the degree of plastic deformation incurred by a powder particle during the initial stages of HIPing and the metastability of a given powder particle following gas atomisation. Both these factors are dependent on powder size therefore the phase and microstructural characteristics of inert gas atomised powder play a critical role in microstructure development during HIPing. M_7C_3 precipitates out during HIPing and the MX precipitates significantly evolve due to equilibration and chemical homogenisation. Precipitation from supersaturated solid solutions increases the volume fraction whilst surface energy driven coarsening increases the average size. Spheroidisation of MX precipitates is also apparent.

9.1.2. Sliding contact tribological behaviour of Tristelle 5183

The tribologically affected material (TAM) generated in response to the self-mated sliding contact of HIPed Tristelle 5183 can be described as a continuum of deformation which results from a sliding induced strain gradient. The mechanisms of strain accommodation furthest from the sliding contact are sensitive to fluctua-

tions in SFE and thus test temperature between 20 and 250 °C. At 20 °C (lower SFE), strain is notably accommodated by mechanisms including: deformation induced martensitic transformation to ϵ -martensite and α' -martensite principally via the $\gamma \rightarrow \epsilon$ and $\gamma \rightarrow \epsilon \rightarrow \alpha'$ transformation pathways, twinning, the generation of planar dislocation arrangements (generated by planar slip), and the generation of dislocation tangles. At 250 °C (higher SFE), the deformation microstructures are characteristic of a higher degree of cross slip activity, dominated by heterogeneous dislocation structures, and absent from deformation induced martensitic transformation and twinning. Within the higher strained region of the TAM at both testing temperatures (closer to the contacting surface), the initial deformation mechanisms become inhibited, the surface becomes unstable, and localised shear phenomena driven by grain boundary mediated deformation mechanisms and crystallographic slip completely engulf the near surface generating a nanocrystalline microstructure. Enormous strains can be accommodated by these deformation mechanisms and this inability to suppress strain localisation phenomena critically influences tribological performance. Microstructural development within this localised microstructure is notably influenced by dynamic recovery and continuous dynamic recrystallisation and the high hydrostatic component of stress generated during loaded sliding contact permits the accommodation of high levels of strain prior to failure.

The tribological degradation of self-mated HIPed Tristelle 5183 in lithiated water is highly variable and sensitive to test temperature between 20 and 250 °C. At 20 °C, degradation is principally governed by plasticity dominated wear. The extrusion of metallic slivers via plastic ratcheting generates ductile shear cracks governed by plastic strain, and the failure of these slivers permits material removal in the form of plate/flake-like wear debris. At 250 °C, degradation is controlled by the synergistic operation of oxidative and plasticity-type wear mechanisms in response to a breakdown in passive behaviour. Oxide accumulations/agglomerates permit the formation of oxide-based tribofilms which reduce both the number of metal to metal contacting asperities and shear strength at the sliding interface. Three notable modes of material removal have been identified during sliding

at 250 °C: (i) the removal of material via plasticity-type wear, (ii) mechanical removal of a corrosion product (wear enhanced corrosion), and (iii) breakdown of oxide-containing tribofilms.

9.1.3. Sliding contact tribological behaviour of Stellite 6

HIPed Stellite 6 contains ~ 13.3 vol% equiaxed M_7C_3 precipitates which are principally surrounded by an (fcc) Co-based solid solution matrix. In response to self-mated sliding contact, the TAM exhibits a subsurface deformation gradient where the highest strains are generated at the contacting surface. Within the lowest strained regions of TAM, furthest from the sliding contact, deformation is principally accommodated by a $\gamma \rightarrow \epsilon$ transformation which eventually consumes all the γ phase. With increasing strain (closer to the sliding surface), plastic deformation is further accommodated by deformation mechanisms including twinning and both basal and prismatic slip of the ϵ -martensite phase. Within the highest strained regions of the TAM closest to the contacting surface, a nanocrystalline ϵ -martensite microstructure is generated where strain and microstructural development are principally driven by dislocation slip. The deformation evolution of the matrix is highly resistant to plastic strain localisation due to an ability to sustain a sufficient strain hardening rate (continued storage of defects at high strains) which prevents the accumulation of large strains in localised regions.

The tribological degradation of self-mated HIPed Stellite 6 in lithiated water at temperatures between 20 and 250 °C is believed to be dominated by the removal of nanoscale particles from the surface due to the synergistic effect of the chemical manipulation of the near surface via passivating behaviour and mechanical stimulation by sliding contact. The unique subsurface deformation characteristics exhibited by Stellite 6 suppress material removal to the nanoscale where chemical oxidative reactions and other environmental factors can greatly influence the nanoscale removal of material during sliding. A synergistic temperature dependent increase in corrosion rate and stacking fault energy are the principal reasons for an increase in wear rate as the temperature is increased from 20 to 250 °C however, the rate of corrosion is believed to be the dominant factor influencing

wear. These factors principally account for a $\sim 16 - 39$ times increase in material removal when the test temperature is increased from 20 to 250 °C because they manipulate: mechanical deformation characteristics, the extent of corrosion enhance wear and/or wear enhanced corrosion, the amount of nanoscale mechanical mixing, the frictional state of the contact, the amount of material detachment and the degree of three-body abrasion.

9.1.4. Comparison of Stellite 6 and Tristelle 5183

The tribological assessment of HIPed Tristelle 5183 and Stellite 6 has shown that the performance of Fe-based hardfacings, specifically Tristelle 5183, is hampered by the deformation characteristics of the austenitic matrix phase - in particular, its inability to suppress the onset of plastic strain localisation relative to Stellite 6. It is believed that an enhanced rate of work hardening at high strains via the ability to store dislocations and resist dislocation annihilation (softening) is a highly desirable deformation characteristic which is essential for excellent sliding contact tribological performance. Regarding deformation microstructural evolution, this may be achieved by hindering dislocation cross slip and encouraging the profuse development of volumetric planar defects irrespective of test temperature. In accord with the above, alloying to reduce the SFE and increase the dislocation-interstitial solute field interactions of the matrix are two pathways which have been identified thorough which the deformation response of a hardfacings matrix may be enhanced.

9.2. FUTURE RESEARCH

The research presented in this thesis reveals the unique chemical and mechanical behaviour of Stellite 6 in lithiated high temperature water and highlights the fact that there is still a significant amount of work required to develop alloys that can replace Stellite hardfacings. Based on the fundamental understanding established in the present work, the performance of conventional Fe-based hardfacings, composed of hard carbide precipitates surrounded by an Fe-based fcc solid solution matrix, can still be significantly improved. The present findings show that the

deformation evolution of the Fe-based austenitic matrix phase, and its inability to suppress plastic strain localisation in response to sliding contact, is the principal factor hindering their performance. In accord with this observation, it is proposed that alloying to reduce the matrix SFE and increase the dislocation-interstitial solute field interactions within the matrix are two pathways through which the performance of conventional-type Fe-based hardfacing alloys may be enhanced. Whilst it is recognised that alloy design to address these two factors often results in a metallurgical trade-off between wear and corrosion resistance, this study reveals that, under the present sliding conditions, a certain degree of oxidation/corrosion favours improved tribological performance in Tristelle 5183. Therefore, depending on the Fe-based hardfacings intended application within the primary system of a PWR, it is possible that the corrosion resistance of next generation hardfacings could be compromised slightly in order to improve overall tribological behaviour. This should be considered as an avenue for future research.

Alloying with nitrogen (> 0.2 wt%) has shown some potential as a means of improving the wear resistance of Fe-based hardfacings without significantly compromising corrosion resistance. Nitrogen additions would significantly reduce the matrix SFE and also increase the dislocation-interstitial solute field interactions within the matrix. One possible processing route which has not yet been explored is the mechanical milling of hardfacing powder within a nitrogen rich atmosphere to permit the extensive uptake of nitrogen prior to HIPing. Mechanical alloying as an intermediary processing step prior to HIPing could also improve the post HIP microstructure of Fe-based hardfacings as it would increase the stored energy within powder particles and promote complete matrix recrystallisation during HIPing. The above is just one example of how both alloy design and processing could be investigated to improve the tribological performance of conventional-type Fe-based hardfacings.

A significant barrier to alloy development work in the field of hardfacings is the lack of understanding of stable and metastable phase equilibria in Fe-Cr based alloys with high Ni, Si and C contents. In several important engineering alloys (e.g. automotive and other engineering steels and superalloys) the development

of thermodynamic databases coupled with the CALPHAD method has been advantageous in searching the alloys design space and formulating improved compositions for specific property trade-offs. Therefore, an opportunity exists to conduct future research leading to the development and application of a validated alloy database.

BIBLIOGRAPHY

- [1] H. Ocken. Reducing the cobalt inventory in light water reactors. *Nuclear technology*, 68(1):18–28, 1985.
- [2] H. Ocken. The galling wear resistance of new iron-base hardfacing alloys: a comparison with established cobalt-and nickel-base alloys. *Surface and Coatings Technology*, 76:456–461, 1995.
- [3] B.G. Mellor. *Surface coatings for protection against wear*. Woodhead Publishing, 2006.
- [4] P. Aubry. Survey on Stellite substitutes for hardfacing in nuclear environments. Technical report, European Commission and Seventh Framework Programme, 2012.
- [5] S. Atamert and J. Stekly. Microstructure, wear resistance, and stability of cobalt based and alternative iron based hardfacing alloys. *Surface engineering*, 9(3):231–240, 1993.
- [6] P. Crook and R.D. Zordan. Nuclear grade steels, 1987. US Patent 4,643,767.
- [7] C. Zhao, D. Stewart, J. Jiang, and F.P.E. Dunne. A comparative assessment of iron and cobalt-based hard-facing alloy deformation using HR-EBSD and HR-DIC. *Acta Materialia*, 159:173–186, 2018.
- [8] News & Views. *Powder Metallurgy*, 36(2):77–97, 1993.
- [9] R.T. Smith, J.A. Siefert, D. Gandy, and S.S. Babu. Tribolayer formation by strain-induced transformations in hardfacing alloys. In D. Gandy and J. Shingledecker, editors, *Advances in Materials Technology for Fossil Power Plants*, pages 482–490, Materials Park, OH, 2014. ASM International.
- [10] J.L. Sulley, I. Hookham, B. Burdett, and K. Bridger. Introduction of hot isostatically pressed, reactor coolant system components in PWR plant. In

-
- International Conference on Nuclear Engineering*, volume 49330, pages 357–367, 2010.
- [11] I. Hutchings and P. Shipway. *Tribology: friction and wear of engineering materials*. Butterworth-Heinemann, 2017.
- [12] H.V. Atkinson and B.A. Rickinson. *Hot isostatic processing*. Springer, 1991.
- [13] E.V. Murphy and I. Inglis. Endurance tests of valves with cobalt-free hard-facing alloys: PWR phase. Technical report, Electric Power Research Inst., 1992.
- [14] P.J. Hofmann and B.C. Friedrich. Laboratory evaluations of iron-based hard-facing alloys: A european study. Technical report, Electric Power Research Inst., 1988.
- [15] Pressurised water reactors, Accessed: 31-08-2020. <https://www.nrc.gov/reactors/pwrs.html>.
- [16] Usnrc technical training center, Accessed: 31-08-2020. <https://www.nrc.gov/reading-rm/basic-ref/students/for-educators/04.pdf>.
- [17] M. Le Calvar and I. De Curières. 15 - corrosion issues in pressurized water reactor (PWR) systems. In *Nuclear Corrosion Science and Engineering*, Woodhead Publishing Series in Energy, pages 473 – 547. Woodhead Publishing, 2012.
- [18] United states geological survey. Mineral commodity summaries 2019. Technical report, United states geological survey.
- [19] T. Nazarewicz. Cobalt: a critical commodity. *Resource World*, pages 52–53, 2016.
- [20] Deloro Stellite. STELLITE ®6 ALLOY, 2008.
- [21] Deloro Stellite. STELLITE ®3 ALLOY, 2008.
- [22] W.J. Schumacher and H. Tanczyn. Galling resistant austenitic stainless steel, 1975. US Patent 3912503.

-
- [23] J.R. Davis. *Alloy Digest Sourcebook: Stainless Steels*. Alloy Digest. ASM International, 2000.
- [24] W.B. Burdett. stainless steel alloy, 1997. US Patent 5660939.
- [25] J.H. Magee. Galling resistant austenitic stainless steel alloy, 1989. US Patent 4814140.
- [26] J.H. Magee. Corrosion resistant austenitic stainless steel with improved galling resistance, 1994. US Patent 5340534.
- [27] E.K. Ohriner, E.P. Whelan, T. Wada, and H. Ocken. Cobalt-free, iron-base hardfacing alloys, 1989. US Patent 4803045.
- [28] J. Kim and S. Kim. The temperature dependence of the wear resistance of iron-base NOREM 02 hardfacing alloy. *Wear*, 237(2):217–222, 2000.
- [29] R.T. Smith, T. Lolla, D. Gandy, L. Wu, G. Faria, A.J. Ramirez, S.S. Babu, and P.M. Anderson. In situ X-ray diffraction analysis of strain-induced transformations in Fe- and Co-base hardfacing alloys. *Scripta Materialia*, 98:60–63, 2015.
- [30] P. Aaltonen and H. Hanninen. Water chemistry and behavior of materials in PWRs and BWRs. Technical report, VTT Manufacturing Technology, 1997.
- [31] PWR primary water chemistry guidelines: Volume 1, revision 4. Technical report, Electric Power Research Inst., 1999.
- [32] C.O.A Olsson and D. Landolt. Passive films on stainless steels - chemistry, structure and growth. *Electrochimica acta*, 48(9):1093–1104, 2003.
- [33] J.E. Castle and C.R. Clayton. The use of in the x-ray photo-electron spectroscopy analyses of passive layers on stainless steel. *Corrosion Science*, 17(1):7–26, 1977.
- [34] G. Okamoto and T. Shibata. Stability of passive stainless steel in relation to the potential of passivation treatment. *Corrosion Science*, 10:371 – 378, 1970.

-
- [35] B. Stellwag. The mechanism of oxide film formation on austenitic stainless steels in high temperature water. *Corrosion science*, 40(2-3):337–370, 1998.
- [36] D.H. Lister, R.D. Davidson, and E. McAlpine. The mechanism and kinetics of corrosion product release from stainless steel in lithiated high temperature water. *Corrosion Science*, 27(2):113–140, 1987.
- [37] Y. Asakura, H. Karasawa, M. Sakagami, and S. Uchida. Relationships between corrosion behavior of AISI 304 stainless steel in high-temperature pure water and its oxide film structures. *Corrosion*, 45(2):119–124, 1989.
- [38] Z. Szklarska-Smialowska, K. Chou, and Z. Xia. The composition and properties of oxide films on type 304 stainless steel on exposure to lithiated water at 100-300 °C. *Corrosion 2013*, 32(5):609–619, 1991.
- [39] J. Robertson. The mechanism of high temperature aqueous corrosion of steel. *Corrosion science*, 29(11-12):1275–1291, 1989.
- [40] H. Sun, X. Wu, and E. Han. Effects of temperature on the oxide film properties of 304 stainless steel in high temperature lithium borate buffer solution. *Corrosion Science*, 51(12):2840–2847, 2009.
- [41] J. Vikstroem. Galling resistance of hardfacing alloys replacing Stellite. *Wear*, 179(1-2):143–146, 1994.
- [42] B.V. Cockeram, R.F. Buck, and W.L. Wilson. Laboratory galling tests of several commercial cobalt-free weld hardfacing alloys. *Surface and Coatings Technology*, 94:495–500, 1997.
- [43] K.L. Johnson and K.L. Johnson. *Contact Mechanics*. Cambridge University Press, 1987.
- [44] Chapter 6 sliding wear. In *Microstructure and Wear of Materials*, volume 10 of *Tribology Series*, pages 351 – 495. Elsevier, 1987.
- [45] D.H. Buckley. *Surface effects in adhesion, friction, wear, and lubrication*. Tribology series. Elsevier Science, 1981.
-

-
- [46] B. Bhushan. *Introduction to tribology*. John Wiley & Sons, 2013.
- [47] R. Chattopadhyay. *Surface Wear: Analysis, Treatment, and Prevention*. ASM International, 2001.
- [48] J.F. Archard and J.F.A. Charj. Contact and Rubbing of Flat Surfaces. *Journal of Applied Physics*, 24:981–988, 1953.
- [49] T. Kayaba and K. Kato. The Adhesive Transfer of the Slip-Tongue and the Wedge. *ASLE Transactions*, 24:164–174, 1981.
- [50] R.J. Bayer. *Mechanical Wear Fundamentals and Testing, Revised and Expanded*. Mechanical Engineering. CRC Press, 2004.
- [51] A.R. Chinha. Metallurgical aspects of steels designed to resist abrasion, and impact-abrasion wear. *Materials Science and Technology*, 35(10):1133–1148, 2019.
- [52] B. Bhushan. *Principles and Applications of Tribology*. A Wiley interscience publication. Wiley, 1999.
- [53] K. Hokkirigawa and K. Kato. An experimental and theoretical investigation of ploughing, cutting and wedge formation during abrasive wear. *Tribology International*, 21(1):51–57, 1988.
- [54] D. Landolt and S. Mischler. *Tribocorrosion of passive metals and coatings*. Elsevier, 2011.
- [55] ASTM Committee G-2 on Erosion and Wear. *Standard Guide for Determining Synergism Between Wear and Corrosion*. ASTM standard. ASTM International, 2016.
- [56] S.W. Watson, F.J. Friedersdorf, B.W. Madsen, and S.D. Cramer. Methods of measuring wear-corrosion synergism. *Wear*, 181:476–484, 1995.
- [57] S. Mischler, A. Spiegel, and D. Landolt. The role of passive oxide films on the degradation of steel in tribocorrosion systems. *Wear*, 225:1078–1087, 1999.

-
- [58] S. Mischler, S. Debaud, and D. Landolt. Wear-accelerated corrosion of passive metals in tribocorrosion systems. *Journal of the Electrochemical Society*, 145(3):750–758, 1998.
- [59] S. Mischler, E.A. Rosset, and D. Landolt. Effect of corrosion on the wear behavior of passivating metals in aqueous solutions. In *Thin Films in Tribology*, volume 25 of *Tribology Series*, pages 245 – 253. Elsevier, 1993.
- [60] D. Landolt, S. Mischler, and M. Stemp. Electrochemical methods in tribocorrosion: a critical appraisal. *Electrochimica acta*, 46(24-25):3913–3929, 2001.
- [61] N. Diomidis, J. Celis, P. Ponthiaux, and F. Wenger. Tribocorrosion of stainless steel in sulfuric acid: Identification of corrosion–wear components and effect of contact area. *Wear*, 269(1-2):93–103, 2010.
- [62] S. Mischler, A. Spiegel, M. Stemp, and D. Landolt. Influence of passivity on the tribocorrosion of carbon steel in aqueous solutions. *Wear*, 251(1-12):1295–1307, 2001.
- [63] M. Godet. The third-body approach: a mechanical view of wear. *Wear*, 100(1-3):437–452, 1984.
- [64] M. Godet, Y. Berthier, J. Lancaster, and L. Vincent. Wear modelling: using fundamental understanding or practical experience? *Wear*, 149(1-2):325–340, 1991.
- [65] D. Landolt, S. Mischler, M. Stemp, and S. Barril. Third body effects and material fluxes in tribocorrosion systems involving a sliding contact. *Wear*, 256(5):517–524, 2004.
- [66] S. Mischler. Triboelectrochemical techniques and interpretation methods in tribocorrosion: a comparative evaluation. *Tribology International*, 41(7):573–583, 2008.
- [67] P. Henry, J. Takadoum, and P. Berçot. Tribocorrosion of 316L stainless steel and TA6V4 alloy in H₂SO₄ media. *Corrosion Science*, 51(6):1308–1314, 2009.
-

-
- [68] A.I. Munoz and L.C. Julián. Influence of electrochemical potential on the tribocorrosion behaviour of high carbon CoCrMo biomedical alloy in simulated body fluids by electrochemical impedance spectroscopy. *Electrochimica Acta*, 55(19):5428–5439, 2010.
- [69] J. Stojadinović, D. Bouvet, M. Declercq, and S. Mischler. Effect of electrode potential on the tribocorrosion of tungsten. *Tribology International*, 42(4):575–583, 2009.
- [70] M. Stemp, S. Mischler, and D. Landolt. The effect of mechanical and electrochemical parameters on the tribocorrosion rate of stainless steel in sulphuric acid. *Wear*, 255(1-6):466–475, 2003.
- [71] Y.N. Kok, R. Akid, and P.E. Hovsepian. Tribocorrosion testing of stainless steel (SS) and PVD coated SS using a modified scanning reference electrode technique. *Wear*, 259(7-12):1472–1481, 2005.
- [72] S. Hassani, K. Raeissi, M. Azzi, D. Li, M.A. Golozar, and J.A. Szpunar. Improving the corrosion and tribocorrosion resistance of Ni–Co nanocrystalline coatings in NaOH solution. *Corrosion science*, 51(10):2371–2379, 2009.
- [73] D.A. Rigney, L.H. Chen, M.G.S. Naylor, and A.R. Rosenfield. Wear processes in sliding systems. *Wear*, 100(1-3):195–219, 1984.
- [74] M. Favero, P. Stadelmann, and S. Mischler. Effect of the applied potential of the near surface microstructure of a 316L steel submitted to tribocorrosion in sulfuric acid. *Journal of Physics D: Applied Physics*, 39(15):3175, 2006.
- [75] J. Perret, E. Boehm-Courjault, M. Cantoni, S. Mischler, A. Beaudouin, W. Chitty, and J.P. Vernot. EBSD, SEM and FIB characterisation of sub-surface deformation during tribocorrosion of stainless steel in sulphuric acid. *Wear*, 269(5-6):383–393, 2010.
- [76] D. Shakhvorostov, B. Gleising, R. Büscher, W. Dudzinski, A. Fischer, and M. Scherge. Microstructure of tribologically induced nanolayers produced at ultra-low wear rates. *Wear*, 263(7-12):1259–1265, 2007.
-

-
- [77] R. Büscher, B. Gleising, W. Dudzinski, and A. Fischer. The effects of subsurface deformation on the sliding wear behaviour of a microtextured high-nitrogen steel surface. *Wear*, 257(3-4):284–291, 2004.
- [78] A. Bidiville, M. Favero, P. Stadelmann, and S. Mischler. Effect of surface chemistry on the mechanical response of metals in sliding tribocorrosion systems. *Wear*, 263(1-6):207–217, 2007.
- [79] Z.Y. Yang, M.G.S. Naylor, and D.A. Rigney. Sliding wear of 304 and 310 stainless steels. *Wear*, 105(1):73–86, 1985.
- [80] R. Büscher and A. Fischer. The pathways of dynamic recrystallization in all-metal hip joints. *Wear*, 259(7-12):887–897, 2005.
- [81] R. Pourzal, R. Theissmann, M. Morlock, and A. Fischer. Micro-structural alterations within different areas of articulating surfaces of a metal-on-metal hip resurfacing system. *Wear*, 267(5-8):689–694, 2009.
- [82] R. Büscher, G. Täger, W. Dudzinski, B. Gleising, M.A. Wimmer, and A. Fischer. Subsurface microstructure of metal-on-metal hip joints and its relationship to wear particle generation. *Journal of Biomedical Materials Research Part B: Applied Biomaterials: An Official Journal of The Society for Biomaterials, The Japanese Society for Biomaterials, and The Australian Society for Biomaterials and the Korean Society for Biomaterials*, 72(1):206–214, 2005.
- [83] N. Espallargas and S. Mischler. Dry wear and tribocorrosion mechanisms of pulsed plasma nitrided Ni–Cr alloy. *Wear*, 270(7-8):464–471, 2011.
- [84] J.R. Davis. *Handbook of thermal spray technology*. ASM international, 2004.
- [85] H.T. Larker and R. Larker. Hot Isostatic Pressing. In *Materials Science and Technology*. Wiley, 2006.
- [86] M.H. Bocanegra-Bernal. Hot isostatic pressing (HIP) technology and its applications to metals and ceramics. *Journal of materials science*, 39(21):6399–6420, 2004.

-
- [87] H.V. Atkinson and S. Davies. Fundamental aspects of hot isostatic pressing: an overview. *Metallurgical and Materials Transactions A*, 31(12):2981–3000, 2000.
- [88] N.L. Loh and K.Y. Sia. An overview of hot isostatic pressing. *Journal of Materials Processing Technology*, 30(1):45–65, 1992.
- [89] M.A. Ashworth, M.H. Jacobs, and S. Davies. Basic mechanisms and interface reactions in HIP diffusion bonding. *Materials & Design*, 21(4):351 – 358, 2000.
- [90] P.K. Samal and J.W. Newkirk. *ASM Handbook, Volume 7: Powder Metallurgy*. ASM Handbook. ASM, 2015.
- [91] B. Burdett. Graded grains make finer parts. *Materials World*, pages 21–23, 2012.
- [92] A.J. Cooper, N.I. Cooper, J. Dhers, and A.H. Sherry. Effect of oxygen content upon the microstructural and mechanical properties of type 316L austenitic stainless steel manufactured by hot isostatic pressing. *Metallurgical and Materials Transactions A*, 47(9):4467–4475, 2016.
- [93] H.S. Kim and D.N. Lee. Power-law creep model for densification of powder compacts. *Materials Science and Engineering: A*, 271(1-2):424–429, 1999.
- [94] W. Li, M.F. Ashby, and K.E. Easterling. On densification and shape change during hot isostatic pressing. *Acta Metallurgica*, 35(12):2831–2842, 1987.
- [95] H.S. Kim. Densification mechanisms during hot isostatic pressing of stainless steel powder compacts. *Journal of materials processing technology*, 123(2):319–322, 2002.
- [96] J.M. Duva and P.D. Crow. The densification of powders by power-law creep during hot isostatic pressing. *Acta Metallurgica et Materialia*, 40(1):31–35, 1992.
- [97] A.J. Yule and J.J. Dunkley. *Atomization of melts for powder production and spray deposition*. Oxford series on advanced manufacturing. Oxford University Press, 1994.
-

-
- [98] S.L. Semiatin. *Elements of induction heating: design, control, and applications*. ASM International, 1988.
- [99] H. Liu. *Science and Engineering of Droplets:: Fundamentals and Applications*. Elsevier Science, 1999.
- [100] J.J. Dunkley and B. Telford. Control of "Satellite" particles in gas atomisation. *Advances in Powder Metallurgy and Particulate Materials*, pages 103–110, 2002.
- [101] S. Özbilen. Satellite formation mechanism in gas atomised powders. *Powder Metallurgy*, 42(1):70–78, 1999.
- [102] A. Ünal. Effect of processing variables on particle size in gas atomization of rapidly solidified aluminium powders. *Materials Science and Technology*, 3(12):1029–1039, 1987.
- [103] R.D. Gray. *Alloys and automobiles : the life of Elwood Haynes*. Guild Press Emmis Publishing, 2002.
- [104] E. Haynes. Metal alloy, 1907. US Patent 873745.
- [105] S. Kapoor. *High-Temperature Hardness and Wear Resistance of Stellite Alloys*. Master of applied science thesis, Carleton University, 2012.
- [106] A. Frenk and W. Kurz. Microstructural effects on the sliding wear resistance of a cobalt-based alloy. *Wear*, 174(1-2):81–91, 1994.
- [107] T. Nishizawa and K. Ishida. The Co (cobalt) system. *Bulletin of Alloy phase diagrams*, 4(4):387–390, 1983.
- [108] Centre d'Information du Cobalt (Bruxelles) and Battelle Memorial Institute. Cobalt monograph. *Brussels, Belgium*, 1960.
- [109] M. Uhl and J. Kübler. Exchange-coupled spin-fluctuation theory: Application to Fe, Co, and Ni. *Physical review letters*, 77(2):334, 1996.
- [110] J.M.D. Coey. *Magnetism and magnetic materials*. Cambridge University Press, 2009.

-
- [111] R. Lizárraga, F. Pan, L. Bergqvist, E. Holmström, Z. Gercsi, and L. Vitos. First principles theory of the hcp-fcc phase transition in cobalt. *Scientific reports*, 7(1):1–8, 2017.
- [112] G.B. Olson and M. Cohen. A general mechanism of martensitic nucleation: Part I. general concepts and the FCC \rightarrow HCP transformation. *Metallurgical Transactions A*, 7(12):1897–1904, 1976.
- [113] R. Bauer, E.A. Jägle, W. Baumann, and E.J. Mittemeijer. Kinetics of the allotropic hcp-fcc phase transformation in cobalt. *Philosophical Magazine*, 91(3):437–457, 2011.
- [114] C.C. Sanderson. *Deformation of polycrystalline cobalt*. PhD thesis, University of British Columbia, 1965.
- [115] K.C. Antony. Wear-resistant cobalt-base alloys. *JOM*, 35(2):52–60, 1983.
- [116] J.R. Davis. *ASM Specialty Handbook: Nickel, cobalt, and their alloys*. ASM international, 2000.
- [117] D. Klarstrom, P. Crook, and J. Wu. *Metallography and Microstructures of Cobalt and Cobalt Alloys*, volume 9. ASM International, 2004.
- [118] D.H. Shin, I. Kim, J. Kim, Y.S. Kim, and S.L. Semiatin. Microstructure development during equal-channel angular pressing of titanium. *Acta Materialia*, 51(4):983–996, 2003.
- [119] J. Van Otterloo and J. De Hosson. Microstructural features and mechanical properties of a cobalt-based laser coating. *Acta Materialia*, 45(3):1225–1236, 1997.
- [120] M.X. Yao, J.B.C. W, and Y. Xie. Wear, corrosion and cracking resistance of some W-or Mo-containing Stellite hardfacing alloys. *Materials Science and Engineering: A*, 407(1-2):234–244, 2005.
- [121] G. Kong, D. Zhang, P.D. Brown, D.G. McCartney, and S.J. Harris. Microstructural characterisation of high velocity oxyfuel thermally sprayed Stellite 6. *Materials science and technology*, 19(8):1003–1011, 2003.
-

-
- [122] P. Sassatelli, G. Bolelli, M.L. Gualtieri, E. Heinonen, M. Honkanen, L. Lusvarghi, T. Manfredini, R. Rigon, and M. Vippola. Properties of HVOF-sprayed Stellite-6 coatings. *Surface and Coatings Technology*, 338:45–62, 2018.
- [123] H. Yu, R. Ahmed, H. Lovelock, and S. Davies. Influence of manufacturing process and alloying element content on the tribomechanical properties of cobalt-based alloys. *Journal of tribology*, 131(1), 2009.
- [124] S. Atamert and H.K.D.H. Bhadeshia. Comparison of the microstructures and abrasive wear properties of stellite hardfacing alloys deposited by arc welding and laser cladding. *Metallurgical Transactions A*, 20(6):1037–1054, 1989.
- [125] S. Atamert. *Stability, wear resistance, and microstructure of iron, cobalt and nickel-based hardfacing alloys*. PhD thesis, University of Cambridge, 1989.
- [126] J.P. Morniroli, E. Bauer-Grosse, and M. Gantois. Crystalline defects in M_7C_3 carbides. *Philosophical Magazine A*, 48(3):311–327, 1983.
- [127] M.A. Ashworth, B.J., M.H. Jacobs, and S. Davies. Microstructure and property relationships in HIPped Stellite powders. *Powder metallurgy*, 42(3):243–249, 1999.
- [128] P. Crook. Cobalt and Cobalt Alloys. In *ASM Handbook Vol. 2: Properties and selection: Nonferrous alloys and special-purpose materials*, pages 446–454. ASM International, 1990.
- [129] R. Ahmed, A. Ashraf, M. Elameen, N. H. Faisal, A.M. El-Sherik, Y.O. Elakwah, and M.F.A. Goosen. Single asperity nanoscratch behaviour of HIPed and cast Stellite 6 alloys. *Wear*, 312(1-2):70–82, 2014.
- [130] L. Remy and A. Pineau. Twinning and strain-induced fcc \rightarrow hcp transformation on the mechanical properties of Co-Ni-Cr-Mo alloys. *Materials Science and Engineering*, 26(1):123–132, 1976.
- [131] R.T. Smith. *Development of a Nitrogen-Modified Stainless-Steel Hardfacing Alloy*. Doctoral thesis, Ohio State University, 2015.
-

-
- [132] E.H. Köster, A.R. Thölen, and A. Howie. Stacking fault energies of Ni–Co–Cr alloys. *Philosophical Magazine*, 10(108):1093–1095, 1964.
- [133] N.K. Taylor and I. Armson. Corrosion product release from stellites and stainless steel in high pressure, high temperature lithiated water. In *Water chemistry of nuclear reactor systems 3: Proceedings of an international conference*, pages 141–151, London, 1983. British Nuclear Society.
- [134] W.H. Hocking, F.W. Stanchell, E. McAlpine, and D.H. Lister. Mechanisms of corrosion of Stellite-6 in lithiated high temperature water. *Corrosion science*, 25(7):531–557, 1985.
- [135] C. Maffiotte, M. Navas, M.L. Castano, and A.M. Lancha. XPS characterization of oxide films formed in cobalt-based alloys during corrosion tests at high temperature. *Surface and Interface Analysis*, 30(1):161–166, 2000.
- [136] N.S. McIntyre, D. Zetaruk, and E.V. Murphy. X-Ray photoelectron spectroscopic study of the aqueous oxidation of stellite-6 alloy. *Surface and Interface Analysis*, 1(4):105–110, 1979.
- [137] W.H. Hocking and D.H. Lister. Corrosion of stellite-6 in lithiated and borated high-temperature water. *Surface and interface analysis*, 11(1-2):45–59, 1988.
- [138] G.N. Karimi, P.H. Shipway, D.A. Stewart, and T. Hussain. Corrosion of cast Stellite-3 analogue in simulated PWR conditions. *Corrosion Science*, 140:402–411, 2018.
- [139] D. Kaczorowski and J.P. Vernot. Wear problems in nuclear industry. *Tribology international*, 39(10):1286–1293, 2006.
- [140] V. Iordache, F. Wenger, P Ponthiaux, A Ambard, J Peybernès, and J Vallory. Comparison between tribocorrosion mechanisms of Stellite 6 and Zircaloy 4 in LiOH-H₃BO₃ solutions. In *Passivation of Metals and Semiconductors, and Properties of Thin Oxide Layers*, pages 495 – 500. Elsevier Science, 2006.
- [141] E. Lemaire and M. Le Calvar. Evidence of tribocorrosion wear in pressurized water reactors. *Wear*, 249(5-6):338–344, 2001.
-

-
- [142] S. Xu, I.L. Kondratova, N. Arbeau, W. Cook, and D.H. Lister. Corrosion of UNS R30006 in high-temperature water under intermittent mechanical contact. *Corrosion*, 61(5):444–451, 2005.
- [143] V.L. Ratia, D. Zhang, M.J. Carrington, J.L. Daure, D.G. McCartney, P.H. Shipway, and D.A. Stewart. The effect of temperature on sliding wear of self-mated HIPed Stellite 6 in a simulated PWR water environment. *Wear*, 420:215–225, 2019.
- [144] V.L. Ratia, D. Zhang, M.J. Carrington, J.L. Daure, P.H. McCartney, D.G. and Shipway, and D.A. Stewart. Comparison of the sliding wear behaviour of self-mated HIPed Stellite 3 and Stellite 6 in a simulated PWR water environment. *Wear*, 426:1222–1232, 2019.
- [145] D.H.E. Persson. *On the Mechanisms behind the Tribological Performance of Stellites*. Doctoral thesis, Uppsala University, 2005.
- [146] P. Crook and C.C. Li. The elevated temperature metal-to-metal wear behavior of selected hardfacing alloys. In *Wear of Materials*, pages 272–279. American Society of Mechanical Engineers, 1983.
- [147] F.H. Stott, C.W. Stevenson, and G.C. Wood. Friction and wear properties of Stellite 31 at temperatures from 293 to 1073 K. *Metals Technology*, 4(1):66–74, 1977.
- [148] L. da Conceição and A.S.C.M. D’Oliveira. The effect of oxidation on the tribolayer and sliding wear of a co-based coating. *Surface and Coatings Technology*, 288:69–78, 2016.
- [149] Y. Birol. High temperature sliding wear behaviour of Inconel 617 and Stellite 6 alloys. *Wear*, 269(9-10):664–671, 2010.
- [150] S. Guadalupe Maldonado, S. Mischler, M. Cantoni, W.J. Chitty, C. Falcand, and D. Hertz. Mechanical and chemical mechanisms in the tribocorrosion of a Stellite type alloy. *Wear*, 308(1-2):213–221, 2013.

-
- [151] K.J. Bhansali and A.E. Miller. The role of stacking fault energy on galling and wear behavior. *Wear*, 75(2):241–252, 1982.
- [152] D.H.E. Persson, S. Jacobson, and S. Hogmark. Antigalling and low friction properties of a laser processed Co-based material. *Journal of laser applications*, 15(2):115–119, 2003.
- [153] D.H.E. Persson, E. Coronel, S. Jacobson, and S. Hogmark. Surface analysis of laser clad Stellite exposed to self-mated high load dry sliding. *Wear*, 261(1):96–100, 2006.
- [154] W.J. Huppmann and M.A. Clegg. The tribological behavior of polycrystalline cobalt as related to crystallographic texture and structure. *ASLE TRANSACTIONS*, 16(2):107–114, 1973.
- [155] M. Barquins and R. Courtel. Plastic deformation by friction of some hexagonal single crystals: Be, Co, Zn, Cd. *ASLE Transactions*, 14(2):81–89, 1971.
- [156] D.R. Wheeler and D.H. Buckley. Texturing in metals as a result of sliding. *Wear*, 33(1):65–74, 1975.
- [157] D.H. Buckley and R.L. Johnson. The influence of crystal structure and some properties of hexagonal metals on friction and adhesion. *Wear*, 11(6):405–419, 1968.
- [158] A.H. Cottrell and B.A. Bilby. Dislocation theory of yielding and strain ageing of iron. *Proceedings of the Physical Society. Section A*, 62(1):49, 1949.
- [159] H. Bhadeshia and R. Honeycombe. *Steels: microstructure and properties*. Butterworth-Heinemann, 2017.
- [160] P. Haasen, P. Haasen, J. Mordike, and B.L. Mordike. *Physical Metallurgy*. Physical Metallurgy. Cambridge University Press, 1996.
- [161] V.G. Gavriljuk and H. Berns. *High nitrogen steels: structure, properties, manufacture, applications*. Springer Science & Business Media, 2013.

-
- [162] K. Oda, N. Kondo, and K. Shibata. X-ray absorption fine structure analysis of interstitial (C, N)-substitutional (Cr) complexes in austenitic stainless steels. *ISIJ International*, 30(8):625–631, 1990.
- [163] D. Bowden, Y. Krysiak, L. Palatinus, D. Tsivoulas, S. Plana-Ruiz, E. Sarakinnou, U. Kolb, D. Stewart, and M. Preuss. A high-strength silicide phase in a stainless steel alloy designed for wear-resistant applications. *Nature communications*, 9(1):1–10, 2018.
- [164] L. Priester. *Grain Boundaries and Crystalline Plasticity*. ISTE. Wiley, 2013.
- [165] D.A. Smith. Interaction of dislocations with grain boundaries. *Le Journal de Physique Colloques*, 43:225–237, 1982.
- [166] E.O. Hall. The deformation and ageing of mild steel: III discussion of results. *Proceedings of the Physical Society. Section B*, 64(9):747, 1951.
- [167] N.J. Petch. The cleavage strength of polycrystals. *Journal of the Iron and Steel Institute*, 174:25–28, 1953.
- [168] R.W. Armstrong, I. Codd, R.M. Douthwaite, and N.J. Petch. The plastic deformation of polycrystalline aggregates. *The Philosophical Magazine: A Journal of Theoretical Experimental and Applied Physics*, 7(73):45–58, 1962.
- [169] V. Bata and E.V. Pereloma. An alternative physical explanation of the Hall–Petch relation. *Acta materialia*, 52(3):657–665, 2004.
- [170] N. Hansen. Polycrystalline strengthening. *Metallurgical Transactions A*, 16(12):2167–2190, 1985.
- [171] Y. Li, A.J. Bushby, and D.J. Dunstan. The Hall–Petch effect as a manifestation of the general size effect. *Proceedings of the Royal Society A: Mathematical, Physical and Engineering Sciences*, 472(2190):20150890, 2016.
- [172] H.S. Kim, Y Estrin, and M.B. Bush. Plastic deformation behaviour of fine-grained materials. *Acta Materialia*, 48(2):493–504, 2000.

-
- [173] Z. Shen, R.H. Wagoner, and W.A.T. Clark. Dislocation pile-up and grain boundary interactions in 304 stainless steel. *Scripta metallurgica*, 20(6):921–926, 1986.
- [174] B.P. Kashyap and K. Tangri. On the Hall-Petch relationship and substructural evolution in type 316L stainless steel. *Acta metallurgica et materialia*, 43(11):3971–3981, 1995.
- [175] L. Remy and A. Pineau. Twinning and strain-induced F.C.C. \rightarrow H.C.P. transformation in the Fe-Mn-Cr-C system. *Materials Science and engineering*, 28(1):99–107, 1977.
- [176] D.T. Pierce, J.A. Jiménez, J. Bentley, D. Raabe, and J.E. Wittig. The influence of stacking fault energy on the microstructural and strain-hardening evolution of Fe–Mn–Al–Si steels during tensile deformation. *Acta Materialia*, 100:178–190, 2015.
- [177] S. Curtze and V.T. Kuokkala. Dependence of tensile deformation behavior of TWIP steels on stacking fault energy, temperature and strain rate. *Acta materialia*, 58(15):5129–5141, 2010.
- [178] D.T. Pierce, J.A. Jiménez, J. Bentley, D. Raabe, C. Oskay, and J.E. Wittig. The influence of manganese content on the stacking fault and austenite/ ϵ -martensite interfacial energies in Fe–Mn–(Al–Si) steels investigated by experiment and theory. *Acta Materialia*, 68:238–253, 2014.
- [179] D. Kaoumi and J. Liu. Deformation induced martensitic transformation in 304 austenitic stainless steel: In-situ vs. ex-situ transmission electron microscopy characterization. *Materials Science and Engineering: A*, 715:73–82, 2018.
- [180] J.F. Breedis and L. Kaufman. The formation of hcp and bcc phases in austenitic iron alloys. *Metallurgical Transactions*, 2(9):2359–2371, 1971.
- [181] P.L. Mangonon and G. Thomas. The martensite phases in 304 stainless steel. *Metallurgical transactions*, 1(6):1577–1586, 1970.
-

-
- [182] J. Talonen and H. Hänninen. Formation of shear bands and strain-induced martensite during plastic deformation of metastable austenitic stainless steels. *Acta materialia*, 55(18):6108–6118, 2007.
- [183] G.B. Olson and M. Cohen. A general mechanism of martensitic nucleation: Part II. FCC \rightarrow BCC and other martensitic transformations. *Metallurgical transactions A*, 7(12):1905–1914, 1976.
- [184] G.B. Olson and M. Cohen. A general mechanism of martensitic nucleation: Part III. kinetics of martensitic nucleation. *Metallurgical Transactions A*, 7(12):1915–1923, 1976.
- [185] K. Sato, M. Ichinose, Y. Hirotsu, and Y. Inoue. Effects of deformation induced phase transformation and twinning on the mechanical properties of austenitic Fe–Mn–Al alloys. *ISIJ international*, 29(10):868–877, 1989.
- [186] Y.F. Shen, X.X. Li, X. Sun, Y.D. Wang, and L. Zuo. Twinning and martensite in a 304 austenitic stainless steel. *Materials Science and Engineering: A*, 552:514–522, 2012.
- [187] P.M. Anderson, J.P. Hirth, and J. Lothe. *Theory of dislocations*. Cambridge University Press, 2017.
- [188] Z. Nishiyama. *Martensitic transformation*. Elsevier, 2012.
- [189] J.A. Venables. The martensite transformation in stainless steel. *The Philosophical Magazine: A Journal of Theoretical Experimental and Applied Physics*, 7(73):35–44, 1962.
- [190] H. Fujita and S. Ueda. Stacking faults and fcc (γ) \rightarrow hcp (ϵ) transformation in 188-type stainless steel. *Acta Metallurgica*, 20(5):759–767, 1972.
- [191] B. Jiang, T. Tadaki, H. Mori, and T.Y. Hsu. In-situ TEM observation of $\gamma \rightarrow \epsilon$ martensitic transformation during tensile straining in an Fe–Mn–Si shape memory alloy. *Materials transactions, JIM*, 38(12):1072–1077, 1997.
- [192] Y. Tanaka. The $\gamma \rightarrow \epsilon \rightarrow \alpha'$ martensitic transformations in an Fe–Mn–C alloy. *Transactions of the Japan Institute of Metals*, 19(12):685–693, 1978.
-

-
- [193] H. Fujita and T. Katayama. In-situ observation of strain-induced $\gamma \rightarrow \epsilon \rightarrow \alpha'$ and $\gamma \rightarrow \alpha'$ martensitic transformations in Fe–Cr–Ni alloys. *Materials Transactions, JIM*, 33(3):243–252, 1992.
- [194] Z. Nishiyama. X-ray investigation of the mechanism of the transformation from face centered cubic lattice to body centered cubic. *Sci. Rep. Tohoku Univ.*, 23:637, 1934.
- [195] L. Bracke, L. Kestens, and J. Penning. Transformation mechanism of α' -martensite in an austenitic Fe-Mn-C-N alloy. *Scripta Materialia*, 57(5):385–388, 2007.
- [196] G.B. Olson and M. Cohen. A mechanism for the strain-induced nucleation of martensitic transformations. *Journal of the Less Common Metals*, 28(1):107–118, 1972.
- [197] J.W. Brooks, M.H. Loretto, and R.E. Smallman. In situ observations of the formation of martensite in stainless steel. *Acta Metallurgica*, 27(12):1829–1838, 1979.
- [198] T. Suzuki, H. Kojima, K. Suzuki, T. Hashimoto, and M. Ichihara. An experimental study of the martensite nucleation and growth in 18/8 stainless steel. *Acta Metallurgica*, 25(10):1151–1162, 1977.
- [199] L.E. Murr, K.P. Staudhammer, and S.S. Hecker. Effects of strain state and strain rate on deformation-induced transformation in 304 stainless steel: Part II. microstructural study. *Metallurgical Transactions A*, 13(4):627–635, 1982.
- [200] C.X. Huang, G. Yang, Y.L. Gao, S.D. Wu, and S.X. Li. Investigation on the nucleation mechanism of deformation-induced martensite in an austenitic stainless steel under severe plastic deformation. *Journal of materials research*, 22(3):724–729, 2007.

-
- [201] J. Choi and W. Jin. Strain induced martensite formation and its effect on strain hardening behavior in the cold drawn 304 austenitic stainless steels. *Scripta Materialia*, 36(1):99–104, 1997.
- [202] R. Smith, M. Doran, D. Gandy, S. Babu, L. Wu, A.J. Ramirez, and P.M. Anderson. Development of a gall-resistant stainless-steel hardfacing alloy. *Materials & Design*, 143:38–48, 2018.
- [203] R.T. Smith, T. Lolla, S.S. Babu, D.W. Gandy, J.A. Siefert, G.J. Fredrick, L. Lherbier, and D. Novatak. Cobalt-free, galling and wear resistant austenitic stainless steel hard-facing alloy, 2015. US Patent 2015/0368766 A1.
- [204] W.J. Schumacher. Metals for non-lubricated wear. *machine design*, 11:60–64, 1976.
- [205] E. Ohriner, T. Wada, E.P. Whelan, and H. Ocken. The chemistry and structure of wear-resistant, iron-base hardfacing alloys. *Metallurgical Transactions A*, 22(5):983–991, 1991.
- [206] R.L. Plaut, C. Herrera, D.M. Escriba, P.R. Rios, and A.F. Padilha. A short review on wrought austenitic stainless steels at high temperatures: processing, microstructure, properties and performance. *Materials Research*, 10(4):453–460, 2007.
- [207] A. Gigovic-Gekic, M. Oruc, and S. Muhamedagic. Effect of the delta-ferrite content on the tensile properties in Nitronic 60 steel at room temperature and 750 °c. *Materiali In Tehnologije*, 46(5):519–523, 2012.
- [208] A.F. Padilha and P.R. Rios. Decomposition of Austenite in Austenitic Stainless Steels. *ISIJ International*, 42(4):325–337, 2002.
- [209] C.V. Robino, J.R. Michael, and M.C. Maguire. The solidification and welding metallurgy of galling-resistant stainless steels. *Welding Journal New-York*, 77:446–457, 1998.

-
- [210] L. Iorio, M. Cortie, and R. Jones. Solubility of nitrogen in experimental low-nickel austenitic stainless steels. *Journal of the Southern African Institute of Mining and Metallurgy*, 94(7):173–177, 1994.
- [211] P. Grobner, E.K. Ohriner, T. Wada, and E.P. Whelan. NOREM wear-resistant, iron-based hard-facing alloys. Technical report, Electric Power Research Inst., Palo Alto, 1989.
- [212] R.E. Schramm and R.P. Reed. Stacking fault energies of seven commercial austenitic stainless steels. *Metallurgical Transactions A*, 6(7):1345, 1975.
- [213] W.J. Schumacher. Wear and galling of nitrogen-strengthened stainless steels. *Machine Design*, 55:87–88, 1983.
- [214] J.H. Dumbleton and J.A. Douthett. The unlubricated adhesive wear resistance of metastable austenitic stainless steels containing silicon. *Wear*, 42(2):305–332, 1977.
- [215] G. Beaurin, J. Mathieu, E. Gauthier, D. Nelias, M. Coret, and F. Arnoldi. Microstructural and mechanical properties evolutions of plasma transferred arc deposited Norem02 hardfacing alloy at high temperature. *Materials Science and Engineering: A*, 528(15):5096–5105, 2011.
- [216] B.V. Cockeram. Some observations of the influence of δ -ferrite content on the hardness, galling resistance, and fracture toughness of selected commercially available iron-based hardfacing alloys. *Metallurgical and Materials Transactions A*, 33(11):3403–3419, 2002.
- [217] M.J. Dickson. The significance of texture parameters in phase analysis by X-ray diffraction. *Journal of applied Crystallography*, 2(4):176–180, 1969.
- [218] K. Lee, G.G. Kim, J.H. Kim, S. Lee, and S. Kim. Sliding wear behavior of hardfacing alloys in a pressurized water environment. *Wear*, 262(7-8):845–849, 2007.

-
- [219] D.H.E. Persson, S. Jacobson, and S. Hogmark. Effect of temperature on friction and galling of laser processed Norem 02 and Stellite 21. *Wear*, 255(1-6):498–503, 2003.
- [220] S. Hogmark, S. Jacobson, and O. Wanstrand. A new universal test for tribological evaluation. In *Proceedings of the 21st IRG-OECD Meeting, Amsterdam*, 1999.
- [221] S.R. Kalidindi, A.A. Salem, and R.D. Doherty. Role of deformation twinning on strain hardening in cubic and hexagonal polycrystalline metals. *Advanced Engineering Materials*, 5(4):229–232, 2003.
- [222] D.J. Bowden. *Assessment of cobalt-free hardfacing stainless steel alloys for nuclear applications*. PhD thesis, Department of Materials, The University of Manchester, 2017.
- [223] D. Bowden, D. Stewart, and M. Preuss. Understanding the microstructural evolution of silicide-strengthened hardfacing steels. *Materials & Design*, 161:1–13, 2019.
- [224] J. Sulley and D. Stewart. HIPed hard facings for nuclear applications: Materials, key potential defects and mitigating quality control measures. In *2016 24th International Conference on Nuclear Engineering*. American Society of Mechanical Engineers, 2016.
- [225] K. Hsu, T.M. Ahn, and D.A. Rigney. Friction, wear and microstructure of unlubricated austenitic stainless steels. *Wear*, 60(1):13–37, 1980.
- [226] D. Hennessy, G. Steckel, and C. Altstetter. Phase transformation of stainless steel during fatigue. *Metallurgical Transactions A*, 7(3):415–424, 1976.
- [227] J.P. Bressanelli and A. Moskowitz. Effects of strain rate, temperature, and composition on tensile properties of metastable austenitic stainless steels. *ASM Trans Quart*, 59(2):223–239, 1966.

-
- [228] C.G. Rhodes and A.W. Thompson. The composition dependence of stacking fault energy in austenitic stainless steels. *Metallurgical Transactions A*, 8(12):1901–1906, 1977.
- [229] K.H. Lo, C.H. Shek, and J.K.L. Lai. Recent developments in stainless steels. *Materials Science and Engineering: R: Reports*, 65(4-6):39–104, 2009.
- [230] P. Pérez, J.L. González-Carrasco, and P. Adeva. Influence of the powder particle size on tensile properties of Ni₃Al processed by rapid solidification and hot isostatic pressing. *Materials Science and Engineering: A*, 199(2):211–218, 1995.
- [231] K. Li, C. Song, Q. Zhai, M. Stoica, and J. Eckert. Microstructure evolution of gas-atomized Fe–6.5 wt% Si droplets. *Journal of Materials Research*, 29(4):527–534, 2014.
- [232] B. Zheng, Y. Lin, Y. Zhou, and E.J. Lavernia. Gas atomization of amorphous aluminum powder: Part II. experimental investigation. *Metallurgical and Materials Transactions B*, 40(6):995, 2009.
- [233] A.M. Mullis, L. Farrell, R.F. Cochrane, and N.J. Adkins. Estimation of cooling rates during close-coupled gas atomization using secondary dendrite arm spacing measurement. *Metallurgical and materials Transactions B*, 44(4):992–999, 2013.
- [234] B.D Cullity. *Elements of X-ray Diffraction*. Addison-Wesley Publishing, 1956.
- [235] B. Fultz and J.M. Howe. *Transmission electron microscopy and diffractometry of materials*. Springer Science & Business Media, 2012.
- [236] W. Clegg. *X-ray Crystallography*. Oxford chemistry primers. Oxford University Press, 2015.
- [237] R.A. Young. *The rietveld method*, volume 6. Oxford university press Oxford, 1993.

-
- [238] P. Thompson, D.E. Cox, and J.B. Hastings. Rietveld refinement of Debye–Scherrer synchrotron X-ray data from Al_2O_3 . *Journal of Applied Crystallography*, 20(2):79–83, 1987.
- [239] R.W. Cheary and A. Coelho. A fundamental parameters approach to X-ray line-profile fitting. *Journal of Applied Crystallography*, 25(2):109–121, 1992.
- [240] R.W. Cheary, A.A. Coelho, and J.P. Cline. Fundamental parameters line profile fitting in laboratory diffractometers. *Journal of Research of the National Institute of Standards and Technology*, 109(1):1, 2004.
- [241] A.J. Schwartz, M. Kumar, B.L. Adams, and D.P. Field. *Electron backscatter diffraction in materials science*, volume 2. Springer, 2009.
- [242] D.B. Williams and C.B. Carter. *Transmission Electron Microscopy: A Textbook for Materials Science*. Springer, second edition edition, 2009.
- [243] E.K.H. Li and P.D. Funkenbusch. Hot isostatic pressing (HIP) of powder mixtures and composites: Packing, densification, and microstructural effects. *Metallurgical and Materials Transactions A*, 24(6):1345–1354, 1993.
- [244] N. Krendelsberger, F. Weitzer, Y. Du, and J.C. Schuster. Constitution of the ternary system Cr–Ni–Ti. *Journal of alloys and compounds*, 575:48–53, 2013.
- [245] S. Ackerbauer, N. Krendelsberger, F. Weitzer, K. Hiebl, and J.C. Schuster. The constitution of the ternary system Fe–Ni–Si. *Intermetallics*, 17(6):414–420, 2009.
- [246] E.I. Gladyshevskii, P.I. Kripyakevich, and Y.B. Kuz’ma. The crystal structure of low-silicon ternary compounds in the Cr–Ni–Si and Cr–Co–Si systems. *Journal of Structural Chemistry*, 3(4):402–410, 1962.
- [247] J.A. Dantzig and M Rappaz. *Solidification*. EPFL press, 2016.
- [248] J. Andersson, T. Helander, L. Höglund, P. Shi, and B. Sundman. Thermo-Calc & DICTRA, computational tools for materials science. *Calphad*, 26(2):273–312, 2002.

-
- [249] E.K. Storms and N.H. Krikorian. The variation of lattice parameter with carbon content of niobium carbide. *The Journal of Physical Chemistry*, 63(10):1747–1749, 1959.
- [250] D. Herlach, D. Holland-Moritz, and P. Galenko. *Metastable Solids from Undercooled Melts*. Elsevier, 2006.
- [251] G. Shao and P. Tsakirooulos. Prediction of phase selection in rapid solidification using time dependent nucleation theory. *Acta metallurgica et materialia*, 42(9):2937–2942, 1994.
- [252] J.H. Perepezko. Nucleation-controlled reactions and metastable structures. *Progress in Materials Science*, 49(3-4):263–284, 2004.
- [253] A. Zambon, B. Badan, A.F. Norman, A.L. Greer, and E. Ramous. Development of solidification microstructures in atomized Fe-Ni alloy droplets. *Materials Science and Engineering: A*, 226:119–123, 1997.
- [254] T.F. Kelly, M. Cohen, and J.B. Vander Sande. Rapid solidification of a droplet-processed stainless steel. *Metallurgical Transactions A*, 15(5):819–833, 1984.
- [255] N. Zeoli, H. Tabbara, and S. Gu. CFD modeling of primary breakup during metal powder atomization. *Chemical engineering science*, 66(24):6498–6504, 2011.
- [256] J.S. Thompson, O. Hassan, S.A. Rolland, and J. Sienz. The identification of an accurate simulation approach to predict the effect of operational parameters on the particle size distribution (PSD) of powders produced by an industrial close-coupled gas atomiser. *Powder Technology*, 291:75–85, 2016.
- [257] T.W. Clyne, R.A. Ricks, and P.J. Goodhew. The production of rapidly solidified aluminium powder by ultrasonic gas atomisation part1: Heat and fluid flow. *International Journal of Rapid Solidification*, 1(1):59–80, 1984.
- [258] W.E. Ranz and W.R. Marshall. Evaporation from drops. *Chem. eng. prog*, 48(3):141–146, 1952.

-
- [259] I.C. Stone and P. Tsakiroopoulos. Cooling rates in gas atomised Al-4wt% Cu alloys powders. *International journal of rapid solidification*, 7(3):177–190, 1992.
- [260] M.J. Carrington, J. Daure, V.L. Ratia, P.H. Shipway, D.G. McCartney, and D.A. Stewart. Microstructural characterisation of Tristelle 5183 (Fe-21%Cr-10%Ni-7.5%Nb-5%Si-2%C in wt%) alloy powder produced by gas atomisation. *Materials & Design*, 164:107548, 2019.
- [261] M. Kowalski. Polytropic structures of $(\text{Cr,Fe})_7\text{C}_3$ carbides. *Journal of applied crystallography*, 18(6):430–435, 1985.
- [262] S. Irukuvarghula, H. Hassanin, C. Cayron, M.M. Attallah, D. Stewart, and M. Preuss. Evolution of grain boundary network topology in 316L austenitic stainless steel during powder hot isostatic pressing. *Acta Materialia*, 133:269–281, 2017.
- [263] S.V. Nair and J.K. Tien. Densification mechanism maps for hot isostatic pressing (HIP) of unequal sized particles. *Metallurgical Transactions A*, 18(1):97–107, 1987.
- [264] W.A. Kaysser, M. Asian, E. Arzt, M. Mitkov, and G. Petzow. Microstructural development and densification during hiping of ceramics and metals. *Powder metallurgy*, 31(1):63–69, 1988.
- [265] H.R. Piehler and D.P. Delo. Physical modeling of powder consolidation processes. *Progress in materials science*, 42(1-4):263–276, 1997.
- [266] R.W. CAHN. Chapter 28 - recovery and recrystallization. In *Physical Metallurgy*, pages 2399 – 2500. Elsevier, Oxford, fourth edition edition, 1996.
- [267] F.J. Humphreys and M. Hatherly. *Recrystallization and related annealing phenomena*. Elsevier, 2012.
- [268] P. Bracconi and G. Gasc. Surface characterization and reactivity of a nitrogen atomized 304L stainless steel powder. *Metallurgical and Materials Transactions A*, 25(3):509–520, 1994.
-

-
- [269] Y. Hedberg, M. Norell, J. Hedberg, P. Szakálos, P. Linhardt, and I. Odnevall Wallinder. Surface characterisation of fine inert gas and water atomised stainless steel 316L powders: formation of thermodynamically unstable surface oxide phases. *Powder metallurgy*, 56(2):158–163, 2013.
- [270] S. Irukuvarghula, H. Hassanin, C. Cayron, M. Aristizabal, M.M. Attallah, and M. Preuss. Effect of powder characteristics and oxygen content on modifications to the microstructural topology during hot isostatic pressing of an austenitic steel. *Acta Materialia*, 172:6–17, 2019.
- [271] V.N. Antsiferov and R.R. Yablonovskaya. Growth of dispersed oxide inclusions in 80% Ni-20% Cr alloys during annealing. *Soviet Powder Metallurgy and Metal Ceramics*, 10(6):482–484, 1971.
- [272] A.V. Serebryakov, T.M. Redkova, and V.I. Lobanov. On recrystallization of dispersion-hardened alloys. *Physica status solidi (a)*, 14(1):77–81, 1972.
- [273] W.J. Chitty, J.P. Vernet, and N.P. Areva. Tribocorrosion issues in nuclear power generation. In *Tribocorrosion of Passive Metals and Coatings*, pages 424–440. Elsevier, 2011.
- [274] S. Guadalupe, S. Cao, M. Cantoni, W.J. Chitty, C. Falcand, and S. Mischler. Applicability of a recently proposed tribocorrosion model to CoCr alloys with different carbides content. *Wear*, 376-377:203–211, 2017.
- [275] A.I Muñoz and N. Espallargas. Tribocorrosion mechanisms in sliding contacts. In *Tribocorrosion of passive metals and coatings*, pages 118–152. Elsevier, 2011.
- [276] N.S. McIntyre, D. Zetaruk, and E.V. Murphy. X-Ray photoelectron spectroscopic study of the aqueous oxidation of stellite-6 alloy. *Surface and Interface Analysis*, 1(4):105–110, 1979.
- [277] J.A. Greenwood and J.B.P. Williamson. Contact of nominally flat surfaces. *Proceedings of the royal society of London. Series A. Mathematical and physical sciences*, 295(1442):300–319, 1966.
-

-
- [278] X. Wu, N. Tao, Y. Hong, J. Lu, and K. Lu. $\gamma \rightarrow \epsilon$ martensite transformation and twinning deformation in fcc cobalt during surface mechanical attrition treatment. *Scripta Materialia*, 52(7):547–551, 2005.
- [279] X. Wu, N. Tao, Y. Hong, G. Liu, B. Xu, J. Lu, and K. Lu. Strain-induced grain refinement of cobalt during surface mechanical attrition treatment. *Acta Materialia*, 53(3):681–691, 2005.
- [280] M.J. Bibby and J.G. Parr. The $\alpha \rightarrow \epsilon$ transformation in polycrystalline cobalt. Technical report, Alberta Univ. Edmonton, 1963.
- [281] H. Bibring, F. Sebilliau, and C.J. Bückle. The kinetics and morphology of the allotropic transformation of cobalt. *Inst Metals*, 87(71), 1959.
- [282] R. Ahmed and H. de Villiers-Lovelock. Friction and wear of cobalt-base alloys. In *Friction, Lubrication, and Wear Technology*. ASM International, 2017.
- [283] Y. Koizumi, S. Suzuki, K. Yamanaka, B. Lee, K. Sato, Y. Li, S. Kurosu, H. Matsumoto, and A. Chiba. Strain-induced martensitic transformation near twin boundaries in a biomedical Co–Cr–Mo alloy with negative stacking fault energy. *Acta materialia*, 61(5):1648–1661, 2013.
- [284] Y. Cao, S. Ni, X. Liao, M. Song, and Y. Zhu. Structural evolutions of metallic materials processed by severe plastic deformation. *Materials Science and Engineering: R: Reports*, 133:1–59, 2018.
- [285] N.R. Tao, X.L. Wu, M.L. Sui, J. Lu, and K. Lu. Grain refinement at the nanoscale via mechanical twinning and dislocation interaction in a nickel-based alloy. *Journal of materials research*, 19(6):1623–1629, 2004.
- [286] H.W. Zhang, Z.K. Hei, G. Liu, J. Lu, and K. Lu. Formation of nanostructured surface layer on AISI 304 stainless steel by means of surface mechanical attrition treatment. *Acta materialia*, 51(7):1871–1881, 2003.
- [287] I. Karaman, H. Sehitoglu, Y.I. Chumlyakov, and H.J. Maier. The deformation of low-stacking-fault-energy austenitic steels. *The Journal of The Minerals, Metals & Materials Society*, 54(7):31–37, 2002.
-

-
- [288] X.Y. Zhang, Y.T. Zhu, and Q. Liu. Deformation twinning in polycrystalline Co during room temperature dynamic plastic deformation. *Scripta Materialia*, 63(4):387–390, 2010.
- [289] Y.T. Zhu, X.Y. Zhang, and Q. Liu. Observation of twins in polycrystalline cobalt containing face-center-cubic and hexagonal-close-packed phases. *Materials Science and Engineering: A*, 528(28):8145–8149, 2011.
- [290] K. Edalati, S. Toh, M. Arita, M. Watanabe, and Z. Horita. High-pressure torsion of pure cobalt: hcp-fcc phase transformations and twinning during severe plastic deformation. *Applied Physics Letters*, 102(18):181902, 2013.
- [291] A. Korner and H.P. Karnthaler. Weak-beam study of glide dislocations in hcp cobalt. *Philosophical Magazine A*, 48(3):469–477, 1983.
- [292] L. Rémy, A. Pineau, and B. Thomas. Temperature dependence of stacking fault energy in close-packed metals and alloys. *Materials Science and Engineering*, 36(1):47–63, 1978.
- [293] M.H. Yoo and C.T. Wei. Slip modes of hexagonal-close-packed metals. *Journal of Applied Physics*, 38(11):4317–4322, 1967.
- [294] M.H. Yoo. Slip, twinning, and fracture in hexagonal close-packed metals. *Metallurgical transactions A*, 12(3):409–418, 1981.
- [295] M.A. Meyers, O. Vöhringer, and V.A. Lubarda. The onset of twinning in metals: a constitutive description. *Acta materialia*, 49(19):4025–4039, 2001.
- [296] Y.T. Zhu, X.Z. Liao, and X.L. Wu. Deformation twinning in nanocrystalline materials. *Progress in Materials Science*, 57(1):1–62, 2012.
- [297] K.Y. Zhu, A. Vassel, F. Brisset, K. Lu, and J. Lu. Nanostructure formation mechanism of α -titanium using SMAT. *Acta Materialia*, 52(14):4101–4110, 2004.
- [298] W.S. Choi, H.S. Ryoo, S.K. Hwang, M.H. Kim, S.I. Kwun, and S.W. Chae. Microstructure evolution in Zr under equal channel angular pressing. *Metallurgical and Materials Transactions A*, 33(3):973, 2002.
-

-
- [299] H. Kashani, A. Amadeh, and A. Ohadizadeh. Effect of temperature on the strain induced $\gamma \rightarrow \epsilon$ phase transformation in Stellite 21 during wear test. *Materials Science and Engineering: A*, 435:474–477, 2006.
- [300] I. Radu, D.Y. Li, and R. Llewellyn. Tribological behavior of Stellite 21 modified with yttrium. *Wear*, 257(11):1154–1166, 2004.
- [301] T. Ericsson. The temperature and concentration dependence of the stacking fault energy in the Co-Ni system. *Acta metallurgica*, 14(7):853–865, 1966.
- [302] W.M. Rainforth, R. Stevens, and J. Nutting. Deformation structures induced by sliding contact. *Philosophical Magazine A*, 66(4):621–641, 1992.
- [303] S.M. Kuo and D.A. Rigney. Sliding behavior of aluminum. *Materials Science and Engineering: A*, 157(2):131–143, 1992.
- [304] D.A. Rigney. Transfer, mixing and associated chemical and mechanical processes during the sliding of ductile materials. *Wear*, 245(1-2):1–9, 2000.
- [305] S.G. Maldonado, S. Mischler, M. Cantoni, W.J. Chitty, C. Falcand, and D. Hertz. Mechanical and chemical mechanisms in the tribocorrosion of a Stellite type alloy. *Wear*, 308(1-2):213–221, 2013.
- [306] G.N. Karimi, M.J. Carrington, J. Thomas, P.H. Shipway, D.A. Stewart, and T. Hussain. The role of microstructural development in the hydrothermal corrosion of cast and HIPed Stellite 6 analogues in simulated PWR conditions. *Corrosion Science*, 159:108141, 2019.
- [307] S. Holdsworth, F. Scenini, G. Burke, G. Bertali, T. Ito, Y. Wada, H. Hosokawa, N. Ota, and M. Nagase. The effect of high-temperature water chemistry and dissolved zinc on the cobalt incorporation on type 316 stainless steel oxide. *Corrosion Science*, 140:241–251, 2018.
- [308] T.Y. Kosolapova. *Carbides: Properties, Production, and Applications*. Springer US, 2012.
- [309] H.O. Pierson. *Handbook of Refractory Carbides & Nitrides: Properties, Characteristics, Processing and Applications*. Elsevier Science, 1996.
-

-
- [310] A. Kapoor. Wear by plastic ratchetting. *Wear*, 212(1):119–130, 1997.
- [311] A. Kapoor and K.L. Johnson. Plastic ratchetting as a mechanism of metallic wear. *Proceedings of the Royal Society of London. Series A: Mathematical and Physical Sciences*, 445(1924):367–384, 1994.
- [312] K.L. Johnson. Contact mechanics and the wear of metals. *Wear*, 190(2):162–170, 1995.
- [313] M. Yajima, M. Ishii, and M. Kobayashi. The effects of hydrostatic pressure on the ductility of metals and alloys. *International Journal of Fracture Mechanics*, 6(2):139–150, 1970.
- [314] L. Mosecker, D.T. Pierce, A. Schwedt, M. Beighmohamadi, J. Mayer, W. Bleck, and J.E. Wittig. Temperature effect on deformation mechanisms and mechanical properties of a high manganese C + N alloyed austenitic stainless steel. *Materials Science and Engineering: A*, 642:71–83, 2015.
- [315] M. Jayalakshmi, P. Huilgol, B.R. Bhat, and K.U. Bhat. Insights into formation of gradient nanostructured (GNS) layer and deformation induced martensite in AISI 316 stainless steel subjected to severe shot peening. *Surface and Coatings Technology*, 344:295–302, 2018.
- [316] V. Shrinivas, S.K. Varma, and L.E. Murr. Deformation-induced martensitic characteristics in 304 and 316 stainless steels during room-temperature rolling. *Metallurgical and Materials Transactions A*, 26(3):661–671, 1995.
- [317] T.S. Byun, E.H. Lee, and J.D. Hunn. Plastic deformation in 316LN stainless steel—characterization of deformation microstructures. *Journal of nuclear materials*, 321(1):29–39, 2003.
- [318] D.J. Michel, J. Moteff, and A.J. Lovell. Substructure of type 316 stainless steel deformed in slow tension at temperatures between 21 and 816 °C. *Acta metallurgica*, 21(9):1269–1277, 1973.

-
- [319] N. Nakada, H. Ito, Y. Matsuoka, T. Tsuchiyama, and S. Takaki. Deformation-induced martensitic transformation behavior in cold-rolled and cold-drawn type 316 stainless steels. *Acta Materialia*, 58(3):895–903, 2010.
- [320] M. Multigner, S. Ferreira-Barragáns, E. Frutos, M. Jaafar, J. Ibáñez, P. Marín, M.T. Pérez-Prado, G. González-Doncel, A. Asenjo, and J. González-Carrasco. Superficial severe plastic deformation of 316 LVM stainless steel through grit blasting: Effects on its microstructure and subsurface mechanical properties. *Surface and Coatings Technology*, 205(7):1830–1837, 2010.
- [321] M. Cuppari and S.F. Santos. Physical properties of the NbC carbide. *Metals*, 6(10):250, 2016.
- [322] C. Lin, C. Chang, J. Chen, and W. Wu. Hardness, toughness and cracking systems of primary $(\text{Cr,Fe})_{23}\text{C}_6$ and $(\text{Cr,Fe})_7\text{C}_3$ carbides in high-carbon Cr-based alloys by indentation. *Materials Science and Engineering: A*, 527(18-19):5038–5043, 2010.
- [323] P.J. Apps, J.R. Bowen, and P.B. Prangnell. The effect of coarse second-phase particles on the rate of grain refinement during severe deformation processing. *Acta Materialia*, 51(10):2811–2822, 2003.
- [324] S.S. Hecker, M.G. Stout, K.P. Staudhammer, and J.L. Smith. Effects of strain state and strain rate on deformation-induced transformation in 304 stainless steel: Part I. magnetic measurements and mechanical behavior. *Metallurgical Transactions A*, 13(4):619–626, 1982.
- [325] K.P. Staudhammer, L.E. Murr, and S.S. Hecker. Nucleation and evolution of strain-induced martensitic (bcc) embryos and substructure in stainless steel: a transmission electron microscope study. *Acta Metallurgica*, 31(2):267–274, 1983.
- [326] G. Kang, Y. Dong, H. Wang, Y. Liu, and X. Cheng. Dislocation evolution in 316L stainless steel subjected to uniaxial ratcheting deformation. *Materials Science and Engineering: A*, 527(21-22):5952–5961, 2010.
-

-
- [327] C. Gaudin and X. Feaugas. Cyclic creep process in AISI 316L stainless steel in terms of dislocation patterns and internal stresses. *Acta Materialia*, 52(10):3097–3110, 2004.
- [328] X. Feaugas. On the origin of the tensile flow stress in the stainless steel AISI 316L at 300 K: back stress and effective stress. *Acta materialia*, 47(13):3617–3632, 1999.
- [329] S. Kang, J. Jung, M. Kang, W. Woo, and Y. Lee. The effects of grain size on yielding, strain hardening, and mechanical twinning in Fe–18Mn–0.6C–1.5Al twinning-induced plasticity steel. *Materials Science and Engineering: A*, 652:212–220, 2016.
- [330] M.S. Pham, C. Solenthaler, K.G.F. Janssens, and S.R. Holdsworth. Dislocation structure evolution and its effects on cyclic deformation response of AISI 316L stainless steel. *Materials Science and Engineering: A*, 528(7-8):3261–3269, 2011.
- [331] K. Dutta, S. Sivaprasad, S. Tarafder, and K.K. Ray. Influence of asymmetric cyclic loading on substructure formation and ratcheting fatigue behaviour of AISI 304LN stainless steel. *Materials Science and Engineering: A*, 527(29-30):7571–7579, 2010.
- [332] Y. Dong, G. Kang, Y. Liu, H. Wang, and X. Cheng. Dislocation evolution in 316 L stainless steel during multiaxial ratchetting deformation. *Materials characterization*, 65:62–72, 2012.
- [333] A. Das. Cyclic plasticity induced transformation of austenitic stainless steels. *Materials Characterization*, 149:1–25, 2019.
- [334] Y. Li, D. Yu, B. Li, and X. Chen. Martensitic transformation of an austenitic stainless steel under non-proportional cyclic loading. *International Journal of Fatigue*, 124:338–347, 2019.

-
- [335] Q. Xue, E.K. Cerreta, and G.T. Gray. Microstructural characteristics of post-shear localization in cold-rolled 316L stainless steel. *Acta materialia*, 55(2):691–704, 2007.
- [336] Q Xue and G.T. Gray. Development of adiabatic shear bands in annealed 316L stainless steel: Part I. correlation between evolving microstructure and mechanical behavior. *Metallurgical and Materials Transactions A*, 37(8):2435–2446, 2006.
- [337] Q. Xue and G.T. Gray. Development of adiabatic shear bands in annealed 316L stainless steel: Part II. TEM studies of the evolution of microstructure during deformation localization. *Metallurgical and Materials Transactions A*, 37(8):2447–2458, 2006.
- [338] J.A. Venables. Deformation twinning in face-centred cubic metals. *Philosophical magazine*, 6(63):379–396, 1961.
- [339] J.W. Christian and S. Mahajan. Deformation twinning. *Progress in materials science*, 39(1-2):1–157, 1995.
- [340] S. Martin, S. Wolf, U. Martin, L. Krüger, and D. Rafaja. Deformation mechanisms in austenitic TRIP/TWIP steel as a function of temperature. *Metallurgical and Materials Transactions A*, 47(1):49–58, 2016.
- [341] Y. Tian, O.I. Gorbatov, A. Borgenstam, A.V. Ruban, and P. Hedström. Deformation microstructure and deformation-induced martensite in austenitic Fe-Cr-Ni alloys depending on stacking fault energy. *Metallurgical and materials transactions A*, 48(1):1–7, 2017.
- [342] T.G. Nieh, J. Wadsworth, and O.D. Sherby. *Superplasticity in metals and ceramics*. Cambridge university press, 2005.
- [343] M.Y. Gutkin, I.A. Ovid’Ko, and N.V. Skiba. Crossover from grain boundary sliding to rotational deformation in nanocrystalline materials. *Acta Materialia*, 51(14):4059–4071, 2003.

-
- [344] O.A. Kaibyshev. *Superplasticity of alloys, intermetallides and ceramics*. Springer Science & Business Media, 1992.
- [345] K. Huang and R.E. Logé. A review of dynamic recrystallization phenomena in metallic materials. *Materials & Design*, 111:548–574, 2016.
- [346] P. Heilmann, J. Don, T.C. Sun, D.A. Rigney, and W.A. Glaeser. Sliding wear and transfer. *Wear*, 91(2):171–190, 1983.
- [347] A.F. Smith. The friction and sliding wear of unlubricated 316 stainless steel at room temperature in air. *Wear*, 96(3):301–318, 1984.
- [348] T. Kjer. A lamination wear mechanism based on plastic waves. *Wear of Materials*, 1:191–198, 1987.
- [349] D.A. Rigney. The role of characterization in understanding debris generation. In *Tribology Series*, volume 21, pages 405–412. Elsevier, 1992.
- [350] E.M. Kopalinsky and P.L.B. Oxley. Explaining the mechanics of metallic sliding friction and wear in terms of slipline field models of asperity deformation. *Wear*, 190(2):145–154, 1995.
- [351] N.P. Suh. The delamination theory of wear. *Wear*, 25(1):111–124, 1973.
- [352] A.T. Alpas, H. Hu, and J. Zhang. Plastic deformation and damage accumulation below the worn surfaces. *Wear*, 162:188–195, 1993.
- [353] B.S. Hockenhull, E.M. Kopalinsky, and P.L.B. Oxley. An investigation of the role of low cycle fatigue in producing surface damage in sliding metallic friction. *Wear*, 148(1):135–146, 1991.
- [354] J.M. Challen, P.L.B. Oxley, and B.S. Hockenhull. Prediction of Archard’s wear coefficient for metallic sliding friction assuming a low cycle fatigue wear mechanism. *Wear*, 111(3):275–288, 1986.
- [355] A. Kapoor. A re-evaluation of the life to rupture of ductile metals by cyclic plastic strain. *Fatigue & fracture of engineering materials & structures*, 17(2):201–219, 1994.

-
- [356] A.D. Hearle and K.L. Johnson. Mode II stress intensity factors for a crack parallel to the surface of an elastic half-space subjected to a moving point load. *Journal of the Mechanics and Physics of Solids*, 33(1):61–81, 1985.
- [357] A.R. Rosenfield. A fracture mechanics approach to wear. *Wear*, 61(1):125–132, 1980.
- [358] T. Terachi, K. Fujii, and K. Arioka. Microstructural characterization of SCC crack tip and oxide film for SUS 316 stainless steel in simulated PWR primary water at 320 °C. *Journal of nuclear science and technology*, 42(2):225–232, 2005.
- [359] R. Soulas, M. Cheynet, E. Rauch, T. Neisius, L. Legras, C. Domain, and Y. Brechet. TEM investigations of the oxide layers formed on a 316L alloy in simulated PWR environment. *Journal of Materials Science*, 48(7):2861–2871, 2013.
- [360] Z. Duan, F. Arjmand, L. Zhang, and H. Abe. Investigation of the corrosion behavior of 304L and 316L stainless steels at high-temperature borated and lithiated water. *Journal of Nuclear Science and Technology*, 53(9):1435–1446, 2016.
- [361] J.L. Sullivan, T.F.J. Quinn, and D.M. Rowson. Developments in the oxidation theory of mild wear. *Tribology International*, 13(4):153–158, 1980.
- [362] J. Jiang, F.H. Stott, and M.M. Stack. Some frictional features associated with the sliding wear of the nickel-base alloy N80A at temperatures to 250 °c. *Wear*, 176(2):185–194, 1994.
- [363] F.H. Stott and G.C. Wood. The influence of oxides on the friction and wear of alloys. *Tribology International*, 11(4):211–218, 1978.
- [364] J. Jiang, F.H. Stott, and M.M. Stack. The role of triboparticulates in dry sliding wear. *Tribology International*, 31(5):245–256, 1998.
- [365] H. Kato and K. Komai. Tribofilm formation and mild wear by tribo-sintering of nanometer-sized oxide particles on rubbing steel surfaces. *Wear*, 262(1-2):36–41, 2007.

-
- [366] J. Glascott, F.H. Stott, and G.C. Wood. The effectiveness of oxides in reducing sliding wear of alloys. *Oxidation of metals*, 24(3-4):99–114, 1985.
- [367] F.C. Frank and B.R. Lawn. On the theory of Hertzian fracture. *Proceedings of the Royal Society of London. Series A. Mathematical and Physical Sciences*, 299(1458):291–306, 1967.
- [368] J.G. Li, M. Umemoto, Y. Todaka, K. Fujisaku, and K. Tsuchiya. The dynamic phase transformation and formation of nanocrystalline structure in SUS304 austenitic stainless steel subjected to high pressure torsion. *Reviews on Advanced Materials Science*, 18:577–582, 2008.
- [369] I.Y. Litovchenko, A.N. Tyumentsev, S.A. Akkuzin, E.P. Naiden, and A.V. Korznikov. Martensitic transformations and the evolution of the defect microstructure of metastable austenitic steel during severe plastic deformation by high-pressure torsion. *The Physics of Metals and Metallography*, 117(8):847–856, 2016.
- [370] Y. Ivanisenko, I. MacLaren, X. Sauvage, R.Z. Valiev, and H.J. Fecht. Shear-induced $\alpha \rightarrow \gamma$ transformation in nanoscale Fe–C composite. *Acta Materialia*, 54(6):1659–1669, 2006.
- [371] J.G. Li, M. Umemoto, Y. Todaka, and K. Tsuchiya. Formation of ultrafine grained structure in SUS 304 stainless steel produced by high pressure torsion (HPT). In *Materials Science Forum*, volume 561, pages 847–852. Trans Tech Publ, 2007.
- [372] I.Y. Litovchenko, A.N. Tyumentsev, N.V. Shevchenko, and A.V. Korznikov. Evolution of structural and phase states at large plastic deformations of an austenitic steel 17Cr-14Ni-2Mo. *The Physics of Metals and Metallography*, 112(4):412, 2011.
- [373] A.N. Tyumentsev, I.Y. Litovchenko, Y.P. Pinzhin, A.D. Korotaev, N.S. Surikova, S.L. Girsova, and V.A. Nesterenkov. A new mechanism of localization of deformation in austenitic steels: I. the model of nonequilibrium

-
- phase (martensitic) transformations in fields of high local stresses. *Phys. Met. Metallogr*, 95(2):186–195, 2003.
- [374] S. Lee, Y. Park, and Y. Lee. Reverse transformation mechanism of martensite to austenite in a metastable austenitic alloy. *Materials Science and Engineering: A*, 515(1-2):32–37, 2009.
- [375] M.S. Paterson. X-ray diffraction by face-centered cubic crystals with deformation faults. *Journal of Applied Physics*, 23(8):805–811, 1952.
- [376] L. Velterop, R. Delhez, T.H. de Keijser, E.J. Mittemeijer, and D. Reefman. X-ray diffraction analysis of stacking and twin faults in fcc metals: a revision and allowance for texture and non-uniform fault probabilities. *Journal of applied crystallography*, 33(2):296–306, 2000.
- [377] A.I. Ustinov and N.M. Budarina. Influence of planar defects on powder diffractograms of fcc metals. *Powder Diffraction*, 17(4):270–277, 2002.
- [378] S. Martin, C. Ullrich, D. Šimek, U. Martin, and D. Rafaja. Stacking fault model of ϵ -martensite and its DIFFaX implementation. *Journal of Applied Crystallography*, 44(4):779–787, 2011.
- [379] B.E. Warren. *X-ray Diffraction*. Courier Corporation, 1990.
- [380] A.I. Ustinov. Effect of planar defects in crystals on the position of powder diffraction lines. In *Defect and Microstructure Analysis by Diffraction*, pages 264–317. Oxford University Press, 2000.
- [381] P.S.G. Cross, G. Limbert, D. Stewart, and R.J.K. Wood. Ratcheting wear of a cobalt-chromium alloy during reciprocated self-mated dry sliding. *Wear*, 426:1142–1151, 2019.
- [382] E. Ma, Y.M. Wang, Q.H. Lu, M.L. Sui, L. Lu, and K. Lu. Strain hardening and large tensile elongation in ultrahigh-strength nano-twinned copper. *Applied physics letters*, 85(21):4932–4934, 2004.

-
- [383] F. Dong, P. Zhang, J. Pang, Q. Duan, Y. Ren, K. Yang, and Z. Zhang. Microstructure and mechanical properties of high-nitrogen austenitic stainless steels subjected to equal-channel angular pressing. *Acta Metallurgica Sinica (English Letters)*, 29(2):140–149, 2016.
- [384] Y. Wang, M. Chen, F. Zhou, and E. Ma. High tensile ductility in a nanostructured metal. *Nature*, 419(6910):912–915, 2002.
- [385] I. Gutiérrez-Urrutia and D. Raabe. Multistage strain hardening through dislocation substructure and twinning in a high strength and ductile weight-reduced Fe–Mn–Al–C steel. *Acta Materialia*, 60(16):5791–5802, 2012.
- [386] S.D. Andrews, H. Sehitoglu, and I. Karaman. Constriction energy in the presence of a solute field. *Journal of Applied Physics*, 87(5):2194–2203, 2000.
- [387] W. Hirst and J.K. Lancaster. The influence of speed on metallic wear. *Proceedings of the Royal Society of London. Series A. Mathematical and Physical Sciences*, 259(1297):228–241, 1960.
- [388] N.C. Welsh. The dry wear of steels I. the general pattern of behaviour. *Philosophical Transactions of the Royal Society of London. Series A, Mathematical and Physical Sciences*, 257(1077):31–50, 1965.
- [389] D.G. Farwick and R.N. Johnson. Thermophysical properties of selected wear-resistant alloys. Technical report, Hanford Engineering Development Lab., Richland, WA (USA), 1980.
- [390] C.S. Kim. Thermophysical properties of stainless steels. Technical report, Argonne National Lab., Ill.(USA), 1975.